ARCHIVES OF ACOUSTICS
18, 1, 3–15 (1993)

AUTOMATIC SPEECH SIGNAL SEGMENTATION WITH CHOSEN PARAMETRIZATION METHOD

Cz. BASZTURA and T. SAWCZYN

Institute of Telecommunication and Acoustics Wrocław Technical University
(50-317 Wrocław, ul. Janiszewskiego 7/9)

This paper is dedicated to the problem of automatic segmentation of a speech signal into so-called phonetic segments, i.e. speech signal segment with homogeneous physical structure which can be ascribed with adequate phonetic mean. This is the second trend in segmentation, as opposed to speech signal segmentation into short fixed segments.

A segmentation algorithm is presented. It is based on calculations of the phonetic function at speech, which makes it possible to find the boundaries of these phonetic segments.

The usability of three different parametrization methods — based on the analysis of zero-crossings, spectral analysis and linear prediction coding — was analyzed. No significant differences were observed in the efficiency of investigated parameters.

1. Introduction

A technological development of the civilized world has led to an increased demand for new means of man-machine communication. New methods of communication include automatic speech and speaker recognition, speech synthesis, among others. Simple ASR systems (Automatic Speech Recognition) are limited to the recognition of several to several hundred isolated words. A limited vocabulary, as well as a need for a definite articulation discipline from the operators are the shortcomings of this method [3, 4, 9]. Therefore, at the same time research has been performed on automatic recognition of continuous speech. Features disadvantageous from the point of view ASR are more clearly distinguishable during continuited language units. These defects are as follows:

— less clear pronounciation and greater differences between speakers,
— consonants pronounced in continuous speech are shorter,
— coarticulation effects are observed between words,
— variable influence of intonation and accent on the speech signal's physical structure.

Speech may be presented in the form of a between the words and weak made evident. This is an additional difficulty in the realization of ASR systems.

The classical ASR procedure requires the first necessary step to be the determination of the number and type of objects (classes), or in other words the so-called base code.

In the case of global recognition of a limited vocabulary the base code consists of all the words included in the vocabulary. When phonems are the base code (e.g. $M = 37$

phonems for the Polish language), then the recognition at the lowest level is limited to the recognition of phonems [2, 5, 6, 8]. In this case the problem of speech signal segmentation into phonetic segments, which can be assigned with phonem designations, arises. A quasistationary section of a speech signal, which can be assigned to a definite phonem or other unit of speech, is called a phonetic segment. Two parallel trends in segmentation can be distinguished [1, 7]:

— segmentation into established permanent quasistationary segments, in literature called also "implicit segementation"

— so-called "explicit segmentation", which consists in the segmentation into segments defined by phonetic transcription. In fact, it is a segmentation into defined above phonetic segments. Definite properties can be distinguished in both trends. Most important ones are presented below:

Constant segmentation

1. The number of segments depends on the word's length.
2. Segments are not related to the phonetic description.
3. Boundaries of segments are precisely defined.
4. There is a great number of segments.

Segmentation into phonetic segments

1. The number of segments is correlated with the description given from phonetic transcription.
2. Segments can be labelled in accordance to the phonetic description.
3. Boundaries of segments are approximate.
4. Limited number of segments.

Segmentation into permanent segments was applied in most cases of research on ASR for continuous speech. This results in a need of great storage capacity when segmentation of a word into 10 to 20 ms permanent segments is performed. Hence, the segmentation procedure became more complex. This led to increased interest in phonetic or quasi-phonetic (phonetic segments) segmentation. When the bulk of calculations are shifted to the segmentation procedure, then decision procedures on beyond acoustic levels can be layed-out more clearly.

Results of previous research [1, 2, 6] indicate that segments formed in the process of time decomposition of a speech signal can be divided into the following qualitative classes:

a) stationary segments,
b) transient segments,
c) short segments,
d) pause (silence).

The "overlapping" effect of physical structures of adjoining phonems is a serious problem in speech signal segmentation. For example:

— a voiced and an unvoiced phonem have overlapping formants and noise structures,

— a phonem and silence (or the other way around) appear at the beginning and end of a word or sequence.

In this case the main problems related with the application of phonetic segmentation are:

1. Selection of such a segmentation algorithm which would allow reproducible generation of a time function $P(t)$, then used as a basis for the determination of boundaries of segments, or their midpoints.

2. Selection of such parametrization methods which would ensure an effective description of the $P(t)$ function.

3. Determination of segmentation criteria and mean of the base code of obtained segments.

This paper is aimed at the investigation of possibilities of segmentation into phonetic segments on the basis of the phonetic function of speech FFM, including chosen parametrization and verification criteria.

2. Methods

2.1. Segmentation algorithm in the recognition process

As segmentation is to be applied in the continuous speech recognition system, it has to be performed with signal parametrization at the same time, but points on the axis, which denote boundaries of segments should be sent to the parametrization block in sequences. Figure 1 presents a simplified block diagram of an ASR input with segmentation.

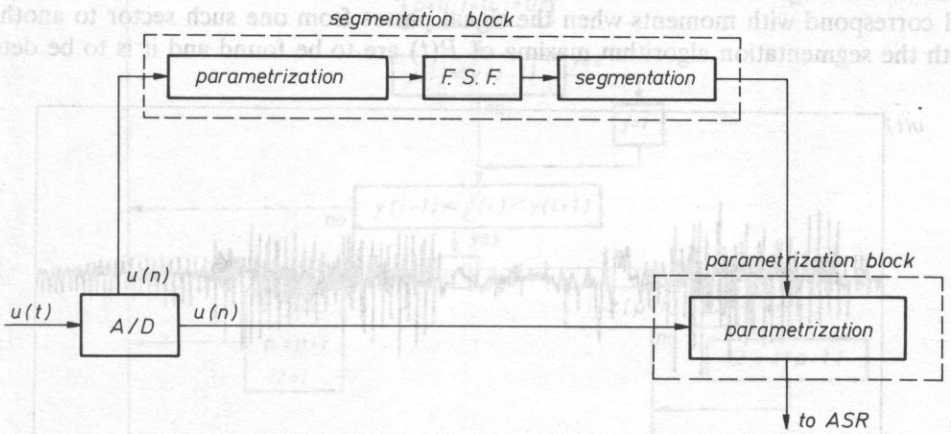

FIG. 1. Block diagram of the acoustic input system of the ARM system.

The input signal $u(t)$ is converted into digital form and then fed independently to two blocks: segmentation block and block of parametric discription. The segmentation block detects boundaries of segments in the arriving signal and transfers this information to the block of parameter extraction in the form of time marks. This is a general scheme, which has to be extended, by such elements for example as signal's buffer store or parametrization block system with a system of syntax rules in a back coupling loop, depending on the model of recognition system. It should be noted that in such a segmentation model, parametrization in the segmentation block and the block of the phonetic function parameter extraction have completely separate functions, although they can apply similar or identical techniques of parameter calculation, e.g. spectral analysis, linear prediction coding or distribution of time internals between zero-crossings of the speech signal.

2.2. *Segmentation procedure*

Three functional parts can be separated in the segmentation block:

1) parametrization,

2) calculation of the phonetic function of speech (F.F.M.), acting as a time function $P(t)$,

3) detection of segments boundaries on the basis of $P(t)$.

Following samples of the input signal $u(n)$ are grouped into time windows with length t_n and for every time point t a vector of parameters describing in a definite manner the state of the signal in the definite time window, is calculated (see part 3). Vectors of parameters are used to calculate $P(t)$ according to formula [2]

$$P(t) = \frac{1}{P} \sum_{p=1}^{p} \alpha_p * \left[\ln \frac{\mathbf{R}(t,p)}{R[(t-\tau),p]} \right]^2 \tag{1}$$

where: $\mathbf{R}(t,p)$ — vector of parameters in time window t_n, α_p — weight of p-parameter, P — number of parameters, τ — time shift.

Then boundaries of segments are determined on the basis of function $P(t)$. If we assume that the signal consists of short quasistationary sectors then boundaries of segments will correspond with moments when the signal passes from one such sector to another. With the segmentation algorithm maxima of $P(t)$ are to be found and it is to be deter-

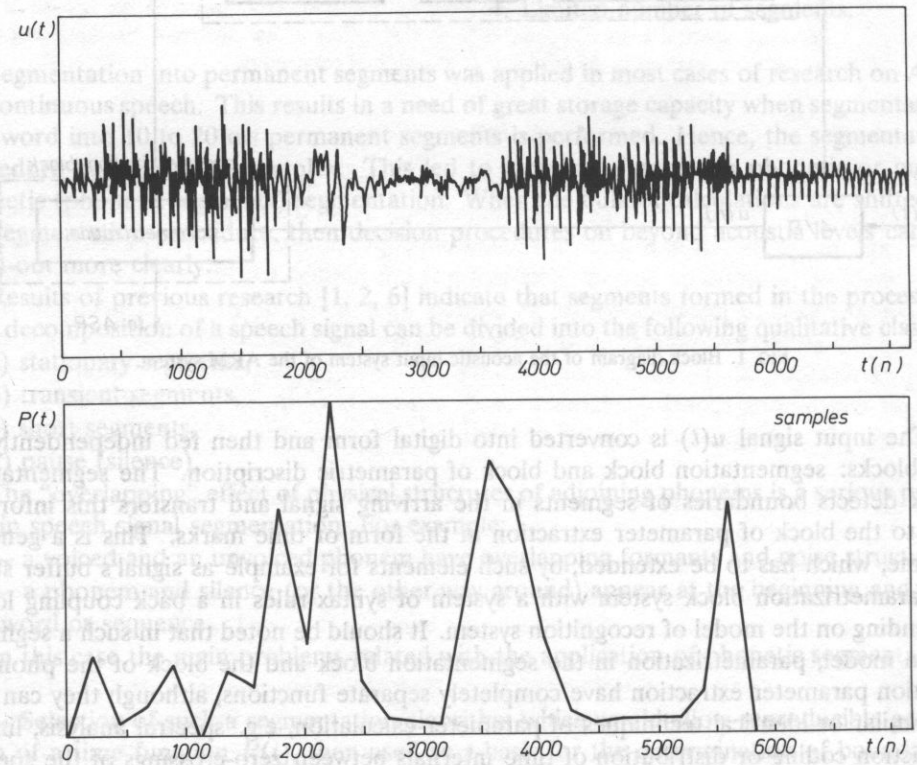

FIG. 2. Speech signal $u(t)$ and its phonetical speech function $P(t)$.

mined on the basis of certain definite additional criteria (discussed further in the paper after the algorithm itself is described) whether the instance indicated by the maximum can be a boundary between two successive segments. For example, Fig. 2 presents the signal of the word /oɕem/ („eight") and the phonetic function of speech for this signal achieved with the described above method with the use of parameters from FFT analysis.

The time function $P(t)$ has several local maxima which denote the boundaries between phonetic segments. They appear as an effect of even small changes in the signals spectral structure, specially within noise segment of speech phoneme, /ɕ/ and in segments accepted

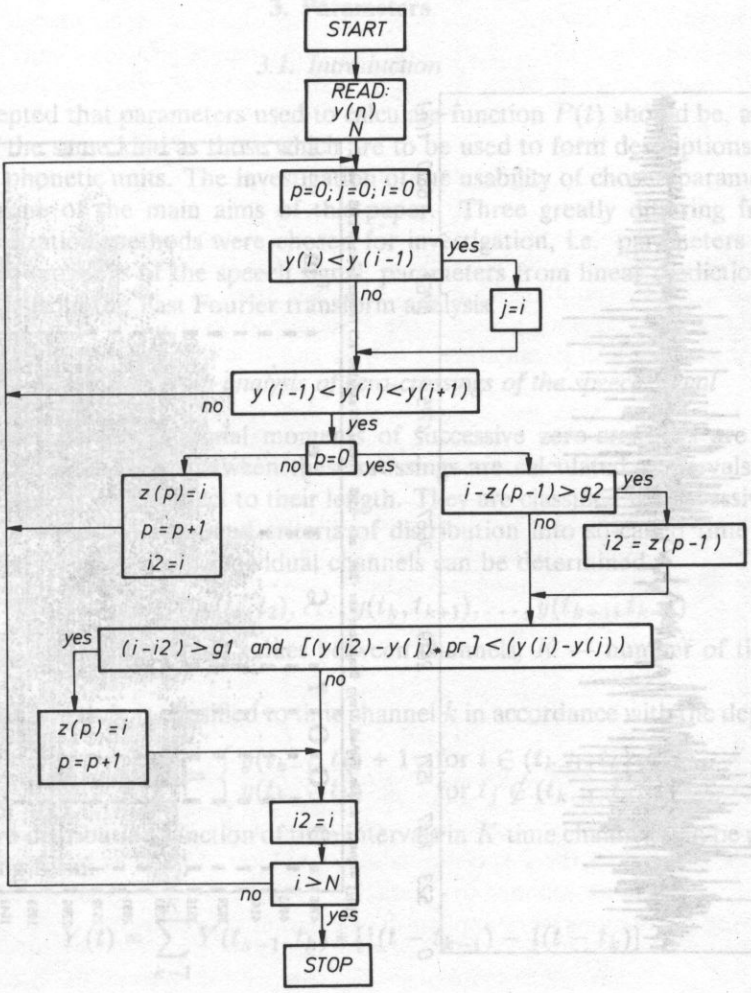

FIG. 3. Flow chart for segment detection algorithm.

as quasistationary (e.g. vowels) for individual or emotional changes in the articulation. The elimination of points denoting local maxima from the set of all hypothetical boundaries of segments is the greatest problem in the realization of the segmentation algorithm. There are two possible approaches here:

1. Application of adequate smoothing filters,
2. expert algorithm created on the basis of heuristic knowledge.

We have accepted the second approach in this paper. The block diagram of the algorithm is shown in Fig. 3.

Succeeding local maxima of function $P(t)$ are found in the algorithm. Every maximum is accepted as a prototype for determination of the boundary between phonetic segments. However, it is accepted that a maximum corresponds with the boundary between segments

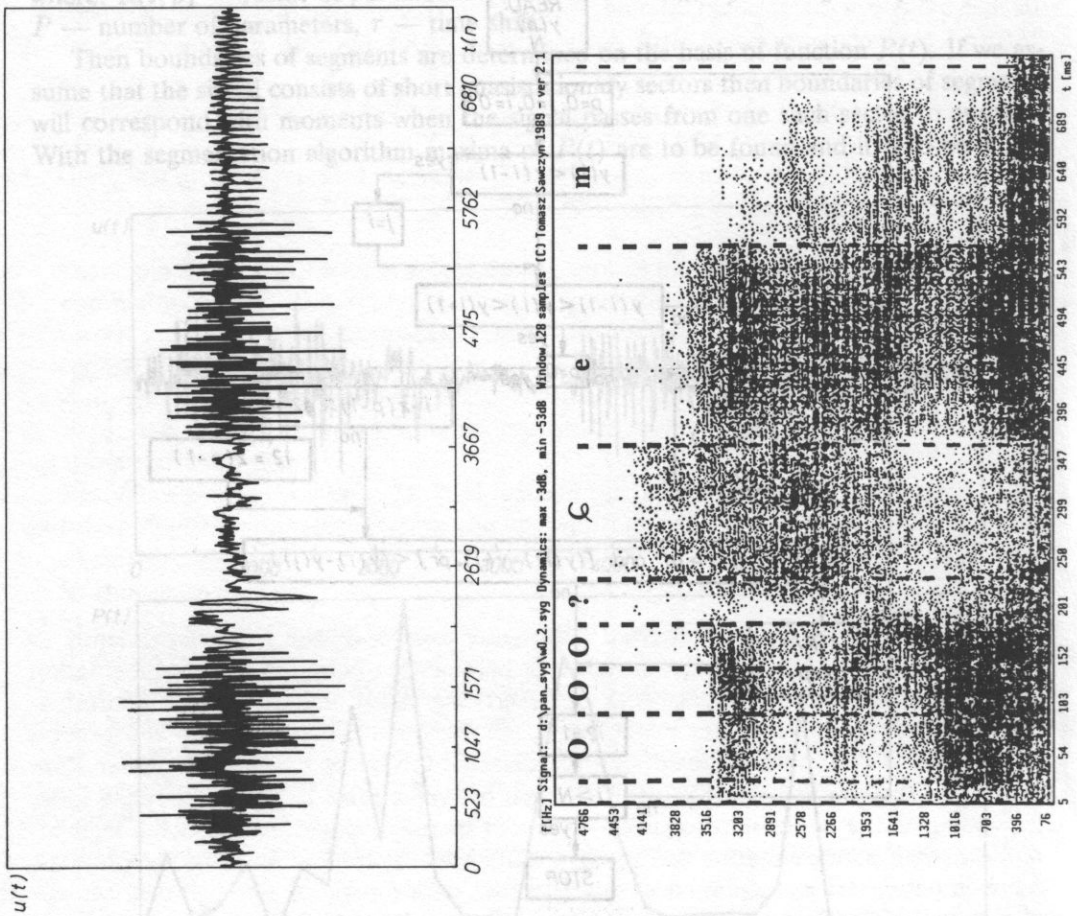

FIG. 4. Speech signal and its digital spectrogram with marked segments and phonetic description.

only after three conditions are checked:

1. the distance in time between the current checked maximum and preceding maximum can not be less than the minimal distance, denoted by $g1$, accepted from experiment;

2. if the distance between the current local maximum mb and local maximum mp, found directly before it, exceeds the complex maximal distance $g2$, then the maximum qualified as the boundary between segments is accepted as the last local maximum mp;

3. the relative value of the maximum has to exceed the assumed fraction of the relative value of the last maximum (pr)

Figure 4 presents the same signal as in Fig. 2 and its digital spectrogram word /osiem/ („eight") with marked boundries of segments obtained from the described algorithm.

3. Parameters

3.1. Introduction

It was accepted that parameters used to calculate function $P(t)$ should be, as far as it is possible, of the same kind as those which are to be used to form descriptions (images) of recognized phonetic units. The investigation of the usability of chosen parametrization methods was one of the main aims of this paper. Three greatly differing from each other parametrization methods were chosen for investigation, i.e. parameters from the analysis of zero-crossings of the speech signal, parameters from linear crediction coding, and parameters from the Fast Fourier transform analysis.

3.2. Parameters from analysis of zero-crossings of the speech signal

For the analysed speech signal moments of successive zero-crossings are detected and lengths of time intervals between these crossings are calculated. Intervals are then grouped and ordered with respect to their length. They are classified to successive groups according to previously determined criteria of distribution into so-called time channels [3]. The number of intervals in individual channels can be determined

$$y(t_d) = (t_0, t_1), y(t_1, t_2), \ldots, y(t_k, t_{k+1}), \ldots, y(t_{k-1}, t_{k=g}) \tag{2}$$

where: $t_d, t_1, \ldots, t_g$ — threshold values between channels, K — number of time channels.

An interval with length t_j is classified to time channel k in accordance with the dependence

$$y(t_{k-1}, t_k) = \begin{cases} y(t_{k-1}, t_k) + 1 & \text{for } t \in (t_{k-1}, t_k) \\ y(t_{k-1}, t_k) & \text{for } t_j \notin (t_{k-1}, t_k) \end{cases} \tag{3}$$

The cumulative distribution function of time intervals in K time channels can be presented in the following form:

$$Y(t) = \sum_{k-1}^{K} Y(t_{k-1}, t_k) * [1(t - t_{k-1}) - 1(t - t_k)] \tag{4}$$

where:

$$1(t) = \begin{cases} 0 & \text{for } t \ll 0 \\ 1 & \text{for } t > 0 \end{cases}$$

3.3. *Spectral parameters* (FFT)

FFT calculation algorithms given by G.D. BERGLAND and M.T. DOLAN [10] were used to calculate spectral parameters. Applied parameters satisfy equation

$$X(k) = \sum_{n=0}^{N-1} x(n) * e^{-j\frac{2\pi}{N}-nk} \tag{5}$$

where $x(n)$ — real input sequence, $X(k)$ — complex transform coefficients, $k, 0, 1, \ldots$ $\ldots, N/2$.

The signal was described with parameters, which were the signal's energies in 16 one-third octave frequency channels or 6 octave channels. The energy in individual frequency bands was calculated in accordance with the following formula:

$$Y_i = \frac{1}{K_i - P_i} * \sum_{j=P_i}^{K_i} [\mathrm{re}\, X(j)]^2 + [\mathrm{im}\, X(j)]^2 \tag{6}$$

where

$$P_i = f_i * N/f_{pr}\,,$$
$$K_i = f_{i+1} * N/f_{pr}\,,$$

f_i — boundary frequency between the $(i-1)$ and i frequency band, N — number of FFT samples, f_{pr} — sampling frequency of signal $x(n)$.

Before FFT was calculated, signals were standarized to the energy equal to unity. A Hamming's window with parameters $\alpha = 0.54$ and $\beta = 0.46$ was superimposed onto the signal.

3.4. *Linear prediction coding* (LPC) *parameters*

Algorithms given by J.D. MARKEL and A.H. GRAY Jr. [10] were applied to calculate these parameters. Linear prediction methods model the signals spectrum through a "only poles" type filter with transmittance function:

$$H(z) = G/A(z) \tag{7}$$

where

$$A(z) = 1 + \sum_{k=1}^{P} a_k z^{-1}$$

is the reverse filter function, G — amplification factor, a_k — prediction coefficient, and p is the number of poles or prediction coefficients of the model. If $H(z)$ is stable, then $A(z)$ can be realized in the form of a ladder-type filter. Coefficients of reflection which are related in a definite manner to prediction coefficients, are used to describe signals. The following expressions were applied in calculation procedures:

$$\begin{aligned} a_m^{(m)} &= k_m \\ a_j^{(m)} &= a_k^{(m-1)} + k_m a_{m-1}^{(m-1)}, \quad 1 \le j \le m-1 \end{aligned} \tag{8}$$

where $a_j^{(m)}$, $1 \le j \le m$ m — prediction coefficients order.

4. Experimental and results

4.1. Introduction

The basic questions, to which our research was to provide answers belong to two problem ranges. Within the first one, the dependence between the effectiveness of segmentation and type of parameters applied in calculations of the phonetic function of speech was to be investigated. While within the second range the effectiveness of automatic segmentation, i.e. carried out with the described algorithm, was compared with manual segmentation, i.e. conducted by an experienced phonetician.

The first one of these experiments was to give a confirmation of the thesis saying that it is possible to apply in FFM analysis parameters achieved from a simple and fast time analysis. This would be of great importance in the realization of systems working in real time. Results of the second experiment were also expected to confirm the given above thesis. They were also supposed to create a better understanding of the problem of segmentation into phonetic segments by comparing automatic and manual segmentation.

4.2. Analysis of segmentation parameters

Three types of parameters applied in FFM calculations were defined. A corpus of 10 words each repeated ten times by 2 speakers was analysed. Values of constants — $g1$, $g2$ and pr — were changed three times for every type of parameters. These values were dependent on the length of applied windows. Table 1 contains values of these parameters for all examined cases.

Table 1. Values of parameters of segmentation with three methods. P — number of parameters, N — length of window, t — shift of window, $g1, g2, g3$ — constants of segmentation algorithm, par 1, par 2, par 3 — sets of parameters.

Method	RICZ			FFT			LPC		
par.	par 1	par 2	par 3	par 1	par 2	par 3	par 1	par 2	par 3
P	8	8	8	16	16	16	12	12	12
N[pr]	150	150	300	128	128	256	150	150	300
[pr]	75	75	150	64	64	128	75	75	150
$g1$	1	5	3	2	5	3	1	5	2
$g2$	15	11	8	13	13	7	15	13	13
pr	0.1	0.1	0.2	0.1	0.2	0.2	0.1	0.2	0.2

In order to perform a comparative analysis a notion of a "coefficient of segmentation conformity" wzs, was introduced. Its definition is as follows:

$$wzs = \frac{1}{N} \sum_{i=1}^{N} \frac{lpw}{ls} \tag{9}$$

where lpw — number of overlapping segments in all repetitions of a word, ls — number of all segments in all repetitions of a word, N — number of words.
The wzs coefficient should be interpreted as a measure of segmentation reliability within one class. The greated the segmentation repeatibility, the better the definition of class standards, and hence increased recognition reliability.

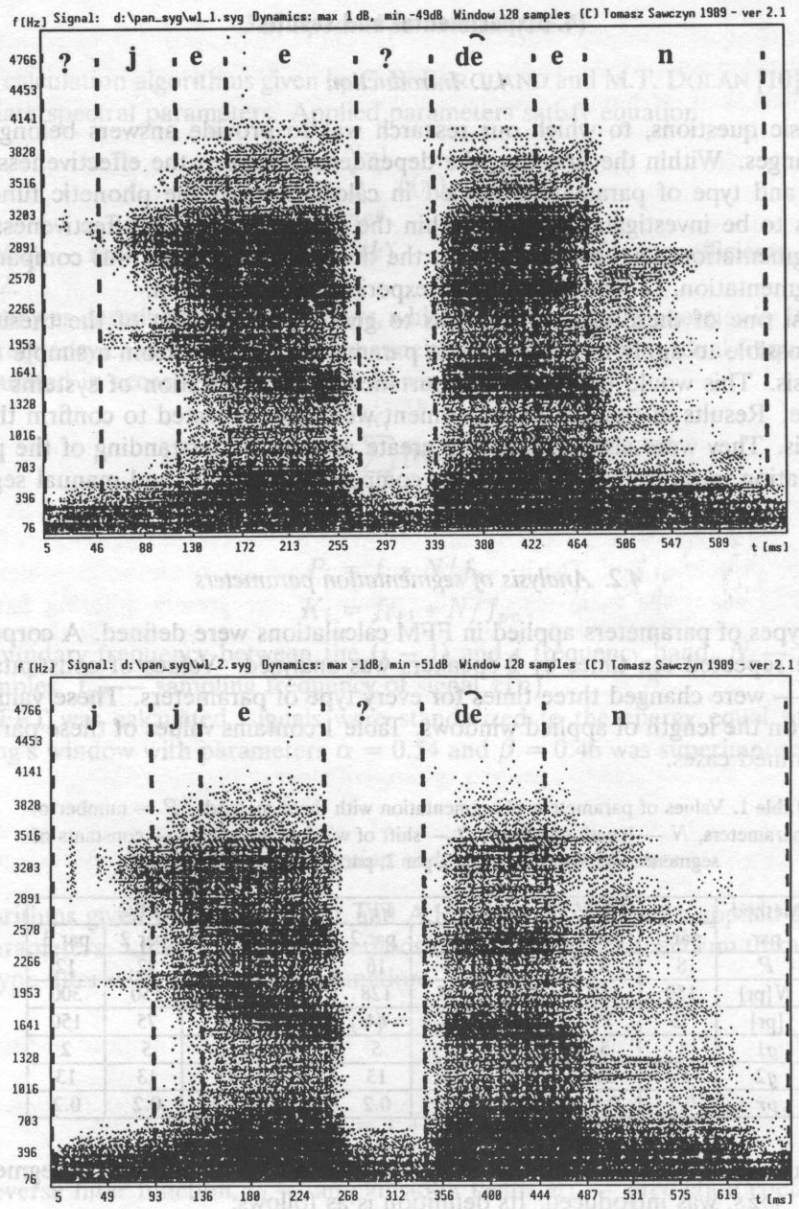

FIG. 5. Two repetitions of word /jeden/ (one) with marked segments.

Table 2 presents wzs coefficients calculated for all 10 words, three parametrization methods and various values of parameters, while in Fig. 5 we have two repetitions of the word "jeden" with marked segments. Except for some cases, wzs values considerably exceed the value of 0.5. High segmentation repeatibility within repetitions of the same words was stated on the basis of the analysis of mean values of the wzs coefficient, contained in the range from 0.59 to 0.8.

Table 2. Values of coefficient "wzs" for 10 words (10 Polish digits from "one" to „zero") and three parametrization methods. par 1, par 2, par 3 — sets of parameters as in Table 1

	RICZ			FFT			LPC		
	par 1	par 2	par 3	par 1	par 2	par 3	par 1	par 2	par 3
"1"	0.88	0.92	0.85	0.85	0.82	0.82	0.88	0.85	0.85
"2"	0.76	0.85	0.65	0.72	0.65	0.58	0.79	0.55	0.65
"3"	0.52	0.67	0.55	0.62	0.51	0.49	0.85	0.48	0.68
"4"	0.65	0.68	0.50	0.65	0.58	0.58	0.85	0.65	0.65
"5"	0.71	0.75	0.55	0.75	0.68	0.45	0.78	0.55	0.62
"6"	0.85	0.85	0.62	0.65	0.52	0.35	0.75	0.30	0.45
"7"	0.85	0.88	0.65	0.75	0.78	0.75	0.85	0.68	0.72
"8"	0.79	0.82	0.75	0.82	0.65	0.65	0.78	0.55	0.62
"9"	0.56	0.65	0.65	0.92	0.85	0.85	0.84	0.72	0.78
"0"	0.65	0.75	0.72	0.89	0.75	0.68	0.65	0.55	0.68
wzs	0.722	0.782	0.629	0.762	0.679	0.620	0.800	0.590	0.670
	0.11	0.09	0.07	0.09	0.11	0.15	0.06	0.15	0.1

Columns in Table 2 correspond with columns in Table 1, i.e. wzs values in the n-column in Table 2 were achieved with the application of parameters given in the n-column of Table 1.

4.3. Analysis of segmentation correctness

The analysis of segmentation correctness was performed on the basis of a comparison between manual and automatic segmentation time functions and digital spectograms of 120 words (40 words, repeated 3 times each) from a vocabulary defined in paper [4]. Manual segmentation was carried out by an experienced phonetician. For questionable boundaries, audio monitoring was also used. Automatic segmentation was done with the application of parametrization according to the method of analysis of zero-crossings with parameter values given in column 3 in Table 2. Figure 4 presents a spectrogram of the word /jeden/ (one) with segments calculated automatically and phonetical transcription resulting from such a segmentation.

As in the previous experiment, a certain measure was introduced to obtain a quantitative description of segmentation correctness. This is the coefficient of segmentation correctness — wps — defined as follows:

$$wps = \frac{lsp}{ls} \tag{10}$$

where lsp — number of correct segments resulting from the phonetic description, ls — number of segments obtained from automatic segmentation.

These coefficients have been calculated for all phonems occurring in the tested vocabulary of 40 words. The results are gathered in Table 3.

It resulted from analysis that frequently more than one segment occurs within one phonem, generally vowels and voiced sounds. Several segments appear in those places of the signal, which do not have an interpretation in the collection of Polish phonems (e.g. silence preceeding plosive consonants), and that segments contain frequently two or more phonems (e.g. in the word "jeden" (one) /j/ merges with /e/ in "dwa" (/dva/-two) — /d/ with /v/ and "pięć" (/p'ɛɲt͡ɕ/-five) a combination of /ɲ/ with /t͡ɕ/ occurs. In order

Table 3. Values of coefficient "*wps*" for all phonemes occuring in the vocabulary under investigation x — denotes the lack of a phoneme in the vocabulary 0 — denotes the lack of segmentation conformability (phoneme not delected)

phoneme	i	ɨ	e	a	o	u	p	b	t	d
wps	0.47	0.50	0.68	0.57	0.68	0.73	1.36	x	2.81	3.75

phoneme	c	ɟ	k	g	f	v	s	z	ʃ	ʒ
wps	x	x	2.40	1.80	1.50	1.50	1.50	1.00	0.57	0.00

phoneme	ɕ	ʑ	x	ts	dz	tʃ	dʒ	tɕ	dʑ	m
wps	0.64	x	0	0	x	1.09	x	0.47	1.50	1.05

phoneme	n	ɲ	ŋ	l	w	j	r
wps	1.50	1.00	4.50	0.75	1.00	1.33	2.18

to describe these two latter phenomena the notions of: a coefficient of indeterminable segment and a coefficient of "merged" segment were introduced. They are denoted by wsn and wsz, respectively, and defined as follows:

$$wsn = \frac{lsn}{ls}; \quad wsz = \frac{lsz}{ls} \tag{11}$$

where lsn — number of all indeterminable segments, lsz — number of all merged segments, ls — number of all segments. The wps coefficient can be interpreted on the basis of described above phenomena. If there is more than one phonetic segment within a phonem, then the wps value exceeds one. The effect of merging or indetermination of a phonetic segments results in a wps value below one. wsn and wsz values indicate the relative number of merged and indeterminable segments. The lower these values are the better the segmentation is. wps values for vowel phonem range from 0.47 to 0.73, what means that on the average there was twice as many phonetic segments as phonem. There was also twice as many phonetic segments for unvoiced phonems /ɕ, ʃ, t͡ʃ/. Automatic segmentation was found to agree with manual segmentation g for phonem /z/ and /ɲ/. In other cases the wps values exceeds 1 and for phonem /t, d, k/ it exceeds even 2. This value indicates a strong tendency to merge these phonems with order ones. wsz and wsn values are equal to 0.22 and 0.067 respectively.

5. Conclusions

This research is related in the sense of applied methods to an earlier paper by BASZTURA, JURKIEWICZ and TYBURCY [4]. Authors of this paper applied the procedure of the phonetic function of speech to segmentation in spectral parametrization. Owing to the dissemination of modern calculation techniques, including A/D conversion and new analysis methods of the speech signal [3], it was possible to widen and continue this research. A similar conception of segmentation can be also found in the mentioned previously paper [1].

The radically different parametrization methods were used in investigations:

— spectral, one based on FFT calculations,

— temporal, based on the analysis of zero-crossings,

— linear prediction coding.

As it results from Table 2, among others, comparably good segmentation results were

achieved with all these methods. This means that the $P(t)$ calculation algorithm and division into phonetic segments is effective, and that the parameters are evaluated from such requirements, as the rate and complexity of the procedure. In respect this, the distribution of time intervals between zero-crossings of a signal meets accepted effectiveness postulates, expressed by coefficients wzs and wps, and calculation rate, at best.

Other parameters, such as spectral or prediction for example used in the parametrization block (see Fig. 1) can be applied at the same time to determine boundaries of segments. This conclusions finds confirmation in Table 2.

Results grouped in Table 3 are of statistic, quantitative as well as qualitative meaning. The complexity of the problem of automatic segmentation can be exhibited on the basis of physical parameters. A wide span of values of the wps coefficient indicates how difficult it is to establish uniform criteria, which would lead to a reduction of the effect of phoneme separation into several segments ($wps < 1$), or merging of two phonems into one ($wps > 1$). These tendencies are also quantitatively defined by introduced here coefficients of merged and indeterminable segments.

On the basis of results achieved from our research a thesis can be formulated that this method of segmentation can advantageously influence the solution to the problem of continuous speech recognition. This thesis should find confirmation in experiments of automatic recognition of phonetic segments and recognition of words and continuous speech on this basis. The topic will be included among others, in further research which will apply "explicite" segmentation in automatic recognition of voices independently of the content of the statement. This is voice recognition with initial recognition of model linguistic elements, applied as key elements [11].

References

[1] R. ANDRE-OBRECHT, *A new statistical approach for the automatic segmentation of continuous speech signals*, IEEE Trans. on Acoustics, Speech and Signal Processing, **36**, 1, 29–39 (1988).

[2] Cz. BASZTURA, J. JURKIEWICZ, E. TRYBURCY, *Phonetic function of speech F.F.M. Applied in continuous speech signal segmentation* (in Polish) Archiwum Akustyki, **4**, 4, 121–130 (1979).

[3] Cz. BASZTURA, *Acoustic sources signals and images* (in Polish), WKiŁ, Warszawa 1988.

[4] Cz. BASZTURA, W. MAJEWSKI, W. BARYCKI, *Effectiveness estimation of parameters of a global description of words in simple systems of automatic speech recognition* (in Polish), (placed for printing in Archives of Acoustics).

[5] A.M.L. DIJK-KAPPERS, *Comparison of parameter sets for temporal decomposition*, Manuscript no. 62 Institute of Perception Research, Eindhoven, The Netherlands, T.b.s.t.: Speech Communication 1988.

[6] A.M.L. DIJK-KAPPERS, S.M. MARKCUS, *Temporal decomposition of speech*, Manuscript no 608/11 Institute for Perception Research Eindhoven. The Netherlands. T.b.s.t.: Speech Communication 1988.

[7] D.J. HERMES, *Vowel-onset detection*, Manuscript no 601/11 Institute for Perception Research Eindhoven, The Netherlands, T.b.s.t: Speech Communication 1988.

[8] J. KACPROWSKI, R. GUBRYNOWICZ, *Automatic recognition of Polish vowels using a method of spectrum segmentation* In: Speech Analysis and Synthesis Ed. W. Jassem vol.2 PWN, Warszawa 1970 pp. 51–170.

[9] W.A. LEA [Ed], *Trends in speech recognition*, Prentice Hall Inc. Englewood Cliffs 1980.

[10] *Programs fordigital signal processing* „IEEE Press 1979.

[11] J. ZALEWSKI, Text dependent speaker recognition in noise. Proc. Eurospeech 89 vol.1 Paris 1989 p. 287–289.

Received November 28, 1989; English version September 17, 1990

ARCHIVES OF ACOUSTICS
18, 1, 17–32 (1993)

MICROSTRUCTURE OF SOUND: FORMANTS IN THE DYNAMICAL SPECTRA OF VIOLIN SOUNDS

H. HARAJDA*, W. MIKIEL**, P. GABRYELCZYK* and P. FEDYNIUK*

*Laboratory of Acoustics, Pedagogical University
65-069 Zielona Góra, Pl. Słowiański 6
**Speech Acoustics Laboratory, Institute of Fundamental
Technological Research, Polish Academy of Sciences
(00-049 Warszawa, Świętokrzyska 21)

The aim of the present study was to obtain the picture of the structural changes occuring in the spectra of a violin sound, with the four bowing techniques: detaché, staccato, legato and martele. FFT analysis has been carried out using the system VOLYZER [19] and SPLIT [13] on IBM XT personal computer. Experimental material selected for this investigation consisted of the isolated sounds g (196 Hz), d^1 (293.7 Hz), a^1 (440 Hz), e^2 (659.3 Hz) and d^3 (1175 Hz) obtained with five instruments. Total number of randomly selected dynamical spectra, was 35. The tone structures have been analysed within 0–220 ms timescale, in 20 ms segments. In this time span the spectrum continually undergoes the changes comprising the range of the spectrum, the number of the formant maxima and their amplitude levels. Three types of formants exist: continuous, non-continuous and fragmentary. The changes of the position of the formant maxima on the frequency scale, the forms in which the amplitude levels of these maxima vary, the durations of the specific formant creation and the stabilization of the full formant set in the spectrum of sound have been analysed.

1. Introduction

In vast literature devoted to the acoustic problems of a violin sound, the natural frequency patterns of vibrating plates relating to so-called material resonances and airborne resonances of the instruments (refered to as "Helmholtz's air resonances") are those most widely dealt with [18]. Despite of the rich experimental material and broad discussions, both problems still remain open [17]. The natural frequencies of the instrument affect its frequency characteristics. The frequency response functions are either obtained from direct monitoring of the amplitude of vibrations at the locations of interest of the instrument (corpus or the bridge) or recording the amplitude of the acoustic signals resulting from these vibrations. In the analysis of resonant structures of frequency response functions when seeking the vocal attributes of an instrument, one may use the term "formant responses" [1]. The term "formant" can also be defined as the maximum on the envelope of the sounds spectrum.

The particular sounds of stringed instruments can be characterized by their detailed structure, also called the microstructure, consisting in the changes of frequency, inten-

sity and spectral structure [16]. Performance of the violin music features a wealth of these intrinsic sound changes [8], [9]. Among other things, it relates to the possibility of applying different bowing techniques. It has been found, in the course of preliminary studies, that the formant patterns in the dynamical spectra of bow generated natural sounds of a violin, as well as the frequency, undergo changes as a function of time [5]. These changes concern the position and amplitude of the formant's maxima. The shifts on the frequency scale of the formant's maxima do not posses a single tone local change character (as exemplified by the study made by B.M. MOORE [15]), but occur in whole ensemble of the partials of a given sound [17]. There are various causes for it. Among other factors, these changes may result from the change of a system of forces, acting on an instrument during different forms of the bow and string interaction [11], [12].

The purpose of the present study is to obtain an analytical picture of structural changes occuring in the process of formation of a dynamical spectrum of natural, isolated sounds of a violin using various bowing techniques, especially including formants patterns.

2. Scope and methods used in the study

Fundamental goal of the investigations described in this paper was to examine a possibility to select the most characteristic structural features of the bowing techniques like: detaché, legato, staccato and martele, using the methods of analysis of the profile of dynamical spectra of a violin sounds.

The specific tasks are as following:

— to determine the changes occuring in the formant pattern during the time of formation of an violin sound,

— to determine the change in amplitude levels of the formant maximum in the sound spectrum in this time,

— to analyse a stabilization process of the formant's pattern.

a. Experimental

Five instruments have been selected for the investigation, including two antique, but regularly in use violins, namely, B. DANKWART'S (17 century violin), (Da) and the violin (Am) from N. AMATI'S shop (16/17 century), two violins from contemporary artists violin-makers (these two instruments, further refered to as Ca and Vi, had been awarded the high prizes at VII th International Wieniawski Competition of Violin-Makers in Poznań, in 1986) and an experimental violin (Ka), whose back plate was finished in a non-standard way.

The instruments were played by a professional musicians with academic degree. The four bowing techniques were used in exciting the isolated sounds in the performed tests consisting g, d^1, a^1, e^2 and d^3 sounds.

Following points have been ascertained with the aim to standarize the conditions of the performance:

— all the recordings took place in the same location with precisely determined configuration of the player and the microphone,

— the violinist repeatedly performed the test sounds on all five instruments in the same test configuration,

— playing vibrato was avoided,

— the violinist was provided an opportunity of a rehearsal of the tests using all five instruments,

— in order to adjust to the modified requirements of the test, regarding a duration of signals and their intensity level, the player was making preliminary performances,

— always the same bow and rosin was used.

With regard to the fact, that every natural sound signal of stringed instruments is an individual and irreproducible phenomenon, the performer of the tests was only provided with general instructions necessary to minimize the differentiation of intensity levels and durations of the produced sounds. He had a freedom of performing the particular tests as to obtain best tone of an instrument when playing "*mf*". Detailed measurement of the intensity level and time during the test, was abandoned. There is no opportunity though, to impose unified criteria for all the signals under study, since they are bound to be of a different character, due to the accepted choice of the different techniques of playing a violin.

The purpose of applying the detaché and legato technique is to obtain quasi-stationary signals, while staccato and martele produces impulse-like-signals. The violinist took a fixed position with reference to the microphone by stepping on a marked place on the floor. The microphone was mounted opposite the bridge in the distance 30 to 35 cm. The amplitude level of the generated signal was monitored before each group of tests, to enable the performer to adjust the dynamics to within 75 to 80 dB range and to adjust the duration of the signal. The violinist was timing the play in such a way, as to obtain one pluck of bow per second with the detaché technique, one sound per second in legato, two with martele and four with staccato techniques.

Recordings have been made in M. Groblicz concert hall in the Museum of Musical Instruments in Poznań the same in which violin instruments were rehearsed at the all International H. Wieniawski Competitions of Violin Makers, as well as the acoustic tests associated with the H. Wieniawski Competitions [5].

The sounds were recorded with tape recorder model MP 223. Best recordings were chosen for the detailed analysis, of which 35 were randomly selected, with due representation of all four performing techniques.

b. Spectral analysis

Spectral analysis was conducted with fully computerized method using an PC IBM XT. Two programs: a modified SPLIT-Signal Analysis Program [13], [14] and System VOLYZER [19], have been used. Sampling rate amounted to 50000 samples per second (kS/s), filter cut-off frequency was 25 kHz at the attenuation 80 dB/octave. Signal segmentation time was 20 ms. The dynamics of the spectra was studied within 0 to 220 ms time interval (Fig. 1). The choice of such an interval was made on the basis of the published data [3], [17] and the results of the authors own preliminary analyses where it is believed that the adopted time-span should encompass the sound formation period (attack) and beginning of the steady state (see Fig. 1). The coding of individual signals is shown in Table 1.

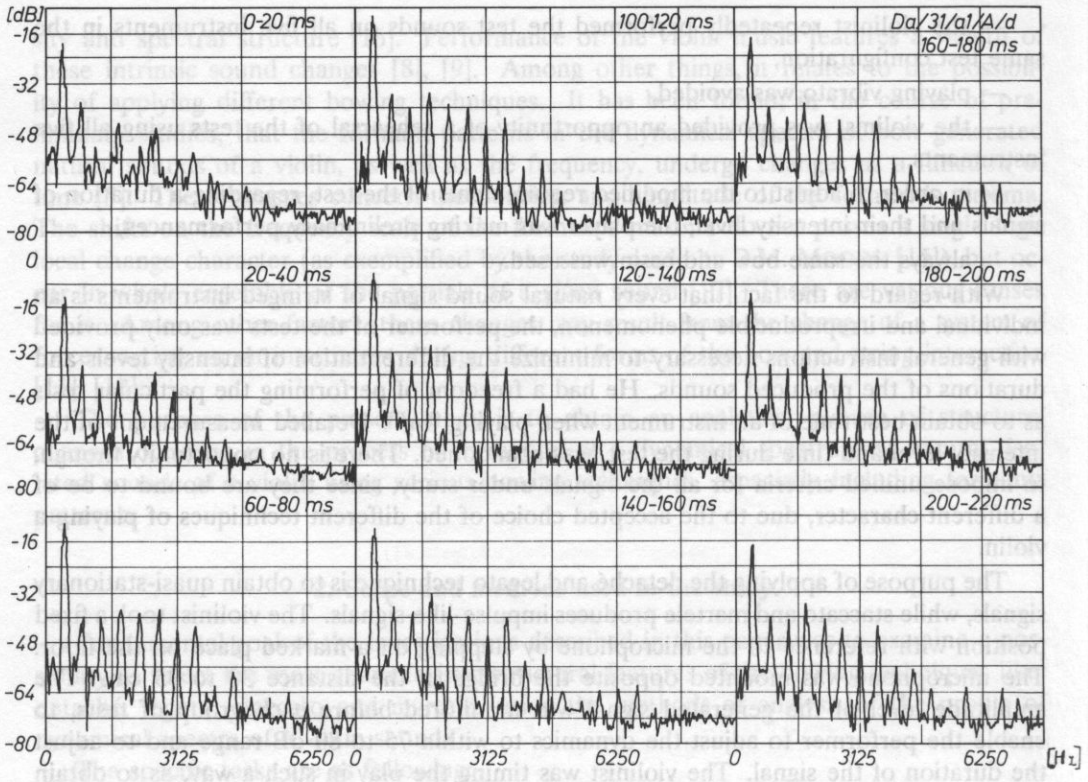

FIG. 1. Time-evolution of the dynamic spectrum of Da31 a^1/A detaché sound.

Table 1. Coding system of the sounds data

1	Da,Ka,Am,Ca,Vi
2	od 1 do 35
3	g, d^1, a^1, e^2, d^3
4	G,D,A,E
5	s,m,l,d

1. Instruments symbol.
2. Sounds number.
3. Sounds frequency: g [196 Hz], d^1 [297.3 Hz], a^1 [440 Hz], e^2 [659.3 Hz], d^3 [1175 Hz]
4. String.
5. Techniques: s — staccato, m — martele, l — legato, d — detaché.

3. Processing and the analysis of the results

The sound material for the analysis are collected in Table 2.

Table 2. List of the sounds selected for the analysis

Sound	Instrument	Techniques			
		detaché	legato	staccato	martele
g	Da	g/G – (29)	—	—	—
	Ca	g/G – (30)	—	—	—
	Ka	g/G – (2)	—	g/G – (5)	—
d^1	Da	—	d^1/D – (10)	—	—
a^1	Da	a^1/A – (17)	a^1/A – (11)	a^1/A – (14)	a^1/A – (8)
		a^1/A – (31)	a^1/A – (16)	a^1/A – (19)	a^1/A – (9)
		a^1/G – (15)	—	—	a^1/A – (35)
		a^1/D – (18)	—	—	—
	Ca	a^1/A – (32)	—	—	—
	Ka	a^1/D – (4)	a^1/A – (28)	a^1/A – (3)	a^1/A – (7)
	Am	a^1/A – (22)	a^1/A – (23)	a^1/A – (21)	a^1/A – (26)
	Vi	a^1/A – (33)	—	—	—
e^2	Da	—	e^2/D – (12)	—	—
	Ca	e^2/E – (34)	—	—	—
	Ka	e^2/E – (6)	e^2/D – (1)	—	—
	Am	—	—	e^2/E – (24)	e^2/E – (25)
d^3	Da	—	—	—	d^3/E – (13)
	Am	d^3/E – (27)	—	d^3/E – (20)	—

Every dynamical spectrum of a sound was undergoing an individual careful analysis. Frequency range of the partial tones in a spectrum and its variability within the separate sounds during the signal persistance, was measured, aimed at obtaining an exact characteristics of the analysed sounds. It has been accepted, that this range is defined by the highest harmonic recorded at least 4 dB above noise level.

Following structural features have been examined in the analysis of the fine structure of a sound:

— distribution of the formants on frequency scale,

— changes of the amplitudes of formants maxima in the duration time of signal,

— time in which the complete formant structure developes.

Formant maximum was identified as the maximum of an amplitude envelope only, if the discrete component tone at which the maximum was localized, exceeded by at least 3 dB, amplitude levels of the adjacent minima on this envelope. Such a predominance creates conditions to effect an acoustic impression by a formant [6], [7].

a. The range of tone components in a spectrum

The range of tone components occuring in the spectra of different sounds of a violin is largely diversified. In spite of the standarization of experiments i.e. the conditions of a sound generation and recording, the sounds of the same pitch, excited with different instruments or with different strings as well as those produced by diverse techniques may, vary with regard to their harmonics contents.

Table 3. Changes of the range of the partials n in a dynamical spectrum of a^1 sound of a violin with reference to the initial state n_1

Technique	Instrument	n_1	$\Delta n = n_k - n_1$ Segmentation Time [ms]									
		0–20	20–40	40–60	60–80	80–100	100–120	120–140	140–160	160–180	180–200	200–220
m	7	15	0	−3	9	9	10	18	16	16	18	18
	8	18	0	−3	−4	−4	−4	−4	−4	−4	−4	−4
	9	10	0	2	1	2	1	1	1	0	0	0
	26	15	3	4	3	3	3	3	3	3	—	—
	35	13	0	8	10	8	12	4	8	8	7	13
l	28	14	−5	0	−1	−4	−1	0	−1	−4	−4	2
	16	15	0	0	0	−1	0	1	1	1	1	1
	11	9	2	11	6	5	5	5	5	8	8	7
	23	13	0	3	11	3	1	2	3	7	4	1
s	3	9	6	7	12	13	13	13	8	7	—	—
	14	15	0	−4	−5	−5	−5	−5	−5	−6	−7	−7
	19	20	−3	−4	−4	−6	−6	−10	−10	—	—	—
	21	13	1	0	0	0	1	0	−1	−2	−3	−4
d	4	12	0	−2	1	2	−1	0	0	−1	−1	−2
	17	10	2	3	0	1	1	0	1	1	0	1
	31	12	0	0	3	3	3	2	1	3	3	4
	32	13	10	6	3	3	3	11	12	11	13	5
	33	8	0	0	2	1	0	0	1	0	0	1
	15	7	0	8	9	1	4	4	3	1	3	5
	18	11	−2	−4	−2	−3	−3	−2	−2	−3	−3	−2
	22	5	3	6	6	8	6	6	6	7	8	7

In Table 3 the results are collected of the analysis of the range changes for a^1 sounds grouped according to various techniques excitation. In the column "n_1" a number is given of the tone components limiting spectral range obtained at the onset of a tone (0–20 ms). In the following columns, the changes of this number, recorded in the process of the spectrum development and calculated with reference to the value of n_1, are given. The results are indicative of the fact, that the changes occur in all these sounds and adopt various forms. In many instances these are oscillational changes. Using staccato technique, for one of these sounds the spectral range was observed to increase up to a certain maximum value and was subsequently, systematically decreasing, with two other sounds the maximum range occured at the beginning of the spectrum, then also diminished. In the fourth sound, a stable pattern was maintained for the first 140 ms, later the range maximum was reduced. In the presented group of 21 spectra, in five cases the oscillations did not exceed 3 dB, which can be understood as a quasi-stabilization For 10 sounds these oscillations were larger. When using martele, detaché and legato techniques, the range and the forms of these changes were diversified; the least changes took place in case of legato. With only 3 spectra, a maximum of the range was recorded at the moment of impact of the bow on the string.

Various factors, like for example, the forces pattern resulting at the contact point of strings and a bow (this factor frequently quoted) [11], [12]. There is no doubt that the design of instruments and material properties are of great importance [2], [10]. Evidently,

apart from oscillations of the frequency [8], [9], the oscillation of the maximum range of a spectrum often occur as a micro-structural feature of the violin sound.

b. Time and frequency distribution of formant maxima

Detailed analysis of the dynamic spectra, conducted with regard to the process of time development of the formant pattern within a sound, allows to distinguish three kinds of the formants: those distinctly stable which persist continuously, with perhaps only a single break during the whole sound duration (Rs), those nearly continuous (with three very short pauses, at most) (Rn) and the formants arising instantaneously at various frequencies (Rf). The latter should be referred to as "flickering".

In Figs. 2, 3 and 4, these three different sets of formants are exemplified. The first shows the formants of a^1/A sound of various instruments (Fig. 2), the second set refers to a^1/A sound of Dankwart's violin excited with varying bowing techniques (Fig. 3) and the third — the sounds a^1 and e^2 excited with legato technique (Fig. 4). The solid line connect formant's maxima of the stable and the discontinuous formants, occurring in the relevant timescale. In a few sounds, particularly in case of the techniques martele and legato, deviations of the formants frequencies within the range of two neighbouring harmonics, take place. It may result from a modification, during the sound generation, of the system of forces exciting oscillations in the sound box of the instrument (repositioning of the bow on the strings, for instance). Then, various parts of the resonant plates, of different eigen-frequencies, become active. Their patterns depend on several factors, including resonant wood structure and the shaping of an instrument. Numerous response functions have been published by several authors, which evidence the possibilities of these factors to have an effect on the generated sound [4]. The formant patterns in the spectra of various instruments, are remarkably different. In all a^1/A sound the lowest formant is present continuously. The "flickering" formants preferably occur at the higher frequencies of the particular sounds. They arise in great number when detaché or staccato techniques are used (more than 17, in g and a^1 sounds spectral). These observations are illustrated in Fig. 5, comprising all the results of the analysis, of the whole set of the investigated sounds spectra. This figure plots the maximum numbers of the formants presented during a sound time-history, are grouped according to the bowing technique used in the experiment (Fig. 5). In the two groups of stable and discontinuous formants, the latter represented 19% within the staccato technique group, 17% — detaché, 14% — martele, whereas in the legato group, the discontinuous formants represented only 9%. In Fig. 6 the maximum numbers of formants in the spectra of particular sounds are given as a function of the maximum ranges of these spectra.

General trend of the dependence of the formants on the number of partial tones is clearly drawn. The correlation coefficient calculated with Spearman's ranking method is 0.79, which points to a high correlation between the spectral range and the number of formants. It results, to some extent, from the fact, that the number of partials is always of limited influence on the number of formants. For example, only three formants may arise within six partials pattern. From the dispersion of the results, it becomes evident that the number of harmonics is not the only factor decisive on the number of formants.

In Fig. 7, the overall range of the number of formants is presented together with the respective spectral ranges, obtained in the durations of a^1/A sound, with different bowing

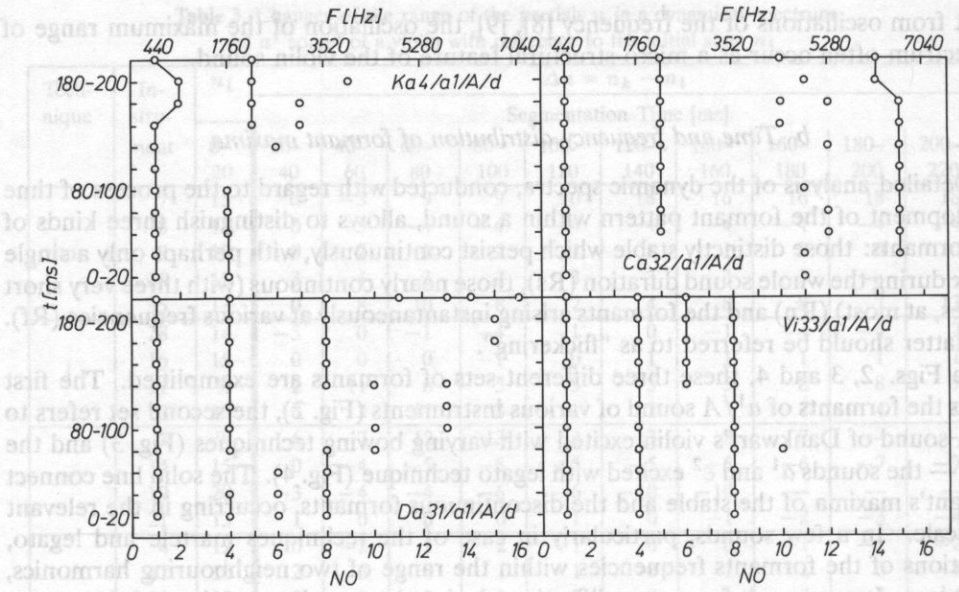

FIG. 2. Distribution of formant maxima in a^1/A sound spectra of various instruments (t — segmentation time, NO — number of a harmonic, F — frequency).

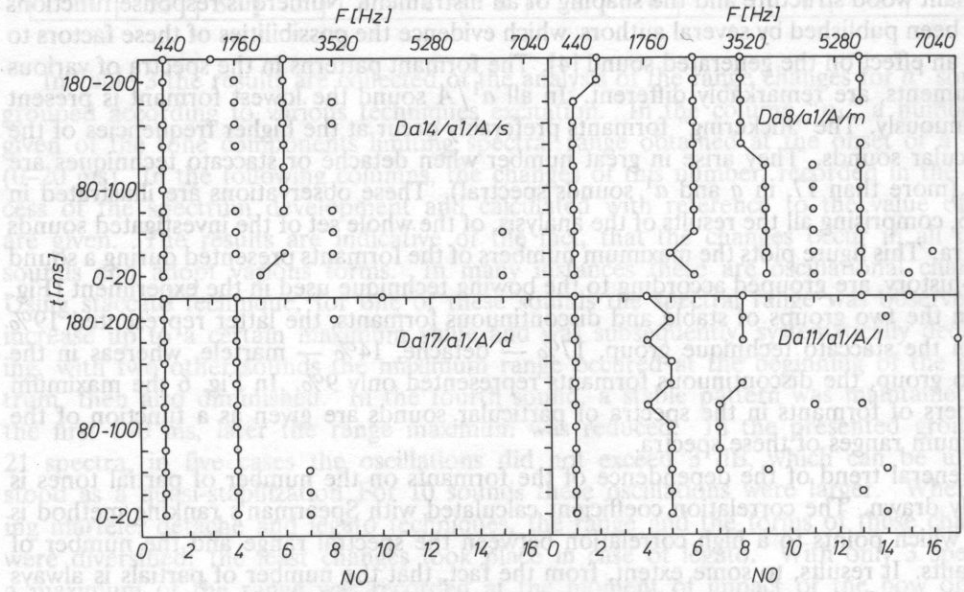

FIG. 3. Distribution of formant maxima of a violin sound a^1/A Da at different bowing techniques (t — segmentation time, NO — number of a harmonic, F — frequency).

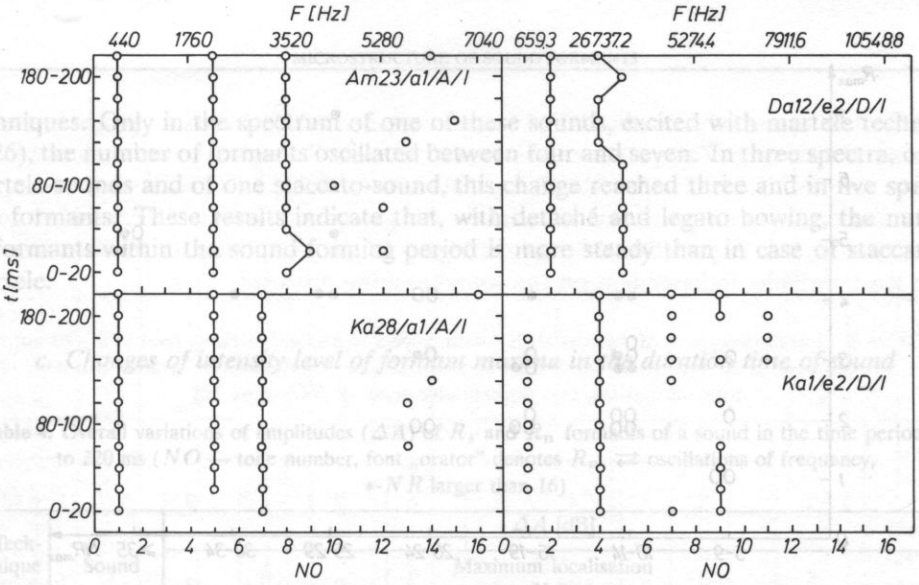

FIG. 4. Distribution of formant maxima of legato generated sounds (t — segmentation time, NO — number of a harmonic, F — frequency).

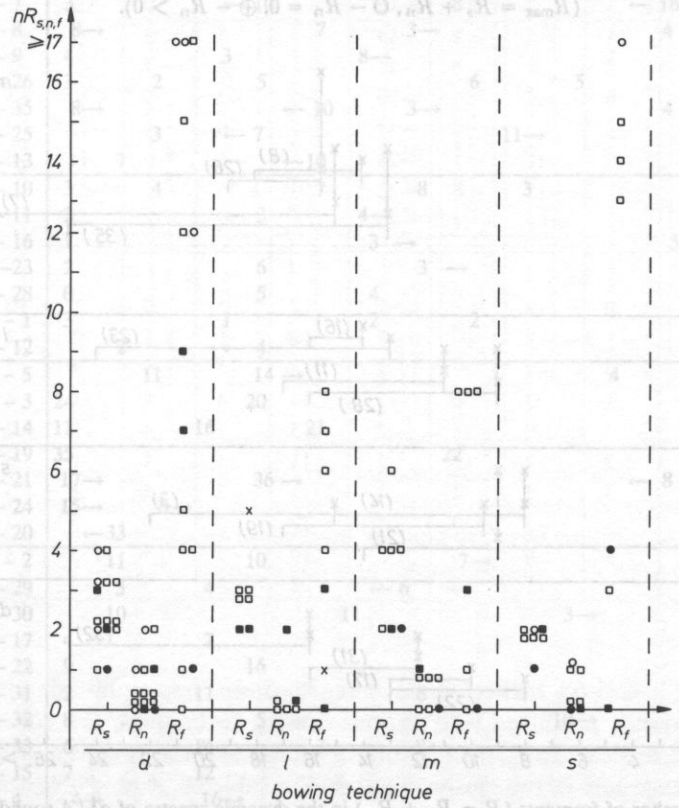

FIG. 5. Number of formants ($nR_{s,n,f}$) in a sound spectrum at various bowing techniques (sound symbols used: ○ — g, x — d^1, □ — a^1, ■ — e^2, ● — d^3).

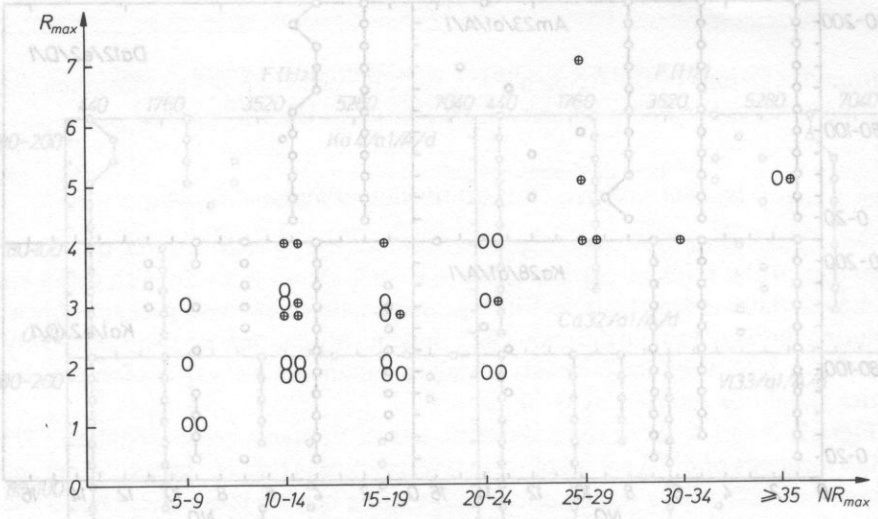

FIG. 6. Maximum numbers of formants (R_{max}) during the time period 20 ms to 220 ms, in the sounds 1 to 35, with reference to the maximum ranges ($N R_{max}$) ($R_{max} = R_s + R_n$, O $- R_n = 0$, $\oplus - R_n > 0$).

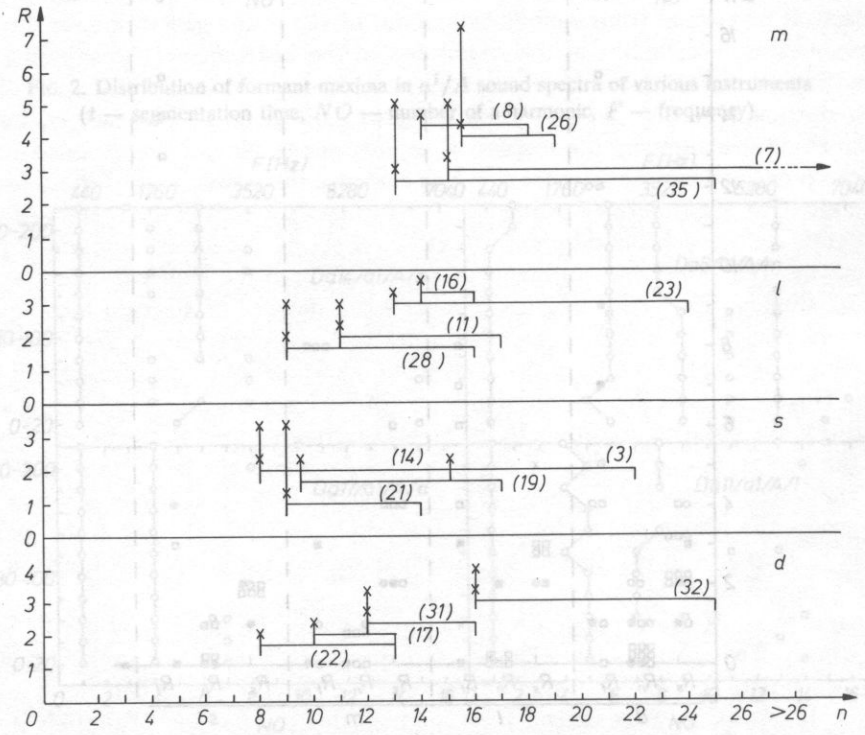

FIG. 7. Number of formants ($R = R_s + R_n$) in the dynamic spectra of a^1/A sounds during the time period from 20 to 220 ms (n — number of the harmonics corresponding to a spectral range, ⌐¬ span of a spectral range, ↕ overall range of the formants variability.

techniques. Only in the spectrum of one of these sounds, excited with martele technique (#26), the number of formants oscillated between four and seven. In three spectra, of two martele-sounds and of one staccato-sound, this change reached three and in five spectra, two formants. These results indicate that, with detaché and legato bowing, the number of formants within the sound forming period is more steady than in case of staccato or martele.

c. Changes of intensity level of formant maxima in the duration time of sound

Table 4. Overall variations of amplitudes (ΔA) of R_s and R_n formants of a sound in the time period 20 to 220 ms (NO — tone number, font „orator" denotes R_n, $\rightleftarrows$ oscillations of frequency, $*$-NR larger than 16)

Technique	Sound	ΔA [dB] Maximum localisation NO 1	2	3	4	5	6	7	8	9	10	11	12	13	14	15	16
	a^1/A – 7	3			←	10				8				←	16	15	
	– 8	8→					7		3→						4		
	– 9	4			3			8→									
m	– 26	3		2		5				6		5				13	4*
	– 35	8→				← 10			3→					4			
	e^2/E – 25			3	←	7					11→						
	d^3/E – 13		7			←10											
	d^1/D – 10	3		4			7		8		3						
	a^1/A – 11	2			←	3		4→									
	– 16	1						3	→					5→			
l	–23	2				6			3	→							
	– 28	0				5		4									
	e^2/D – 1	3			1			2		2							
	– 12		2		←	4											
	g^2/G – 5			11		14	→						4				
	a^1/A – 3	24				20											
	– 14	11			16		21										
s	– 19	35								22							
	– 21	17→				36	→							← 8			
	e^2/E – 24	15→		8→													
	d^3/E – 20	←33															
	g/G – 2		11			10				7→						9	
	– 29		5		4				← 6							12*	
	– 30		10					11					3→			10*	
	a^1/A – 17	4			7												
	– 22	9				16											
	– 31	2			11				8								
d	– 32	8				5							10→			←12	
	– 33	6			14			3		2							
	a^1/G – 15	7			12												
	a^1/D – 4	4→			16→												
	– 18	10			7		10										
	e^2/E – 6				←11			14									
	– 34	6						7							4	7	
	d^3/E – 27	3															

Table 4 comprises the amplitudes of formant maxima of R_s and R_n type (in brackets) and their positioning. The greatest variations in an overall formant pattern occur for the staccato sounds; the smallest are the changes are observed for the legato sounds. Also, the differentiation between particular sounds of each group is different. In case of staccato excited sounds it is larger than those of the legato origin. Amplitude of the first formant is the least variable, independent on the sound exciting process.

Table 5. Overall changes A of the partials NR with respect to a sound intensity level in 0 – 20 ms time-segment of dynamic spectrum of a^1/A sound of Dankwart's violin (font "orator" denotes formant maxima, t — segmentation time → NO above 12)

t [ms]	ΔA [dB]											
	NO											
	1	2	3	4	5	6	7	8	9	10	11	12
a) Da14 staccato												
20–40	5	2	0	6	−13	−2	0	9	3	3	−1	0
40–60	8	4	2	9	−7	−3	3	10	3	3	0	4→
60–80	10	4	2	10	−12	−2	2	9	2	2	0	—
80–100	10	4	3	9	−13	−3	3	3	1	−1	—	—
100–120	9	2	1	6	−21	−4	−2	−7	−3	−3	—	—
120–140	7	0	−2	3	−20	−6	−2	−2	−10	−5	—	—
140–160	5	−2	−6	2	−17	−7	−6	−1	−11	2	0	2
160–180	1	−7	−11	−1	−25	−7	−5	−6	−12	−6	—	—
180–200	−4	−11	−12	−6	−25	−20	−11	−15	−13	—	—	—
200–220	−11	−11	−11	−11	−30	−23	−12	−14	—	—	—	—
b) Da17 detaché												
20–40	0	0	−1	−2	−1	−12	0	0	0	0	−2	
40–60	0	−1	−2	0	−2	10	1	2	1	−2	−4	
60–80	1	0	−7	0	2	23	4	6	4	1	0	
80–100	2	1	3	0	−1	14	4	6	6	4	1	
100–120	2	2	0	2	2	13	1	4	3	2	0	
120–140	3	2	−2	2	2	15	1	4	0	0	0	
140–160	3	3	3	4	1	15	−2	5	6	5	0	
160–180	3	3	−3	5	4	19	0	6	5	2	−1	
180–200	4	4	0	5	5	19	−3	7	3	4	0	
200–220	4	4	11	5	4	21	−5	3	3	5	1	

In Table 5a, b and 6a, b the typical changes of the time-amplitude structure of the partials of a^1 sounds produced with various bowing techniques, are collected. All the formant maxima are emphasized with "orator" font. Several discontinuities can be seen in the time dependences of the maxima, e.g. #14 in Table 6a, #11 in Table 6b, #8 in Table 5a. The most stable formant patterns occur in "legato" group and the highest number of "flickering" formants, of the largest amplitude changes, can be found in "detaché" group. It does not rule out an existence of these patterns in other bowing techniques, but they appear most characteristically in legato and detaché.

Table 6. Changes of a intensity level ΔA of the partials NR with respect to the intensity level measured in 0–20 ms segment, of the dynamic spectrum of a^1/A sound of Dankwart's violin (font "orator" denotes the formant maxima, t — segmentation time, → NO above 15)

t [ms]	ΔA [dB]														
	NO														
	1	2	3	4	5	6	7	8	9	10	11	12	13	14	15
a) Da11 legato															
20–40	1	−1	4	2	2	−1	−1	3	3	5	5	0	0	4	0
40–60	1	2	5	3	3	−1	1	4	5	5	5	0	5	0	0
60–80	1	−2	7	2	1	−2	−1	3	4	7	2	0	0	4	0
80–100	1	0	6	1	1	−6	−2	4	7	4	5	0	0	4	0
100–120	1	−3	7	3	−1	−5	−4	6	6	−8	5	0	5	0	0
120–140	1	1	6	5	2	−4	−3	6	6	0	5	0	0	0	0
140–160	2	−1	8	3	1	−2	−4	6	7	8	0	0	0	0	0
160–180	2	2	8	6	3	−5	−2	7	6	8	0	0	0	0	0
180–200	2	−1	9	4	1	−6	−4	6	6	11	5	0	0	4	4→
200–220	2	3	7	7	3	2	−7	8	8	4	0	0	4	0	4
b) Da8 martele															
20–40	10	8	4	5	9	4	3	12	10	4	0	4	5	6	10→
40–60	14	9	5	1	7	4	0	12	12	3	4	2	8	8	2
60–80	13	11	−2	4	5	8	−11	16	11	8	5	5	8	10	−4
80–100	12	12	−5	4	7	8	0	16	12	9	4	4	9	9	−6
100–120	12	12	−14	0	6	8	−9	16	10	8	3	7	8	8	−5
120–140	12	12	−11	2	4	7	−2	17	7	7	1	3	6	1	−2
140–160	8	10	−5	0	−5	1	−3	14	2	2	−4	2	−1	5	−5
160–180	9	13	−4	6	1	7	1	17	7	4	−2	1	5	10	−1
180–200	8	13	−6	7	3	6	2	16	8	3	−2	−6	5	8	0
200–220	6	13	−5	8	4	6	5	17	8	4	-3	−6	4	5	−4

Some formants R, occur repeatedly on the same harmonic tones. One may expect, that these frequencies coincide with the resonant maxima of an instrument. Activation of these resonances, featured as the sound formants, depends on several conditions. Similarly to the spectral range, the amplitudes of formant maxima undergo continuous transformations in time. Only in few cases the formants change monotonically, following the same pattern in the whole frequency range.

d. Time development of a complete formant structure

Table 7 contains the times of the formation of R_s and R_n formant patterns within 20 to 220 ms time segment. The data from the first segment 0–20 ms were disregarded, because, as it frequently happens in this time span, a harmonic structure is not fully developed yet and a strong noise component is present. A formant pattern is regarded quasi-stable, when its maximum amplitudes change less than 5 dB; the time it takes to reach such a state is accepted as the time of the quasi-stabilization.

Table 7. Formation of R_s and R_n formant patterns within 0–220 ms timescale, (t_p — initial time of a formant, t_sA — time of amplitude quasistabilization, n_sA — unstable amplitude)

Technique	Sound	t_p [ms]		t_sA [ms]
		R_s	R_n	
	a^1/A – 7	80	40	100
	– 8	20	—	nsA
	– 9	20	—	100
m	– 26	60	40	100
	– 35	60	—	100
	e^2/E – 25	20	60	60
	d^3/E – 13	20	—	80
	d^1/D – 10	20	—	80
	d^1/A – 11	60	—	40
	– 16	20	—	40
l	– 23	20	—	60
	e^2/D – 1	20	40	40
	– 12	20	—	40
	g/G – 5	20	40	nsA
	a^1/A – 3	40	—	80
	– 14	20	40	nsA
s	– 19	20	—	nsA
	– 21	20	—	nsA
	e^2/E – 24	20	20	nsA
	d^3/E – 20	40	—	nsA
	g/G – 2	60	—	120
	– 29	40	60	100
	– 30	40	40	140
	a^1/A – 17	20	—	60
	– 22	40	—	120
	– 31	20	—	140
d	– 32	60	60	160
	– 33	120	—	120
	a^1/G – 15	40	—	nsA
	a^1/D – 4	20	—	nsA
	– 18	60	—	nsA
	e^2/E – 6	20	—	nsA
	– 34	40	60	180
	d^3/E – 27	20	—	40

The time of a formant creation R_s, for the sounds under investigation, vary between 20 and 60 ms, except for one sound (#7) generated with martele technique, where it amounted to 80 ms and the sound #33, excited with detaché technique, where it was 120 ms. The non-stabilized formants developed during 40 to 60 ms, irrespectively of the bowing technique. The quasi-stabilization of the complete formant pattern can be attained within 40 ms. It only occurs with martele, legato and detaché techniques, but in the latter case, the spectral structure of four tones was not stable within 220 ms time span. Generally, the staccato sounds are not stable, as far as their amplitudes are concerned.

4. Conclusions

Results of the analysis of the dynamical spectra of 35 violin sounds, intoned with various bowing techniques, indicate that during the attack stage and their transition into a

quasi-steady state to (0 to 220 ms), the observed structures undergo various modifications. These changes may be considerable and subsequently may influence the forms of tone perception. The obtained results positively verify the approach taken by POLLARD who, referring to the microstructure of musical tones, includes the changes of such features as pitch and loudness together with the effects of timbre in his definition of "microstructure" [16].

Following conclusions may be drawn:

1. Irrespective of the bowing technique used during the process of a violin sound formation (attack), structural changes occur in spectral range and the formant structure. As a rule, the harmonic structure is preceeded by as short period of anharmonicity. No correlation was found between the changes in the spectral range and the changes in formant structure.

2. Spectral range is an individual attribute of a signal. Namely, in the attack stage, changes of this range assume various forces. When staccato is used, a two-step form prevails: the spectral range increases very quickly, then gradually decreases. With other techniques these changes are individually divergent. The legato features the least diversified spectral ranges.

3. During the attack stage, separate formants undergo transformations, irrespective of their positioning. These transformations do not sustain a unified form of the whole arrangement within a sound. Formant maxima can be divided into three groups: stable, discontinuous and fragmentary, according to their continuity in time. Irrespective of the bowing technique, the first formant maximum is mostly continuous. Fragmentary maxima, most frequently occur at the higher harmonics of a signal. In the sounds excited with the technique detaché, these maxima are observed more often than with the other bowing techniques.

Positioning of the stable and/or discontinuous formant maxima on frequency scale, often (approx. 30%) undergoes deviations within two neighbouring harmonics. In the stage of the development of a signal pattern the number of formant maxima oscillates. This features is more frequent with staccato and martele techniques than with detaché and legato.

4. Amplitudes of formant maxima of all the sounds of violin, pass through numerous and diversified changes, of which the oscillatory changes occur most often. The variability of these maxima is most pronounced with staccato, and the smallest for legato technique.

5. Generally, the time of a formation of an individual formant does not exceed 60 ms, sporadically the upper limits reach higher values. With the three techniques: detaché, legato and martele, a quasi-stabilization of the whole formant pattern may already be reached after 40 ms. However, in the group of the investigated signals, the upper limit was 80 ms and 100 ms, for the legato and martele techniques, correspondingly. These times are longer than the time of initial transients (51 ms), chosen by MCINTYRE and WOODHOUSE in their attempt to simulate the martele-signals [3], in case of the detaché technique, the time required for the formant structure of separate sounds to reach quasi-stabilisation is individually, very diversified. CRAMER suggests, that initial transients in the case of legato are longer than with martele technique [3]. It may however, refer only to the process of a signal amplitude formation. When the structure formation is concerned, the obtained results of analyses indicate that the stabilization in the legato technique lasts shorter as compared to martele technique.

6. The above arguments point to an individual character exhibited by the ensemble of structural changes of a violin sounds intoned by the same technique, irrespective of which

technique is used. It is related to an simultaneous effect of various factors on the process of a signal formation. They are more numerous in the natural, bow excited sounds than in the acoustic characteristics of an instrument obtained with laboratory methods, since they also contain contributions due to "the violinist's menagerie", the term refered to by MCINTYRE and WOODHOUSE [11].

The obtained results elucidate the problem of the internal changes occuring in the spectral structure of natural sounds of a violin. They should be regarded as a guiding rule to further the studies of this domain of the microstructure of sounds of stringed instruments.

Acknowledgements

The authors wish to thank Prof. dr W. KAMINSKI for lending the instruments from the collection of the Museum of Musical Instruments in Poznań and for his kind permission to use the location. Both Dr A. KRUPA and Eng. A. ŁAPA are acknowledged for their assistence with the recordings. The logistics of the recordings was secured by mgr A. GEWERTH.

This work was supported by a grant CPBP 02.03/7.10 1990

References

[1] G. CALDERSMITH, *The violin quality debate: subjective and objective parameters*, Journ. of the CAS, **43**, 6–12 (1985).

[2] G. CALDERSMITH, *Vibration theory and wood properties*, Journ. of CAS, **42**, 4–11 (1984).

[3] L. CRAMER, *Consideration of the duration of transients in bowed instruments*, CAS NL.38, 1, 13–18 (1982).

[4] W. FLETCHER, *Transient responses and the musical characteristics of bowed-strings instruments*, CAS NL.34, 8–14 (1980).

[5] H. HARAJDA, *Changes in amplitude of violin sounds in a Concert Hall*, the CAS NL.33, 1, 13–17 (1980).

[6] H. HARAJDA, *Der Einfluss mancher Veränderungen in der Struktur der Klänge nach dem Muster der Simulierten Geigenklänge auf die Veränderungen des Gehöreindrucks*, ISMA Mittenwald, 139 (Journ. preprint) (1989).

[7] H. HARAJDA, W. MIKIEL, *Audibility of changes in spectral structure of saw-tooth stimuli*, Arch. of Acoustics, **16**, 3–4 (1991).

[8] H. HARAJDA, *Structure detaillée de la composante fondamentale de sons du violon*, Proc. of the 9th Conf. on Acoustics, Budapest 165–170 (1988).

[9] H. HARAJDA, *Application of intonoscope method in research on detailed structure of instrumental musical sounds*, Proc. the 28th Acoustic Conf. Strbske Pleso, Proc. 278–281 (1989).

[10] C.M. HUTCHINSON, *Effect of an air-body coupling on the tone and playing qualities of violins*, Journ. of the CAS, **44**, 12–15 (1985).

[11] M.E. MCINTYRE, J. WOODHOUSE, *A parametric study of the bowed string*, Journ. of CAS, **42**, 18–21 (1984).

[12] B.O. LAWERGREN, *A new and rediscovered type of motion of the bowed violin string or new bowing position effects the shape and the sound of the string*, CAS NL. **30**, 8–13 (1978).

[13] K. MARASEK, D. MADEJ, *Signal analysis program*, Split Cop. (1988).

[14] K. MARASEK, D. MADEJ, *Microcomputer system of the acoustic signals processing, especially, of the speech sound* (in Polish), Proc. of OSA 35 Warszawa, 136–141 (1988).

[15] B.C.J. MOORE, B.R. GLASBERG, R.W. PETERS, *Relative dominance of individual partials in determining the pitch of complex tones*, J. Acoust. Soc. Am., **77**, 5, 1853–1860 (1985).

[16] H.F. POLLARD, *Perception and specification of musical sounds*, CAS NL, **17**, 11–14 (1981).

[17] *Reports of CPBP 02.03/7.10* [ed] H. Harajda (in Polish), WSP Zielona Góra 1989, 1990.

[18] R. SACKSSTEDER, *How well do we understand Helmholtz resonance*, Journ. of the CAS, **48**, 27–28 (1987).

[19] VOLYZER, *User manual* (in Polish), PPUH MAST Poznań (1990).

Received on November 19, 1990; English version June 8, 1992

ARCHIVES OF ACOUSTICS
18, 1, 33–45 (1993)

MEASUREMENT OF REVERBERATION TIME USING TIME DELAY SPECTROMETRY (TDS)

G. PAPANIKOLAOU, V. PSAROUDAKIS and M. NISTIKAKIS

Department of Electrical Engineering
University of Thessaloniki, Greece

1. Introduction

In a series of papers printed in the Journal of Audio Engineering Society in late sixties and early seventies, Richard C. Heyser introduced a revolutionary measurement technique which he named Time Delay Spectrometry (TDS) [1–6]. This technique allowed measurements to be conducted on systems that are inherently time-delaying, such as acoustic and electroacoustic systems, even non-linear ones, and being difficult to be measured by means of traditional techniques, due to the time delay involved in the measurements.

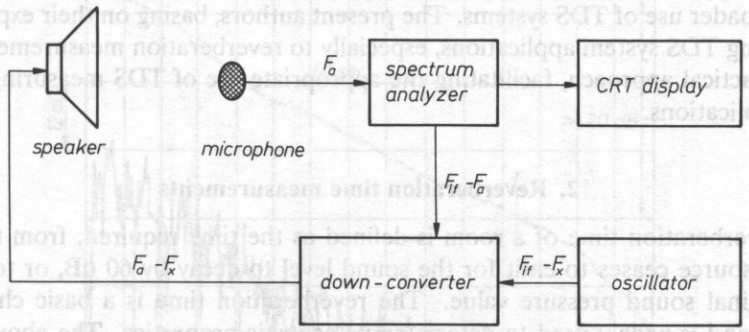

FIG. 1. Simplified block diagram of a TDS measuring system.

In Fig. 1, the simplified block diagram is shown of a system capable of performing measurements using TDS. The frequency converter is heterodynously connected to an oscillator which produces the intermediate frequency f_{if} of the analyzer. The difference signal is shifted in frequency into the acoustic region by the converter and produces a control signal that is fed to the system under test. The spectrum analyzer receives the microphone output and displays it on the vertical axis of a CRT display; while on the horizontal axis, it represents the corresponding frequency of the control signal.

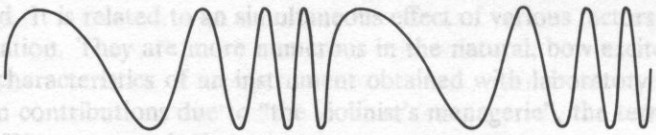

FIG. 2. Periodic swept tone used as a test signal in TDS

Figure 2 shows the periodic swept tone that is used as a control signal by the measurement system. The instantaneous frequency of such a signal is given by the expression

$$\omega_{0T} = (D/T)t + \omega_c \,,$$

where D is the measurement bandwidth, T is the sweeping period and ω_c is the carrier angular frequency. It can be proved [8] that for a given bandwidth the above signal carries the maximum possible energy, thus resulting in the optimization of the signal-to-noise (S/N) ratio.

Although simple in its basic conception, the TDS technique involves many theoretical and technical problems. The first ones were recently thoroughly examined by VANDERKOOY and LIPSCHITZ [13], who discussed mainly theoretical limitations inherent in that technique, due to its dependence on the use of energy-time curves (ETC). The second ones are connected with measuring systems implementations conceived by various producers and depend rather on the intended system applications.

While theoretical approach to the TDS technique is widely known due to the above mentioned papers, and, first of all, to the anthology of Heyser's works [9], as well as to other recent publications devoted to those problems [10], [11], many practical questions concerning applications of the TDS techniques remain unexplained, which impedes or delays a broader use of TDS systems. The present authors, basing on their experience collected during TDS system applications, especially to reverberation measurements, present below a practical approach, facilitating the appropriate use of TDS measuring systems in various applications.

2. Reverberation time measurements

The reverberation time of a room is defined as the time required, from the moment the sound source ceases to emit for the sound level to decay by 60 dB, or to the 1/1000 of the original sound pressure value. The reverberation time is a basic characteristics of a room and is widely used to determine its acoustic properties. The above definition is related to the characteristic listening properties of the human ear, since it represents an attenuation from a normal listening level down to the threshold of audibility. As the differential sensitivity of hearing organ to sound intensity, described by the so-called Weber-Fechner formula, has a logarithmic character, i.e. linear versus a logarithmic intensity scale, so an objective measurement of the decaying sound, adequately representing the subjective sensation of reverberation time, may be sufficiently limited to a two-point approximation of the decay, i.e. to the direct measurement of time elapsed between two prescribed levels of the decaying sound. Such technique of reverberation measurement was intuitively introduced by W. C. Sabine, pioneer acoustician at Harvard University. His measurements led him to establish his empirical formula, showing dependence of the

reverberation time on room parameters: volume and absorption; theoretical explanations came later to.

Many improvements have been introduced since Sabine's works into reverberation measurement technique. Reviewing them now would be time consuming and irrelevant in this context. A general tendency to improve the accuracy of measurements may be, however, concluded. The last improvement of these techniques is described in the following sections.

3. Measurements of reverberation time using TDS

One of the implementations of TDS has been developed by Crown International. It is a computer-based self-contained measurement system, known commercially as TEF 12 and TEF 12 +. This system uses three Z–80, 8–bit microprocessors, an arithmetic coprocessor, a 12–bit A/D–D/A converter, 98 Kbytes of RAM, 6 Kbytes of ROM and two 1–Mbyte floppy disk drives under the CP/M operating system. The TEF 12 system provides the capabilities for an extensive range of measurements such as, Energy-Time (ETC), Energy, Time-Frequency 3 D, ..., 3 D reverberation and reverberation time RT–60.

The reverberation in a room can be accurately examined using the TDS technique. A special software package, named 3D Reverb, supports the TEF system and allows the three-dimensional representation of the reverberation in a room. The mathematical and acoustic principles on which 3D Reverb is based were developed by Ben Kok of Peutz and Associates in Holland as a support package for the basic TEF programme [8].

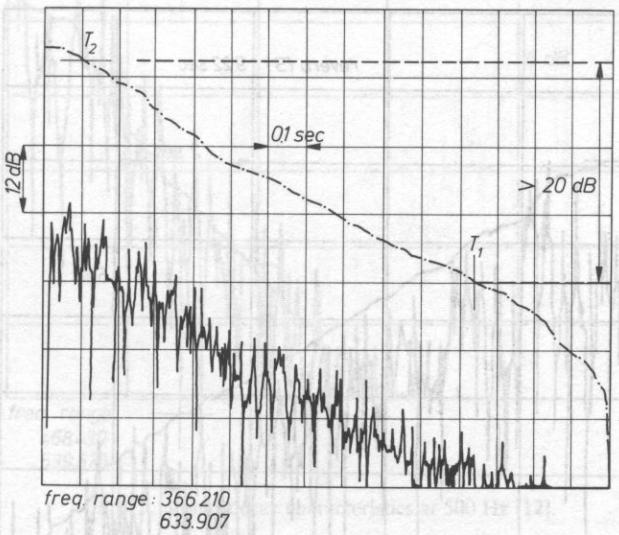

FIG. 3. Typical Energy-Time curve (ETC) [8].
Schroeder 1027288 usec; 1160.8260 Feet; -41.66 dB; dif. -38.79 dB; Sweep Rate 20 Hz/s JOB 00; Time Spar 0 usec, 1490489 usec; Dif. Spar 0.000E+00,1.684E+03 Feet.

At the beginning of the measurements we will have to set the starting time T_2 and the ending time T_1. This is done using the ETC curve (Fig. 3) [8], so that the dynamic range

of the data between T_2 and T_1 exceeds 20 dB. Moreover, proper setting of the sweeping rate S, the initial frequency F_1 and the final frequency F_2 must be made depending on the measured room. Thus, we have two categories of rooms: "small" and "large" ones. The second category includes churches, theatres and concert halls with a seating capacity of more than 1000.

The reverberation time of a room is measured using the existing sound system of the room or using a separate source placed at the speaker's position. The microphone is placed at a predetermined point and the measurements are repeated in various places, in order to minimize the possibility of an unwanted physical parameter affecting the calculations. Finally, it should be stated that this technique relies on the statistical sampling of a number of measurement points. The accuracy of the measurement can be improved by increasing the number of those points but at the cost of a longer time required to complete the measurement.

In Sec. 4 we examine the use of TDS in evaluating the reverberation characteristics of a domed stadium whereas in Sec. 5 we describe similar measurements made inside a theatre hall. In both cases the results obtained by TDS are compared to those yielded by traditional techniques.

4. Reverberation time measurements in a domed stadium

As a first example of reverberation time measurements using TDS, we consider a study by David E. Marsh, Jack E. Radoff and Ashton Taylor conducted on Harris County

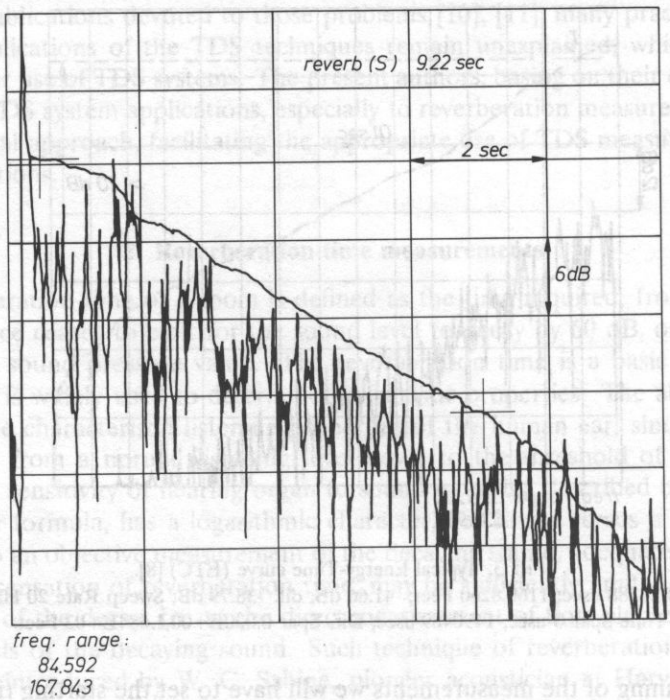

FIG. 4. Sound decay characteristics at 125 Hz [12].

Domed Stadium, Houston, known around the world as Astrodome [12]. Astrodome has a total volume of more than 13×10^6 m^3 and a seating capacity often exceeding 40000.

Table 1. Reverberation times obtained from ETC measurements made on various seating levels [12]

FREQUENCY	31.5	63	125	250	500	1*k*	2*k*	4*k*	8*k*
MEZZANINE LEVEL-AISLE 461, ROW C, SEAT 2									
RT-60	9.09	18.71	9.22	6.49	4.56	4.92	4.30	4.50	0.62
LOGE-AISLE 672, ROW A, SEAT 3									
RT-60	10.82	14.02	8.21	7.12	6.67	6.28	5.60	3.99	0.93
RAINBOW LEVEL-AISLE 757D, ROW 7, SEAT 10									
RT-60	14.36	19.12	9.28	6.30	5.71	5.70	4.00	4.95	0.99
FIELD LEVEL-AISLE 267, ROW P, SEAT 1									
RT-60	11.03	20.73	10.26	6.93	5.48	5.99	4.62	4.04	*N/A*
FIELD LEVEL-CENTER OF FIELD									
RT-60	14.67	21.93	12.25	6.86	5.44	4.98	*N/A*	*N/A*	*N/A*
AVERAGE REVERB TIMES									
	11.99	18.90	9.84	6.74	5.57	5.57	4.63	4.37	0.85

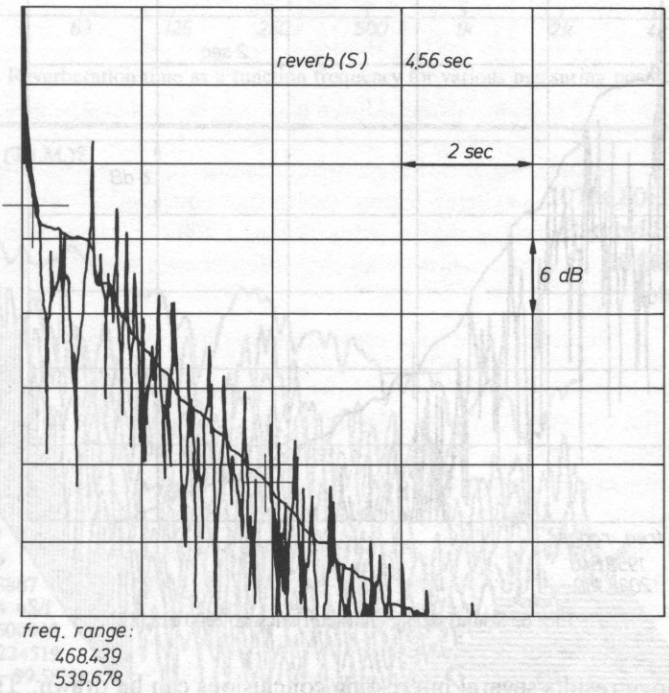

FIG. 5. Sound decay characteristics at 500 Hz [12].

The measurements were conducted in two different ways. The first was based on the TDS technique, while the second — on the traditional measurement of the reverberation time. According to the first method, the TEF system produces a control signal that drives the existing sound system of the room and measurements are taken at various positions. For the traditional measurement of reverberation time, a small cannon was used in order to produce the high sound pressure level required to disturb adequately the huge volume

noise levels encountered during the measurements. Most of the measurements were made in the octave bands ranging from 63 Hz to 4000 Hz. The cannon blasts were recorded and subsequently analyzed in a laboratory.

Figures 4 through 6 illustrate the typical sound decay characteristics produced by the existing sound system in the frequency range from 125 Hz to 2000 Hz. Table 1 shows the values of the reverberation time obtained from ETC measurements at various listening positions, whereas Fig. 7 gives a graphical representation of the reverberation time as a function of frequency. In Fig. 8 we have a three-dimensional representation of the reverberation time as measured at points in the mezzanine seating areas. Figure 9 shows a comparison between the reverberation time measured using the TDS technique and the time obtained from the traditional measurements.

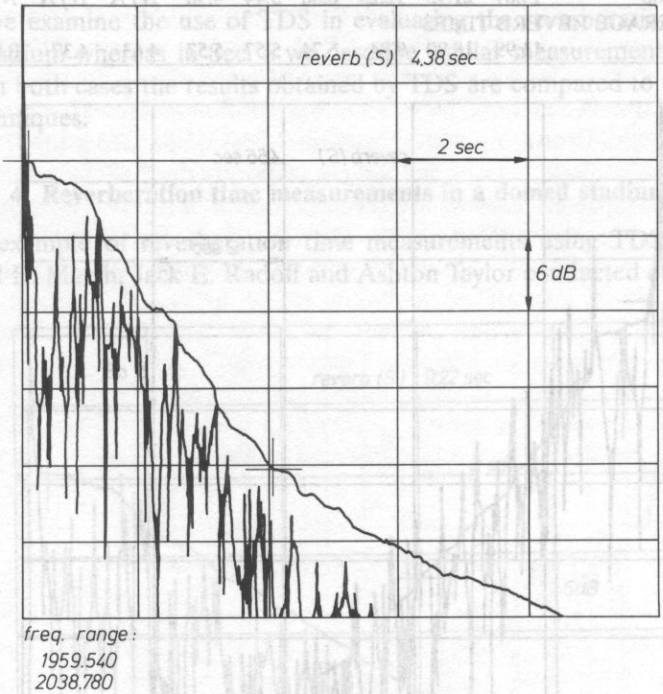

FIG. 6. Sound decay characteristics at 2000 Hz [12].

From the above results several interesting conclusions can be drawn. The ETC curves represent the energy of discrete sounds arriving at a point as a function of frequency. From these curves it can be seen that the reverberant sound field does not appear immediately but some 500 ms after the arrival of the direct sound at the listening position. Table 1 shows that the reverberation time is nearly independent of measurement position at frequencies between 250 Hz and 8000 Hz. Below 250 Hz, the dependence is more pronounced but the curves for various measuring points are essentially the same (Fig. 7). Moreover, the reverberation time at 63 Hz appears to be considerably longer that at other frequencies including that of the 31.5 Hz, which probably is due to particular resonant conditions.

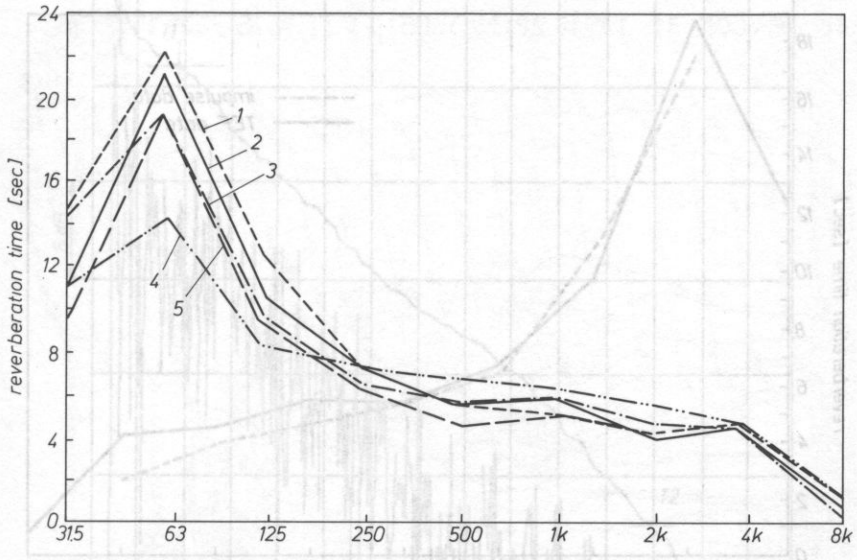

FIG. 7. Reverberation time as a function frequency for various measuring positions [12].

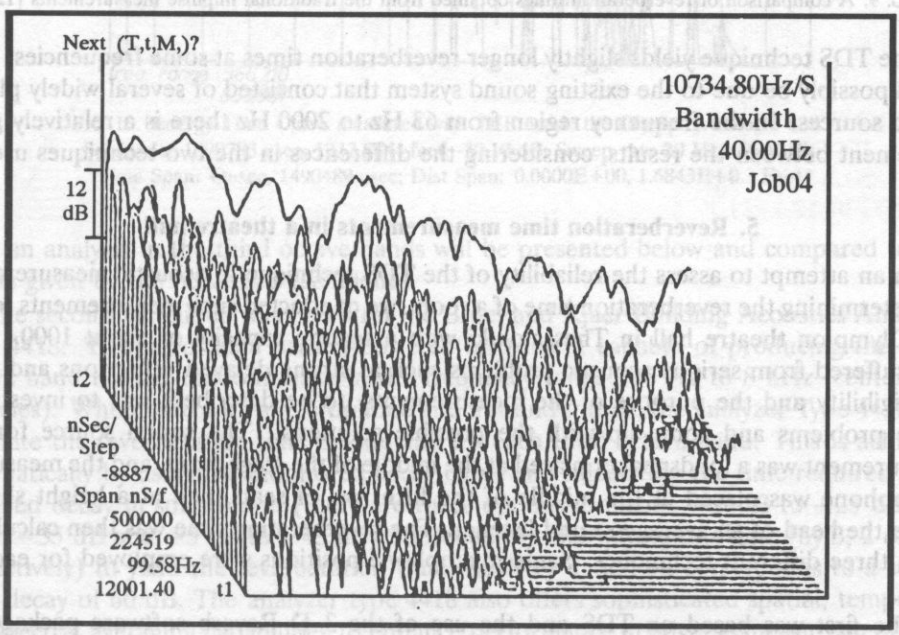

FIG. 8. Three-dimensional sound decay characteristics as obtained from measurements on the mezzanine level [12].

Figure 8 shows that the sound decay is faster at high frequencies than at midrange and low frequencies due to the increased air absorption. Finally, it is interesting to compare the two techniques used for the measurements (Fig. 9). The curves have the same shape

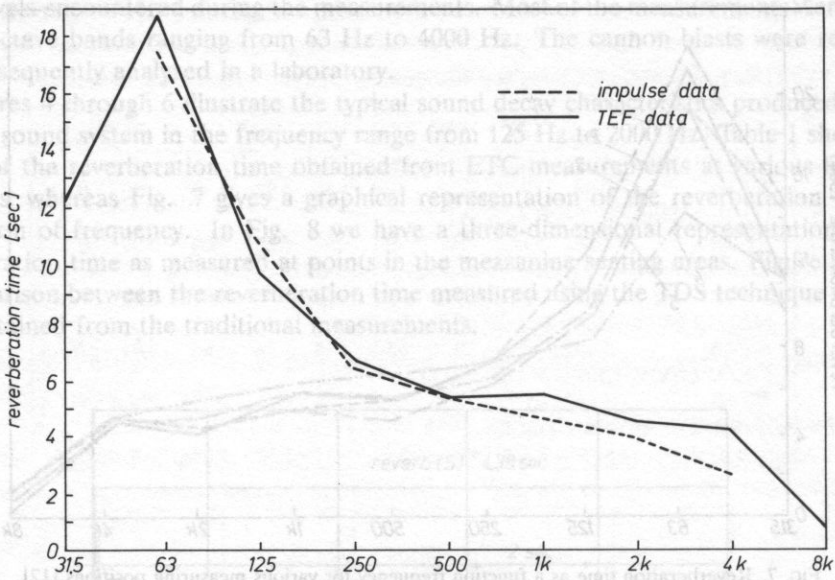

FIG. 9. A comparison of reverberation times obtained from the traditional impulse measurements [12].

but the TDS technique yields slightly longer reverberation times at some frequencies. This could possibly be due to the existing sound system that consisted of several widely placed sound sources. In the frequency region from 63 Hz to 2000 Hz there is a relatively good agreement between the results, considering the differences in the two techniques used.

5. Reverberation time measurements in a theatre hall

In an attempt to assess the reliability of the TDS technique in acoustic measurements for determining the reverberation time of a room, we conducted such measurements inside the Olympion theatre hall in Thessaloniki with a seating capacity of about 1000. This hall suffered from serious acoustic problems such as strong delayed reflections and poor intelligibility and the purpose of the measurements, to be described, was to investigate those problems and come up with the possible solutions. The sound source for the measurement was a loudspeaker placed at the middle of the stage front, and the measuring microphone was placed at the middle of the fifth row of seats, and at a height slightly above the head of an average seated listener. The reverberation time was then calculated using three different techniques. Same microphone positions were employed for each of them.

The first was based on TDS and the use of the 3 D Reverb software package, as described in Sec. 3. Figure 10 shows the Energy-Time Curve (ETC) as obtained in the theatre hall. The Schroeder integration curve is also plotted and the two time instants T_1 and T_2 corresponding to the chosen sound levels are marked on that curve. Figure 11 shows the three-dimensional TDS plot of the room response taken in the time interval set by T_1 and T_2 of the ETC plot. The 3 D Reverb programme used these TDS data to calculate the reverberation time in various frequency bands. The final results obtained

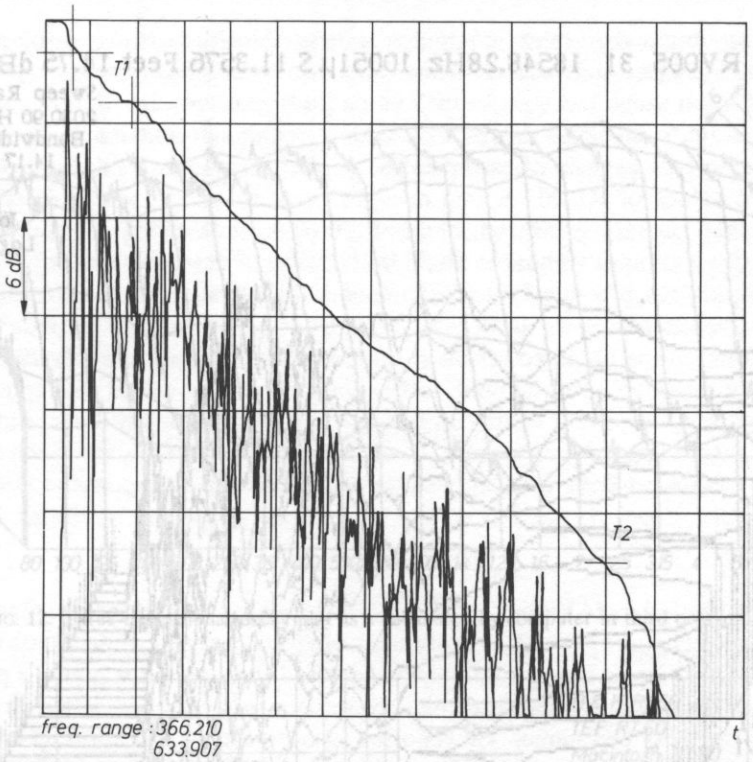

FIG. 10. Energy-Time Curve measured with TEF inside the Olympion theatre hall. Schroeder 1090783 usec, 1232.5844 feet, -30.10 dB; Sweep rate 20 Hz/s JOB 18; Time Span: Ousec, 1490489 usec; Dist Span: 0.0000E+00, 1.6843E+0.3 Feet

from an analysis in the third octave bands will be presented below and compared to the results given by the other two techniques.

The second technique was based on the Bruel and Kjaer Building Acoustics Analyzer Type 4418. This a portable battery-powered instrument capable of producing the third octave band limited random noise in the frequency range 100 Hz to 8 kHz (center frequencies). When used with a microphone and a sound source, the analyzer Type 4418 can calculate the reverberation time on-site and for each third octave band. This is achieved automatically by using the monitored decay curve and calculating the time required for a specified decay in sound level (there are three options available: -5 dB to -25 dB, -5 dB to -35 dB and -5 dB to -45 dB), subsequently multiplying this time (by 3, 2 or 1.5, respectively) to yield the reverberation time which by definition corresponds to a sound level decay of 60 dB. The analyzer type 4418 also offers sophisticated spatial, temporary and spectral averaging capabilities to enhance performance in adverse measurement conditions. In the measurements described here, three decay samples were taken for each third octave band and an average reverberation time was calculated. The above technique is well established and widely used in similar applications and hence it will serve as a reference in our case.

Finally, the third technique employed in the measurements was based on the use of a computer and a signal analysis programme for the computation of the reverberation

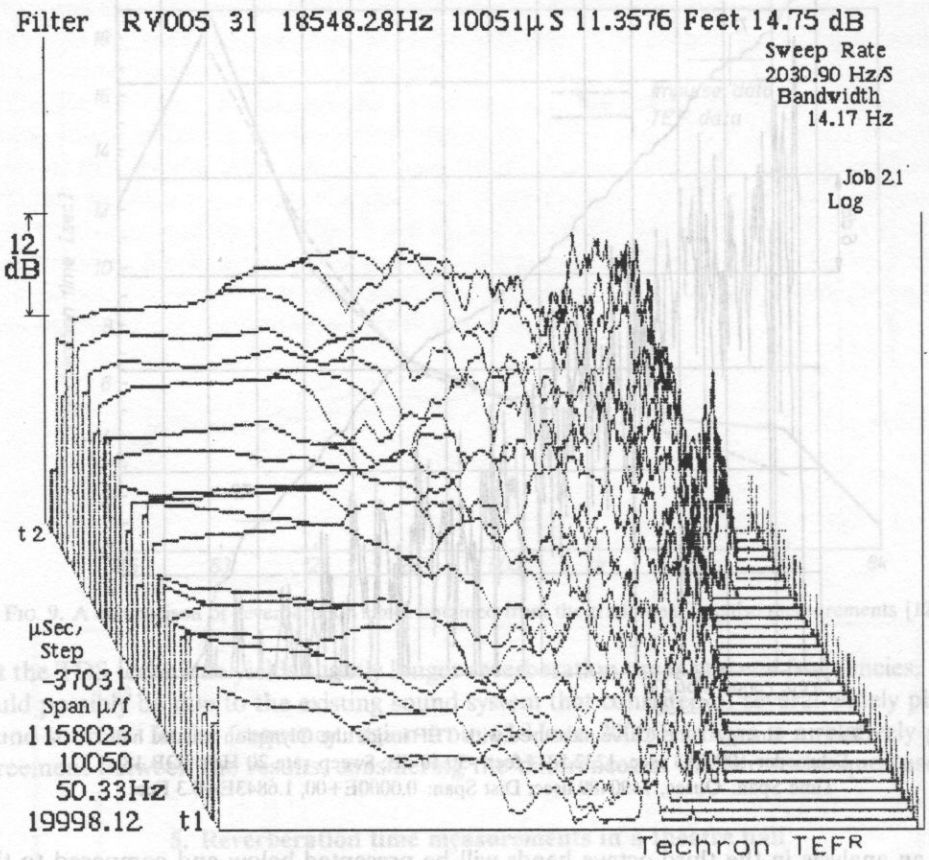

FIG. 11. Three-dimensional decay plot measured with TEF inside the Olympion theatre hall.

time in various frequency bands. The loudspeaker was fed with three successive bursts of pink noise and the responses were digitally recorded on the hard disk of a Macintosh IIx microcomputer. A dedicated signal analysis programme was taken written to process those responses by performing third octave frequency analysis of the decay transients. A three-dimensional decay plot obtained from such analysis is shown in Fig. 12. The reverberation time in each frequency band was calculated by measuring the time required for the sound level to fall from −3 dB to −23 dB relative to its steady-state value and then extrapolating it to find the time needed for a 60 dB fall. The final estimate of the reverberation time was then obtained by averaging the corresponding times calculated for each of the three recorded responses.

The reverberation times yielded by the three techniques described above, are presented graphically in Fig. 13. The low frequency end of scale is limited to 100 Hz according to the range attainable by the B and K 4418 analyzer. It is obvious that the measurements confirmed the suspected problems of the theatre hall. At lower frequencies the reverberation time is excessively long while in the frequency range typical for the human voice 500 Hz to 4 kHz it is nearly twice as long as the time regarded optimum for this type and size of room.

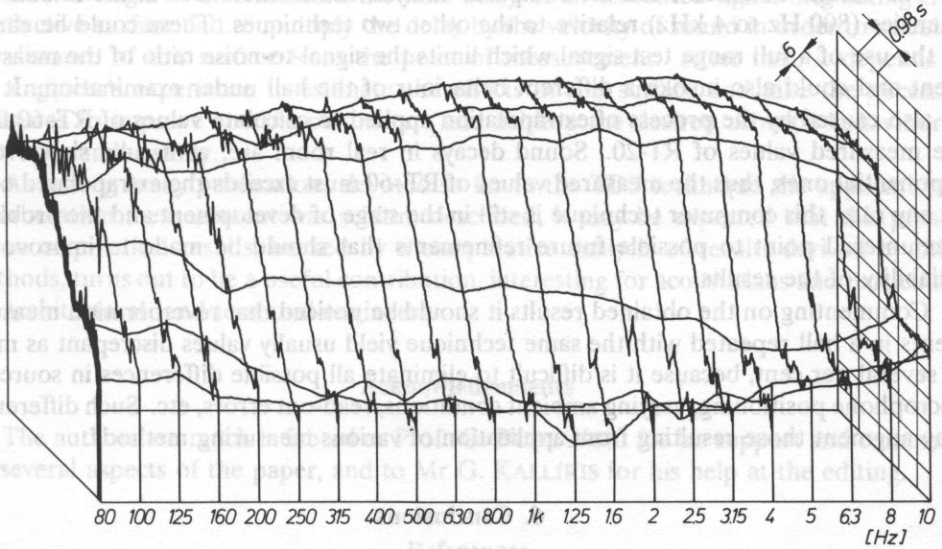

FIG. 12. Three-dimensional decay plot as a calculated by computer in third octave bands.

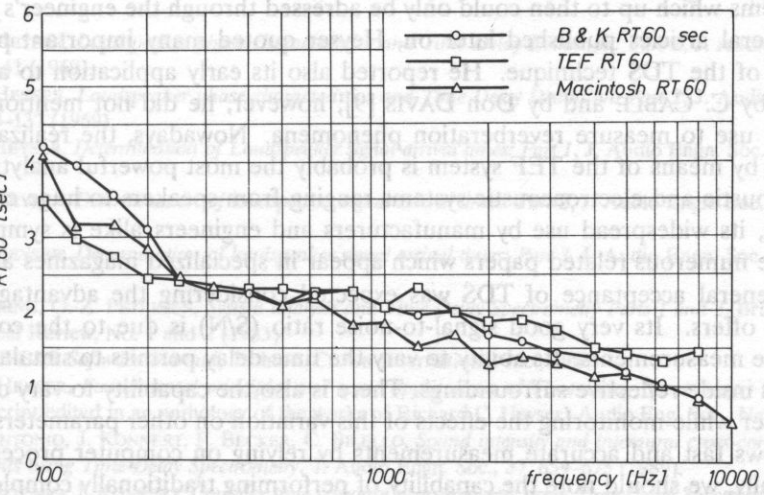

FIG. 13. Comparison between the reverberation times obtained from the three techniques.

Comparing the curves of Fig. 13, it can be seen that TEF system and B and K Type 4418 analyzer gave fairly similar results at frequencies above 250 Hz, a proof that the TDS technique can be used in such applications with equal confidence as the established techniques, while offering at the same time a level of measurement versatility that is almost impossible to achieve using a dedicated equipment. The somewhat increased difference in the reverberation times at frequencies below 200 Hz is probably due to the relatively limited frequency resolution of the TDS measurements, although this could not be verified using a different measurement setup.

The results obtained from the computer analysis show differences in the middle frequencies (800 Hz to 4 kHz) relative to the other two techniques. These could be caused by the use of a full range test signal which limits the signal-to-noise ratio of the measurement and could also invoke a different behaviour of the hall under examination. It can be also caused by the process of extrapolation applied to calculate values of RT–60 from the measured values of RT-20. Sound decays in real room are, as a rule, slower than exponential ones, thus the measured values of RT–60 must exceeds the extrapolated ones. At any rate, this computer technique is still in the stage of development and the problems encountered point to possible future refinements that should be made to improve the reliability of the results.

Commenting on the obtained results it should be noticed that reverberation measurements in a hall repeated with the same technique yield usually values discrepant as much as several per cent, because it is difficult to eliminate all possible differences in source or microphone positioning, varying ambient conditions, read-out errors, etc. Such differences may augment those resulting from application of various measuring methods.

6. Conclusions

In a paper printed in JAES in October 1967 [1] Richard C. HEYSER introduced a revolutionary new technique for the measurement of electroacoustic systems solving several old problems which up to then could only be adressed through the engineer's experience. In his several articles published later on, Heyser quoted many important practical applications of the TDS technique. He reported also its early application to architectural acoustics by C. CABLE and by Don DAVIS [9]; however, he did not mention explicitely any direct use to measure reverberation phenomena. Nowadays, the realization of this technique by means of the TEF system is probably the most powerful analytical tool for testing acoustic and electroacoustic systems ranging from speakers to huge concert halls. Therefore, its widespread use by manufacturers and engineers alike is symptomatic, as well as the numerous related papers which appear in specialized magazines and journals.

The general acceptance of TDS was expected considering the advantages that this technique offers. Its very good signal-to-noise ratio (S/N) is due to the control signal used in the measurements. Its ability to vary the time delay permits to simulate free-field conditions inside reflective surroundings. There is also the capability to vary continuously a parameter while monitoring the effects of this variation on other parameters. The technique allows fast and accurate measurements by relying on computer processing of the data. Finally, we should note the capability of performing traditionally complex measurements of electroacoustic systems and also of various characteristic acoustical parameters of listening rooms, reverberation characteristics included.

In the case of reverberation time measurements in particular, we have a portable analyzer having the size of a common personal computer and capable of generating its own control signal and calculating the reverberation time with 1/3 octave-band frequency resolution at any desired position inside a listening room, in contrast to traditional techniques.

The comparison between TDS and the traditional impulsive technique, discussed on the example given in the previous Section, shows that the TEF system is a convenient and versatile tool for measuring the reverberation time with negligible error. The three--dimensional display illustrates the variation of the sound level at all frequencies. It is even

possible through ETC to measure the time delay of an unwanted signal originating from a reflective surface and to multiply the delay by the velocity of sound in order to calculate the distance of this surface from the point of measurement. After that, it depends on the engineer's experience to estimate the effects of this surface and take the necessary measures to improve specific parameters and achieve the desired acoustic behaviour of the room under study.

As among many publications devoted so far to the TDS technique the application to reverberation measurement was seldom described, it may be expected that this presentation of practical results, backed by a comparative analysis of results derived by other methods, turns out to be a useful contribution, interesting for acousticians and particularly for architectural- and to sound-engineers.

Acknowledgements

The authors are much indebted to Prof. G. BUDZYŃSKI for his support and comments on several aspects of the paper, and to Mr G. KALLIRIS for his help at the editing.

References

[1] R. C. HEYSER, *Acoustical measurements by Time Delay Spectrometry*, J. Audio Engn. Soc., **15**, 370–382 (1967).

[2] R. C. HEYSER, *Loudspeaker phase characteristics and Time Delay Distortion: Part 1*, J. Audio Engn. Soc., **17**, 30–41 (1969).

[3] R. C. HEYSER, *Loudspeaker phase characteristics and Time Delay Distortion: Part 2*, J. Audio Engn. Soc., **17**, 130–137 (1969).

[4] R. C. HEYSER, *Determination of Loudspeaker signal arrival times: Part 1*, J. Audio Engn. Soc., **19**, 734–743 (1971).

[5] R. C. HEYSER, *Determination of loudspeaker signal arrival times: Part 2*, J. Audio Engn. Soc., **19**, 829–834 (1971).

[6] R. C. HEYSER, *Determination of loudspeaker signal arrival times: Part 3*, J. Audio Engn. Soc., **19**, 902–905 (1971).

[7] H. BIERING, O. Z. PETERSEN, *System analysis and Time Delay Spectrometry Parts 1 and 2*, Bruel and Kjaer Technical Review, No. 1 and 2 (1983).

[8] *3 D REVERB Software Manual*, Techton. Crown International Inc., 1987.

[9] R. C. HEYSER, *Fundamental principles and some applications of Time Delay Spectrometry* (Posthumous Manuscript edited in an anthology of the works of Richard C. Heyser) Audio Eng. Soc., New York 1988.

[10] P. D'ANTONIO, J. KONNERT, F. BECKER, C. BILELLO, *Sound intensity and interaural cross-correlation measurements using Time-Delay Spectrometry*, J. Audio Engn. Soc., **37**, 659–675 (1989).

[11] P. D'ANTONIO, J. KONNERT, *Complex time response measurements using Time Delay Spectrometry*, J. Audio Engn. Soc., **37**, 674–690 (1989).

[12] D. E. MARSH, J. E. RANDOFF, A. TAYLOR, *Researching the Astrodome's acoustics*, Sound and Video Contractor, p. 16 (1990).

[13] J. VANDERKOOY, S. P. LIPSCHITZ, *Uses and abuses of the energy-time curve*, J. Audio Engn. Soc., **38**, 819–836 (1990).

Received on May 14, 1991

ARCHIVES OF ACOUSTICS
18, 1, 47–66 (1993)

VIBROACOUSTIC MONITORING OF BEARING POINTS FAILURES IN THE DRIVING SYSTEM OF THE MINING MAIN VENTILATION FANS

T. ZAKRZEWSKI

Silesian University of Technology
(44-100 Gliwice)

Bearing points constitute the integral part of present-day machinery. They often limit in the service life of machines. As there is no access to them in the course of operation, diagnostic methods which can be applied without dismantling the machine, and particularly vibroacoustic methods based on the fact that there is a dependence between failure-free operation and the vibroacoustic condition of bearings become more and more essential. The evaluation of the technical condition of rolling and slide bearings, based on measures of a vibratory signal, made on the basis of amplitude values of discrete components occurring in the spectra of the recorded vibratory signals, has been the subject of diagnostic examinations. The study also covered the rolling bearings and slide bearings supporting the main shaft of the mine fans driving system of WPK type, designed for main ventilation in normal conditions of their operation. It is worth noting that considerably less work has been devoted to the elaboration of methods of vibroacoustic diagnosis for slide bearings than the methods for rolling bearings although slide bearings also constitute weak points in a number of machines. Many reasons account for such a situation, above all the fact that a slide bearing is characterized by low vibroactivity in comparison with that of other points of machines. This means that weak vibroacoustic signals are generated in slide bearings and it is sometimes difficult to isolate them from the noise present, in particular, in sophisticated machinery. The purpose of the examinations carried out on separated bearing points was to evaluate the range of sensitivity of the introduced, relatively simple, estimates of the recorded vibratory signals, to changes of the degree of wear in the conditions of constant loading and increasing period of operation. The obtained results, and the analysis of these results, served as the basis for elaborating the criteria for the evaluation of the technical state of bearing points. Here, such diagnostic estimates were selected that their values determined at the moment of checking, allowed to draw conclusions on the functional characteristics of the bearing points.

1. Introduction

Recent advances in technology, as well as the growing sophistication of technical equipment, set greater requirements for design engineers as regards reliability of functioning, service life, and the determination of a predicted failure-free period of operation.

In order to meet these requirements it is necessary to check often the technical state of the equipment of essential importance, by performing an intermediate examination of residual processes [1, 2]. Because of frequent operational failures of bearing points in the driving system of mine fans, designed for the main ventilation systems, the elaboration

of effective methods used for a complex evaluation of the technical state of the bearing points is what matters in the course of their service.

Consequently, a proper schedule of repairs should be set up which would not be limited by the period of operation, but by the technical state of the major bearing points. Therefore, methods aimed at defining the degree of their usability for further operation, expressed in the time period, as well as the continuous improvement of methods become more and more important when checking the technical state of bearings in the fan driving systems [3, 4].

Because of the kinematics of rolling elements, bearings are divided into two types: rolling bearings and slide bearings. Vibrations of slide bearings may be caused by many factors. They depend mainly on the design of the bearing itself, on its size, manufacture accuracy, quality of the co-operating surfaces, assembly conditions, and on the design solution of the whole bearing unit.

The following mistakes are often made already when designing bearing supports for horizontal rotors:

the lack of sufficient stiffness of the body in transverse and in longitudinal direction results in high vibrations of bearing supports;

the frequency values of free vibrations of the bearing body in the transverse and in longitudinal direction, which approximate to rotational speed of the rotor may cause supplementary resonant vibrations of the support;

the asymmetric load of a bearing body accounts for the fact that apart from a vertical force which applies symmetrically a load to this body, a bending moment is also produced, and this causes vibrations of the bearing support.

The existing vibrations, together with processes of usual wear, make bearings lose their functional ability in a shorter time than that anticipated on the basis of the occurrence of wearing processes only. Therefore, there is no possibility of predicting the failure-free service time of a rolling bearing which is incorporated in a complex mechanism.

There are two processes of usual wear which take place in rolling bearings: fatigue wear and abrasive wear of working surfaces. The effect of surface abrasive wear increases with time. Continuous rolling of the rolling elements results in changes of quality of the material only, and surface fatigue itself appears as spalling in the final phase of the service life of the bearing. The process takes the form of an avalanche growth from the moment the first spalling takes place, and this causes directly a breakdown of the bearing. From the observations made so far it is evident that about 20–30% of the bearings in operation lose their functional ability due to excessive clearance, caused both by abrasive wear, and by excessive transverse vibrations [5].

Failures of slide bearings occurring in operating conditions may be divided into the following groups:

failures caused by fatigue of material,

failures caused by increased wear,

failures caused by changing of clearances and fits between a shaft and a bearing shell,

failures caused by improper lubrication.

Of all undesirable effects which are found in slide bearings of machinery, seizures leading to the formation of burrs in a bearing and, consequently, resulting in shaft keying should be considered the most deteriorative.

Some of the deteriorative processes specified, e.g., processes of wear leading to an increase of clearances, and to changes in fits, and particularly the effect of seizure, produce measurable pulses in the vibroacoustic signal of the bearing point.

2. Sources of generation of vibration effects in bearing points

The damage of bearing points occurring under operational conditions is often the consequence of defects of some elements of the bearing and of the simultaneous growth of a number of failures. Under these circumstances the process of damage may be illustrated in spectrograms showing a change in the amplitudes of a number of discrete components. In the case of practical industrial applications it is most convenient to diagnose the state of a bearing taken as a whole, by evaluating the degree of the growth of deterioration processes in the bearing, and the predicted duration of its reliable service. This is a strict, practical approach to the problem, because when a given mechanism becomes unoperational, the operating personnel is not interested in which element of the bearing has been subject to failure, but in the fact that the bearing must be replaced. In the case of a number of exceptionally simple mechanisms, there is a possibility of determining in the amplitude and frequency spectrum some discrete components corresponding to definite, characteristic operational failures [6].

2.1. Influence of operational failures on the level of rolling bearing vibrations

Any type of damage a bearing race influences, to a considerable degree, the vibroacoustic state of rolling bearings. Since the rolling elements roll between surfaces of curvilinear generators, the real motion is very complex. This is even more complex due to the friction and inertia forces, acting on the rolling elements which, depending on the location of certain mechanical damage during the motion, are a source of vibrations, the amplitudes of which come within various frequency bands [7, 8]. Figure 1 shows three typical kinds of bearing damage, producing periodical vibroacoustic pulses:

local damage of a bearing outer ring,
local damage of a bearing inner ring,
damage of one rolling element.

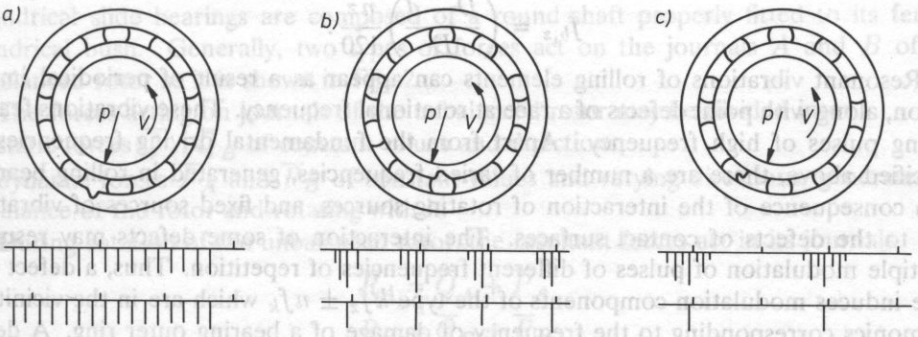

FIG. 1. Typical kinds of bearing failures causing periodical vibroacoustic pulses.

The damage causes pulse functions with repetition frequency:
in the case of damage of a bearing outer ring

$$f_z = \left(\frac{z}{2}\right) f_0 \left(1 - \frac{d}{D}\cos\beta\right) \tag{1}$$

in the case of damage of a bearing inner ring

$$f_n = \left(\frac{z}{2}\right) f_0 \left(1 + \frac{d}{D}\cos\beta\right) \tag{2}$$

in the case of damage of a rolling element

$$f_e = \left(\frac{D}{d}\right) f_0 \left[1 - \left(\frac{d}{D}\cos\beta\right)^2\right] \tag{3}$$

in the case of damage of bearing cage

$$f_k = \frac{f_0}{2}\left(1 - \frac{d}{D}\cos\beta\right) \tag{4}$$

where f_0 — frequency of ring revolution, z — number of rolling elements, β angle of force action pressure angle, d — diameter of rolling element, D–pitch diameter of a cage.

When damage of the structural components of bearings occurs and develops in the course of their service, discrete components appear in the spectrum of a working mechanism, and their frequencies oneconditioned by the kind of damage.

These defects are highly diversified and have the form of waviness of rotating races, increased clearance in a bearing housing, ovality of rolling elements and of rings, roughness, increased clearance in the seats of a cage, slips and others. The fundamental frequencies of excitation, generated as a result of the damage of roller bearings, are conditioned by the following defects:

defect of the shape of rolling elements

$$f_{e,t} = \left(\frac{D+d}{d}\right)\left(\frac{D-d}{d}\right)\frac{n}{30}, \tag{5}$$

defect of the shape of inner race

$$f_{b,w} = \left(\frac{D+d}{D}\right)\frac{nz}{120}, \tag{6}$$

defect of the shape of outer race

$$f_{b,z} = \left(\frac{D-d}{D}\right)\frac{nz}{120}. \tag{7}$$

Resonant vibrations of rolling elements can appear as a result of periodical impact action, along with point defects of a race at rotational frequency. These vibrations feature fading pulses of high frequency. Apart from the fundamental driving frequencies, as specified above, there are a number of varied frequencies, generated in rolling bearings as a consequence of the interaction of rotating sources, and fixed sources of vibrations due to the defects of contact surfaces. The interaction of some defects may result in multiple modulation of pulses of different frequencies of repetition. Thus, a defect of a cage induces modulation components of the type $kf_z \pm nf_k$ which are in the vicinity of harmonics corresponding to the frequency of damage of a bearing outer ring. A defect of a bearing inner ring induces, in turn, the frequencies corresponding to the interaction

of this ring, and the bearing outer ring $kf_z \pm nf_w$, and that with the rolling elements $k(f_w - f_h)z$. This is why we may find, in the spectrum of vibration, diversified frequency components of the type:

$$\begin{aligned} &kf_w \pm n(qf_z \pm pf_w) \\ &kf_z \pm n(qf_w \pm pf_k) \end{aligned} \tag{8}$$

where the factors k, n, p, q are integers defining the order of harmonics. Other combinations of driving frequencies are possible, and these cover the rotational frequencies of rotors which, in many cases, reflect the degrees of unbalance of a rotating shaft.

One of the most common defects of assembling rolling bearings is the bevelling of rings.

Bevelling of bearing outer ring generates discrete components, corresponding to the frequencies:

$$f_{z,p} = kf_k z\,. \tag{9}$$

Bevelling of a bearing inner ring generates discrete components of the frequencies

$$f_{w,p} = k(f_0 - f_k)z\,. \tag{10}$$

Defects of rolling elements having the form of wear zones can be also a source of vibrations, the frequency of each of them is lateral to harmonics of double rotating frequency, defined by the expressions

$$f_{\substack{k,z \\ k,w}} = f_k\left[2k\frac{D}{d}\left(1 + \frac{d}{D}\right) \pm 1\right]. \tag{11}$$

Other defects of elements of a rolling bearing may also appear in the frequencies specified (9)–(11) and, in particular, defects of squeeze, scratches and the like.

The complex nature of the vibration spectrum of rolling bearings, occurrence of a great number components of modulation, cause net difficulties when examining the technical state of bearing points.

2.2. Effect of operational defects on the level of vibrations of slide bearings

Slide bearings differ essentially from rolling bearings. They feature the following advantages:

it is possible to design them for any loads and rotational speeds,

they have low susceptibility to errors of manufacture and to inaccuracy of assembly,

they have a low level of vibrations and noise.

Cylindrical slide bearings are composed of a round shaft properly fitted to its female cylindrical bush. Generally, two types of forces act on the journals A and B of the unbalanced rotor as it is shown in Fig. 2.

The forces acting on journals of the unbalanced rotor may be divided into:

static forces $\overline{Q}_A$, $\overline{Q}_B$ of constant values and directions;

dynamic forces $\overline{P}_A$ and $\overline{P}_B$ of constant values and varying directions, generated by unbalance of the rotor and rotating with it.

During rotation of the unbalanced rotor, the resultant forces act in its journals

$$\begin{aligned} \overline{R}_A &= \overline{Q}_A + \overline{P}_A \\ \overline{R}_B &= \overline{Q}_B + \overline{P}_B\,. \end{aligned}$$

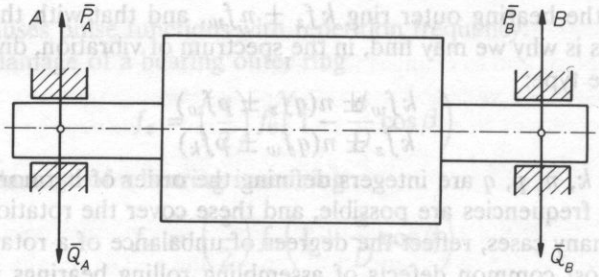

FIG. 2. Forces acting on journals of an unbalances rotor.

The effect of the unbalance on the operation of both bearings may be defined by means of the factors of the unbalance (8)

$$\varepsilon_A = \frac{P_A}{Q_A}, \quad \varepsilon_B = \frac{P_B}{Q_B}$$

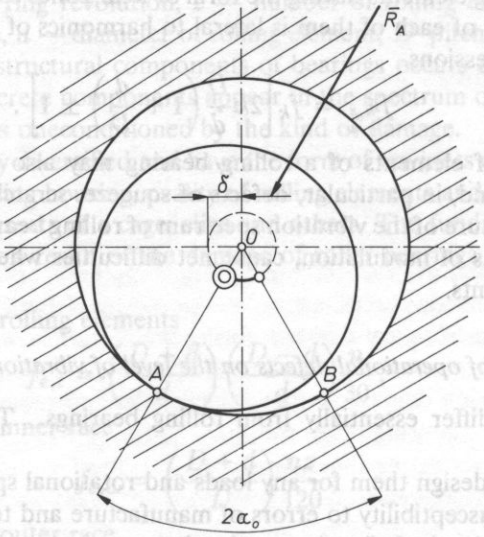

FIG. 3. A trajectory of the centre of a bearing journal in the case of one-sided wear of a bearing bush.

The centre of the journal displaces, effecting an oscillating motion over the circular arc of radius δ, what has been marked in Fig. 3. The arc AB is a geometric locus of points of contact of the journal with the bearing bush. It may be assumed that in the case considered, the centre of the journal effects oscillatory motion with angle amplitude α_0. As a result of these vibrations, wear of the journal occurs over the full circumference, whereas the bearing bush wears only on the arc AB over the length

$$L = \frac{r\pi}{90}\alpha_0$$

where r — radius of the bush chamber, α_0 — angle measured as degree.

As the journal becomes worn, the mass eccentricity of the rotor increases as a result of the force $\overline{R}_A$ increase, and this in turn, causes more intensive wearing of the journal and of the bush. Therefore, wear of the journal and the bush advances with time, and this results in a continuous increase of unbalanced centrifugal forces, and in uninterrupted impairing of the vibroacoustic state of the machine. From the experimental examinations made so far, and referring to the vibration diagnosis of slide bearings, it appears that increased clearance at untight fit of the bearing produces polyharmonic vibrations with frequencies which are a multiple of half frequency of the rotor revolution $k \cdot f_0/2$.

In the vibration spectrum the half subharmonic of the rotation frequency is often higher than the level of noise disturbances of 20–25 dB [9]. Distinguishing the type of damage in slide bearings may be carried out on the basis of the exact reading of a component of frequency, constituting 42–48% (and not exactly 50%) of the frequency of shaft rotation. The occurrence of this frequency is a typical indication of the instability of journal vibrations in the oil layer, which finally reduces considerably the service life of a slide bearing. The natural frequency of the bearing point $f_{w,w}$ is also of essential importance, and its extraction from the summary signal, by means of a narrow-band filter, will make it possible to obtain a narrow-band signal $x(t)$, the time realizations of which differ very much from each other, as regards the normal state of the bearing, and the damaged one.

The normal state of the bearing is characterized by "stable" time realizations without any evident pulse components, whereas the appearance of seizure causes a sudden increase of amplitude of a narrow-band signal, related to a given type of defect.

The so-called factor of excess [10] is of great significance in the qualitative and quantitative evaluation of changes in the vibratory signal, as conditioned by the progress of deterioration of the slide bearing

$$E_k = \frac{\mu_4}{\delta^4} - 3 \tag{12}$$

where δ is the variance of the signal, μ_4 — central moment of the fourth order.

The specified quantities are determined by the expressions

$$\delta^2 = \lim_{N\to\infty} \frac{1}{N} \sum_{i=1}^{N} [x_i(t_j) - m(t_j)]^2, \tag{13}$$

$$\mu_4 = m_4 - 4m_3m_1 + 6m_2m_1^3 - 3m_1^4, \tag{14}$$

where

$$m_p(t_j) = \lim_{N\to\infty} \frac{1}{N} \sum_{i=1}^{N} x_i^p(t_j)$$

and m_p stands for the initial moment of the pth order.

In an ideal case, when a vibrational signal is of normal distribution then $E_k = 0$.

From a series of our examinations it appears that in the normal state of a slide bearing, the value of the excess coefficient averaged over the time set of instantaneous values is $\overline{E}_k = 0.04$, whereas in the case of a defect, for example, such as the burr of a sliding bearing mounted in a reduction gear $\overline{E}_k = 5.0$. It is also evident that the excess coefficient can serve as an important diagnostic indicator, by means of which it is possible to

determine both the moment when the initial state is impaired, and the current technical state. Defects of a slide bearing can also be evaluated by means of the parameters characterizing the depth of phase modulation of the forced vibrations of the bearing point. The coefficient of the n-dimensional vector rising may be used as a diagnostic measure of wear of a slide bearing. The components of the vector are the differences of the values

$$S_n(f_i, \Delta f) = \sum_{i=1}^{n} |S^0_{xi}(f_i, \Delta f) - S_{xi}(f_i, \Delta f)|, \tag{15}$$

where $S^0_{xi}(f_i, \Delta f)$; $S_{xi}(f_i, \Delta f)$ — respective amplitudes of the harmonic components of the function of spectral power density corresponding to the rotational speeds of the bearing in normal state and in worn state.

An analysis of results of experimental examinations carried out in the field of vibroacoustic diagnosis of slide bearings has indicated that the simplest and most reliable algorithm of the diagnosis of progressive burr in contact surfaces of slide bearings are quite analogous to the algorithms of diagnosis of the state of seizure of the gear wheels mesh [11]. Using these algorithms, it is possible to diagnose the process of seizure of slide bearings already in the phase of its formation.

3. Description of the subject of examinations

Fans are machines designed to compress and to force through, gas where the total head produced by fans does not usually exceed 10.000 N/m^2.

According to the function, the mine fans are divided into:

main ventilation fans, also called main fans,

auxiliary fans used, first of all, for local ventilation.

Three-phase asynchronous compact motors are usually applied to drive fans.

Both centrifugal fans and axial-flow fans are used as main mine fans. When comparing centrifugal fans with axial-flow ones, it should he stated that centrifugal fans are simpler, less noisy, easier to make and are thus cheaper than axial-flow fans.

The evaluation of the technical state of rolling bearings and slide bearings of main ventilation fans drive systems of the type WPK-2.1 and WPK-3.3 with shafts of rotational speed of 600 r.p. m. and 500 r.p. m. respectively, were the subject of diagnostic examinations. The diagram of the drive system of the fans of WPK type is shown in Fig. 4. When carrying out vibroacoustic measurements, the location of the measuring points, accordingly situated on the housing of a bearing point, is of great importance. The arrangement of measuring points on the housing of the bearing points 3, 4 is shown in Fig. 5. The measuring points fixed in this way cover both axial vibrations, and radial vibrations as related to the main shaft.

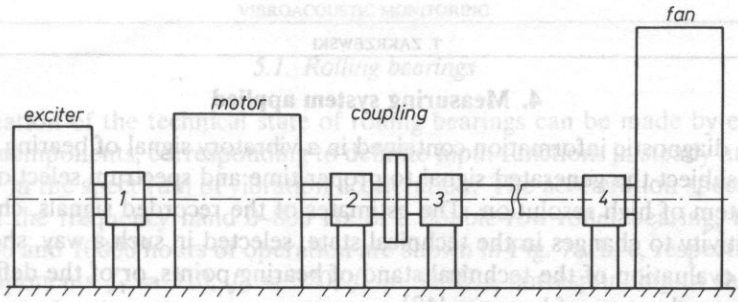

FIG. 4. Kinematic diagram of a driving system of mine fans. Designations: *1, 2* — slide bearings, *3, 4* — rolling bearings.

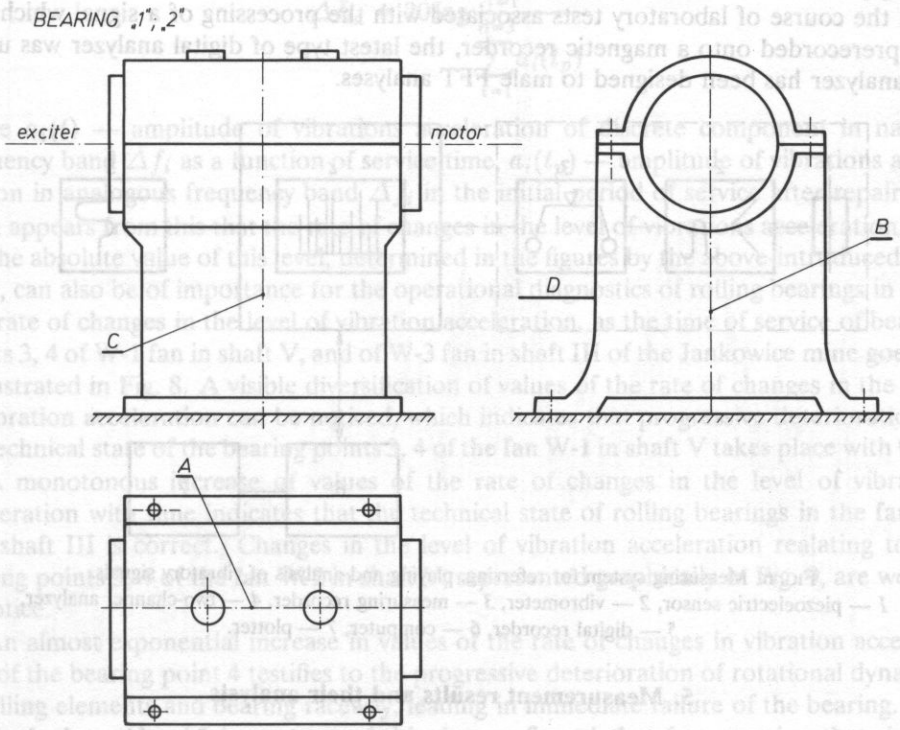

FIG. 5. Arrangement of measuring points on the body of slide bearings.

4. Measuring system applied

To obtain diagnostic information contained in a vibratory signal of bearing points, it is necessary to subject the generated signal to proper time and spectrum selection, using an analyzing system of high resolution. The estimates of the recorded signals, characterized by high sensitivity to changes in the technical state, selected in such a way, should be the basis for the evaluation of the technical stand of bearing points, or of the defined typical failures of some elements of bearings [12].

A laboratory measuring system designed for recording, analyzing and processing of measuring data is shown in Fig. 6. Signals from a piezoelectric sensor (1) were recorded by a measuring recorder (3) via a vibrometer (2); the system constituted a separate whole, and served to record directly the vibration parameters.

The further part, including the recorder, formed a laboratory system which incorporated a two-channel analyzer made by Bruel and Kjaer of the type 2034/4/, a digital recorder of the type 2313/5/. A computer and a plotter formed an autonomous system, necessary to calculate the number of estimates for the evaluation of the dynamic state of bearing points.

In the course of laboratory tests associated with the processing of a signal which has been prerecorded onto a magnetic recorder, the latest type of digital analyzer was used. This analyzer has been designed to male FFT analyses.

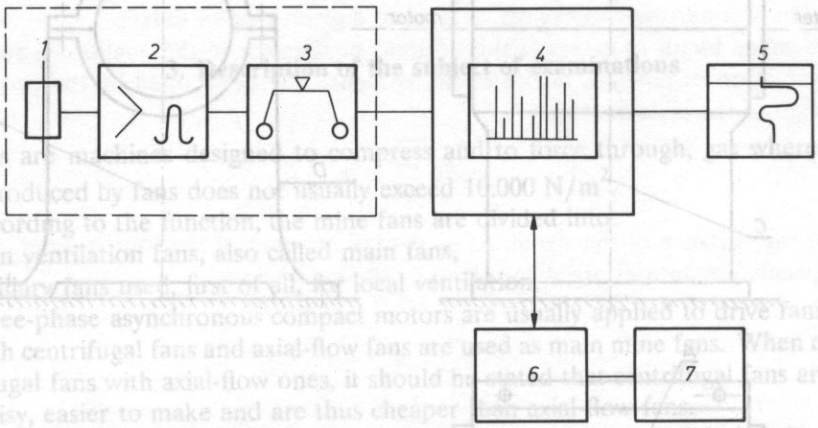

FIG. 6. Measuring system for referring, playing and analysis of vibratory signals.
1 — piezoelectric sensor, *2* — vibrometer, *3* — measuring recorder, *4* — two-channel analyzer, *5* — digital recorder, *6* — computer, *7* — plotter.

5. Measurement results and their analysis

The subject of measurement analysis were discrete estimates, formed on the basis of the distribution of the characteristic frequencies polyharmonic spectrum of the vibration acceleration, corresponding to the occurring most frequently failures of bearing points. The correct elaboration of a method used to investigate the technical state of bearing points consists in the calculation of such vibroacoustic estimates which could be the ground for the evaluation of changes in service characteristics of rolling bearings and of slide bearings as well.

5.1. Rolling bearings

An estimation of the technical state of rolling bearings can be made by extraction of the discrete components, corresponding to definite input functions in steady narrow bands of frequency in the spect rum of vibration acceleration. The acceleration spectra or radial vibrations in the frequency hand 0–800 Hz of a double-row roller bearing, type 2234H, after 50, 2000 and 10000 hours of operation are shown in Fig. 7a, b, c, respectively. Three discrete components $f_1 = 310$, $f_2 = 320$, $f_3 = 330Hz$, corresponding to the frequency of "flickering" of rolling elements, and to input functions caused by the interaction of rolling elements and bearing raceways, are predominant. In the case of bearing points comprising rolling bearings (nos 3, 4 according to Fig. 4), the averaged value of vibrations acceleration within the frequency band 300–330 Hz from the interval of minimum values within the range of changes of 20%, has been assumed as a reference level. Taking into account the assumed reference level, a relative evaluation parameter of the technical state of rolling bearing has been introduced

$$\Delta L_a = 20 \log \frac{\sum_{i=1}^{n=3} a_i(t)}{\sum_{i=1}^{n=3} a_i(t_p)} \tag{16}$$

where $a_i(t)$ — amplitude of vibrations acceleration of discrete component in narrow frequency band Δf_i as a function of service time, $a_i(t_p)$ — amplitude of vibrations acceleration in analogous frequency band Δf_i in the initial period of service after repairing.

It appears from this that the rate of changes in the level of vibrations acceleration, and not the absolute value of this level, determined in the figures by the above-introduced estimate, can also be of importance for the operational diagnostics of rolling bearings in fans. The rate of changes in the level of vibration acceleration, as the time of service of bearing points 3, 4 of W-1 fan in shaft V, and of W-3 fan in shaft III of the Jankowice mine goes by, is illustrated in Fig. 8. A visible diversification of values of the rate of changes in the level of vibration acceleration can be noticed, which indicates that progressive deterioration of the technical state of the bearing points 3, 4 of the fan W-1 in shaft V takes place with time.

A monotonous increase of values of the rate of changes in the level of vibration acceleration with time indicates that the technical state of rolling bearings in the fan W-3 in shaft III is correct. Changes in the level of vibration acceleration realating to the bearing points 3, 4 of the fan W-2 in shaft V, represented graphically in Fig. 9, are worthy of notice.

An almost exponential increase in values of the rate of changes in vibration acceleration of the bearing point 4 testifies to the progressive deterioration of rotational dynamics of rolling elements and bearing raceway, leading in immediate failure of the bearing. The repair done on the driving system of thin fan confirmed that fact, proving that the increase in values of the level of vibration acceleration was caused by spallings of the rolling elements, and by transverse cracks of the bearing raceway.

The increase of level of the acceleration rate of $\Delta L_a = 11$ dB (Fig. 9) occurring in the final phase after the service period of 4 thousand hours, was the direct reason for turning off the fan. A failure hazard could be expected at any moment.

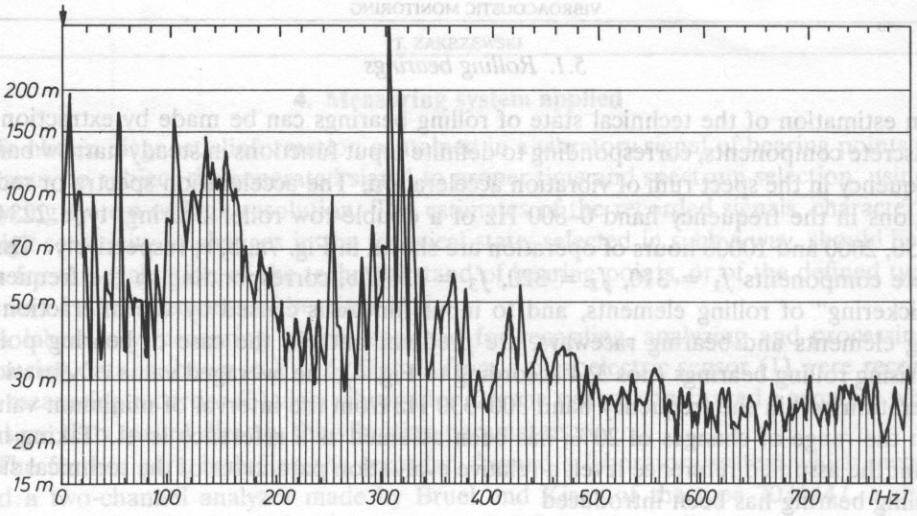

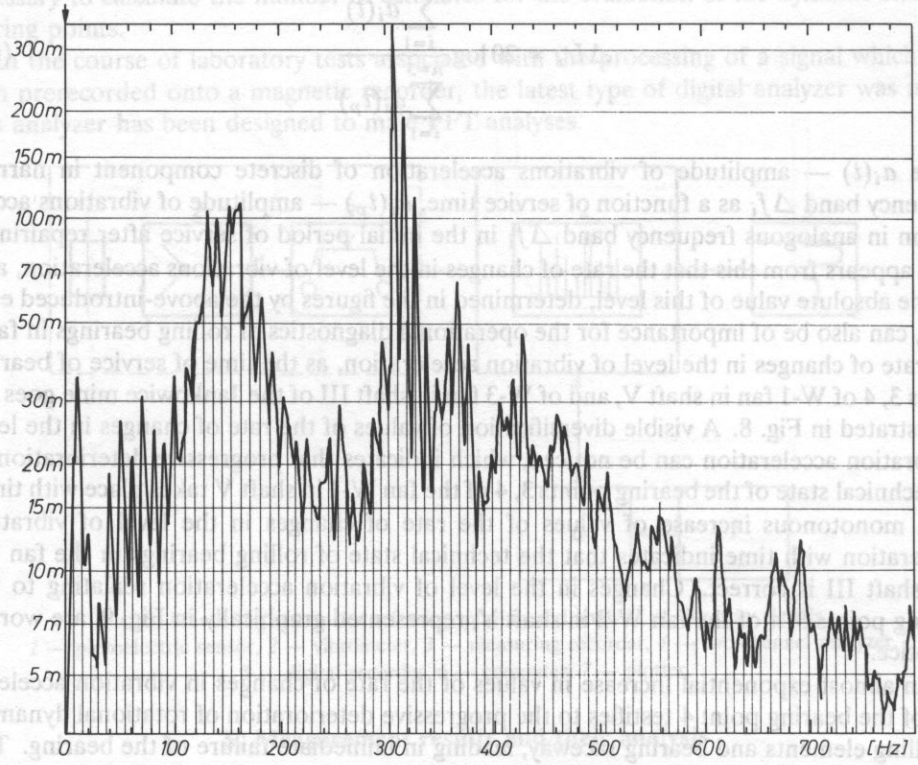

FIG. 7a. Acceleration spectrum of radial vibrations measured for a rolling bearing after a service period of t_E = 50 hours frequency range of analysis 0–800 Hz.

b. Acceleration spectrum of radial vibration measured for a rolling bearing after a service period of t_E = 2000 hours frequency range of analysis 0–800 Hz.

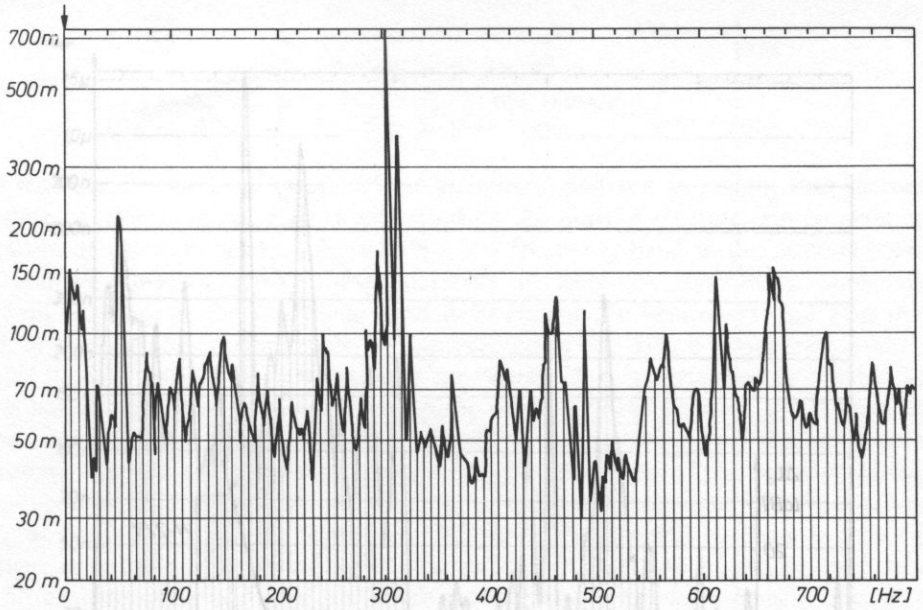

FIG. 7c. Acceleration spectrum of radial vibrations measured for a rolling bearing after a service period of t_E = 10000 hours frequency range of analysis 0–800 Hz.

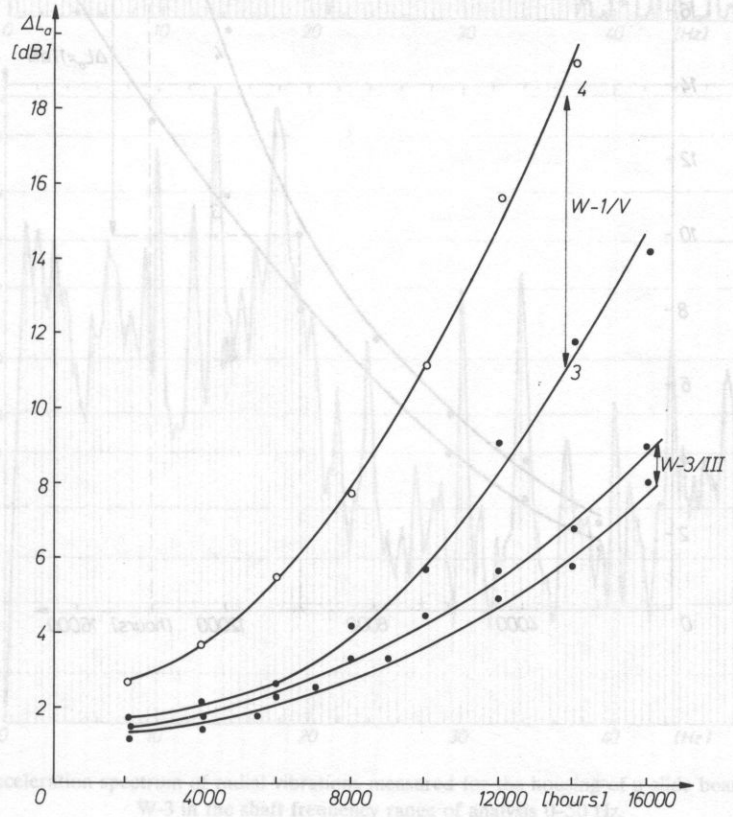

FIG. 8. Time evolution of the level of amplitude acceleration measured for the bearing points 3, 4 of the fan W-1 in shaft V, and the fan W-3 in shaft III with time.

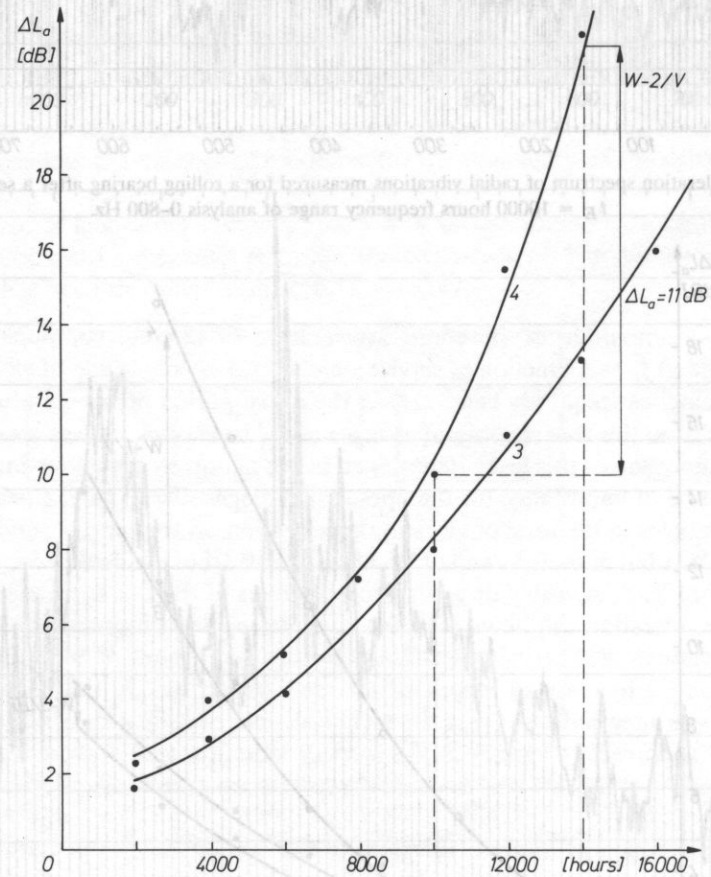

FIG. 9. Time evolution of the level of amplitude acceleration measured for the bearing points 3, 4 of the fan W-2 in shaft V with time.

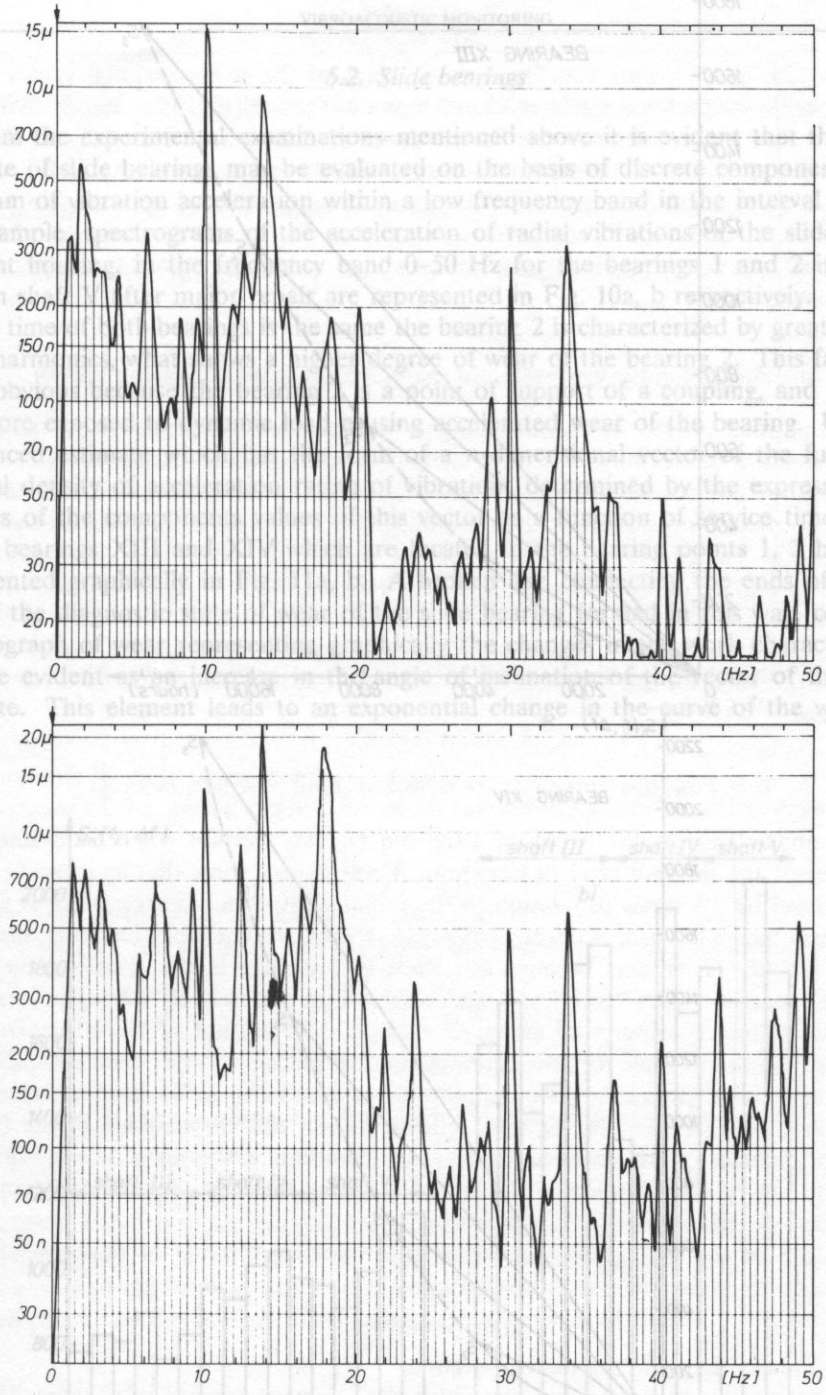

FIG. 10a. Acceleration spectrum of radial vibrations measured for the housing of a slide bearing for the fan W-3 in the shaft frequency range of analysis 0–50 Hz.

b. Acceleration spectrum of radial vibrations for the housing of a slide bearing 2 for the fan W-3 in shaft V frequency range of analysis 0–50 Hz.

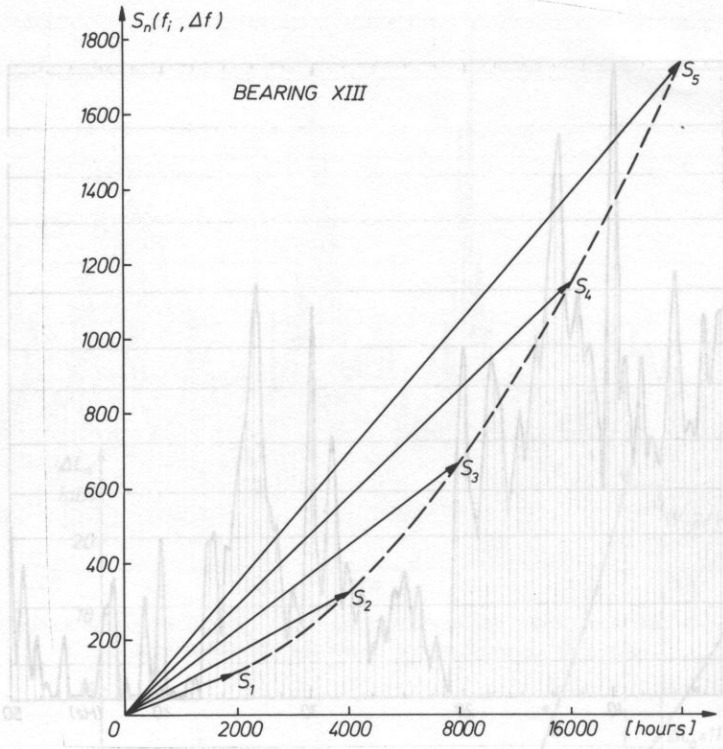

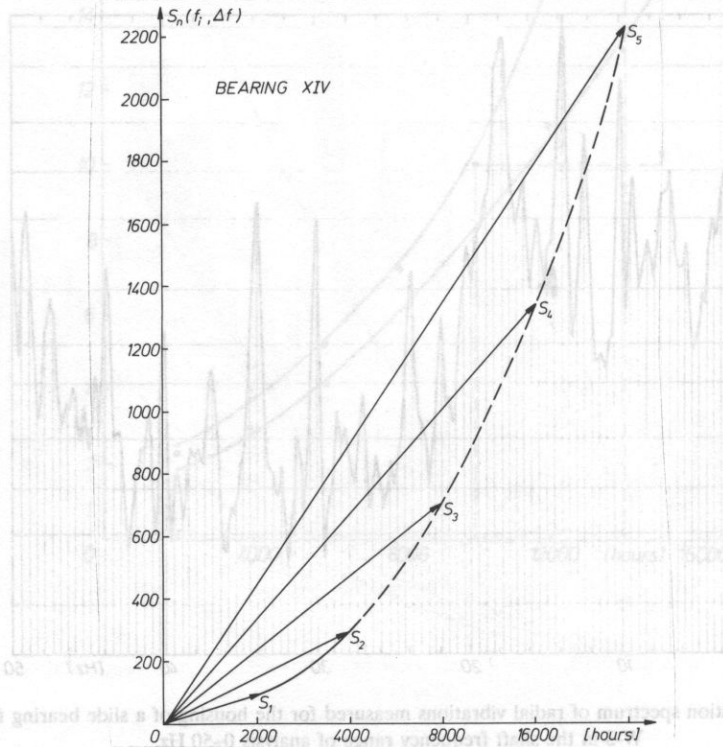

FIG. 11a. Hodograph of wear of the slide bearing XIII.
b. Hodograph of wear of the slide bearing XIV.

5.2. *Slide bearings*

From the experimental examinations mentioned above it is evident that the technical state of slide bearings may be evaluated on the basis of discrete components of the spectrum of vibration acceleration within a low frequency band in the interval 0–50 Hz. For example, spectrograms of the acceleration of radial vibrations of the slide bearing moment housing, in the frequency band 0–50 Hz for the bearings 1 and 2 in the fan W-3, in shaft V after major repair are represented in Fig. 10a, b respectively. Although service time of both bearings is the same the bearing 2 is characterized by greater amplitudes harmonics, what shows a higher degree of wear of the bearing 2. This fact seems to be obvious because the bearing 2 is a point of support of a coupling, and therefore it is more exposed to dynamic load causing accelerated wear of the bearing. Using the introduced estimate which has the form of a n-dimensional vector of the function of spectral density of acceleration rating of vibrations determined by the expression (13), changes of the components values of this vector as a function of service time relating to the bearings XIII and XIV which are located in the bearing points 1, 2 have been represented graphically in Fig. 11a, b. A broken line connecting the ends of the vectors of the diagnostic state of wear of the slide bearing formed in this way, constitutes a hodograph of wear representing graphically the changes in the work character which become evident as an increase in the angle of inclination of the vector of the technical state. This element leads to an exponential change in the curve of the war hodograph.

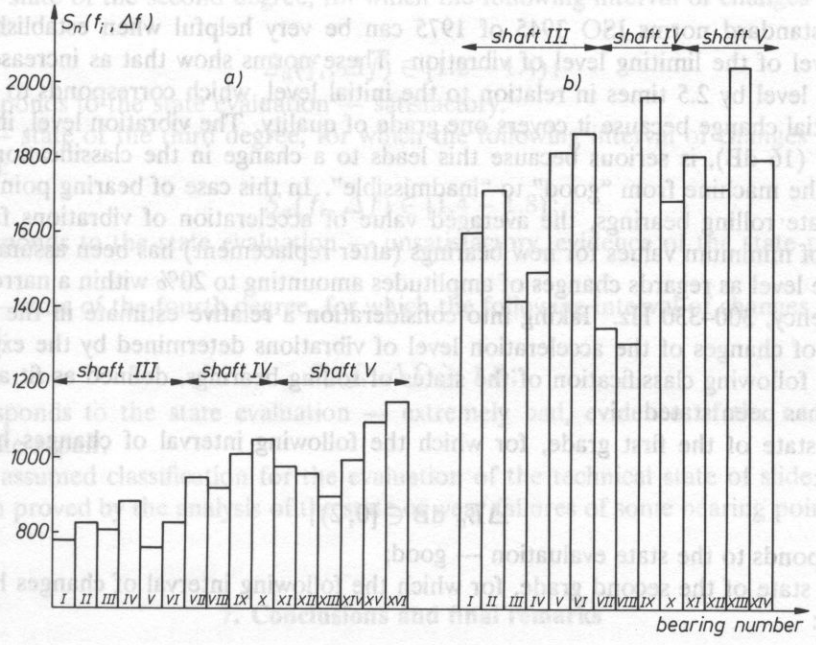

FIG. 12. Distributions of changes of values of the n-dimensional vector of state for satisfied slide bearings after a runing period of 10.000 hours a and 30.000 hours b.

Figure 12a, b represents distributions of values of the n-dimensional vector of the state of specified slide bearings after 10.000 hours of service (Fig. 12a) and 30.000 hours, respectively. A great diversification in the value of this vector, especially in the case of the service duration of 30.000 hours, proves the deterioration of the technical state of some slide bearings. When taking into account the introduced measures to evaluate the technical state of slide bearings, it is possible to distinguish tbe bearings which are characterized by a considerable degree of wear and thus, to present fans from approaching a state nearing failure.

6. Criteria for the evaluation of the technical state of bearing points

From the point of view of vibration diagnostics, the standards determining the criteria for the evaluation of machines and their elements with respect to the vibratory characteristic belong to the most important standards. To make the criteria useful, it is necessary to formulate them on the basis of the experimental data obtained as a result of vibration measurements. These measurements should be carried out under definite conditions of airflow in ventilation ducts. The criteria for the evaluation of the dynamic state of rolling bearings have been elaborated with regard to the numerical values of the rate of changes in the level of vibration acceleration, whereas in the case of slide bearings, distributions of changes in the value of the n-dimensional vector of the technical stand have been taken into account.

6.1. Vibratory criteria of the technical stand of rolling bearings

The standard norms ISO 3945 of 1975 can be very helpful when establishing the initial level of the limiting level of vibration. These norms show that as increase of the vibration level by 2.5 times in relation to the initial level, which corresponds to 8 dB, is an essential change because it covers one grade of quality. The vibration level, increased six times (16 dB), is serious because this leads to a change in the classification of the state of the machine from "good" to "inadmissible". In this case of bearing points which incorporate rolling bearings, the averaged value of acceleration of vibrations from the interval of minimum values for new bearings (after replacement) has been assumed for a reference level as regards changes of amplitudes amounting to 20% within a narrow band of frequency, 300–330 Hz. Taking into consideration a relative estimate in the form of the rate of changes of the acceleration level of vibrations determined by the expression (16), the following classification of the states of rolling bearings, defined as fit and unfit for use, has been stated:

I — state of the first grade, for which the following interval of changes has been assumed:

$$\Delta L_a \text{ dB} \in [0, 2);$$

it corresponds to the state evaluation — good;

II — state of the second grade, for which the following interval of changes has been assumed:

$$\Delta L_a \text{ dB} \in [2, 4);$$

it corresponds to the state evaluation — satisfactory.

III — state of the third grade, for which the following interval of changes has been assumed:

$$\Delta L_a \text{ dB} \in [4, 6);$$

it corresponds to the state evaluation unsatisfactory, equivalent to the state preceding failure.

IV — state of the fourth degree, for which the following interval of changes has been assumed:

$$\Delta L_a \geq 6 \text{ dB};$$

it corresponds to the state evaluation — inadmissible, evidence of the necessity of immediate repair.

6.2. Vibratory criteria of the technical stand of slide bearings

On the basis of the introduced n-dimensional vector of the technical stand of slide bearings, and obtained therefrom time distribution of values of this vector, a relative classification of the states of slide bearings, defined as fit and unfit for use, has been stated:

I — state of the first degree, for which the following interval of changes has been assumed

$$S_a(f_i, \Delta f) \in [0.8 - 1.2);$$

it corresponds to the state evaluation — good.

II — state of the second degree, for which the following interval of changes has been assumed:

$$S_a(f_i, \Delta f) \in [1.2 - 1.4);$$

it corresponds to the state evaluation — satisfactory.

III — state of the third degree, for which the following interval of changes has been assumed:

$$S_a(f_i, \Delta f) \in [1.4 - 1.8);$$

it corresponds to the state evaluation — unsatisfactory, evidence of the state preceding failure.

IV — state of the fourth degree, for which the following interval of changes has been assumed:

$$S_a(f_i, \Delta f) \geq 1.8;$$

it corresponds to the state evaluation — extremely bad, evidence of the necessity of immediate repair.

The assumed classification for the evaluation of the technical state of slide bearings has been proved by the analysis of the state of wear failures of some bearing points under repair.

7. Conclusions and final remarks

The results of the study, the aim of which was the vibratory diagnosis of rolling and slide bearings as represented in the paper are the basis for the evaluation of the technical state of drive systems of mine fans in the course of their operation. The introduced

estimates of a vibratory signal in the form of the rate of changes of the acceleration level of vibrations, as well as the n-dimensional vector of the state, made it possible to set up. A relative classification of the technical state of both rolling and slide bearings. This classification made it possible to state the points characterized by values exceeding the limite of the introduced estimates, and thus, to identify the technical state of bearing nearing failure. When using the introduced diagnostic measures it is possible to develop and construct an automatic system of control of the technical state which allows for a diversified evaluation of the technical state of bearing points.

The now-applied procedure of operation of many machines in the conditions of continuous running is based on a system of scheduled preventive repairs. It is quite often that a repair of a machine is carried out too early, and it seldom happens that it is effected too late, leading to a failure. The possibility of carrying out a repair, based on the knowledge of the real technical state of the machine is an alternative. This repair, conditioned by the technical state of the machine, shortens considerably the duration of repair, and allows to predict the time and range of the necessary repair. This results in a considerable reduction of operating costs of machines and equipment.

References

[1] Cz. CEMPEL, *The elements of vibroacoustic diagnosis of machines* (in Polish), PWN, Warszawa 1982.

[2] T. ZAKRZEWSKI, *Identification of dynamic parameters of a driving system of shearer gearheads in a view of evaluation of their service life and reliability in Polish*. Scientific facsimile of the Silesian Technical University. Series: Mining No 167 (1988).

[3] T. ZAKRZEWSKI, *Spectral analysis of vibrations in control investigations of vibroacoustic heads KGS-320*, Archives of Acoustics, **12**, 2, (1987).

[4] T. ZAKRZEWSKI, *Discrimination of dynamic states in the course of control diagnosis of gearheads in ranging arms* (in Polish), Problems of machine operation, No 2, 74 (1988).

[5] A. L. KNIGHT, *A brief review of the monitoring of vibration in rotating machines*, Noise control, vibration insulation. **8**, 5 (1977).

[6] T. ZAKRZEWSKI, *Identification method for location of impact vibroacoustic pulses when examining the hoisting machine* (in Polish), Proc. of the Mining Mechanization Centre KOMAG Gliwice No 3 (1984).

[7] T. ZAKRZEWSKI, *Evaluation of the usability of simple vibration estimates to diagnosis of rolling bearings* (in Polish), Scientific facsimiles of the Silesian Technical University, Series: Mechanics No 86 (1987).

[8] R. ŁACZKOWSKI, *Vibroacoustics of machines and equipment* (in Polish), PWN, Warszawa 1983.

[9] M. D. GENKIN, A. G. SOKOLOVA, *Vibroacoustic diagnosis of machine and mechanism* (in Russian), Moscow 1987.

[10] J. I. BROCH, *Mechanical vibration and shock measurements*, Bruel and Kjaer 1980.

[11] L. MÜLLER, *Gear transmission — examination* (in Polish) PWN, Warszawa 1984.

[12] H. KRZEMIŃSKI-FREDA, *Rolling bearings* (in Polish) PWN, Warszawa 1985.

Received on October 30, 1990

ARCHIVES OF ACOUSTICS
18, 1, 67–82 (1993)

ANALYSIS AND IMPLEMENTATION OF HYDROACOUSTIC METHODS FOR ESTIMATION OF HIGH DENSITIES OF FISH IN SEA PENS

A. STEPNOWSKI

Technical University of Gdańsk, Department of Electronics
(80-952 Gdańsk)

The paper presents the feasibility study of different acoustic methods with reference to system design, capable of estimating high density of fish, e.g. in aquaculture facilities. The velocity, attenuation and backscattering measurement methods are critically examined. The new, recursive echo integration method is introduced, which accounts for attenuation loss by dense collections of fish. The proposed implementation of this estimation technique employs the modified design of a dual-beam sonar-system ECOLOG II. The system provides the real-time absolute estimates of fish density in sea pens.

1. Introduction

The dynamically developing fish farming industry in recent years is in real need of new methods and techniques to estimate the number or biomass of fish in sea pens. In addition, the monitoring of these encaged fish spatial distribution patterns and their behaviour is also required. The newly introduced estimation techniques should provide quick and reliable data with high acuracy [1], [2]. Therefore the main objective of this paper is twofold. The first is to investigate the feasibility of hydroacoustic methods for quantitative estimation of dense fish populations in the sea pens. The second, is to develop a hydroacoustic system, capable of producing rapid and reliable estimates of the number density of the encaged fish concentrations. The proposed system design would have to materialize the results of the feasibility study and utilize the recent advances in new VLSI technology and digital signal processing techniques of the modern fisheries research sonar systems [3], [4].

The current methods of hydroacoustic fisheries assessment assume no acoustic interactions between insonified fish, i.e. first-order single scattering (FOSS) approximation is assumed. This implies that the received echo signal is directly proportional to the number (and size) of fish insonified at a corresponding depth, and independent of the number of fish in the sound beam at intermediate depth [5]. This can be a reasonable assumption when the collection of fish is neither dense nor of a large extent in the direction of sonar transmission. The most common acoustic technique which has been successfully used to quantify fish stocks in oceans and lakes is, at present, the echo integration technique (EIT). It is based on a single scattering approximation and a linear relationship between

the integrated echo intensity and the density of fish N_v in a volume sampled by the sonar transmit pulse. The echo integration technique depends only upon the backscattering characteristics of fish targets, determined in terms of their backscattering cross section σ_{bs} or, more generally, of their volume backscattering strength $S_v = 10 \log \sigma_{bs} + 10 \log N_v$ [5], [6].

In those situations where high-density aggregations of fish are encountered (e.g., sea pens or dense schools), the FOSS approximation is no longer valid; excessive sound attenuation, and possibly multiple scattering also, may significantly reduce the backscattering from the deeper parts of the fish collection. Consequently, due to such "shadowing effects", the density estimates obtained from an echo integration may be remarkably biased — usually underestimated [7], [8][1].

Therefore the development of the hydroacoustic assessment technique, adequate for estimating the high density of fish in sea pens, must be preceded by the introduction of a more complete model of scattering and associated effects. Additionally, alternative approaches based on the measurement of acoustical magnitudes different from backscatter which could provide data for the calculation of fish density estimates, should also be examined.

2. Analysis of acoustical methods for fish density estimation

Basically there are three methods allowing at least potentially to obtain acoustical estimates of the high density of fish in sea pens. These methods utilize the measurement of sound velocity, sound attenuation and sound backscattering.

2.1. Sound velocity measurement for fish density estimation

The sound velocity can be a very important and useful signature of the medium characteristics. Its measurements are used concurrently with other acoustical magnitudes in various applications of which acoustical tomography is probably most spectacular. Although this measurement does not seem very promising for the considered application, it will be shortly examined in order to be sure that any potentially possible method has not been neglected.

When a sound wave travels through water and strikes "bubble-like" targets (e.g. swimbladder of fish) of markedly different density and compressibility than seawater, the resonance response may occur. The resonating target may be viewed as intercepting a portion of the exciting sound wave characterized by the extinction cross section, and reradiating it as scattered sound in all directions as well as absorbing by converting it into heat. In addition, "bubble-like" targets change the compressibility of the water and cause the phase speed of sound to be a function of frequency. In the vicinity of resonance the sound velocity may be altered remarkably if the bubble concentration is high enough. When the bubbles are much smaller or much larger than the resonant size, the effect is not so profound.

[1] It should be noted, however, that under certain conditions high extinction cross section and a low absorption cross section of scatterers, the multiple, or more precisely second-order scattering, may increase the backscattered echo energy an appreciable amount above that expected by the FOSS theory alone [9].

The equation of an acoustic plane wave propagating through a bubbly medium can be written as

$$p(t,r) = P_i \exp[j(\omega t - kr)] = \\ = P_i \exp(-k_{im} r) \exp[j(\omega t - k_{re} r)] \tag{1}$$

where: P_i — amplitude of the sound pressure, $k = \frac{\omega}{c} = k_{re} - jk_{im}$ the complex propagation constant.

The imaginary part k_{im} of the complex propagation constant represents the excess attenuation of the wave through the bubbly region, while the real part k_{re} is the wave number for the propagation of constant phase surfaces. The ratio ω/k_{re} is the phase velocity of the sound wave in a bubbly medium. It is a function of frequency and the medium is said to be dispersive [9]:

$$c = \omega/k_{re} = c_0 \left[1 - \frac{2\pi a N c_0^2}{\omega^2} \frac{(\omega_r/\omega)^2 - 1}{[(\omega_r/\omega)^2 - 1]^2 + \delta^2]}\right] \tag{2}$$

where c_0 speed of sound through the bubble-free water, N — number of bubbles per unit volume (numbers density), a — equivalent average radius of a bubble, ω_r resonance frequency, δ — damping constant.

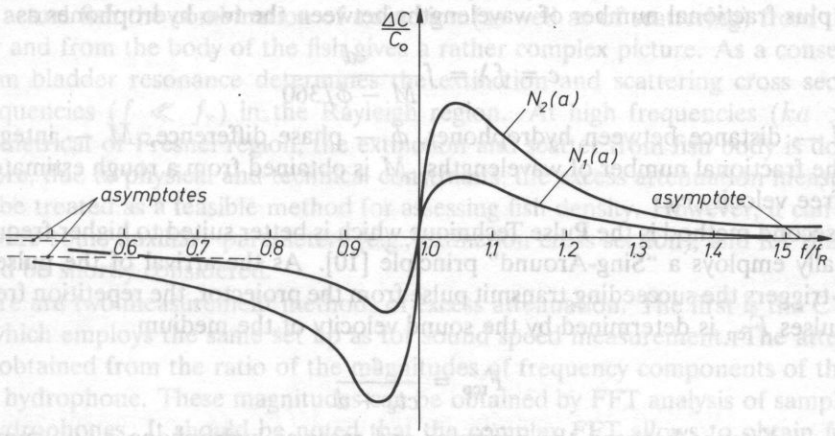

FIG. 1. Fractional change in sound velocity for two different bubble densities $N_2 > N_1$.

The fractional change in phase velocity $\Delta c/c_0$ derived from Eq. (2), for bubbles of uniform size and two different densities N is shown in Fig. 1. As it is seen from dispersion curves, the change in velocity is proportional to N. The velocity passes through the c_0 value at the resonance frequency. The high frequency asymptote is zero and the low frequency asymptote is proportional to the fraction of gas in bubble form $V = 4/3\pi a^3 N$. Any significant changes of sound velocity occur only in the resonant region, while well beyond the resonance (which is most likely the range of feasible measurement) the relative changes of velocity are too small for accurate measurement.

The resonance frequency of our "bubble of interest" (fish swim bladder) f_r can be obtained from a simplified formula [9]:

$$f_r = \frac{1}{2\pi a'}\left(\frac{3\gamma P^{1/2}}{\rho}\right) \tag{3}$$

where: γ — ratio of specific heats of bladder gas ($\gamma = 1.4$ for air), P ambient pressure, $P = 105(1 + 0.1z)$, where z is depth [m], ρ density of sea water ($\rho = 1035\text{kg/m}^3$), a' — equivalent radius of a swim bladder, $a' = (3 \text{ bladder volume } /4\pi)^{1/3}$.

For fish size of commercial interest (20–100 cm), the bladder representing about 5% of the animal volume has its equivalent radius ranging from 0.3 to 3 cm. It gives a range of resonance frequencies from 0.1 to 1 kHz. Unfortunately, it is rather difficult to provide the efficient transmission of underwater sound at such low frequencies. Thus, as a consequence, there are two different kinds of constraints: poor sensitivity or accuracy for high frequency measurement and technical limitations for low frequency measurement. Despite this rather not optimistic conclusion, there are two existing methods of sound speed measurement which should be reported as feasible but have rather limited applicability for the extraction of fish density data.

The first method is the CW Phase Measurement Technique which is best suited for lower frequencies [9]. It requires only a sound projector and two hydrophones separated by a fixed and known distance. The speed of sound is easily obtained by measuring the integral plus fractional number of wavelengths between the two hydrophones as

$$c = f\lambda = f\frac{d}{M - \phi/360} \tag{4}$$

where d — distance between hydrophones, ϕ — phase difference, M — integral and $\phi/360$ the fractional number of wavelengths. M is obtained from a rough estimate of the bubble-free velocity c_0.

The second method is the Pulse Technique which is better suited to higher frequencies, and usually employs a "Sing-Around" principle [10]. As the arrival of the pulse at the receiver triggers the succeeding transmit pulse from the projector, the repetition frequency of the pulses F_{rep} is determined by the sound velocity of the medium

$$F_{\text{rep}} = \frac{c}{ct_e + d} \tag{5}$$

where d — distance between the projector and receiver hydrophone, t_e — sum of the electrical delay and time lost in the pulse front growing above the noise threshold.

The resulting pulse repetition frequency can be measured by the frequency counter connected to the "Sing-Around" loop, and t_e and d are obtained by direct calibration in a medium of known sound speed.

2.2. *Sound attenuation measurement*

The presence of bubble-like targets at sea, in addition to scattering, introduces also excess attenuation of acoustic waves[2] which, when properly measured and scalled, can also

[2] The term "excess" is used purposely to differentiate the effect introduced by the targets from „common" attenuation in the sea which is due to shear viscosity and molecular relaxation processes in the medium [10].

be used as a signature of the targets numbers density. Let us consider the aggregation of bubble-like targets (fish) of uniform size and assume that the targets are apart far enough to neglect interaction effects (multiple scattering)[3]. Then the excess attenuation per unit distance can be written as [10]:

$$\alpha_e = -\Delta SPL/x = 4.34\sigma_e N_v \tag{6}$$

where: σ_e — extinction cross section of the target, N_v — number of targets per unit volume, x distance traversed by the sound wave, $\Delta SPL = 20 \log p(x)/p_1$ loss in sound pressure level over a distance x, p_i incident sound pressure.

If a population of targets has some size distribution function $n(a)$ and the number of targets per unit volume with sizes between a and $a + da$ is denoted by $n(a)da$, the effective extinction cross section

$$S_e = \int \sigma_e n(a)\, da \tag{7}$$

replaces the product $\sigma_e N_v$ in the formula (6) when attenuation due to a random mixture of bubble-like targets has to be obtained [10].

The estimates of bubble-like target density can be obtained from the excess attenuation measurement if the extinction cross section of bubbles is known or can be measured. Like the scattering and absorption cross sections, the extinction cross section has a maximum at the resonant frequency and falls off with frequency away from resonance. However, for the actual fish the combination of extinction (as well as of scattering) from the swim bladder and from the body of the fish gives a rather complex picture. As a consequence, the swim bladder resonance determines the extinction and scattering cross sections at low frequencies ($f \ll f_r$) in the Rayleigh region. At high frequencies ($ka > 1$), in the geometrical or Fresnel region, the extinction and scatter from fish body is dominant. Therefore, due to physical and technical constraints, the excess attenuation measurement cannot be treated as a feasible method for assessing fish density. However, it can be used to measure some auxiliary parameters (e.g., extinction cross section), and for this reason it should be shortly considered.

There are two measurement methods of excess attenuation. The first is the CW Technique which employs the same set up as for sound speed measurement. The attenuation can be obtained from the ratio of the magnitudes of frequency components of the signal at each hydrophone. These magnitudes can be obtained by FFT analysis of sampled data from hydrophones. It should be noted that the complex FFT allows to obtain from the same data the phase difference, what yields the sound velocity [9].

The second method is the Pulse Echo Technique which allows to obtain the excess attenuation introduced by an aggregation of fish, by measuring the variations of echo level, received from the special reference target, of known target strength (TS). If the sonar system used for measurement is calibrated acoustically (i.e., its source level (SL) and receiver sensitivity (SR) are known), then the echo level (EL) measurement allows, by the sonar equation, to obtain the entire two-way transmission loss ($2TL$)

$$EL = SL + SR + TS - 2TL \tag{8}$$

[3] Efectively this will be valid if the packing density of targets is so low that the separation is greater than the wavelength λ of the impinging sound wave, or alternatively greater than the square root of the extinction cross section σ_e of the target [10].

where $2TL$ includes two-way transmission loss of the medium combined with two-way excess attenuation of the fish aggregation:

$$2TL = 40\log(R_s/R_1) + 2\alpha(R_s - R_1) + 2\alpha_e(R_s - R_1) \tag{9}$$

where R_s is the range of reference target, $R_1 = 1m$, and α is the attenuation coefficient of sound in the sea. As all other parameters but excess attenuation coefficient α_e are known, this can be easily extracted from Eqs. (8) and (9).

An alternative option in estimating α_e might be to make a similar measurement of the standard targer echo level twice: in the presence (EL_2) and in the absence (EL_1) of a fish aggregation. In such a case, the estimate of α_e can be easily derived from the increment $\Delta EL = EL_2 - EL_1$. This option does not require acoustic calibration of the sonar system.

2.3. Sound backscattering measurement — Echo Integration Technique

The sound backscattering measurement is the most common method of hydroacoustic assessment of fish density, especially when it is implemented as an echo integration technique (EIT). Skipping the details for incoherent addition of the individual fish echoes, the backscattered echo intensity due to the collection of randomly distributed fish scatterers, received from a shell volume at range R, can be written as [2]:

$$I_{(R)} = I_0 10^{-0.2\alpha R} \cdot R^{-2}(c\tau/2)\sigma_{bs}N_v b_{eq}^2 \tag{10}$$

where: $I_0 = I_1 10^{0.1SL}$ — incident intensity, W/m^2, R — range to sonar transducer, m, $10^{-0.2\alpha R}R^{-2}$ antilog of two-way transmission loss $2TL$, σ_{bs} — mean backscattering cross section of fish, m^2, N_v — average number of fish per unit volume, m^{-3} $b_{eq}^2 = \int_\Omega b^2(\theta,\phi)\,d\Omega$ equivalent two-way beam width (mean squared beam pattern factor), $b(\theta,\phi)$ beam pattern of sonar transducer, $d\Omega = \sin\theta\, d\theta\, d\phi$ — elemental solid angle, srd; τ — pulse length, s; c — speed wave of sound wave in sea water, m/s; I_1 — reference intensity, W/m^2.

The corresponding echo envelope squared voltage, at the output of the sonar receiver, can then be written as

$$V_{(R)}^2 = I_{(R)}s_r^2 g_{TVG(R)}^2 \tag{11}$$

where: $s_r = s_1 10^{0.1(SRT+G)}$ receiving sensitivity, V/Pa, G — constant gain of the receiver, dB, SRT — sensitivity of receiving transducer, dB, $g_{TVG} = 10^{0.1G_{TVG}(R)}$ time varied gain of the receiver, V/V, $G_{TVG}(R) = 10\log(R/R_1) + \alpha(R - R_1)$. dB. As this TVG function compensates for two-way transmission loss $2TL = 20\log R/R_1 + 2\alpha(R - R_1)$, the backscatter echo squared $V_{(R)}^2$ is proportional to the product of fish density and backscattering cross section

$$V_{(R)}^2 = C_s\sigma_{bs}N_v \tag{12}$$

where the proportionality coefficient C_s is a sonar system constant

$$C_s = I_0(c\tau/2)s_r^2 b_{eq}^2 \tag{13}$$

Thus, the measurement of the backscatter echo squared output voltage allows to obtain an estimate of fish density in insonified volume, assuming the system constant C_s and backscattering cross section of fish σ_{bs} are known.

To obtain the estimates of the average fish density, which are of practical interest, the backscatter echo squared output voltage $V^2_{(R)}$ must be averaged over some depth interval $\Delta R = R_2 - R_1$ and over some number p of pings. This is realized by the Echo Integration Technique (EIT). The first averaging is obtained by integrating the squared echo envelope (12) over the time interval $\Delta t = 2\Delta R/c$ for each ping

$$\int_{t}^{t+\Delta t} V^2(t)\,dt = C_s \int_{R}^{R+\Delta R} N_v(R)\sigma_{bs}(R)\,dR = \\ = C_s\sigma_{bs}(\Delta R)N_v(\Delta R) \tag{14}$$

where $\sigma_{bs}(\Delta R)$ average backscattering cross section of fish in layer ΔR, $N_v(\Delta R)$ average fish density in depth layer ΔR.

If the second averaging over the specified number of pings is done, the average fish density ρ_v in a layer ΔR can be estimated by

$$\rho_v(\Delta R) = (\text{const})^{-1} M \tag{15}$$

where $M = avg\{\int_{\Delta t} V^2(t)dt\}$ is the so-called "integrator output" [6] and the proportionality constant is the product of the constant C_s and the average σ_{bs} of fish surveyed in the layer ΔR. Thus, if the C_s has been measured and the σ_{bs} is known, or can be estimated, the mean integrator output yields the absolute estimate of average fish density.

Echo integration is implemented with a digital integrator which accomplishes an integration similar to Eq. (14), by using a "sum-of-squares" approach [12]. For each ping, the consecutive digital samples of the echo envelope within each depth layer are squared and summed. For the j-th layer on the k-th ping, the partial sum of m squared samples with the sampling interval i is given by

$$S_{jk} = \sum_{i-1}^{m} (V_i)^2_{jk} \tag{16}$$

After acquiring the data for all pings in a specified sequence of p pings, the accumulated sum is calculated for each layer:

$$S_j = \sum_{k-1}^{p} S_{jk} = \sum_{k-1}^{p} \sum_{i-1}^{m} (V_i)^2_{jk} \tag{17}$$

The accumulated sums are then averaged over the total number of pings p in the sequence and the number of samples m in the depth layer, giving the "integrator outputs" representing the relative estimate of fish density in the layers. Such a mean squared voltage of backscatter echo constituting the integrator output for the j-th layer is

$$V^2_{(\Delta R)j} = M_j = \overline{m}^1 \overline{p}^1 \sum_{k}^{p} \sum_{i}^{m} (V_i)^2_{jk} \tag{18}$$

where: m — number of samples integrated within the j-th depth interval ΔR for a sampling increment of T_s seconds, $m = 2\Delta R/cT_s$; p — number of pings integrated within the ping sequence, i — current number of the voltage sample, k — current number of ping in the sequence, $(V_i)^2_{jk}$ — squared sampled voltage for the i-th increment in j-th depth interval and k-th ping.

Assuming the system parameters are constant within the averaging constraints, then the mean integrator output (18) can be finally converted to the absolute estimate $\hat{\rho}$ of the average density of fish in arbitrary depth layer:

$$\hat{\rho}_j = C^{-1}\overline{V}_j^2 \tag{19}$$

where $C = C_s\hat{\sigma}_{bs}$ is the overall integrator scalling constant, and $\hat{\sigma}_{bs}$ is an estimate of the average backscattering cross section of the surveyed fish.

The echo integration data can be alternatively expressed in terms of the mean volume backscattering strength [6], [11]

$$MVBS = 10\log\overline{V}^2 - (SL + SRT + G + 10\log c\tau/2 + 10\log b_{\text{eq}}^2) \tag{20}$$

where V^2 is determined by Eq. (19) and the expression in parenthesis is the system constant C in decibels, and MVBS is related to the average fish density as

$$MVBS = 10\log\overline{N}_v + \overline{TS} \tag{21}$$

where $\overline{TS} = 10\log\overline{\sigma}_{bs}/4\pi$ the average target strength of fish.

3. Development of the modified echo integration technique for estimation of high density of fish

3.1. Single scattering with attenuation approximation (SSA)

This approximation constitutes the extension of the single scattering solution, as additionally it assumes that the backscattered echoes from each scatterer are similarly diminished, as they are partly scattered or absorbed — extinguished in general — by other scatterers. This excess attenuation of the backscatter echo from fish at a given depth by other fish at intermediate depth violates the assumption on the integrated echo intensity dependence upon the backscattering characteristics of fish only. As a consequence, the application of the SSA requires knowledge of the mean backscattering cross section $\overline{\sigma}_{bs}$ as well as the average extinction cross section $\overline{\sigma}_e$ [5].

Let us consider an aggregation of randomly distributed scatterers with an average extinction cross section $\overline{\sigma}_e$ and assume that the volume number density of scatteres is in general a function of the range $N_v(R)$. If the acoustic wave of incident intensity $I(R)$ at the range R travels a distance dR, it encounters $N_v dR$. This is equivalent to the loss of the incident intensity dI over dR

$$dI(R)/dR = -\overline{\sigma}_e N_v(R) I(R) \tag{22}$$

which, after integration, gives

$$I(R) = I(R_0)\exp\left\{-\int_{R_1}^{R}\overline{\sigma}_e N_v(R)\,dR\right\} \tag{23}$$

where R_0 is an initial range, and the exponent $\gamma(x) = \int_0^x \sigma_e N_v(x)dx$ is sometimes called the optical distance[4].

The echo intensity received from the range R for SSA approximation can be derived by using the attenuated intensity (23) in place of unattenuated incident intensity, viz.:

$$I_{a(R)} = I_{(R)} \exp\left\{ -2 \int_{R_1}^{R} \overline{\sigma}_e N_v(R')\, dR' \right\} \tag{24}$$

where $I_{(R)} = I_0^{-0.2\alpha R} R^{-2} (c\tau/2) b_{eq}^2 \sigma_{bs} N_v(R)$ is the received intensity in the absence of attenuation (see the formula (10)) and the factor 2 in the exponent is due to the two-way attenuation.

Proceeding in a similar way as for unattenuated echo intensity in Section 2.3 we can derive the echo squared voltage at the output of a sonar receiver as

$$V_{a(R)}^2 = C_s \sigma_{bs} N_v(R) \exp\left\{ -2 \int_{R_1}^{R} \overline{\sigma}_e N_v(R')\, dR' \right\} \tag{25}$$

The last equation shows that in contrary to FOSS approximation (12) the simple proportionality relation between the echo squared voltage and fish number density does not hold any more. Due to the presence of an excess attenuation, not only the average backscattering cross section but also the average extinction cross section of fish must be known. Consequently the echo integration technique algorithm must be modified to fulfill the new requirements introduced by SSA approximation on fish density estimates.

3.2. Modified echo integration algorithm for SSA model

Let us consider the integration of the squared echo signal (25) in the depth interval $\Delta R = R_2 - R_1$ carried out in thin depth increments of thickness δR. If one assumes the average values of the backscattering and extinction cross sections $\overline{\sigma}_{bs}$ and $\overline{\sigma}_e$ for all depth layers, then the echo integrator output for the j-th layer can be written as

$$M_j = C_s \overline{\sigma}_{bs} \rho_1(R) \exp\left\{ -2\overline{\sigma}_e \sum_{j-1}^{n} \rho_j \delta R_j \right\} \tag{26}$$

As it is seen from the last equation, and from the preceding integral form (25), the exponential attenuation factor comprising the fish density, affects all successive depth layers. For this reason the solution of Eq. (26) is recursive and, in order to extract the fish density in the j-th layer, the densities in preceding $j-1$ layers must be known [5]. In other words, the integrator output must be recursively updated by the data from the preceding layers.

The structure of the proposed density estimation technique is as follows. The squared echo voltages are integrated over the time intervals δt_j, associated with the successive

[4] The quantity $\gamma(x)$ indicates the extent to which the incident wave has encountered scatterers in the intervening volume and represents the merit of applicability of various approximations of scattering. If $\gamma \ll 1$ (low density case), the single scattering model is valid. If $\gamma \cong 1$ (medium and high densities) SSA approximation applies. If $\gamma \gg 1$ (very high densities), diffusion approximation is valid [5].

depth layers δR_j, and then multiplied by the gain factors $\exp\{\gamma(Rj)\}$ which compensate for the attenuation affecting each depth layer and which are computed from the density estimates of these preceding intervals. Thus the fish density estimate in the j-th layer is calculated from the estimates in previous $j-1$ layers as

$$\hat{\rho}_j = C_s^{-1}\overline{\sigma}_{bs}^{-1} M_j \exp\left\{2\overline{\sigma}_e \sum_{r=1}^{j-1} \hat{\rho}_r \delta R_r\right\} \tag{27}$$

By this means, we estimate the fish density in a given layer in such a way, as it is no attenuation in this particular layer, accounting the effect of attenuation in all preceding layers.

In order to employ the proposed density estimation technique, the two parameters must be known, viz.: the mean backscattering cross section $\overline{\sigma}_{bs}$ and the mean extinction cross section $\overline{\sigma}_e$. One method allowing for a direct "in situ" estimation of $\overline{\sigma}_{bs}$ is the Dual-Beam Method. This method has been implemented sucessfully in a newly developed ECOLOG II real-time computerized sonar system, [3], [12] and as an estimation technique it will be used in the considered application. The estimation of $\overline{\sigma}_e$ is a different matter and will be the subject of the next section.

3.3. Extinction cross section measurement

Unlike the well established measurement methods of the backscattering cross section, or target strength, the extinction cross section "in situ" measurements are not so well developed. One possible and feasible approach is an indirect method based on the excess attenuation measurement using a reference target see (Sect. 2.2). Thus performing a single measurement of the standard target echo level EL, and comparing Eq. (10) with Eq. (6), we obtain

$$\sigma_e = \frac{EL - [SL + SRT + TS - 40\log R_s/R_1 - 2\alpha(R_s - R_1)]}{2(R_s - R_1)4.34N_v} \tag{28}$$

For the case of double measurement of the standard target echo. i.e., in the presence ($EL2$) and in the absence ($EL1$) of the fish aggregation in the pen we have

$$\sigma_e = \frac{EL_2 - EL_1}{2(R_s - R_1)4.34N_v} \tag{29}$$

The only unknown which appears in Eqs. (28) and (29) is the mean numbers density of fish N_v. This must be known or must be obtained from some other experiment in order to extract the extinction cross sections estimate from one of these equations. Apparently the proposed approach seems to be contradictory as the extinction cross section is estimated in order to improve the unknown fish density estimate. Therefore the latter one cannot be used to obtain the first one. Fortunately it is not so since usually in aquaculture facilities some a priori information on fish density is available. These data can be used as a first approximation of the actual density of fish in pen for calculating a rough estimate of the extinction cross section. Alternatively this first approximation can be obtained from the echo integration when implemented in a conventional manner (see Eqs. (18) and (19)).

Substituting the approximate estimate of fish density in Eqs. (28) or (29) gives the rough estimate of σ_e which in turn will be used for calculating the fish density estimates in depth layers, according to the modified integration algorithm (27). Due to the recursive

structure of the proposed estimation algorithm, the density estimate for the first layer is assumed to be "accurate" as there is practically no excess attenuation for this layer. This density estimate can be used in calculating the corrected estimate of the extinction cross section which will then be used for calculating the final estimates of fish density according to the recursive algorithm (27).

4. Implementation of the estimation technique for high densities of fish

4.1. General system description

The recursive fish density technique proposed in Sect. 3.2 has been implemented in the modified design of the real time dual-beam signal processing sonar system ECOLOG II [3], [12], [13]. This system option has been labelled "Fish Counter" and its basic configuration consists of three major subassemblies:

Dual-Beam Transducer Unit

Sounder-Processor Unit

Host Computer Workstation

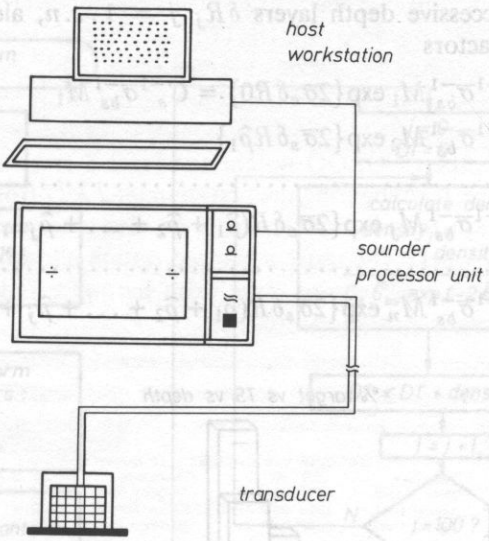

FIG. 2. Major subassemblies of the FISH COUNTER system.

The transducer unit consists of a dual-beam transducer mounted inside a versatile housing, along with the matching/tuning network. The transducer can operate either as downward-looking, when floating on the surface above the pen, or as upward-looking when placed on the bottom below the pen.

The sounder/processor unit contains the compact, precision echo sounder and a powerful, high performance internal computer based on the Motorola M68010 16 bit microprocessor. The sounder parameters are fully programmable by the user from the host computer workstation. The high power electrical burst from the sounder transmitter is

routed to the transducer and radiated vertically in the water column on the narrow beam. The fish echoes received on both narrow and wide beams are subject to analog and digital processing in the two-channel receiver and digital signal processor (DSP). The DSP output data is processed immediately by the internal computer which performs in real-time the Echo Integration or Target Estimation mode of operation. The real-time computer output data is formated and sent by high speed data transfer to the host computer.

The host computer workstation is an IBM PC/XT/AT or any other compatible one. It is responsible for the whole user control and operation of the sounder/processor unit. It also provides post processing, data storage and graphics presentation of output data. The user friendly software is provided for system setup data entry and output.

Since the majority of the system hardware and software is the same as in the ECOLOG II system [3], [12], we will confine ourselves only to the discussion of the modified echo integration which is the specific operating mode of the proposed FISH COUNTER system design.

4.2. Modified recursive echo integration software

The proposed recursive estimation algorithm (27) can be expanded to show the density estimates in the successive depth layers δR_j $j = 1 \ldots n$, along with the exponential compensating gain factors

$$
\begin{aligned}
&\hat{\rho}_1 = C_s^{-1}\overline{\sigma}_{bs}^{-1} M_1 \exp\{2\overline{\sigma}_e \delta R0\} = C_s^{-1}\overline{\sigma}_{bs}^{-1} M_1 \\
&\hat{\rho}_2 = C_s^{-1}\overline{\sigma}_{bs}^{-1} M_2 \exp\{2\overline{\sigma}_s \delta R\hat{\rho}_1\} \\
&\ldots\ldots\ldots\ldots\ldots\ldots\ldots\ldots\ldots\ldots\ldots\ldots\ldots\ldots\ldots\ldots \\
&\hat{\rho}_j = C_s^{-1}\overline{\sigma}_{bs}^{-1} M_j \exp\{2\overline{\sigma}_e \delta R(\hat{\rho}_1 + \hat{\rho}_2 + \ldots + \hat{\rho}_{j-1})\} \\
&\ldots\ldots\ldots\ldots\ldots\ldots\ldots\ldots\ldots\ldots\ldots\ldots\ldots\ldots\ldots\ldots \\
&\hat{\rho}_0 = C_s^{-1}\overline{\sigma}_{bs}^{-1} M_n \exp\{2\overline{\sigma}_s \delta R(\hat{\rho}_1 + \hat{\rho}_2 + \ldots + \hat{\rho}_j + \ldots + \hat{\rho}_{n-1})\}
\end{aligned}
\tag{30}
$$

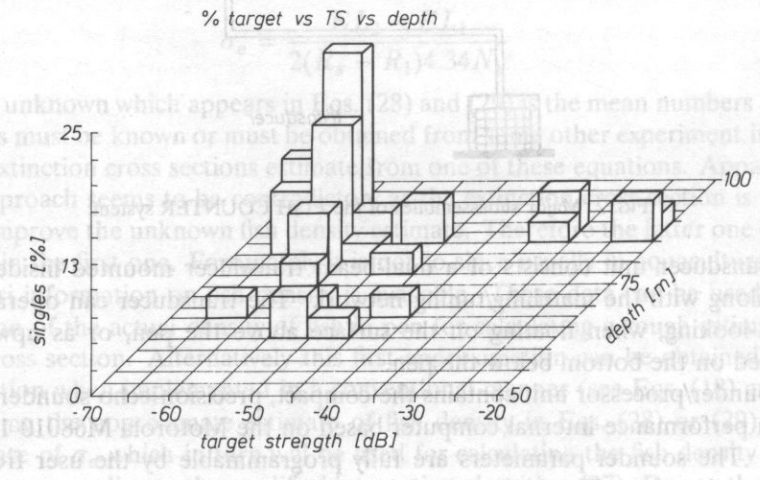

FIG. 3. Target strength versus depth 3 – D histogram.

The average backscattering cross section $\overline{\sigma}_{bs}$ can be obtained from the target strength data which are extracted from the single fish echoes by the dual-beam processing in the TS Estimation mode of the ECOLOG II system operation [3], [12]. The sample TS versus depth $3-D$ histogram provided by the ECOLOG II system is shown in Fig. 3. The average extinction cross section $\overline{\sigma}_e$ can be obtained according to the procedure described in Sect. 3.3.

The modified echo integration mode of system operation providing the recursive density estimates is implemented as follows. The wide beam data is processed only using the "sum-of-squares" approach (see Sect. 2.3). The internal computer maintains an array of data "table", $i = 0 \ldots 1023$, where i represents the depth and "table i" is the sum of squared echo voltages samples received at that depth. The data is accumulated over N_p pings and then transferred to the host computer. Once the host receives the array of the accumulated sums, it calculates the system constant C_s and the relative fish density array $\{M_j\}$, $j = 0 \ldots 99$. Finally this data is converted to the absolute fish density array "density"$_j$ employing the recursive procedure (30).

The flow chart of the recursive echo integration algorithms which are executed by the host computer is explained in Fig. 4.

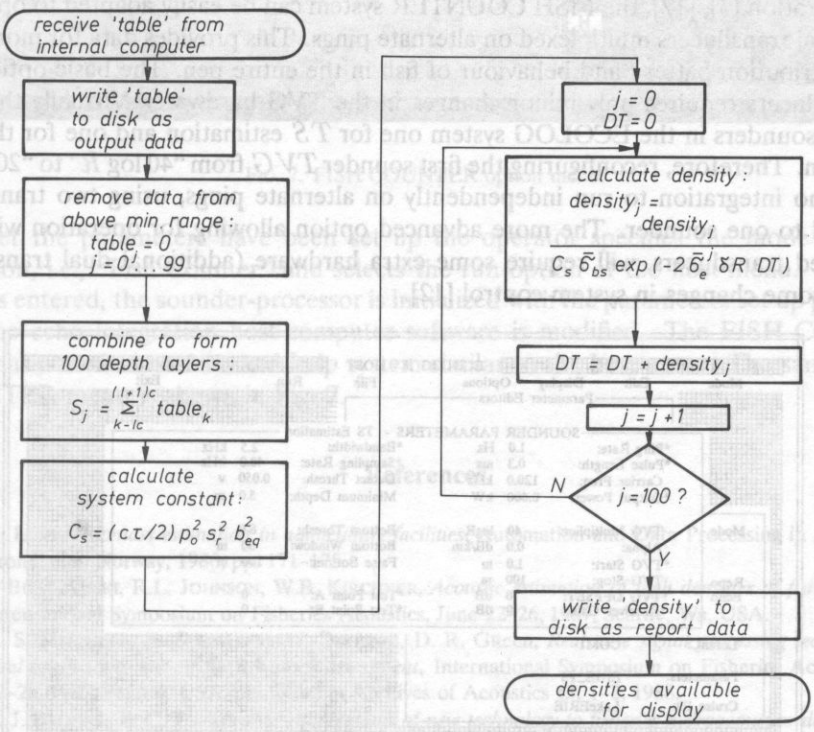

FIG. 4. The recursive fish density estimation flow chart - host computer modified echo integration software.

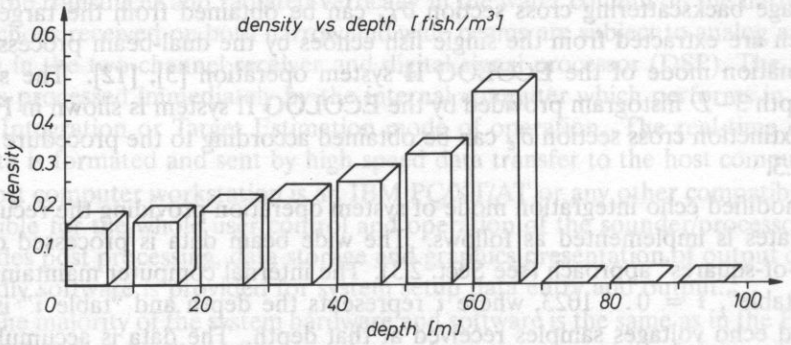

FIG. 5. Fish density versus depth distribution.

After each sequence of N_p pings the fish density data is copied to the display buffer for graphic presentation. A sample fish density profile in depth layers is shown in Fig. 5.

4.3. One system option with multiplexed transducers

Due to a unique feature of the ECOLOG II system, which is a simultaneous dual-mode operation [3], [12], the FISH COUNTER system can be easily adapted to operation with several transducers multiplexed on alternate pings. This provides data for monitoring of the distribution pattern and behaviour of fish in the entire pen. The basic option with two transducers requires only minor changes in the TVG hardware. Virtually there are two echo sounders in the ECOLOG system one for TS estimation and one for the echo integration. Therefore, reconfiguring the first sounder TVG from "40 log R" to "20 log R" allows echo integration to run independently on alternate pings, using two transducers connected to one sounder. The more advanced option allowing for operation with four multiplexed transducers, will require some extra hardware (additional dual transmitter) and also some changes in system control [12].

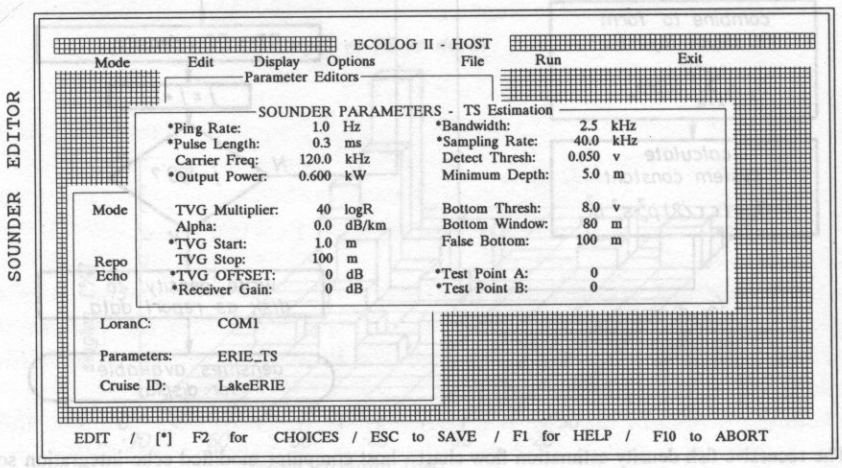

FIG. 6. ECOLOG II host menu and Sounder settings window.

4.4. System operation

The operation of the "Fish Counter" system is practically the same as the basic ECOLOG II system version. To run the system the operator enters the HOST command which loads, and runs the host computer programs. Once the host menu is displayed, the operator enters the desired parameters into the editing window or loads a parameter file. A sample ECOLOG II sounder settings editor of the host menu is shown in Fig. 6.

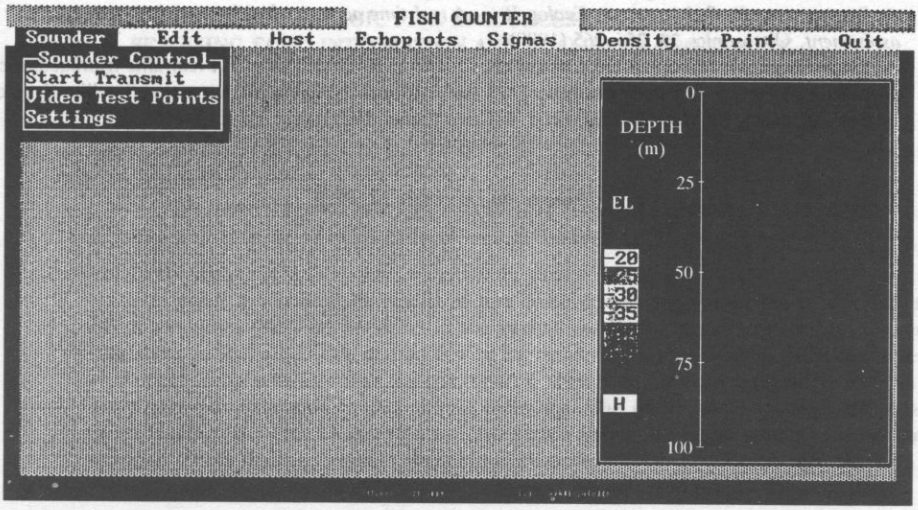

FIG. 7. FISH COUNTER option menu.

After the parameters have been set up the operator specifies the mode of system operation, i.e., "Fish Counter" and selects the run option of the host menu. When this mode is entered, the sounder-processor is initialized with the parameters set up previously. Also the echo integration host computer software is modified. The FISH COUNTER mode has a menu interface and help system similar to the host menu. The sample FISH COUNTER menu is shown in Fig. 7.

References

[1] A. LOVIK, *Biomass estimation in aquaculture facilities*, Automation and Data Processing in Aquaculture, Trondheim, Norway, 1986, pp. 171–175.

[2] J. BURCZYŃSKI, R.L. JOHNSON, W.B. KIRCHNER, *Acoustic estimation of high densities of fish in sea pens*, International Symposium on Fisheries Acoustics, June 22–26, 1987, Seattle, Wa, USA.

[3] R. S. MITCHELL, A. STEPNOWSKI, J. DROBNIK, D. R. GREEN, *Real time signal processing techniques in a dual beam sonar system for fish stock assessment*, International Symposium on Fisheries Acoustics, June 22–26, 1987, Seattle, USA, published in Archives of Acoustics **13**, 1–2, 1988.

[4] T. J. BROOKS, T. C. TORKELSON, *Applications of new technology to fisheries hydroacoustics data collection and analysis*, International Symposium on Fisheries Acoustics, June 22–26, 1987, Seattle, USA.

[5] D. W. LYTLE, D. R. MAXWELL, *Hydroacoustic assessment in high density fish schools*, ICES/FAO Symposium on Fisheries Acoustics June 21–24, 1982, Bergen, Norway, FAO Fish. Rep. 300, pp. 157–171.

[6] K. OLSEN, *Sound attenuation within scholls of herring*, Con. Meet. ICES 44, 1986.

[7] K. G. FOOTE, *Linearity of fisheries acoustics with addition theorem*, J. Acoust. Soc. Am., **73**, 6, 1932–1940 (1983).

[8] T. K. STANTON, *Effects of second-order scattering on high resolution sonars*, J. Acoust. Soc. Am., **76**, 3, 861–866 (1984).

[9] C. C. CLAY, H. MEDWIN, *Acoustical oceanography*, J. Wiley and Sons Ins., 1977.

[10] R. J. URICK, *Principles of underwater sound*, McGraw Hill, New York 1975.

[11] A. STEPNOWSKI, J. BURCZYŃSKI, *The analysis of calibration constant in the hydroacoustic system of fish abundance estimation*, In: Meeting on Hydroacoustic Methods for the Estimation of Marine Fish Populations, June 25–29, 1979 Cambridge, USA, vol. 2 part A pp. 325–336.

[12] A. STEPNOWSKI, R. S. MITCHELL, *Ecolog II — A real time acoustic signal processing system for fish stock assessment*, Ultrasonics **28**, 256–265 (1990).

[13] A. STEPNOWSKI, R. MITCHELL, S. LAWRENCE, L. KILIAN, R. GUDELEWICZ, *A real time hydroacoustic data processing system for fich stock assessment*, 13 International Congress on Acoustics, Satellite Symposium on Sea Acoustics, Dubrovnik Yugoslavia, 4–6 September 1989, vol. 5 pp. 213–216.

Received on December 12, 1989

ARCHIVES OF ACOUSTICS
18, 1, 83–104 (1993)

ASSESSMENT OF THE PELAGIC FISH RESOURCES IN THE SOUTHERN BLACK SEA USING ECHO INTEGRATION AND DUAL-BEAM PROCESSING

A. STEPNOWSKI*, A. CEMAL GÜCÜ and F. BINGEL

Institute of Marine Sciences, Middle East Technical University,
(33731 Erdemli — Icel, Turkey)

The paper synthesizes the results of two hydroacoustic surveys on the pelagic fish stocks off the southern (Turkish) Black Sea coast, carried out during the winter seasons '89 and '90. The acoustic data acquisition and processing for estimating surveyed fish populations have been performed using real-time data analysis system, employing an echo integration and "in situ" target strength estimation by dual-beam processing. The results of the surveys are presented in the form of fish density and biomass distribution charts, 3D target strength histograms and reports. These findings provide quantitative measures of fish abundance together with their statistical characteristics and distribution patterns of the surveyed pelagic fish populations.

1. Introduction

During the last two decades acoustical methods of fish stock assessment have gained preference over conventional trawl catch methods like the Catch Curve Method (CCM) [5] or other methods of biostatistics, such as Virtual Population Analysis (VPA) [12], [14], and Length based Fish Stock Assessment (LFSA) techniques [12], [14], [22]. Moreover, the acoustical methods are in no danger of being displaced by satellite remote sensing methods, such as the Advanced Very High Resolution Radiometer (AVHRR) on the NOAA series [3] or the Coastal Zone Colour Scanner (CZCS) sensors on NIMBUS [4], to estimate the range of fishery resources, to identify ocean fronts and to study surface circulation patterns — which determine the fate of fish eggs and larvae [17].

The biostatistical methods, despite many advantages, have at least three important limitations, namely: the long time required for acquiring the data and producing the results, the high costs and limited capabilities of automatization. While the satellite remote sensing methods, although possessing such advantages as: rapid large area coverage, long term monitoring and nodisturbance to the medium, they are confined to surface phenomena, are inaccurate, limited in resolution and needing calibration.

The attractions of acoustic methods in fishery research, and particularly in fish stock assessment are many, with the most important being [10], [11]:

*On leave from the Technical University of Gdańsk, Departament of Electronics, 80-952 Gdańsk, Poland

1. They offer a means of acquiring timely and synoptic information about the state of a number of fish stocks with:

— relatively large area coverage,

— relatively high accuracy and reliability,

— rapidity of data collection and data processing,

— flexibility and high degree of automatization.

2. They allow estimation of the abundance of a stock without recourse being made to other sources.

3. They may allow some features of fish biology to be measured which are otherwise less accessible (e.g. orientation distribution of fish under survey).

4. When used together with other environmental sampling techniques, acoustic methods may also contribute to the solution of some basic problems in marine biology (e.g. that of relating fish behaviour, such as aggregation and migration, to hydrography and the occurrence of prey).

Since the late 60's the abundance of exploited and unexploited fish stock has been acoustically estimated mainly by an **echo integration**. The principle which governs the generation of integrator-abundance estimates is that the **energy of echo signal**, scattered by the fishes is **proportional to the density of scatterers** [7], [11], [18]. This assessment technique, due to its versatility, accuracy and reliability has become the routine or standard method [2], [11], [16]. It has also shown promise in establishing indices of fish abundance, especially for the situations, which are difficult for other methods i.e. [10]:

— a temporarily closed fishery, resulting in a lack of catch and effort data,

— when catch and effort data are misreported,

— where is a need of rapid assessment of a widely distributed stock (e.g. for evaluation of the investment criteria)

— for a stock which becomes suddenly available for assessment within a few hours or days (e.g. spawning stock)

— for fish species with a short life span, where series of catch and effort data are hard to obtain for VPA.

The basic prerequisities for an acoustic survey are: a hydroacoustic transducer that is usually mounted in a towed body, an echosounder for acoustic signal transmission and reception of fish echoes, signal processing equipment for real-time (preferable) and post processing of acoustic data, plus some navigational aids (usually Sat. Nav. or Global Positioning System receiver) for vessel navigation and mappings of acquired and processed data. In addition, the hydroacoustic data are frequently "truthed" by fishing trawls and also compared with data from sonars.

The essential stages of an acoustic survey are the following:

1. The acoustically calibrated transducer is towed along the search track (trancsects) over the area of interest.

2. The echo signals acquired from successive transmissions are usually recorded on digital magnetic tape and simultaneously displayed as an echogram.

3. The processing of the echo signals consists of **echo integrating** the whole echo signal from single and multiple fish targets, over selected depth intervals, or in **echo counting** single-fish echoes if resolvable. Additionally, "*in situ*" **target strength estimation** may be performed to convert echo integrator readings into absolute fish den-

sity estimates. In complementary surveying by sonar, fish schools may be counted and mapped.

4. The outputs from the echo integration are classified into the groups of presumed fish species and extraneous scatterers (plankton, jelly fish, etc.).

5. Results of the classification process are expressed as "one-dimensional" fish densities along the transects, in depth strata.

6. These data are extrapolated to the "two-dimensional" density estimates over the entire area of interest and the total abundance or biomass of the surveyed scatterer classes is computed.

2. The material and method

2.1. Acoustic surveys

The primary objectives of the hydroacoustic surveys, carried out on November 1989 and December 1990 on board R/V "Bilim", were to estimate the absolute abundance of anchovy and other pelagic fish species of major commercial interest in the southern Black Sea [1]. The secondary objective was to obtain complementary data on behaviour and the migratory patterns of the surveyed populations, particularly the anchovy stock.

The "zig-zag" track pattern was used in surveying the apparent fish distribution. The transects were confined to water depths exceeding 15 meters, for safety reasons, particularly because of the uncertainty of the bathymetric charts and the presence of small fishing boats and fixed nets in the inshore waters. Offshore the surveys were limited to the 200 meters isobath, i.e. the continental shelf edge. The acoustic surveys were carried out at an average vessel speed of 8 knots, which was a reasonable compromise between the operational requirements and stability of the towed body and the noise level [1]. The sample track pattern from the second cruise is presented in Fig. 1.

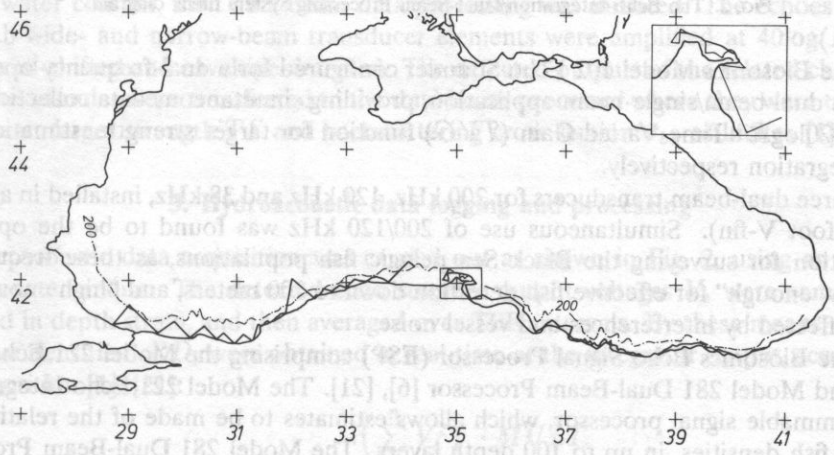

FIG. 1. The sample track pattern of R/V "Bilim", from the second Black Sea acoustic cruise (December 1990).

2.2. *The echo integration/dual-beam processing system*

2.2.1. *System block diagram*

The echo-integration/dual-beam processing system, which was installed on board R/V "Bilim" for surveying the pelagic fish resources over the Southern Black Sea, is capable of **real-time fish density and target strength output from acoustic data**. The entire signal processing in the system is completely configured and controlled by the PC host computer, using Microsoft Windows operational environment, which provide series of menus, windows and data editors for system setup data entry and output [6], [20]. The system consists of the following units [1] — see Fig. 2:

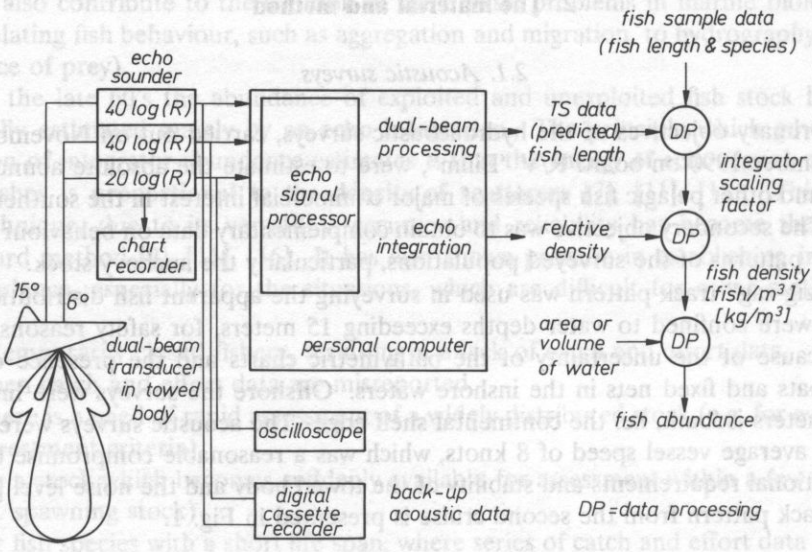

FIG. 2. The Echo-Integration/Dual-Beam Processing System block diagram.

1. The Biosonics Model 102 Echo Sounder configured for a dual-frequency operation and for a dual-beam/single-beam application, providing simultaneous data collection with "40log$R$/20log$R$" Time Varied Gain (TVG) function for target strength estimation and echo integration respectively.

2. Three dual-beam transducers for 200 kHz, 120 kHz and 38 kHz, installed in a towed body (4-foot V-fin). Simultaneous use of 200/120 kHz was found to be the optimum combination for surveying the Black Sea pelagic fish populations, as these frequencies were "low enough" for effective fish detection down to 200 meters, and "high enough" to be less affected by interferences and vessel noise.

3. The Biosonics Echo Signal Processor (ESP) comprising the Model 221 Echo Integrator and Model 281 Dual-Beam Processor [6], [21]. The Model 221 Echo Integrator is a programmable signal processor, which allows estimates to be made of the relative and absolute fish densities, in up to 100 depth layers. The Model 281 Dual-Beam Processor identifies and measures single and multiple target echoes at the echo sounder output, giving "*in situ*" target strentgh estimation [8], [15].

4. A Compaq III host computer for system control.

5. Two Thermal Chart Recorders which produce the echograms using the detected output signal of the echo sounder.

6. Two Sony Digital Audio Tape (DAT) Recorders as the recording/playback system for post-processing the acoustic data ashore.

7. A Satellite Navigation Receiver for mapping the survey data.

2.2.2. System operation

The echo sounder's trigger interval was set at 0.5 s and therefore, due to multiplexing between two frequencies, each transducer transmitted one pulse per second. The detected outputs of the echo sounder were directed to the chart recorders and to the ESP for either real time echo integration or dual-beam processing. A parallel data stream was sent to the DAT recorders. All sounding pulses were transmitted on the narrow beam elements of the transducers. For echo integration, echoes were received on the narrow beam elements only, whereas for dual-beam processing both the narrow and wide beam elements were used to receive the echoes.

Echo integration

The signals received for echo integration were amplified in the echo sounder receiver set at $20\log(R)$ TVG and recorded continuously throughout the survey. The gain-corrected signals were then band-shifted to a 10 kHz intermediate frequency for data recording and display. The detected outputs of the echo sounder, constituting a full-wave rectified, filtered version of the 10 kHz outputs, were squared and transferred to the echo integrator. The integrator averaged echo returns in 2-min intervals — so called Time Between Reports TBR. The integrated outputs were converted to absolute fish densities and recorded [1], [6].

Dual-Beam Processing

While signals amplified for echo integration were recorded continuously, the dual-beam recording system was on stand by until well defined single echoes from individual fish were encountered. When the echograms indicated such dispersed fish configurations in the water column, then dual-beam data processing was initiated. The echoes received on both wide- and narrow-beam transducer elements were amplified at $40\log(R)$ TVG, then band-shifted and envelope-detected. The detected outputs of the related channels of the echo sounder were transferred to the dual-beam processor where they were translated into mean target strength TS and backscattering cross section σ_{bs} estimates [1], [6].

3. Hydroacoustic data logging and processing

The acoustic data acquisition was carried out as shown in Fig. 2, using an echo integration technique. The detected echo sounder output voltages V_e were sampled and squared in depth strata, and then averaged over TBR intervals. By these means, so called "relative densities" RD_i were obtained in real-time at the integrator output, according to the algorithm [1], [21]:

$$RD_i = \frac{\left(\sum_{i=1}^{n} V_e^2\right)_i \cdot MULT_i}{(PP \cdot N_i) - MS_i} \tag{1}$$

where $(\sum V_e^2)_i$ sum of sampled squared voltages in "i" depth stratum, $MULT_i$ multiplier correcting for non ideal TVG function, PP number of processed pings during TBR, N_i number of samples in range interval "i", MS_i number of missing samples in interval "i" during TBR.

The component parameters of the RD_i are written to files, and stored as echo integration data files for post-processing. Simultaneously, the raw data (echo envelope at the sounder output) were recordered on the digital magnetic tape recorder (DAT) along the ship's track, as a standard data acquisition procedure throughout the cruise.

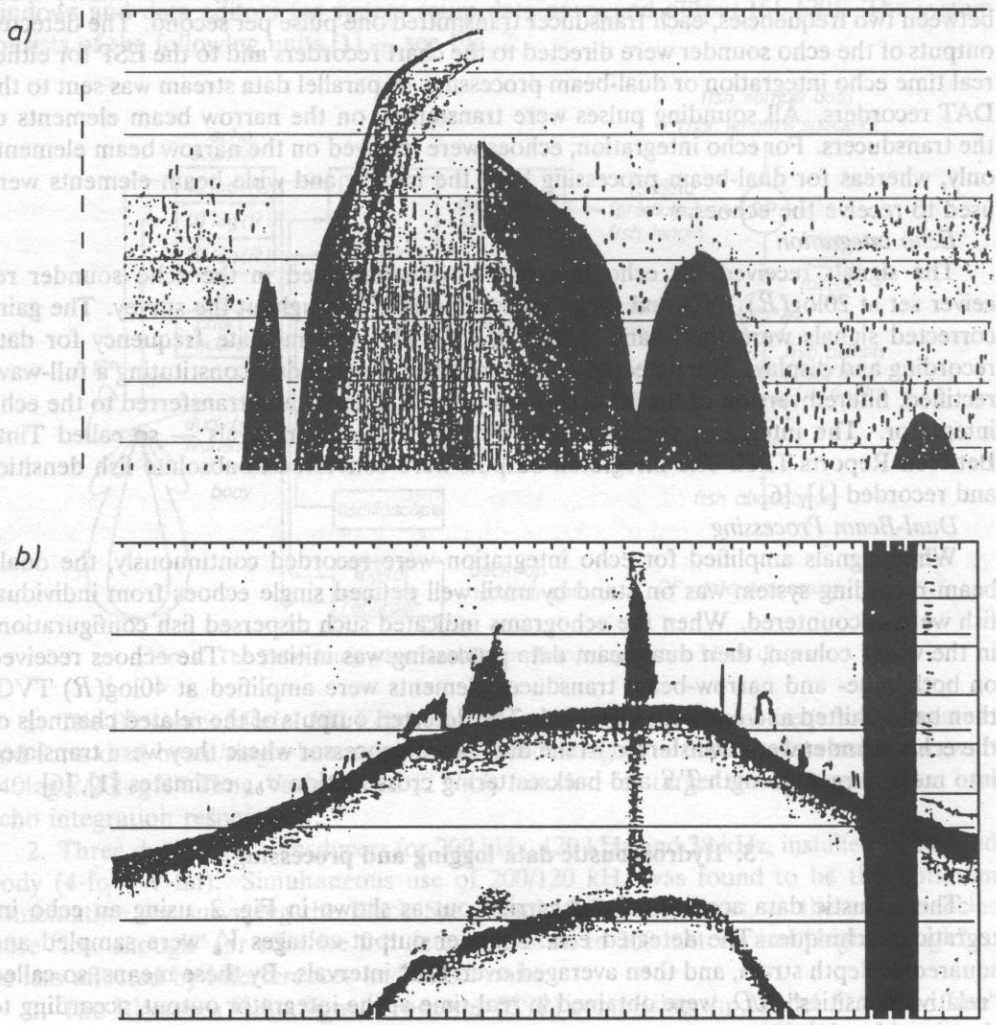

FIG. 3. The echograms of the surveyed pelagic fish populations:
(a) Dispersed schools of anchovy mixed with jelly fish,
(b) Dense schools of anchovy: corresponding target strength histogram (see Fig. 5)

The conventional echogram recording was carried out concurrently to the digital recording and processing of the echo integration data. The echograms were recorded on the dry thermo-sensitive paper for subsequent comparative analysis (scatterers identification and data interpretation) and checks. The examples of the echo records obtained on 200 kHz from the various fish concentrations, surveyed during second cruise are shown in Figs. 3.

For improving the precision of the calculated fish density and biomass estimates, the southern Black Sea was divided into two main regions: western and eastern, whose size and shape were determined by geographical and hydrographic factors related to the pelagic fish

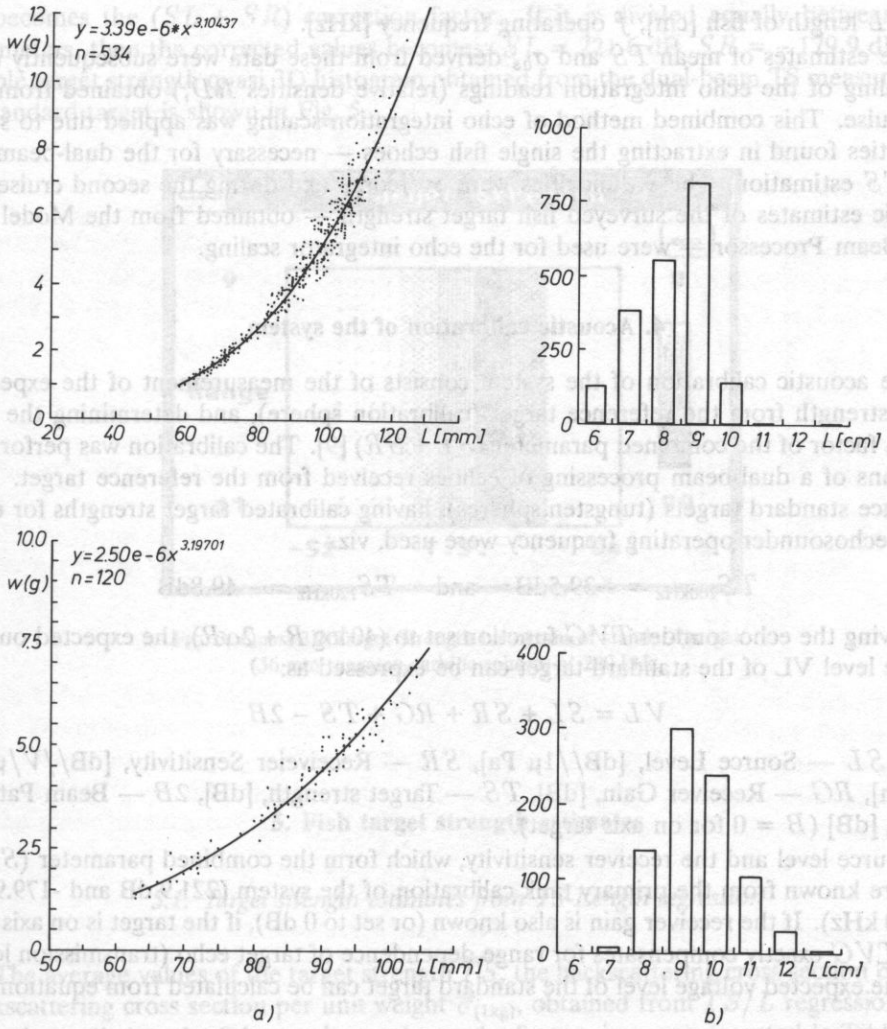

FIG. 4. The experimental relationship of weight and length data obtained from the samples of anchovy and sprat and the best fit curves (a). Corresponding length histograms for both species (b).

distribution. Additionally, during the first cruise these two regions were further divided into the thirteen subregions due to some requirements of data processing[1].

Concurrent fishing activities were performed during the acoustic surveys with the standard pelagic trawl, employing 7 mm stretched mesh size. The fish sample data from control trawl catches were used for determining the species composition and length and weight distributions of the surveyed fish populations. The relationship between the weight and length data for anchovy and sprat is shown in Fig. 4, together with their best fit curves. The corresponding fish length histograms are also presented. The length data were in turn converted to the equivalent target strength distribution estimates according to Love's formula [13]:

$$TS = 19.1 \log L - 0.9 \log f - 62, \text{ dB} \tag{2}$$

where L length of fish [cm], f operating frequency [kHz].

The estimates of mean TS and σ_{bs} derived from these data were subsequently used for scaling of the echo integration readings (relative densities RD_i) obtained from the first cruise. This combined method of echo integration scaling was applied due to some difficulties found in extracting the single fish echoes — necessary for the dual-beam *"in situ"* TS estimation. These difficulties were overcome and during the second cruise the acoustic estimates of the surveyed fish target strength — obtained from the Model 281 Dual-Beam Processor — were used for the echo integrator scaling.

4. Acoustic calibration of the system

The acoustic calibration of the system consists of the measurement of the expected target strength from the reference target (calibration sphere), and determining the correction factor of the combined parameter $(SL + SR)$ [9]. The calibration was performed by means of a dual-beam processing of echoes received from the reference target. Two reference standard targets (tungsten spheres), having calibrated target strengths for each of the echosounder operating frequency were used, viz.:

$$TS_{200\text{kHz}} = -39.5\text{dB} \quad \text{and} \quad TS_{120\text{kHz}} = -40.8\text{dB}$$

Having the echo sounder TVG function set to $(40 \log R + 2\alpha R)$, the expected output voltage level VL of the standard target can be expressed as:

$$VL = SL + SR + RG + TS - 2B \tag{3}$$

where SL — Source Level, [dB//1μ Pa], SR — Receiveier Sensitivity, [dB//V/μ Pa ref. 1m], RG — Receiver Gain, [dB], TS — Target strength, [dB], $2B$ — Beam Pattern Factor, [dB] ($B = 0$ for on axis target).

The source level and the receiver sensitivity, which form the combined parameter $(SL + SR)$ are known from the primary tank calibration of the system (221.9 dB and -179.9 dB for 200 kHz). If the receiver gain is also known (or set to 0 dB), if the target is on axis and if the TVG exactly compensates for range dependence of target echo (transmission loss), then the expected voltage level of the standard target can be calculated from equation (3).

[1] Stratification into subregions was done mainly due to limited number (20) of files which can be processed by post processing echo integration routines (ESP CRUNCH program) [21].

Taking the difference between this and the measured level gives the $(SL + SR)$ correction factor required for system's calibration.

The calibration procedure is simplified if the Dual-Beam Processor is used, as this allows direct measurement of target strength of the standard target. The speed of sound c required for the dual-beam processing was calculated using Wilson formula [19]:

$$c = 1445 + 4.66T - 0.055T^2 + 1.3(S - 35) \tag{4}$$

where T temperature [°C], S salinity [‰].

The dual-beam TS measurements performed on 200 kHz gave the measured $TS_m = -40.1$ dB. The difference between the expected and the measured values $\Delta TS = 0.6$ dB becomes the $(SL + SR)$ correction factor. If it is divided equally between both parameters, then the corrected values becomes: $SL = 221.6$ dB, $SR = -179.9$ dB. The sample target strength quasi 3D histogram obtained from the dual-beam TS measurement of standard target is shown in Fig. 5.

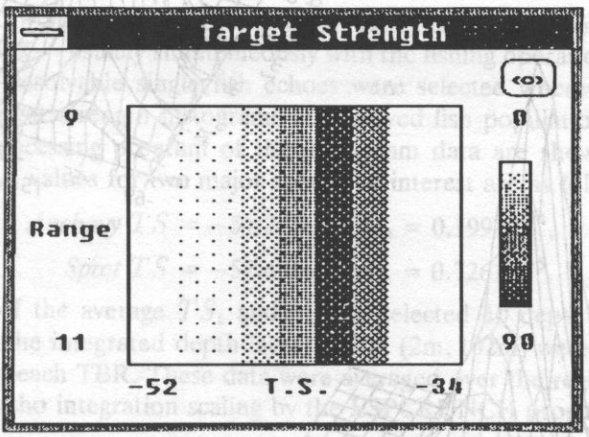

FIG. 5. Quasi 3D Target Strength histogram of standard target (36 mm tungsten carbide sphere) at 200 kHz.

5. Fish target strength estimates

5.1. Target strength estimates from TS-Length regression

The average values of the target strength $\overline{TS}$, the backscattering cross section $\overline{\sigma}_{bs}$ and backscattering cross section per unit weight $\overline{\sigma}_{(1kg)}$, obtained from TS/L regression Love formula applied to the fish sample caught on the first cruise, are presented in Table 1. In addition, the average length $\overline{L}$ and weight $\overline{w}$ of the four major fish species surveyed, are also given.

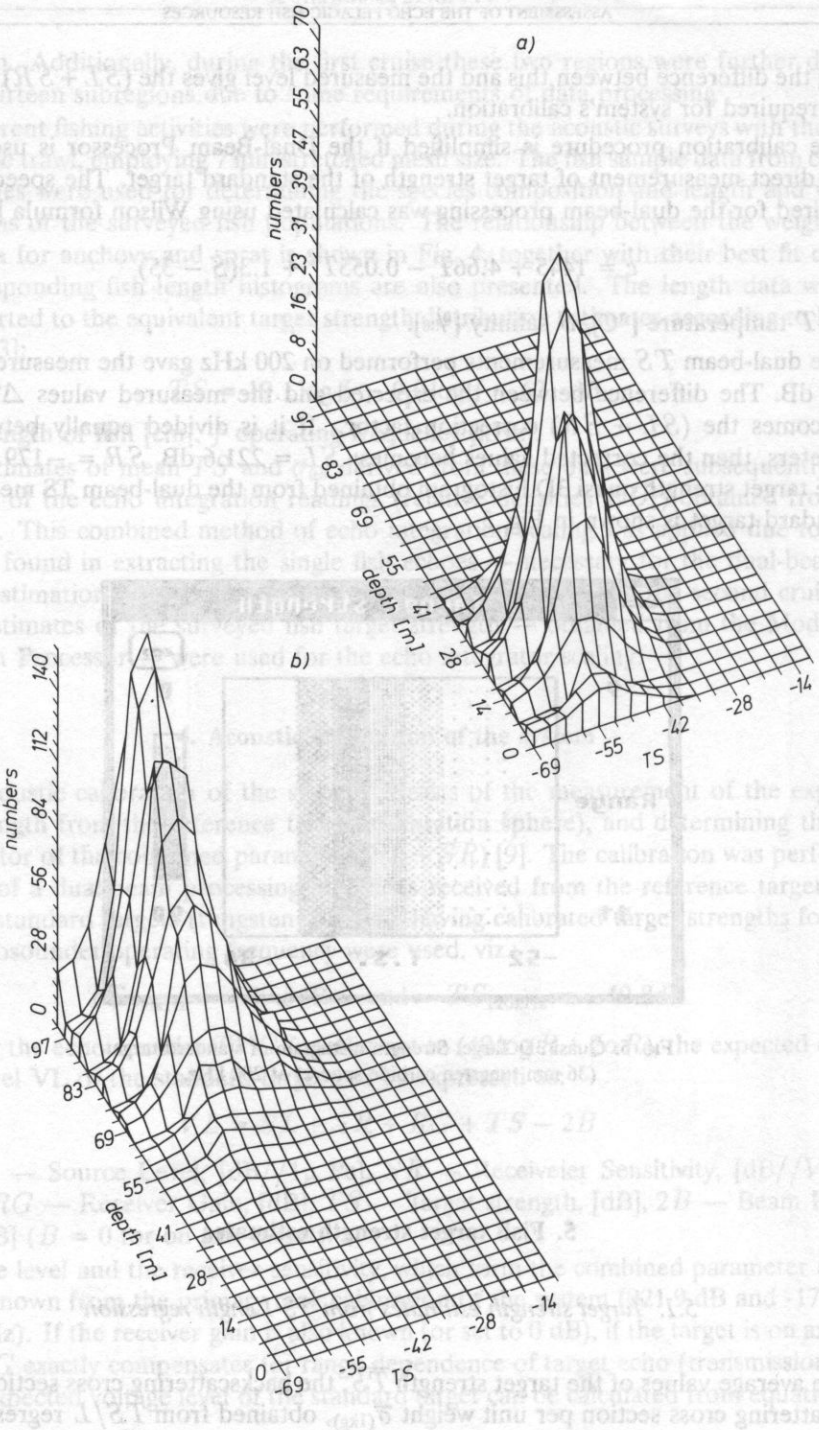

FIG. 6. 3 D Target Strength histograms for anchovy (a) and sprat (b) obtained from a dual-beam processing.

Table 1.

Fish species	Length cm	average Weight g	TS dB	σ_{bs} m^2	$\sigma_{(1kg)}$ m^2/kg
Anchovy	8.23	4.93	-46.59	2.19E-5	0.00444
Horse mackerel (west)	9.60	8.91	-45.31	2.94E-5	0.00333
Horse mackerel (east)	13.23	19.67	-42.65	5.43E-5	0.00276
Whiting	10.82	14.74	-44.32	3.70E-5	0.00251
Whiting+Sprat (west)	9.42	6.62	-45.47	2.84E-5	0.00429
Whiting+Sprat (east)	9.86	13.04	-45.09	3.10E-5	0.00237

5.2. Fish target strength estimates from dual-beam processing

The dual-beam processing for target strength estimation was applied in between the echo integration runs — usually simultaneously with the fishing operations. The dispersed populations giving resolvable single fish echoes were selected wherever possible. The examples of 3D target strength histograms of surveyed fish populations, obtained from the ESPTS post-processing program of the dual-beam data are shown in Fig. 6. The average TS and σ_{bs} values for two major species of interest are as follows:

$$\textit{Anchovy}\ TS = -51.2\text{dB}, \quad \sigma_{bs} = 0.19910^{-4},$$

$$\textit{Sprat}\ TS = -52.4\text{dB}, \quad \sigma_{bs} = 0.72610^{-5}.$$

The estimates of the average TS_i and σ_{bsi} in selected 10 depth strata (10 meters intervals) covering the integrated depth layer ΔR = (2m, 102m) were calculated by the ESPDB program in each TBR. These data were averaged over the region and stored for further use in the echo integration scaling by the ESPCRUNCH program [21].

6. Results of acoustic estimation of fish density and biomass

The fish abundance estimates were obtained from the echo integration data in depth strata. The echo integrator "relative densities" (RD_i) were converted to the absolute fish density estimates (AD_i) by ESPCRUNCH post processing program, using the integrator scaling factor C, incorporating the system parameters obtained during acoustic calibration and the mean backscattering cross section obtained from the dual-beam processing [16], [21]:

$$AD_i = C \cdot RD_i \tag{5}$$

where AD the estimate of absolute density of fish, [fish/m^3], RD the estimate of the relative density of fish, [V^2], (integrator output),

$$C = [\pi c \tau p_0^2 s_x^2 \mathrm{E}\{b^2(\theta, \phi)\} \mathrm{E}\{\sigma_{bs}\}]^{-1} \tag{6}$$

τ = transmit pulse width [s], c = speed of sound [m/s], p_0 = rms transmitted pressure measured at one meter from the transducer on its acoustical axis [μPa], $p_0 = 10^{0.05SL}$, s_x = system through sensitivity (including receiver fixed gain g_s and transducer sensitivity

s_i, $s_x = s_i g_s$) [V/μPa], $\mathrm{E}\{b(\theta,\phi)\} = \frac{1}{2\pi}\int_0^{2\pi}\int_0^{\theta_{\max}} b^2(\theta,\phi)\sin\theta d\theta d\phi$ average beam pattern factor, $\mathrm{E}\{\sigma_{bs}\} \equiv \overline{\sigma}_{bs}$ average backscattering cross section [m^2/fish].

There have been two different methodologies applied for extrapolating the absolute fish densities AD obtained from echo integration along ship's transects, to the total area density or biomass over the regions of interest. For the first cruise only the data acquired over the extent of existing fish concentrations along the transects were integrated, so measured integrator outputs (RD) were extrapolated to the entire region areas. During the second cruise all integrated data from the transects were written to ESP EI files. These allow the full and direct utilization of the ESPCRUNCH program outputs [1], [21].

However, although there have not been any fish echoes on some certain transects, the echo integrator program output some values due to noise, bottom intrusions and interferences from porpoises. Therefore, files from the transects in which no fish echoes were detected (which was determined by comparative analysis of the corresponding echograms), were replaced by artificially produced dummy files. Dummy files contained exactly the same auxiliary parameter as original files, i.e. number of sequences TBR's, processed pings PP's and missing samples MS's, but their integrator outputs RD's were replaced by zeros. The sample ESPCRUNCH program printout for dummy files with zero padded integrator outputs is shown in Table 4. Because of this difference the results are divided into two groups. The first group refers to the November '89 cruise, while the second refers to the December '90 cruise.

6.1. The fish biomass abundance estimates obtained from the first acoustic survey

Table 2 summarizes the acoustical estimation of fish biomass in the Southern Black Sea. It consists of two parts. The upper part gives the partial biomass estimates for four major fish species measured along the transects in all 13 subregions, together with the sums of these estimates over the regions and species and the overall sum — labelled as a Quantity Measured in kilograms. Additionally, it gives the areas of the transects surveyed in each subregion, as well the total areas of the subregions as their sum are also given. In the lower part, the biomass estimates extrapolated for the area of subregions are presented, and the total biomass extrapolated for the entire surveyed area of the Southern Black Sea, labelled as a Total Quantity in tons, is also given. The table was produced as a spread-sheet using the EXCEL 3.0 program.

The partial biomass estimates in subregions (Quantity Measured — q_k) have been calculated from the integrator outputs (RD) measured over the extent of existing fish concentration along transect. The RD values were first converted to the corresponding volume biomass densities (d_k) and then multiplied by the adequate surveyed volumes (V_k), for each stratum i.e.:

$$q_k = d_k V_k = (C\overline{\sigma}_{(1\mathrm{kg})})^{-1} RD_k V_k \tag{7}$$

where $C_e = C/\overline{\sigma}_{(1\mathrm{kg})}$ sounder constant — see equation (6), $\overline{\sigma}_{(1\mathrm{kg})} = \overline{\sigma}_{bs}/\overline{w}$ mean backscattering cross section per unit weight, $\overline{w}$ average weight of surveyed fish.

These measured biomass estimates have been extrapolated to the entire area of subregion to give the total biomass (Total Quantity — Q) by multiplying by the volume ratio [1]:

Table 2. Acoustic estimates of fish biomass („Quantity") in the southern Black Sea for four major pelagic species — November 1989 cruise echo integration data

Sub-region	Reg. #	H. mack.	Anchovy	Whiting	Whit+Sprat	All	Trans. area	Total area
		(kg)	(kg)	(kg)	(kg)	(kg)	km^2	km^2
Igne Ada - Ist. Bog.	I	294.5			1555.225	1849.725	0.86561866	4338.452
Istanbul - Kefken	II	1412	14.91			1426.91	0.41808	2345.45
Kefken-Eregli	III	737.1				737.1	0.41141	1590.45
Eregli - Amasra	IV		3.09	430.569		433.659	0.1978	329.8
Amasra - Inebolu	V		141.76		306.4972	448.2572	0.43234	10.47.87
Ineblu - Inceburun	VI	II	94.99			105.99	0.3858	2481.22
Inceburun - Bafra	VII	754.38	26.43	11.8746		792.6846	0.50829	2065.161
Bafra - Civa brn.	VIII	436.4	273.68			710.08	0.559882	1077.77
Civa brn. - Tasun	IX	488.3	61.41	1.973222		551.68322	0.348778	1354.903
Yasun - Tirebolu	X	48.7	154.79			203.49	0.399734	787.87
Tirebolu - Trabzon	XI	66.5	601.41			667.91	0.210789	394.516
Trabzon - Pazar	XII	93.1	282.85			375.95	0.48297	228.515
Pazar - Batumi	XIII	1121	196.27			1317.47	0.487716	305.58
QUANTITY		5463.18	1851.59	444.4168	1861.7222	9620.909	5.70920766	18347.557
MEASURED (kg)								
Sub region	Reg #	H. mack.	Anchovy	Whiting	Whit+Sprat	All		
		(tons)	(tons)	(tons)	(tons	(tons)		
Igne Ada - Ist. Bog.	I	1476.0242	0	0	7794.7361	9270.7603		
Istanbul - Kefken	II	7921.3916	83.645856	0	0	8005.0375		
Kefken - Eregli	III	2849.5192	0	0	0	2849.5192		
Eregli - Amasra	IV	0	5.1520829	717.9052	0	723.05732		
Amasra - Inebolu	V	0	343.58618	0	742.86261	1086.4488		
Ineblu - Inceburun	VI	70.744997	610.91521	0	0	681.66021		
Inceburun - Bafra	VII	3065.0144	107.38398	48.246	0	3220.6444		
Bafra - Civa brn.	VIII	840.06778	526.83261	0	0	1366.9004		
Civa brn. - Yasun	IX	1896.9062	238.56033	7.665404	0	2143.1319		
Yasun - Tirebolu	X	95.987004	305.08888	0	0	401.07588		
Tirebolu - Trabzon	XI	124.46244	1125.6084	0	0	1250.0708		
Trabzon - Pazar	XII	44.04983	133..82916	0	0	177.87899		
Pazar - Batumi	XIII	702.4914	122.97359	0	0	825.46499		
Western Black Sea	I–VI	12317.68	1043.2993	717.9052	8537.5987	22616.483		
Eastern Black Sea	VII–XI	6768-979	2560.2769	55.91141	0	9385.1673		
TOTAL QUANTITY		19086.659	3603.5763	773.8166	8537.5987	32001.651		
(Tons)								

$$\widehat{Q}_k = q_k \frac{A_{Tk}\overline{R}_{Tk}}{\sum_{t=1}^{m} A_t \overline{R}_{trn}} \tag{8}$$

where
A_{Tk} total area of subregion "k",
A_t transect area,
R_{Tk} average depth over the total area of subregion "k",
R_{trn} average depth over the sum of transects area.

Assuming that survey pattern was designed so that the difference between the average depth of the entire area under examination and the average depth of the transect area is negligible, equation (8) can be rewritten as follows:

$$Q_k = q_k \frac{A_{Tk}}{\sum_{t=1}^{m} A_t} \tag{9}$$

6.2. The fish biomass abundance estimates obtained from the second acoustic cruise

The results of the second acoustic survey are presented in Fig. 7 and in the Tables 3 and 4. Fig. 7 shows the vertical (depthwise) distribution of the total biomass estimates of pelagic fish populations (without differentiating into species) in the Eastern and Western regions of the Southern Black Sea Coast.

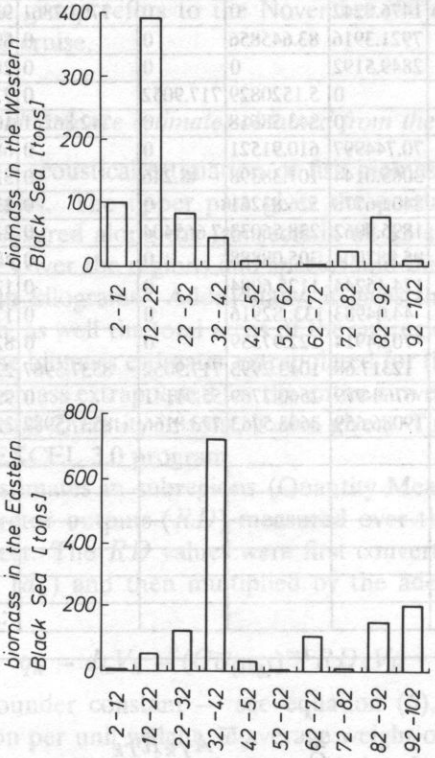

FIG. 7. Depthwise distribution of the total biomass estimates of surveyed pelagic fish populations in the Black Sea.

Table 3 constitutes the report printout from the echo integration post-processing program ESPCRUNCH and summarizes the acoustical estimates of the surveyed fish biomass in the Southern Black Sea. Similarly to the Table 2, it consists of two parts. The upper half presents the data on biomass estimates — labelled as Quantity (in kg) — for the Western Region, and the lower half presents the data from the Eastern Region. Along with the biomass estimates the corresponding estimates of absolute density (AD's) — labelled as Density of Fish (in fish/km^2), are given as well as the Integrator Output (RD's) data. All data were calculated in ten meters depth strata — covering the range interval (2m,102m). The average $\overline{\sigma}_{bs}$ values, calculated by the ESPDB and ESPTS programs for all these depth strata are also included in the table. In addition, the statistics of fish biomass estimates — i.e. Fish Quantity Variance and its Confidence Limits calculated by ESPCRUNCH program are also presented in two last columns of the table. Both parts of the table are complemented by two associated sets of the calibration data for two regions, comprising also the surface area of the regions.

The biomass estimate of surveyed fish populations in each depth stratum (Q_i's), as well as of the total biomass (Q) in the entire water column sampled (ΔR = 100 m), were calculated for both regions from the relative (RD_i's) or absolute density estimates (AD's) according to the formula [1]:

$$\hat{Q}_i = (C\overline{\sigma}_{i(1\text{kg})})^{-1} RD_i V_i = C_{i(w)} AD_i V_i \tag{10}$$

where

$\overline{\sigma}_{i(1\text{kg})} = \overline{\sigma}_{\text{ibs}}/\overline{w}$ mean backscattering cross section of fish per unit weight in i-th depth stratum,

$\overline{w}$ average weight of fish in i-th depth stratum,

$\overline{\sigma}_{bs(i)}$ mean fish backscattering cross section in i-th stratum,

V_i volume sampled in the i-th depth stratum,

$C_{i(w)} = C_i/\overline{w}$ integrator scaling constant per unit weight

and

$$\hat{Q} = \sum_{i=1}^{10} \hat{Q}_i \tag{11}$$

The strata population (biomass) totals ($\hat{Q}$'s) are the products of two random components $\sigma_{bs(i)}$ or $\sigma_{(1\text{kg})i}$ and RD_i. Therefore, the normalized variance of Q_i is calculated as a sum of the component variances, assuming their statistical independence:

$$\text{Var}\,\hat{Q}_i = \hat{Q}_i^2[\text{Var}(\overline{RD}_i)/(\overline{RD}_i^2) + \text{Var}(\overline{\sigma}_{i(1\text{kg})})/(\overline{\sigma}_{i(1\text{kg})}^2)] \tag{12}$$

where

Var $(\overline{RD}_i)$ is the integrator output variance of the mean,

Var $(\overline{\sigma}_{i(1\text{kg})})$ is the variance of backscattering cross section per unit weight mean.

The confidence limits (CL_i's) of the strata population (biomass) totals Q_i's, at the 95% level of significance were calculated for i-th stratum as follows:

$$CL_i = \hat{Q}_i \pm 1.96[\text{Var}(\hat{Q}_i)]^{1/2} \tag{13}$$

Table 3. Echo integration post-processing report printout:
Acoustic estimates of biomass and density of pelagic fish populations in the Southern Black Sea — December 1990 cruise data.

DEPTH STRATUM	STRATUM VOLUME	MEAN SIGMA	# FISH USED	STD DEV SIGMA	A CONSTANT	INTEGRATOR OUTPUT	# OF SEQUENCES	VARIANCE OF INTEG MEAN	DENSITY OF FISH	QUANTITY KILOGRAMS	FISH QUANTITY VARIANCE	CONFIDENCE LIMITS(95%)
2.0– 12.0	1208D+12	.680BE–01	900	.2225E–04	.1048E–02	.8102E–03	↑↑↑↑	.17570–06	.8193E–06	.10262E+06	.2817E+10	.1041E+06
12.0– 22.0	.1197D+12	.6704E–01	3535	.5467E–04	.1064E–02	.3081E–02	↑↑↑↑	.1504 05	.3780E–05	.39371E+06	.2450E+11	.3068E+06
22.0– 37.0	.1148D+12	.6468E–01	13022	.2300E–04	.1103E–02	.6776E–03	↑↑↑↑	.1012D–06	.7478E–06	.86087E+05	.1624E+10	.7900E+05
32.0– 42.0	.1102D+12	.3366E–01	6002	.2272E–04	.2120E–02	.2017E–03	↑↑↑↑	.1307D–08	.4277E–06	.47350E+05	.7178E+08	.1663E+05
42.0– 52.0	1014D+12	1035E+00	765	.2292E–03	.6871E–03	.1711E–03	↑↑↑↑	.3108D–08	.1179E–06	.11953E+05	.1518E+08	.7635E+04
57.0– 62.0	.9224D+11	.8796E–01	1658	.1035E–03	.8113E–03	.4776E–04	↑↑↑↑	.6576D–10	.4053E–07	.37388E+04	.3655E+06	.1185E+04
62.0– 72.0	.8062D+11	.8052E–01	2366	.7648E–04	.8863E–03	.7173E–04	↑↑↑↑	.2346D–07	.6375E–07	.51395E+04	.1198E+07	.2145E+04
72.0– 82.0	.6686D+11	.5056E–01	3310	.3499E–04	.1411E–02	.2666E–03	905.	.8060D–08	.3762E–06	.25155E+05	.2891E+08	.1741E+05
82.0– 92.0	.5495D+11	.4076E–01	2260	.2573E–04	.1751E–02	.8324E–03	778.	.3434D–06	.1457E–05	.80077E+05	.3178E+10	.1105E+06
92.0–102.0	.4470D+11	.3888E–01	837	.1087E–04	1835E-02	.1504E–03	644.	.1377D–08	.2760E–06	.12336E+05	.9269E+07	.5967E+04
	.9070D+12								.76766E+06	+ OR –	.3522E+06	

CALIBRATION DATA

SURFACE AREA IN METERS SQUARED =	.12133E+11
PULSE WIDTH IN MILLISECONDS =	.400
VELOCITY OF SOUND, METERS//SECOND, =	1474.4
SQUARED BEAM PATTERN FACTOR =	.51370E 03
SOURCE LEVEL IN dB =	.2220E+03
RECEIVING SENSITIVITY AT 1 METER, 20LOGR, =	–.15028E+03
RECEIVER GAIN DURING DATA ACQUISITION =	.00

Western Black Sea Region

Table 3. [cont.]

DEPTH STRATUM	STRATUM VOLUME	MEAN SIGMA	# FISH USED	STD DEV SIGMA	A CONSTANT	INTEGRATOR OUTPUT	# OF SEQUENCES	VARIANCE OF INTEG MEAN	DENSITY OF FISH	QUANTITY KILOGRAMS	FISH QUANTITY VARIANCE	CONFIDENCE LIMITS(95%)
2.0— 12.0	.6174D+11	.6808E-01	900	.2225E-04	.1048E-02	.1609E-03	↑↑↑↑	.17670-08	.1686E-06	.10417E+05	.7410E+07	.5335E+04
17.0— 77.0	.5938D+11	.6704E-01	3535	.5467E-04	.1064E-02	.8617E-03	↑↑↑↑	.4837D-07	.9167E-06	.54433E+05	.1933E+09	.2725E+05
22.0— 32.0	.5485D+11	.6468E-01	13022	.2300E-04	.1103E-02	.2187E-02	↑↑↑↑	.2147D-06	.2413E-05	.13234E+06	.7870E+09	.5198E+05
32.0— 42.0	.4872D+11	.3366E-01	6002	.2272E-04	.2120E-02	.7081E-02	↑↑↑↑	.2836D-04	.1501E-04	.73134E+06	.3026E+12	.1078E+07
42.0— 57.0	.4143D+11	.1035E+00	765	.2297E-03	.6875E-03	.1186E-02	↑↑↑↑	.5074D-06	.8175E-06	.33868E+05	.4793E+09	.4271E+05
52.0— 62.0	.3339D+11	.8796E-01	1658	.1035E-03	.8113E-03	.4884E-03	↑↑↑↑	.1823D-07	.3962E-06	.13228E+05	.1338E+08	.7168E+04
62.0— 72.0	.2705D+11	.8052E-01	2366	.7618E-04	.7763E-03	.4863E-02	↑↑↑↑	.9642D-05	.4310E-05	11657E+06	.5539E+10	.1457E+06
77.0— 82.0	.1925D+11	.5056E-01	3310	.3499E-04	.1411E-02	.6916E-03	767.	.1007D-06	.9762E-06	.18791E+05	.7433E+08	.1670E+05
82.0— 92.0	.1407D+11	.4076E-01	2260	.2573E-04	.1751E-02	.6411E-02	601.	.3091D-04	.1129E-04	.15797E+06	.1876E+11	.2684E+06
92.0—102.0	.9555D+10	.3888E-01	837	.1087E-04	.1835E-02	.1203E-01	432.	.1179D-03	.2209E-04	.21104E+06	.3628E+11	.3733E+06
	.3674D+12								.14799E+07	+ OR −	.1184E+07	

CALIBRATION DATA

SURFACE AREA IN METERS SQUARED =	.67143E+10
PULSE WIDTH IN MILLISECONDS =	.400
VELOCITY OF SOUND, METERS//SECOND, =	1474.4
SQUARED BEAM PATTERN FACTOR =	.51370E-03
SOURCE LEVEL IN DB =	.2220E+03
RECEIVING SENSITIVITY AT 1 METER, 20LOGR. =	−.15028E+03
RECEIVER GAIN DURING DATA ACQUISITION =	.00

Eastern Black Sea Region

Table 4. Echo integration post-processing report printout for dummy files.

DATA FOR PRIMARY STRATA, MULTIPLEX CHANNEL 1

DEPTH STRATUM	STRATUM VOLUME	MEAN SIGMA	# FISH USED	STD DEV SIGMA	A CONSTANT	INTEGRATOR OUTPUT	NUMBER OF SEQUENCES	VARIANCE OF INTEG MEAN	DENSITY OF FISH	QUANTITY NUMBERS	FISH QUANTITY VARIANCE	CONFIDENCE LIMITS(95%)
2.0– 12.0	.0000D+00	.1000E+01	0	.0000E+00	.1000E+00	.0000E+00	300.	.0000D+00	.0000E+00	.00000E+00	.0000E+00	.0000E+00
12.0– 22.0	.0000D+00	.1000E+01	0	.0000E+01	.0000E+00	.0000E+00	295.	.0000D+00	.0000E+00	.00000E+00	.0000E+00	.0000E+00
22.0– 32.0	.0000D+00	.1000E+01	0	.0000E+00	.1000E+01	.0000E+00	274.	.0000D+00	.0000E+00	.00000E+00	.0000E+00	.0000E+00
32.0– 42.0	.0000D+00	.1000E+01	0	.0000E+00	.1000E+01	.0000E+00	254.	.000D+00	.0000E+00	.00000E+00	.0000E+00	.0000E+00
42.0– 52.0	.0000D+00	.1000E+01	0	.0000E+00	.1000E+01	.0000E+00	220.	.0000D+00	.0000E+00	.00000E+00	.0000E+00	.0000E+00
52.0– 62.0	.0000D+00	.1000E+01	0	.0000E+00	.1000E+01	.0000E+00	182.	.0000D+00	.0000E+00	.00000E+00	.0000E+00	.0000E+00
62.0– 72.0	.0000D+00	.1000E+01	0	.0000E+00	.1000E+01	.0000E+00	151.	.0000D+00	.0000E+00	.00000E+00	.0000E+00	.0000E+00
72.0– 82.0	.0000D+00	.1000E+01	0	.0000E+00	.1000E+01	.0000E+00	114.	.0000D+00	.0000E+00	.00000E+00	.0000E+00	.0000E+00
82.0– 92.0	.0000D+00	.1000E+01	0	.0000E+00	.1000E+01	.0000E+00	88.	.0000D+00	.0000E+00	.00000E+00	.0000E+00	.0000E+00
92.0–102.0	.0000D+00	.1000E+01	0	.0000E+00	.1000E+01	.0000E+00	63.	.0000D+00	.0000E+00	.00000E+00	.0000E+00	.0000E+00
TOTAL:	.0000D+00							.00000E+00	+ OR –	.0000E+00		

SUMMARY OF DATA STARTING AT Wed May 15 14:38:18 1991
AND ENDING AT Fri May 17 13:59:41 1991

Table 4. [cont.]

DATA FOR PRIMARY STRATA, MULTIPLEX CHANNEL 2

DEPTH STRATUM	STRATUM VOLUME	MEAN SIGMA	# FISH USED	STD DEV SIGMA	A CONSTANT	INTEGRATOR OUTPUT	NUMBER OF SEQUENCES	VARIANCE OF INTEG MEAN	DENSITY OF FISH	QUANTITY NUMBERS	FISH QUANTITY VARIANCE	CONFIDENCE LIMITS(95%)
2.0— 12.0	.0000D+00	.1000E+01	0	.0000E+00	.10000E+01	.0000E+00	300.	.0000D+00	.0000E+00	.00000E+00	.0000E+00	.0000E+00
12.0— 22.0	.0000D+00	.1000E+01	0	.0000E+00	.1000E+01	.0000E+00	295.	.0000D+00	.0000E+00	.00000E+00	.0000E+00	.0000E+00
22.0— 32.0	.0000D+00	.1000E+01	0	.0000E+00	.1000E+01	.0000E+00	274.	.0000D+00	.0000E+00	.00000E+00	.0000E+00	.0000E+00
32.0— 42.0	.0000D+00	.1000E+01	0	.0000E+00	.1000E+01	.0000E+00	254.	.0000D+00	.0000E+00	.00000E+00	.0000E+00	.0000E+00
42.0— 52.0	.0000D+00	.1000E+01	0	.0000E+00	.1000E+01	.0000E+00	220.	.0000D+00	.0000E+00	.00000E+00	.0000E+00	.0000E+00
52.0— 62.0	.0000D+00	.1000E+01	0	.0000E+00	.1000E+01	.0000E+00	182.	.0000D+00	.0000E+00	.00000E+00	.0000E+00	.0000E+00
62.0— 72.0	.0000D+00	.1000E+01	0	.0000E+00	.1000E+01	.0000E+00	151.	.0000D+00	.0000E+00	.00000E+00	.0000E+00	.0000E+00
72.0— 82.0	.0000D+00	.1000+01	0	.0000E+00	.1000E+01	.0000E+00	114.	.0000D+00	.0000E+00	.00000E+00	.0000E+00	.0000E+00
82.0— 92.0	.0000D+00	.1000E+01	0	.0000E+00	.1000E+01	.0000E+00	88.	.0000D+00	.0000E+00	.00000E+00	.0000E+00	.0000E+00
92.0—102.0	.0000D+00	.1000E+01	0	.0000E+00	.1000E+01	.0000E+00	63.	.0000D+00	.0000E+00	.00000E+00	.0000E+00	.0000E+00
TOTAL:	.0000D+00							.00000E+00	+ OR −	.0000E+00		

LIST OF FILES PROCESSED:

a:dummy1.dat

and for the total population biomass in the entire water column:

$$CL = \sum_{i=1}^{10} \hat{Q}_i \pm 1.96\Big[\sum_{i=1}^{10} \mathrm{Var}(\hat{Q}_i)\Big]^{1/2} \tag{14}$$

7. Conclusion

It is known from present and historical catch data that a rough estimate of the total abundance of pelagic fish in the Black Sea should be in the range of hundreds of thousands of tons [1]. The acoustic estimates in the present study — about 30 000 tons from the first survey and about 2200 tons from the second survey — are remarkably low. Despite the evident decrease of the pelagic fish stock reported throughout the last years, such a discrepancy between the acoustic and other data can not be explained by statistical underestimation. There are obviously some other reasons likely related to non-representativeness of the acoustic data.

It is assumed that a reliable acoustic estimate of fish stock size can be achieved from the echo integration technique, provided following conditions are satisfied [10], [11]:

1. The fish stock is known to be available for acoustic measurement in the surveyed area.
2. The stock is not inextricably mixed with other populations.
3. The fish are neither too deep, nor too shallow to be detected by hydroacoustic system.
4. The distribution of fish over the area is sufficiently constant for extrapolations to be made from density measurement along widely-spaced survey transects.
5. The fish avoidance effect (reaction to vessel and system) is negligible.

For the Black Sea pelagic fish stocks, and especially anchovy stock, which can be considered as relatively small and dispersed, because of in general low productivity area (no patchiness and low degree of school activity) majority of the above requirements are not fulfilled. Practically, only the condition 1 and 5 could be considered as satisfied in full. The others are only partly fulfilled if there are at all. Therefore, the population estimates obtained from acoustic surveys are not necessary fully reliable, and particularly in the context of unknown degree of fulfillment of the conditions 2, 3 and 4, the surveyed stock seems to be underestimated by acoustic assessment.

There are at least two other factors which might be partly responsible for underestimating pelagic stocks. The first refers to the survey coverage and the second to the conceivable changes of the fish migratory space-time pattern. It was observed that most of the surveyed pelagic fish populations (particularly anchovy) exhibited an almost littoral distribution. This would require the survey vessel to run the transects into the shallows rather than staying seaward of a depth of 15 meters (see section 2). As a consequence, the survey coverage was incomplete as it was not feasible to carry out the sampling across the entire fish distribution area. This evidently decreases the final estimate of the fish biomass obtained from the acoustic data. However, the underestimation "factor" can not be determined easily, due to the lack of data on catches from the unsurveyed area.

The second factor is that commercial fishery observations of the anchovy stocks migratory patterns in the Black Sea suggest that they are most probably presente in the Southern part of the sea between November and February, [1]. For this reason, both

acoustic surveys in successive years were undertaken in the Winter season. However, on these cruises the fish distribution was restricted to small areas in the East. Thus, there are basically two possible explanations of this fact. The first is the conceivable change in fish migratory seasonal habits. The second is the possible change of their distribution pattern, which can be in turn related to migration or not. In any case, the explanation of the obtained low estimates requires continuing of the acoustic surveys, complemented with the more frequent concurrent fishing operations, and extended if possible to the other seasons.

Acknowledgements

This study has been carried out within the framework of a Project sponsored by NATO Science for Stability Program, Turkish Scientific and Research Council (TUBITAK) and Turkish State Planning Office. We also extend our sincere thanks to Institute of Marine Science — Middle East Technical University (IMS–METU) Personnel who accompanied us in various ways.

References

[1] F. BINGEL, A. STEPNOWSKI, A. GUCU, *Hydroacoustic methods of fish stock assessment along the Turkish coast of the Black Sea*, Nato-TU Fisheries Report, NATO- Sciences for Stability Programme, Institute of Marine Sciences, Middle East Technical University, Erdemli 1991.

[2] J. BURCZYŃSKI, A. STEPNOWSKI, R. SALAMON, *The hydroacoustic system on R/V "Professor Siedlecki" and its use in fish stock assessment by integration of thin depth layers*, Rapp. P.-V. Reun. CIEM, 170, 142–151 (1977).

[3] N. CASTIGNE, L. E. BURGONE, J. LE VOURCH, J. P. ORLY, *Operational measurements of sea surface temperatures at CMS Lannion from NOAA-7 AVHRR data*, Int. Journ. on Remote Sensing **7**, 8 (1986).

[4] D. K. CLARK, *Phytoplankton pigments algorithm from the Nimbus-7* CZCS, in Oceanography from space, J.F.R.Gower [Ed.], Plenum Press, New York 1981, 227–238.

[5] S. CLARK, *Use of trawl data in assessment*, Can. Spec. Publ. Fish. Aquat. Sci., **58**, 82–92 (1981).

[6] J. J. DAWSON, T. J. BROOKS, E. S. KUEHL, *An innovative acoustic signal processor for fisheries science*, Proc. I.O.A. **11**, 8, 131–140 (1989).

[7] O. DRAGESUND, S. OLSEN, *On the possibility of estimating year class strength by measuring echo abundance of O-group fish*. Fisk. Dir. Skr. Havunders **13**, 8, 47–71 (1965).

[8] J. E. EHRENBERG, *A review of in situ target strength estimation techniques*, ICES/FAO Symp. Bergen 1982, art. No. 104; also in: FAO Fish Rep., **300**, 85–90 (1982).

[9] K. G. FOOTE, P. H. KNUDSEN, G. VESTNES, *Standard calibration of echo-sounders and integrators with optimal cooper spheres*, ICES/FAO Symp. Bergen 1982, art. No. 40.

[10] K. G. FOOTE, *Fisheries acoustics diagnosis and prognosis*, Proc. I.O.A. vol. 11, Part 3, 1989.

[11] K. A. JOHANESSON, R. B. MITSON, *Fisheries acoustics*, A practical manual for acoustic biomass estimation, FAO Fisheries Technical Paper 240, FAO Rome 1983.

[12] R. JONES, *Assessing the effects of changes in exploitation pattern using length composition data with notes of VPA and cohort analysis*, FAO Fish. Techn. Paper. 256 (1984).

[13] R. H. LOVE, *Dorsal aspect target strength of an individual fish*, J. Acous. Soc. Am., **49**, 3, 816–823 (1971).

[14] P. SPARRE, E. URSIN, S. VENEMA, *Introduction to tropical fish stock assessment*, Part 1. FAO Fish Techn. Paper No 306/1, FAO Rome 1989.

[15] A. STEPNOWSKI, *Fish target strength estimation methods and techniques*, VIIIth Symposium on Hydroacoustics SHA'91 Gdańsk 1991.

[16] A. STEPNOWSKI, R. S. MITCHELL, *ECOLOG II — A real time acoustic signal processing system for fish stock assessment*, Ultrasonics **28**, 256–265 (1990).

[17] J. M. STRETA, M. PETIT, *Teledetection aero-spatiale et peche thoniere en Atlantique inter-tropical*. FAO Doc. Techn. sur les Pech. 302 J.Y. Le Gall ed FAO Rome 99–109 (1989).

[18] R. E. THORNE, *Investigations into the relation between integrated echo voltage and fish density*, J. Fish. Res. Board Can. **28**, 9, 1269–1273 (1971).

[19] R. J. URICK, *Principles of underwater sound*, 3 ed. McGraw Hill, New York 1983.

[20] Anon.1: Microsoft windows user's guide, Microsoft Co., Doc. 050050051-200-R01-0887, Redmont, USA 1987.

[21] Anon. 2: Echo signal processor manual with model 281 dual-beam processor and model 221 echo integrator software, Biosonics Inc. Seattle USA 1989.

[22] Anon. 4: Methods of collecting and analysing size and age data for fish stock assessment, FAO Fish. Circ. No. 736 FAO Rome 1981.

Received on December 10, 1991

ARCHIVES OF ACOUSTICS
18, 1, 105–111 (1993)

ULTRASONIC AND THERMODYNAMIC EFFECTS OF SELF-ASSOCIATION OF ALIPHATIC ALCOHOLS IN c–C_6H_{12}. II. PRIMARY AND TERTIARY PENTANOLS*

K. BEBEK, R. MANIKOWSKI AND S. ERNST

Institute of Chemistry, Silesian University
(40-006 Katowice, ul. Szkolna 9)

The ultrasound velocities in and densities of mixtures of cyclohexane with n-pentanol $\{x_1\text{n}-C_5H_{11}OH+(1-x_1)C_6H_{12}\}$ and with 2-methylbutan-2-ol $\{x_1\text{tert}-C_5H_{11}OH+(1-x_1)C_6H_{12}\}$ have been measured at 293.15 K. Using the measurement results in connection with the literature data, the following quantities have been determined: isothermal and adiabatic compressibility coefficients, $\beta_T = -1/V(\partial V/\partial p)_T$ and $\beta_s = -1/V(\partial V/\partial p)_s$, respectively, the adiabatic compressibility, $\varkappa_s = -(\partial V/\partial p)_s$, the free intermolecular length, L, and the excess values of the molar volume, V^E, of the adiabatic compressibility coefficient, β_s^E, and of the adiabatic compressibility, $\varkappa_s^E$. The dependences of those excess functions on the mixture composition, expressed in mole fractions, were represented by Redlich-Kister equations.

1. Introduction

The subject of this paper were two binary liquid mixtures containing one rather inert component (cyclohexane) and another one capable of being highly associated by hydrogen bonds. Two monohydric pentanols, the primary n-pentanol and the tertiary 2–methylbutan–2–ol, were used as the associating components. We have focussed our attention especially on deviations of the properties of the mixtures under test from the thermodynamic ideality in relation to intermolecular interactions and the free intermolecular lengths.

Numerical values characterising the mixtures were determined from ultrasonic velocity and density measurements in connection with some auxiliary data available in literature.

The results have been discussed in the ligth of the intermolecular interactions and the capability of space-filling related to the molecular structure of the components and their capability for association by formation of hydrogen bonds. We have also tried to find some correlation between the excess thermodynamic functions and the intermolecular free length in the studied binary liquid mixtures.

---

* The first part of this series appeared in Archives of Acoustics **15**, 3–4, 239 (1990).

2. Experimental

For dehydration and purification, the components (cyclohexane, n-pentanol, POCh Gliwice, Poland, and 2-methylbutan–2–ol, BDH Chemicals, England, all of analytical grade) were shaked for a longer time with molecular sieves A3 and A4 of granulation 1/16″ (POCh Gliwice, Poland) and distilled under reduced pressure.

The mixtures were prepared by weighing immediately before the measurements.

The densities of the pure components and mixtures were determined by the Kohlrausch method, i.e. by using a quartz float that has been weighted at 293.15 + / − 0.01K in air and after immersing it in the liquid under test. The weights were reduced to vacuum. The accuracy was +/ − 0.1kg/m^3.

The ultrasound velocities were measured by the well-known sign-around method using an equipment designed and constructed at our laboratory (the frequency was measured with a frequency -meter KZ–2026A–2, ZOPAN Warsaw, Poland) [8]. The temperature deviations did not exceed +/ − 0.002K. The repeatability of the ultrasound velocity measurements was better than +/ − 0.05m/s.

3. Measurement results

The isentropic and isothermal compressibility coefficients, β_s and β_T, and the molar heat capacity under constant volume, C_v were calculated from the measured ultrasound velocity, c, and density, ϱ, using the following equations:

$$\begin{aligned} \beta_s &= 1/(\varrho c^2) \\ \beta_T &= \beta_s + \alpha^2 VT/C_p \\ C_V &= C_p \beta_s/\beta_T \end{aligned} \tag{1}$$

where T — temperature, V — molar volume, α — coefficient of thermal expansion, C_p — molar heat capacity under constant pressure.

The values calculated for the pure components from Eq. (1) together with the heat capacities under constant pressure and coefficients of thermal expansion taken from literature [1–3] are collected in Table 1.

Table 1. Properties for pure components at 293.15 K.

Property	n − $C_5H_{11}OH$	tert−$C_5H_{11}OH$	C_6H_{12}
c/(m/s)	1292.9	1192.3	1277.1
ϱ/(kg/m^3)	814.6	808.9	778.2
β_s/(1/TPa)	734.2	869.5	791.1
β_T/(1/TPa)	867.1	1100.8	1090.1
C_v/(J/molK)	170.71	193.01	113.01
C_p/(J/molK)	201.67[a]	244.35[a]	156.01[b]
α/(1/kK)	0.92[a]	1.33[a]	1.216[b]

[a] Reference [1]. [b] Reference [2].

The excess adiabatic compressibility coefficients were calculated according to BENSON et al. [4, 5] using the following relations:

$$\begin{aligned} \beta_s^E &= \beta_s - \beta_s^{\mathrm{id}}, \quad \beta_s^{\mathrm{id}} = \beta_T^{\mathrm{id}} - (\alpha^{\mathrm{id}})^2 V^{\mathrm{id}} T/C_p^{\mathrm{id}} \\ \beta_T^{\mathrm{id}} &= x_{V,1}\beta_{T,1}^0 + (1 - x_{V,1})\beta_{T,2}^0 \end{aligned} \tag{2}$$

$$x_{V,1} = x_1 V_1^0 / V^{id}$$
$$V^{id} = x_1 V_1^0 + (1 - x_1) V_2^0$$
$$\alpha^{id} = x_{V,1} \alpha_1^0 + (1 - x_{V,1}) \alpha_2^0 \qquad (2) \text{ [cont.]}$$
$$C_p^{id} = x_1 C_{p,1}^0 + (1 - x_1) C_{p,2}^0 ,$$

were the lower indices "1" and "2" refer to both the components and the upper ones "0" and "id" indicate quantities related to the pure components and to the thermodynamically ideal mixtures, respectively.

The excess volume and compressibility can be written as follows:

$$V^E = V - V^{id} \qquad (3)$$
$$\varkappa_s^E = \varkappa_s - V^{id} \beta_s^{id} \qquad (4)$$

where $\varkappa_s = (V^E + V^{id})\beta_s$.

According to JAcobson [6], the free intermolecular length L is related to the adiabatic compressibility coefficient by the following equation:

$$\beta_s = k_\beta L^{2.4} \qquad (5)$$

where k_β is an empirical constant given in [3, 6].

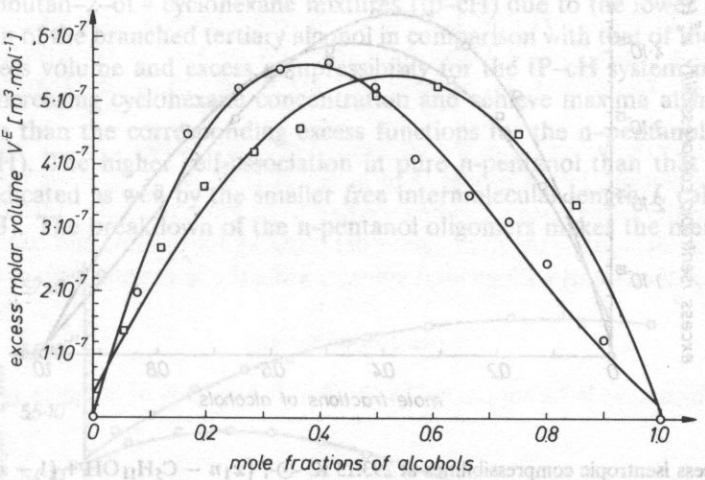

FIG. 1. Excess molar volumes at 293.15 K -⊙-, $\{x_1 n - C_5H_{11}OH + (1 - x_1)C_6H_{12}\}$; -○-, $\{x_1 \text{tert} - C_5H_{11}OH + (1 - x_1)C_6H_{12}\}$.
The lines represent the best-fit excess values calculated from Eq. (7).

It was found that the dependence of the ultrasound velocity, c, mean molar volume, V, as well as β_s, $\varkappa_s$ and L on the mole fraction of alcohol, x_1, can be satisfactorily represented by simple polynomials

$$F = \sum_{j=1}^{n} A_j x_1^{j-1} \qquad (6)$$

The A_j parameter values together with the mean standard deviations are given in Table 2.

Table 2. Parameters of equation (6) and standard deviations s.

	A_1	A_2	A_3	A_4	A_5	s
	$\{x_1 n - C_5H_{11}OH + (1 - x_1)C_6H_{12}\}$					
c/(m/s)	1275.41	−128.11	233.85	−89.04	–	0.18
V/(m^3/mol) * 10^7	1081.0	41.11	−93.31	78.7	−25.7	0.21
β_s/(1/TPa)	789.7	185.3	−525.4	432.5	−147.9	0.60
$\varkappa_s$/(m^3/Pa mol) * 10^{16}	854.951	607.954	−590.177	171.001	–	0.36
L/(m) * 10^{13}	542.240	137.303	−132.818	37.374	–	0.09
	$\{x_1$ tert $- C_5H_{11}OH + (1 - x_1)C_6H_{12}\}$					
c/(m/s)	1273.66	−195.12	167.16	−54.13	–	0.15
V/(m^3/mol) * 10^7	1082.46	23.104	−9.447	−6.172	–	0.17
β_s/(1/TPa)	791.10	282.52	−477.61	499.57	−226.19	0.40
$\varkappa_s$/(m^3/Pa mol) * 10^{16}	858.085	479.159	−259.391	43.624	–	0.49
L/(m) * 10^{13}	542.798	121.079	−72.160	14.993	–	0.13

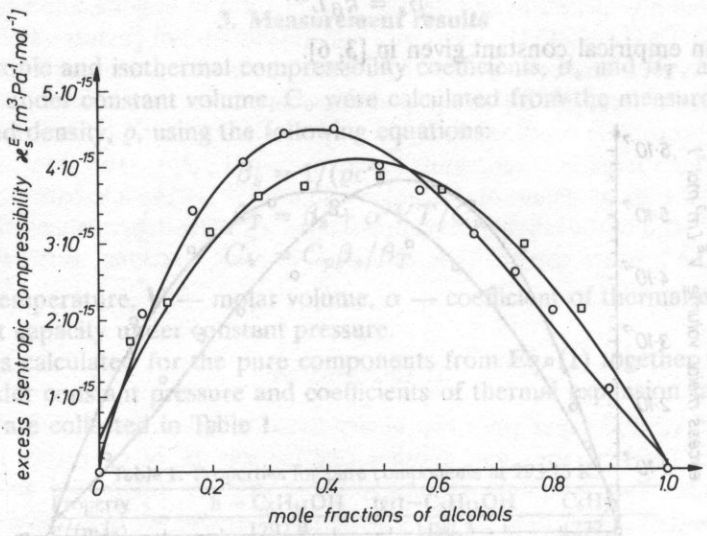

FIG. 2. Excess isentropic compressibilities at 293.15 K. -⊙-, $\{x_1 n - C_5H_{11}OH + (1 - x_1)C_6H_{12}\}$; -□-, $\{x_1$tert $- C_5H_{11}OH + (1 - x_1)C_6H_{12}\}$.
The lines represent the best-fit excess values calculated from Eq. (7).

The dependence of the excess functions on the mole fraction of alcohol is described with good accuracy by the Redlich-Kister equation

$$F^E = x_1(1 - x_1)\sum_{j=1}^{n} A_j(1 - 2x_1)^{j-1} \tag{7}$$

The parameters A_j and the corresponding mean standard deviations are collected in Table 3.

Table 3. Parameters of Eq. (7) of the excess functions and standard deviations s.

	A_1	A_2	A_3	A_4	s
		$\{x_1 n - C_5H_{11}OH + (1 - x_1)C_6H_{12}\}$			
$V^E/(m^3/mol) * 10^8$	187.75	133.85	27.753	−12.147	0.06
$\beta_s^E/(1/TPa)$	77.773	60.696	37.112	−1.094	0.02
$\varkappa_s^E/(m^3/Pa\,mol) * 10^{16}$	99.090	77.158	42.203	−2.825	0.04
		$\{x_1$ tert $- C_5H_{11}OH + (1 - x_1)C_6H_{12}\}$			
$V^E/(m^3/mol) * 10^8$	207.22	−20.058	50.394	49.519	0.10
$\beta_s^E/(1/TPa)$	93.738	18.503	60.743	9.335	0.15
$\varkappa_s^E/(m^3/Pa\,mol) * 10^{16}$	119.634	17.321	69.583	13.720	0.23

4. Discussion and conclusions

The excess molar volumes, V^E, and the excess adiabatic compressibilities, $\varkappa_s^E$, shown as functions of composition in Figs. 1 and 2 are positive in the whole concentration range for both the systems studied which suggests that the interaction between unlike molecules are weaker than those occurring in the pure components or at least in one of them [7]. This could be expected because of the high degree of self-association in the alcohols.

The dilution of the alcohols with cyclohexane results in a gradual breakage of the alcohol oligomers. As indicated by Figs. 1 and 2, this effect becomes more pronounced in the 2–metylbutan–2–ol – cyclohexane mixtures (tp–cH) due to the lower capability for self-association of the branched tertiary alcohol in comparison with that of the n–pentanol. Thus, the excess volume and excess compressibility for the tP–cH system increase more rapidly with increasing cyclohexane concentration and achieve maxima at higher alcohol concentrations than the corresponding excess functions for the n–pentanol–cyclohexane system (nP–cH). The higher self-association in pure n-pentanol than that in pure tert-pentanol is indicated as well by the smaller free intermolecular length L calculated from Eq. (5) (Fig. 3). The breakdown of the n-pentanol oligomers makes the mean free inter-

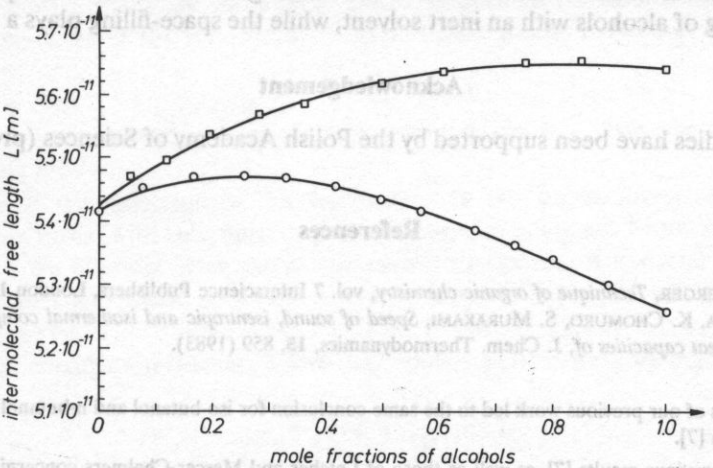

FIG. 3. The free intermolecular lengths at 293.15 K. -⊙-, $\{x_1 n - C_5H_{11}OH + (1 - x_1)C_6H_{12}\}$; -□-, $\{x_1$ tert $- C_5H_{11}OH + (1 - x_1)C_6H_{12}\}$.
The lines represent the best-fit values calculated from Eq. (6).

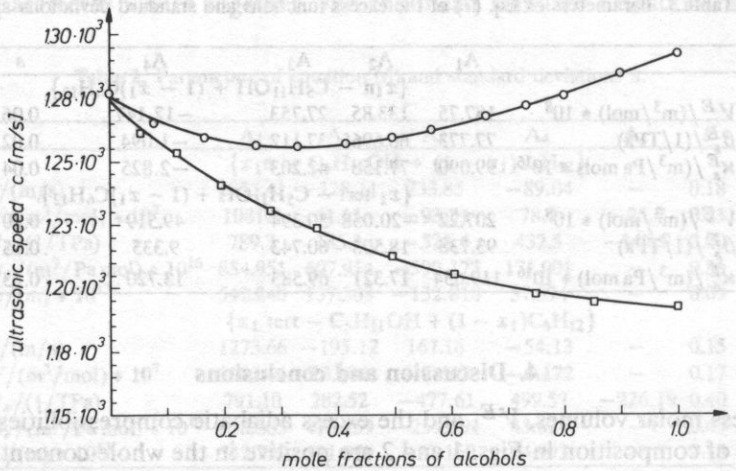

FIG. 4. Ultrasonic speed at 293.15 K. -⊙-, $\{x_1 n - C_5H_{11}OH + (1 - x_1)C_6H_{12}\}$; -□-, $\{x_1 \text{ tert} - c_5H_{11}OH + (1 - x_1)C_6H_{12}\}$.
The lines represent the best-fit values calculated from Eq. (6).

molecular length in the nP-cH mixtures increase with increasing dilution of the alcohols up to $x \approx 0.3$ in the tP-cH mixtures the mean free intermolecular length is decreasing within the same concentration range most probably because of the greater space-filling capability of the tert-pentanol molecules that are more ball-shaped than the n-pentanol molecules [1].

It should also be noticed that the ultrasound propagates faster in the system of higher molecular association, i.e. in nP-cH than in tP-cH (Fig. 4), in spite of the fact that the space-filling in the latter system can be expected to be more perfect. Thus, the results suggest that self-association is the main factor determining the volume and compressibility effects of mixing of alcohols with an inert solvent, while the space-filling plays a minor role [2].

Acknowledgement

These studies have been supported by the Polish Academy of Sciences (problem CPBP 02.03).

References

[1] A. WEISSBERGER, *Technique of organic chemistry*, vol. 7 Interscience Publishers, London 1955.
[2] K. TAMURA, K. CHOMURO, S. MURAKAMI, *Speed of sound, isentropic and isothermal compressibilities and isochoric heat capacities of*, J. Chem. Thermodynamics, **15**, 859 (1983).

[1] The results of our previous work led to the same conclusion for iso-butanol and n-butanol binary mixtures with cyclohexane [7].

[2] Also our previous results [7], as well as those of Letcher and Mercer-Chalmers concerning cyclohexane-alcohol systems [9] indicate that association, decreasing with increasing length and branching of the carbon chain, is the main factor determining the volume and compressibility effects of dilution of the alcohols by the inert solvent.

[3] B. JACOBSON, *Association numbers in liquid systems from intermolecular free length relationships*, Acta Chem. Scand. **9**, 997 (1955).
[4] O. KIYOCHARA, C.J. HALPIN, G.C. BENSON, J. Chem. Thermodynamics, **10**, 721 (1978).
[5] G.C. BENSON, O. KIYOCHARA, *Evaluation of excess isentropic compressibilities and isochoric heat capacities*, J. Chem. Thermodynamics, **11**, 1061 (1979).
[6] B. JACOBSON, *Intermolecular free lengths in the liquid state. I. Adiabatic and isothermal compressibilities*, Acta Chem. Scand., **6**, 1485 (1952).
[7] K. BEBEK, S. ERNST, *Ultrasonic and thermodynamics effects of self-association of aliphatic alcohols in c – C_6H_{12}. I. Primary Butanols.*, Arch. of Acoust., **15**, 3–4, 239 (1990).
[8] S. ERNST, W. MARCZAK, R. MANIKOWSKI, E. ZORĘBSKI, M. ZORĘBSKI, *A sing-around apparatus for group velocity measurements in liquids. Testing by standard liquids and discussion of the errors*, Acoustics Letters **15**, 7, 123 (1992).
[9] T.M. LETCHER, J. MERCER-CHALMERS, *Excess molar volumes of a cycloalkane + an alkanol at* 298.15K., Can. J. Chem., **69**, 1259 (1991).

Received on December 2, 1991

ARCHIVES OF ACOUSTICS
18, 1, 113–130 (1993)

WAVE PROPAGATION AND SCATTERING IN ELASTIC PLATE WITH PERIODICALLY GROOVED SURFACE

E. DANICKI and D. BOGUCKI

Institute of Fundamental Technological Research
Polish Academy of Sciences
(00-049 Warszawa, Świętokrzyska 21)

Bragg reflection of plate waves in isotropic elastic plate with a periodically grooved surface is analyzed. Mode-coupling effect is also taken into account. The analysed problem may be applied in the construction of piezoelectric resonators and RAC filters.

1. Introduction

SAW propagation and Bragg reflection phenomena on piezoelectric substrate with periodically corrugated surface were investigated in details [1], [2], [3]. In the substrate (piezoelectric halfspace) usually propagates one surface mode [1], [4] and the Bragg condition has the form $K = 2k_v$, where K — wave number of grooves system and k_v — SAW wavenumber.

In the elastic plate case situation is more complicated because of multimodal propagation of plate waves [5], [6], [7], [8]. Different plate modes may be coupled by formula

$$\mathbf{K} = \mathbf{k}_1 + \mathbf{k}_2 ,$$

where $\mathbf{k}_1$ — wave vector of forwards propagating mode, $\mathbf{k}_2$ — wave vector of backwards propagating mode.

This is Bragg reflection of the first order. In this paper Bragg reflection of slant propagating wave (with reference to groove system) is analysed. Mode conversion is also discussed. We consider isotropic elastic plate to be made of material characterised by ρ-mass density and Lamé constants λ and μ. Upper surface of plate is corrugated, the lower is flat (Fig. 1).

Surface corrugation is small, so we may apply a perturbation theory:

$$\left|\frac{h}{\Lambda}\right| \ll 1 , \left|\frac{h}{d}\right| \ll 1$$

h — groove amplitude, Λ — period of groove system, d — plate thickness.

We consider waves which are propagating in any direction on a (x, z) plane. According to Floquet theorem, displacements and stresses in the plate may be written in the form

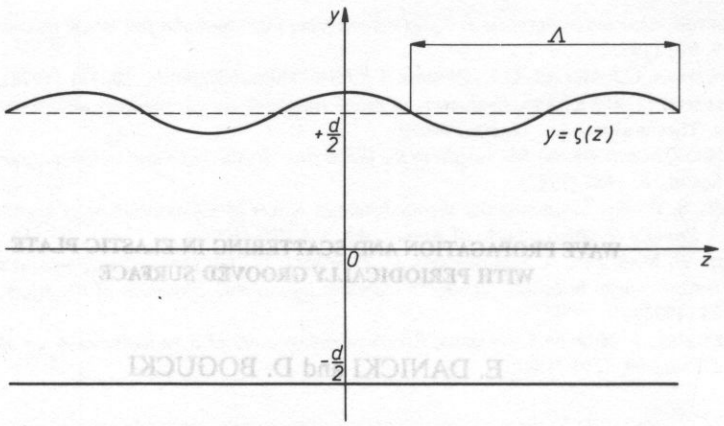

FIG. 1. Elastic plate with grooved upper surface (cross-section).

of Fourier series:

$$T_{ij} = \sum_n T_{il}^{(n)} e^{-j(s+nK)z} e^{-jrx} e^{j\omega t}, \tag{1}$$

$$u_i = \sum_n u_i^{(n)} e^{-j(s+nK)z} e^{-jrx} e^{j\omega t}, \tag{2}$$

where $i, j = x, y, z$ (1,2,3 analogously), and $r > 0$, $s > 0$ — components of wave vector of the incident wave in x and z axis direction respectively (Fig. 2).

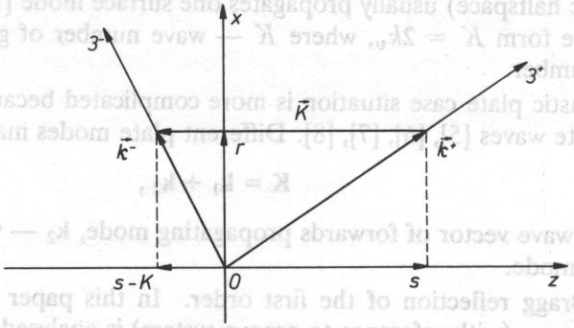

FIG. 2. Wavevectors for $n = 0(k^+)$, $n = -1(k^-)$ Auxiliary coordinate systems-axes $3^I \| \mathbf{k}^I$ are presented.

In this paper, for simplicity, we will take into account only the lowest harmonic components, coupled by Bragg condition i.e. components corresponding to $n = 0, -1$ (Fig. 2)

$$T_{il} = (T_{il}^+ e^{-jsz} + T_{il}^- e^{-j(s-K)z}) e^{-jrx} e^{j\omega t}, \tag{3}$$

$$u_i = (u_i^+ e^{-jsz} + u_i^- e^{-j(s-K)z}) e^{-jrx} e^{j\omega t}. \tag{4}$$

This simplification is sufficient in analisys of the first order Bragg reflection of slant propagating wave with possibility of mode conversion. In the case of propagation along the grooves (eg. for $s = 0$), it is necessary to with components account for $n = -1, 0, 1$

(which is discussed in section 3). Factor $\exp(j\omega t)$ is ommited in a further part of this article.

In section 2 basic plate equations and so-called generalized Tiersten boundary conditions are discussed. Numerical results are presented in section 3. Appendix A shows the influence of higher harmonic components in series (1) (2) on results. Appendix B presents a form of solution in the case of plate corrugated on both surfaces (upper and lower).

2. Formulation of the problem

2.1. *Generalised Tiersten boundary conditions*

Let us consider free material surface streaching for $y > \zeta(z)$, where

$$y = \zeta(z) = he^{-jKz} + h^* e^{jKz} \tag{5}$$

described sinusoidally corrugated surface with period $\Lambda = 2\pi/K$ and amplitude $h \ll \Lambda$. In [1] were presented so-called generalized Tiersten boundary conditions. These are relationships between stresses on mean surface $y = 0$, and known displacements on the same surface. On other hand, generalized Tiersten boundary conditions replace homogeneous boundary conditions on corrugated surface by inhomogeneous boundary conditions on mean surface (in simplification of small corrugation).

Relations presented in [1] are (detonation of complex amplitudes of stresses and displacements are analogous to (3) (4)).

$$\begin{bmatrix} T_{xy}^+ \\ T_{yy}^+ \\ T_{zy}^+ \end{bmatrix} = h \begin{bmatrix} G_{11} & 0 & G_{13} \\ 0 & G_{22} & 0 \\ G_{31} & 0 & G_{33} \end{bmatrix} \begin{bmatrix} u_x^- \\ u_y^- \\ u_z^- \end{bmatrix}, \tag{6}$$

where

$$\begin{aligned} G_{11} &= \rho\omega^2 - \mu\left(4\frac{\lambda+\mu}{\lambda+2\mu}r^2 + s(s-K)\right), \\ G_{13} &= -\mu\left(rs + \frac{2\lambda}{\lambda+2\mu}r(s-K)\right), \\ G_{22} &= \rho\omega^2, \\ G_{31} &= -\mu\left(r(s-K) + \frac{2\lambda}{\lambda+2\mu}rs\right), \\ G_{33} &= \rho\omega^2 - \mu\left(4\frac{\lambda+\mu}{\lambda+2\mu}s(s-K) + r^2\right). \end{aligned} \tag{7}$$

Relationship for T_{yi}^- as a function of u_j^+ can be obtained from (6) (7) by replacements:

$$\begin{aligned} h &\to h^* \\ s &\leftrightarrow s - K \\ - &\leftrightarrow + \end{aligned} \tag{8}$$

For our purposes it is more useful to write relations (6)–(8) in another form [1]. We now introduce two additional coordinate systems such that axis $3^l \| \mathbf{k}^l$, $l^l \perp 3^l$ and $2^l \equiv y$, $l = +, -$ (Fig. 2).

In the same way as in [1] and [9], we can transform tensor components from (6)–(8) to new coordinate systems. After transformations we obtain

$$\mathbf{T}^+ = h\mathbf{g}\mathbf{u}^-, \tag{9}$$

$$\mathbf{T}^- = h^*\mathbf{g}^T\mathbf{u}^+, \tag{10}$$

where

$$\mathbf{g} = \begin{bmatrix} g_{11} & 0 & g_{13} \\ 0 & g_{22} & 0 \\ -g_{13} & 0 & g_{33} \end{bmatrix}, \tag{11}$$

$$g_{11} = \frac{1}{k^+k^-}\{(r^2 + s(s-K))[\rho\omega^2 - \mu(r^2 + s(s-K))] + \mu r^2K^2\}$$

$$g_{13} = \frac{rK}{k^+k^-}[\rho\omega^2 - 2\mu(r^2 + s(s-K))]$$

$$g_{22} = \rho\omega^2$$

$$g_{33} = \frac{1}{k^+k^-}\left\{(r^2 + s(s-K))[\rho\omega^2 - 4\mu\frac{\lambda+\mu}{\lambda+2\mu}(r^2 + s(s-K))] - \mu\frac{2\lambda}{\lambda+2\mu}r^2K^2\right\} \tag{12}$$

where vectors $\mathbf{T}^l$ i $\mathbf{u}^l$ are (in short matrix notation) $\mathbf{T}^l = [T_6^l, T_2^l, T_4^l]^T$, $\mathbf{u}^l = [u_1^l, u_2^l, u_3^l]^T$ $l = +, -$, and wave numbers k^+ i k^- are such that

$$k^+ = |\mathbf{k}^+| = \sqrt{s^2 + r^2}$$

$$k^- = |\mathbf{k}^-| = \sqrt{(s-K)^2 + r^2}. \tag{13}$$

2.2. *Impedance relations for elastic plate*

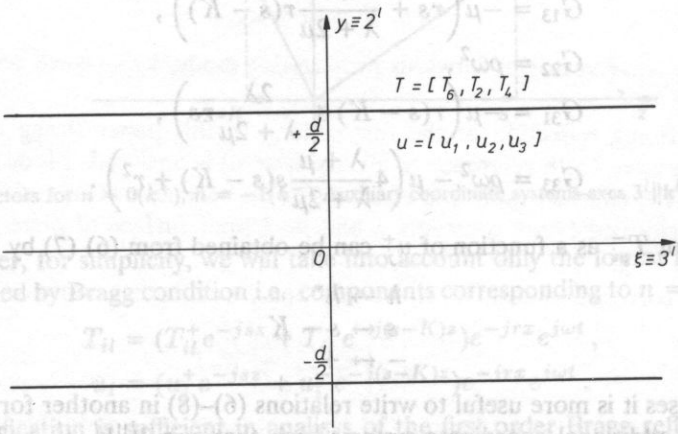

FIG. 3. Elastic plate with heterogenous boundary conditions on upper surface (cross-section).

Let us consider now the elastic plate bounded by planes $y = \pm d/2$ (Fig. 3), with its bottom surface stress-free and upper surface by harmonic stresses subjected to $\exp(-jk\xi)$.

Making use of equations of motion for elastic plate, after some transformations [10] we obtain so-called impedance relations for plate, i.e. relations between stresses and displacements on upper plate surface

$$\mathbf{u} = \mathbf{x}\mathbf{T}, \tag{14}$$

$$\mathbf{x} = \begin{bmatrix} x_{11} & 0 & 0 \\ 0 & x_{22} & x_{23} \\ 0 & x_{32} & x_{33} \end{bmatrix}, \tag{15}$$

where: $\mathbf{T} = [T_6, T_2, T_4]^T$, $\mathbf{u} = [u_1, u_2, u_3]^T$ in our (Fig. 3) coordinate system (η, y, ξ).

Nonzero elements of matrix $\mathbf{x}$ are

$$x_{11} = \frac{-\cos\beta d}{\mu \cdot \Delta_T} \tag{16}$$

$$x_{22} = \frac{1}{2\mu \cdot \Delta_L}\alpha(k^2+\beta^2)\left(\sin\alpha\frac{d}{2}\sin\beta\frac{d}{2}\Delta_1 - \cos\alpha\frac{d}{2}\cos\beta\frac{d}{2}\Delta_2\right) \tag{17}$$

$$x_{33} = \frac{1}{2\mu \cdot \Delta_L}\beta(k^2+\beta^2)\left(\sin\alpha\frac{d}{2}\sin\beta\frac{d}{2}\Delta_2 - \cos\alpha\frac{d}{2}\cos\beta\frac{d}{2}\Delta_1\right) \tag{18}$$

$$x_{23} = j\frac{k}{2\mu \cdot \Delta_L}\left((2\alpha\beta\Delta_2 + (k^2-\beta^2)\Delta_1)\sin\beta\frac{d}{2}\cos\alpha\frac{d}{2} + \right.$$
$$\left. + (2\alpha\beta\Delta_1 + (k^2-\beta^2)\Delta_2)\sin\alpha\frac{d}{2}\cos\beta\frac{d}{2}\right) \tag{19}$$

$$x_{32} = x_{23}^* \tag{20}$$

where

$$\alpha^2 = \left(\frac{\omega}{V_L}\right)^2 - k^2, \quad \beta^2 = \left(\frac{\omega}{V_T}\right)^2 - k^2, \quad V_T = \sqrt{\frac{\mu}{\rho}}, \quad V_L = \sqrt{\frac{2\mu+\lambda}{\rho}}. \tag{21}$$

Signs of α and β may be assumed both plus or minus because relations (16)–(20) are even with respect to this variables.

$$\Delta_1 = (k^2-\beta^2)\sin\alpha\frac{d}{2}\cos\beta\frac{d}{2} + 4k^2\alpha\beta\cos\alpha\frac{d}{2}\sin\beta\frac{d}{2} \tag{22}$$

$$\Delta_2 = (k^2-\beta^2)\sin\beta\frac{d}{2}\cos\alpha\frac{d}{2} + 4k^2\alpha\beta\cos\beta\frac{d}{2}\sin\alpha\frac{d}{2} \tag{23}$$

$$\Delta_L = \Delta_1 \cdot \Delta_2 \tag{24}$$

$$\Delta_T = \beta \cdot \sin\beta. \tag{25}$$

Formula (14) is the Fourier transform of Green's function for elastic plate (k is Fourier transform variable). Dispersion relations for plate waves may be obtained, if we put zero to determinant of the inverse matrix from (15) ($\mathbf{T} = 0$ is boundary condition in this case). Element x_{11} describes propagation of SH plate waves, other nonzero elements — propagation of Lamb modes.

2.3. *Dispersion relations*

For isotropic plate, relations (15) are independent of the wave propagation direction. So if the system of coordinates on Fig. 3 is such that axis $\xi \equiv 3^+ (y \equiv 2^+)$ then by substitution $k = k^+$ we have relations for incident wave.

$$\mathbf{u}^+ = \mathbf{x}^{(0)}\mathbf{T}^+ . \tag{26}$$

If we put $k = k^- (\xi \equiv 3^-, y \equiv 2^-)$ we obtain relations for reflected wave.

$$\mathbf{u}^- = \mathbf{x}^{(-1)}\mathbf{T}^- . \tag{27}$$

Relations (9), (10), (26), (27) are sufficient for the determination of dispersion relations of waves propagating in corrugated plate. Substituting (10) to (27) and (11) to (26) we obtain

$$\begin{cases} \mathbf{u}^+ = h\mathbf{x}^{(0)}g\mathbf{u}^- \\ \mathbf{u}^- = h^*\mathbf{x}^{(-1)}\mathbf{g}^T\mathbf{u}^+ \end{cases} \tag{28}$$

So we have a system of 6 equations with 6 unknowns $[u_i^+; u_i^-]$ $i = 1, 2, 3$. Dispersion relations may be determined by putting to zero determinant of equations set (28). It is easy to reduce set (28) to equivalent set 3×3 equations:

$$\{\mathbf{I} - |h|^2\mathbf{A}\}\mathbf{u}^+ = \mathbf{0}, \tag{29}$$

where:

$$\mathbf{A} = \mathbf{x}^{(0)}\mathbf{g}\mathbf{x}^{(-1)}\mathbf{g}^T . \tag{30}$$

Finally, the dispersion relation is

$$\det\{\mathbf{I} - |h|^2\mathbf{A}\} = D = 0 . \tag{31}$$

To solve equation (31) generally is quite difficult and only numerically possible, but equation (31) is much simpler in two special cases:

1. for $r = 0$, i.e. normal incidence of wave onto grooves
2. for $s = 0$, i.e. wave propagation along the grooves Those special cases are investigated in the next part of this paper.

3. Numerical results

3.1. *Normal incidence onto grooves*

In numerical calculations presented in this section it is assumed that:

— $s \in (0, K)$, i.e. s is in the first Brillouin zone;
— angular frequency ω is normalised to $\Omega = \omega/V_T$, $\Omega \in (0, K)$;
— it is assumed that $h = 0.01\Lambda$;
— it was assumed $V_L = 2V_T$;
— plate thickness d is normalised $\Lambda d = m\Lambda$, in our case: $m = 1$.

For $r = 0$, i.e. in the case of normal incidence of wave onto grooves the non-zero

elements of **A** matrix are

$$\begin{aligned} A_{11} &= x_{11}^{(0)} x_{11}^{(-1)} g_{11}^2 \\ A_{22} &= x_{22}^{(0)} x_{22}^{(-1)} g_{22}^2 + x_{23}^{(0)} x_{32}^{(-1)} g_{22} g_{23} \\ A_{23} &= x_{22}^{(0)} x_{23}^{(-1)} g_{22} g_{33} + x_{23}^{(0)} x_{33}^{(-1)} g_{33}^2 \\ A_{32} &= x_{32}^{(0)} x_{22}^{(-1)} g_{22}^2 + x_{33}^{(0)} x_{32}^{(-1)} g_{22} g_{33} \\ A_{33} &= x_{32}^{(0)} x_{23}^{(-1)} g_{22} g_{33} + x_{33}^{(0)} x_{33}^{(-1)} g_{33}^2 . \end{aligned} \tag{32}$$

So equation (31) takes the form:

$$D = D_T D_L = 0 , \tag{33}$$

where:

$$D_T = 1 - |h|^2 A_{11} , \tag{34}$$

$$D_L = 1 - |h|^2 (A_{22} + A_{33}) + |h|^4 (A_{22} A_{33} - A_{23} A_{32}) . \tag{35}$$

Relation (34) describes the propagation of SH (transverse) plate modes, and (35) the propagation of Lamb modes. It is worth to note that in $r = 0$ case SH and Lamb waves propagation is independent, so may be independently analysed. Fig. 4a shows dispersion curves $\Omega = \Omega(s)$ for free (uncorrugated $h = 0$) plate, at $m = 1 (d = \Lambda)$. In this case in our structure always (independent of plate thickness) propagate three modes: — Antisymmetric A_0 and symmetric S_0 Lamb modes, — SH_0 transverse mode.

In corrugated plate ($h \neq 0$), corresponding relations are more complicated — Fig. 4b. Existence of forbidden frequency bands — marked A, B, C, D, E on figure, is characteristic for this case. In those frequency bands wavenumber has complex values — which is connected with effect of Bragg reflection: band A is connected with reflection of SH_0 mode backwards to SH_0, band $B : A_0 \to A_0$, and band $C : S_0 \to S_0$. For bands $A - C$ solutions for s may be written in the form $s = K/2 \pm j \operatorname{Im}\{s\}$, where $\operatorname{Im}\{s\}$ is small in relation to K (and dependent on h magnitude). Bands D and E are connected with Bragg reflection and mode conversion ($S_0 \leftrightarrow A_0$). It is interesting that in those cases inside frequency band $\operatorname{Re}\{s\} \neq \text{const} \neq K/2$, because of the different velocity of coupled modes. For SH_0 mode, we approximate the form of dispersion relation. Assuming that

$$\sin \beta d \approx \beta d ; \; \cos \beta d \approx 1 ,$$

we obtain from (34)

$$(\Omega^2 - s^2)(\Omega^2 - (s - K)^2) - \kappa^2 (\Omega^2 - s(s - K))^2 = 0 , \tag{36}$$

where $\kappa = |h|/d$, so complex solutions for s we obtain if

$$\Omega \in \left(\frac{K}{2} \sqrt{\frac{1 - \kappa}{1 + \kappa}}, \frac{K}{2} \sqrt{\frac{1 + \kappa}{1 - \kappa}} \right) , \tag{37}$$

(then $\operatorname{Re}\{s\} = K/2$). Finally width of frequency band is

$$\Delta\Omega = K \frac{\kappa}{\sqrt{1 - \kappa^2}} . \tag{38}$$

For plates thicker then $m = 3$, higher plate modes may propagate and corresponding dispersion relations are much more complicated.

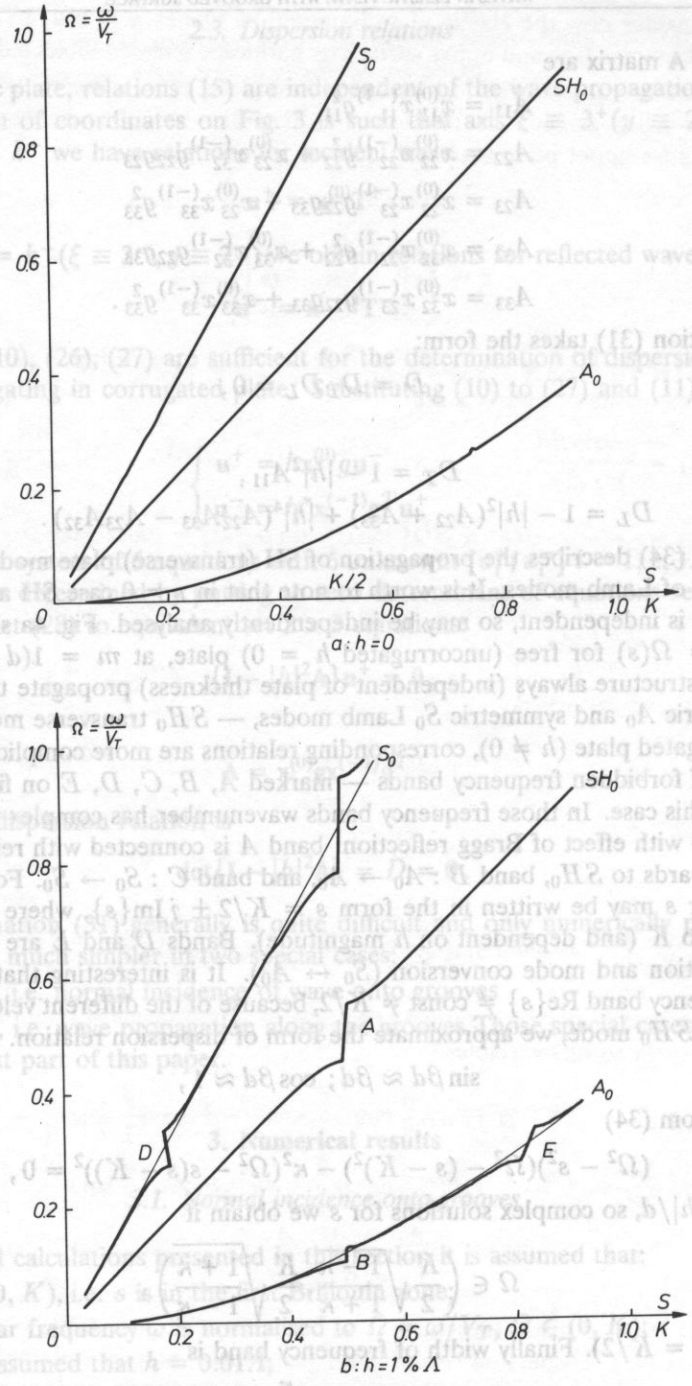

Fig. 4. Dispersion curves for a) uncorrugated plate with $d = \Lambda$
b) corrugated plate $d = \Lambda$ and $\kappa = |h|/d = 1\%$.

3.2. *Propagation along the grooves*

As it was mentioned in Sect. 1, in this case we must regard 3 harmonic components in series (1) i (2) that is $n = -1, 0, 1$

$$T_{il} = (T_{il}^{+} e^{-jsz} + T_{il}^{-} e^{-j(s-K)z} + T_{il}^{\sim} e^{-j(s+k)z}) e^{-jrx}, \tag{39}$$

$$u_i = (u_i^{+} e^{-jsz} + u_i^{-} e^{-j(s-K)z} + u_i^{\sim} e^{-j(s+K)z}) e^{-jrx}. \tag{40}$$

In our case (Fig. 5)

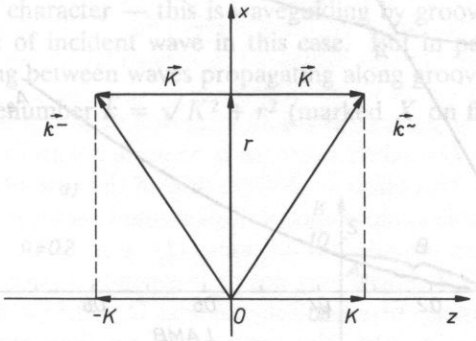

FIG. 5. Wavevectors taken under consideration in the case of propagation along the grooves

$$k^{+} = r$$

$$k^{\sim} = k^{-} = \overline{k} = \sqrt{K^2 + r^2}. \tag{41}$$

Generalized Tiersten boundary conditions have now form

$$\mathbf{T}^{+} = h\mathbf{g}\mathbf{u}^{-} + h^{*}\mathbf{g}^{T}\mathbf{u}^{\sim}, \tag{42}$$

$$\mathbf{T}^{-} = h^{*}\mathbf{g}^{T}\mathbf{u}^{+}, \tag{43}$$

$$\mathbf{T}^{\sim} = h\mathbf{g}\mathbf{u}^{+}, \tag{44}$$

where

$$g_{11} = \frac{r}{\overline{k}}(\rho\omega^2 - \mu(r^2 - K^2)), \tag{45}$$

$$g_{13} = \frac{K}{\overline{k}}(\rho\omega^2 - 2\mu r^2), \tag{46}$$

$$g_{22} = \rho\omega^2, \tag{47}$$

$$g_{33} = \frac{r}{\overline{k}}\left((\rho\omega^2 - 4\mu\frac{\lambda+\mu}{\lambda+2\mu}r^2) - \mu\frac{2\lambda}{\lambda+2\mu}K^2\right) \tag{48}$$

at $\mathbf{T}^{l} = [T_6^{l}, T_2^{l}, T_4^{l}]^T$, $\mathbf{u}^{l} = [u_6^{l}, u_2^{l}, u_4^{l}]^T$, where $l = +, -, \sim$.

Impedance relations for $n = +1$ may be find analogously as in section 2.3

$$\mathbf{u}^{\sim} = \mathbf{x}^{(l)}\mathbf{T}^{\sim} \tag{49}$$

it is easy to find from (41) that for $n = -1$ in our case $\mathbf{x}^{(-1)} = \mathbf{x}^{(1)}$. Finally we obtain an analogous to (28) system 9 equations with 9 unknowns.

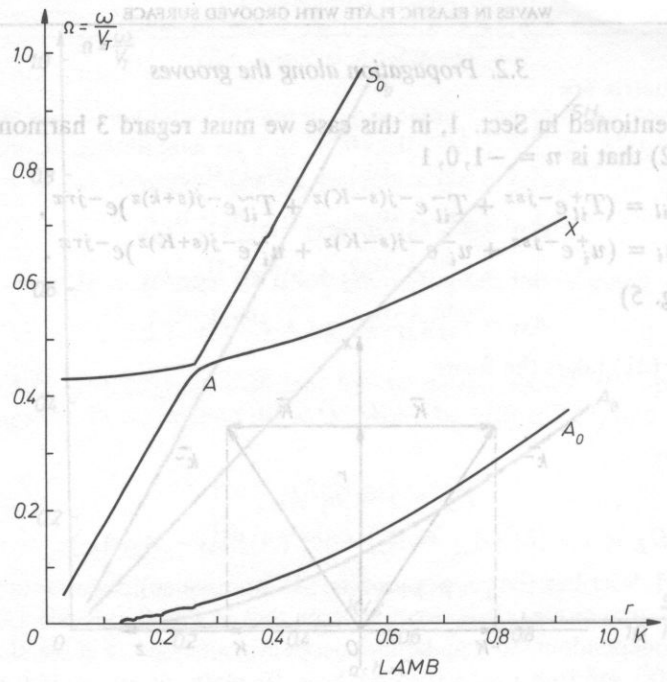

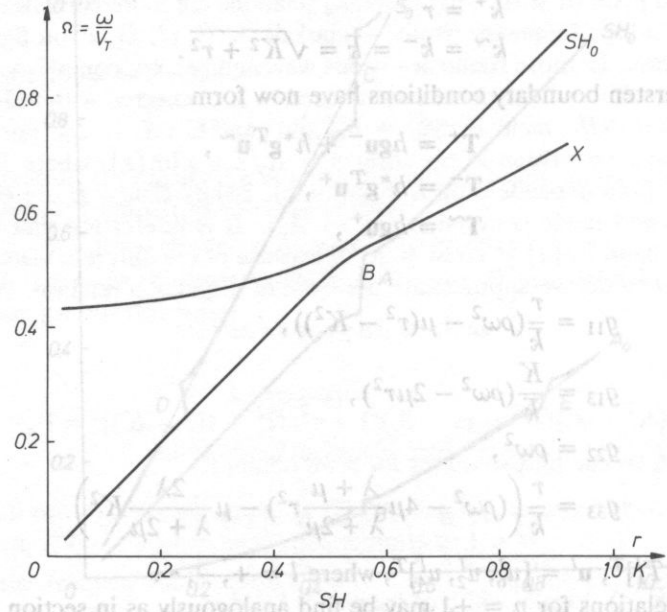

Fig. 6. Dispersion curves for propagation along the grooves ($s = 0$), $d = \Lambda$ a) SH modes b) Lambda modes.

$$\begin{cases} \mathbf{u}^{+} = h\mathbf{x}^{(0)} = \mathbf{g}\mathbf{u}^{-} + h^{*}\mathbf{x}^{(0)}\mathbf{g}^{T}\mathbf{u}^{\sim}, \\ \mathbf{u}^{-} = h^{*}\mathbf{x}^{(-1)}\mathbf{g}^{T}\mathbf{u}^{+}, \\ \mathbf{u}^{\sim} = h\mathbf{x}^{(-1)}\mathbf{g}\mathbf{u}^{+}. \end{cases} \tag{50}$$

This set may be easily reduced to an equivalent system 3×3 analogous (29) with

$$\mathbf{A} = \mathbf{x}^{(0)}\mathbf{g}\mathbf{x}^{(-1)}\mathbf{g}^{T} + \mathbf{x}^{(0)}\mathbf{g}^{T}\mathbf{x}^{(-1)}\mathbf{g}. \tag{51}$$

It is important that dispersion equation has analogous form to (33), but solutions have a quite different character — this is waveguiding by groove system (Fig. 6). There is no Bragg reflection of incident wave in this case. But in parts marked A and B on Fig. 6 we have coupling between waves propagating along grooves (S_0, SH_0) with modes propagating with wavenumber $\bar{k} = \sqrt{K^2 + r^2}$ (marked X on figure). Those modes are

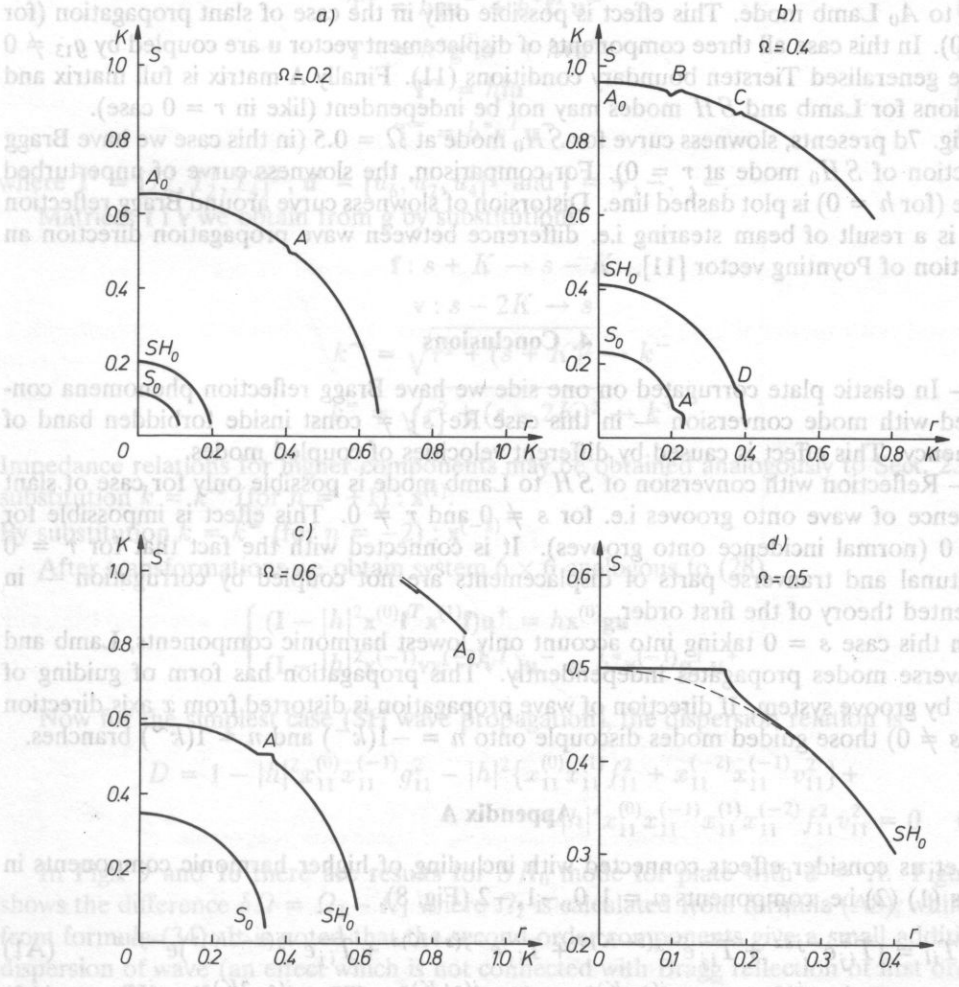

FIG. 7. Slowness curves for $d = \Lambda$.

connected with harmonic components $n = \pm 1 (k^- = k^\sim)$. Numerical calculations show that in the case of small distorsion (about 10°) influence of components $n = +1$ i.e. $k^\sim$ may be ommited.

Results presented in this paper are essentially good agree with results published in [2].

3.3. General case (slant incidence onto grooves)

In this case $D = D(r, s, \Omega)$ depends, in a complicated way, on the frequency and wave propagation direction. The most natural is to analyse D on (r, s) plane, for $\Omega = \text{const}$ — in that way we obtain so-called slowness curves (Fig. 7). In our problem those curves have the form of concentric circles disfigured in regions where we have Bragg reflection, i.e. in area of complex values of wavenumber.

In Figs. 7a, 7b, 7c slowness curves for Ω increased with step 0.2 are presented. Very interesting are bands C i D — their existence is connected with Bragg reflection of mode SH_0 to A_0 Lamb mode. This effect is possible only in the case of slant propagation (for $r \neq 0$). In this case all three components of displacement vector **u** are coupled by $g_{13} \neq 0$ in the generalised Tiersten boundary conditions (11). Finally **A** matrix is full matrix and solutions for Lamb and SH modes may not be independent (like in $r = 0$ case).

Fig. 7d presents, slowness curve for SH_0 mode at $\Omega = 0.5$ (in this case we have Bragg reflection of SH_0 mode at $r = 0$). For comparison, the slowness curve of unperturbed mode (for $h = 0$) is plot dashed line. Distorsion of slowness curve around Bragg reflection area is a result of beam stearing i.e. difference between wave propagation direction an direction of Poynting vector [11].

4. Conclusions

— In elastic plate corrugated on one side we have Bragg reflection phenomena connected with mode conversion — in this case $\mathrm{Re}\{s\} \neq \text{const}$ inside forbidden band of frequency. This effect is caused by different velocities of coupled modes.

— Reflection with conversion of SH to Lamb mode is possible only for case of slant incidence of wave onto grooves i.e. for $s \neq 0$ and $r \neq 0$. This effect is impossible for $r = 0$ (normal incidence onto grooves). It is connected with the fact that for $r = 0$ longitunal and tranverse parts of displacements are not coupled by corrugation — in presented theory of the first order.

In this case $s = 0$ taking into account only lowest harmonic components, Lamb and transverse modes propagates independently. This propagation has form of guiding of wave by groove system. If direction of wave propagation is distorted from x axis direction (for $s \neq 0$) those guided modes discouple onto $n = -1 (k^-)$ and $n = 1 (k^\sim)$ branches.

Appendix A

Let us consider effects connected with including of higher harmonic components in series (1) (2) i.e. components $n = 1, 0, -1, -2$ (Fig. 8),

$$T_{il} = (T_{ij}^{+} e^{-jsz} + T_{ij}^{-} e^{-j(s-K)z} + T_{ij}^{\sim} e^{-j(s+K)z} + T_{ij}^{=} e^{-j(s-2K)z}) e^{-jrx} \tag{A1}$$

$$u_i = (u_i^{+} e^{-jsz} + u_i^{-} e^{-j(s-K)z} + u_i^{\sim} e^{-j(s+K)z} + T_{ij}^{=} e^{-j(s-2K)z}) e^{-jrx} \tag{A2}$$

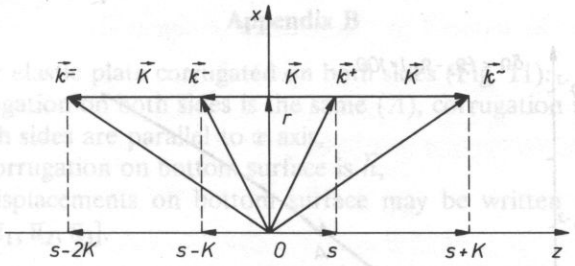

FIG. 8. Wavevectors taken under consideration in analysis of influence of second order components.

Other assumptions are the same as in previous section. Generalised Tiersten boundary conditions then have the form (higher powers of h are ommited)

$$\mathbf{T}^{+} = h\mathbf{g}\mathbf{u}^{-} + h^{*}\mathbf{f}^{T}\mathbf{u}^{\sim} \tag{A3}$$

$$\mathbf{T}^{-} = h^{*}\mathbf{g}^{T}\mathbf{u}^{+} + h\mathbf{v}\mathbf{u}^{=} \tag{A4}$$

$$\mathbf{T}^{\sim} = h\mathbf{f}\mathbf{u}^{+} \tag{A5}$$

$$\mathbf{T}^{=} = h^{*}\mathbf{v}^{T}\mathbf{u}^{-} \tag{A6}$$

where $\mathbf{T}^{l} = [T_6^l, T_2^l, T_4^l]^T$, $\mathbf{u}^{l} = [u_6^l, u_2^l, u_4^l]^T$ and $l = +, -, \sim, =$.

Matrices **f** i **v** we obtain from **g** by substitutions:

$$\mathbf{f} : s + K \to s - K$$

$$\mathbf{v} : s - 2K \to s$$

$$k^{\sim} = \sqrt{r^2 + (s+K)^2} \to k^{-}$$

$$k^{=} = \sqrt{r^2 + (s-2K)^2} \to k^{+}$$

Impedance relations for higher components may be obtained analogously to Sect. 2.3 By substitution $k = k^{\sim}$ (for $n = +1$) : $\mathbf{x}^{(1)}$.
By substitution $k = k^{=}$ (for $n = -2$) : $\mathbf{x}^{(-2)}$.

After transformations we obtain system 6×6 analogous to (28)

$$\begin{cases} (\mathbf{I} - |h|^2\mathbf{x}^{(0)}\mathbf{f}^{T}\mathbf{x}^{(1)}\mathbf{f})\mathbf{u}^{+} = h\mathbf{x}^{(0)}\mathbf{g}\mathbf{u}^{-} \\ (\mathbf{I} - |h|^2\mathbf{x}^{(-1)}\mathbf{v}\mathbf{x}^{(-2)}\mathbf{v}^{T})\mathbf{u}^{-} = h^{*}\mathbf{x}^{(-1)}\mathbf{g}^{T}\mathbf{u}^{+} \end{cases} \tag{A7}$$

Now for the simplest case (SH wave propagation), the dispersion relation is

$$D = 1 - |h|^2 x_{11}^{(0)} x_{11}^{(-1)} g_{11}^2 - |h|^2 \{x_{11}^{(0)} x_{11}^{(1)} f_{11}^2 + x_{11}^{(-2)} x_{11}^{(-1)} v_{11}^2\} + \\ + |h|^4 x_{11}^{(0)} x_{11}^{(-1)} x_{11}^{(1)} x_{11}^{(-2)} f_{11}^2 v_{11}^2 = 0 \tag{A8}$$

In Figs. 9 and 10 there are results for SH_0 mode for plate with $d = \Lambda$. Figure 9 shows the difference $\delta\Omega = \Omega_2 - \Omega_1$ where Ω_2 is calculated from formula (A8), while Ω_1 from formula (34). It is noted that the second order components give a small additional dispersion of wave (an effect which is not connected with Bragg reflection of first order), and little change in the width of frequency band (A — Fig. 9).

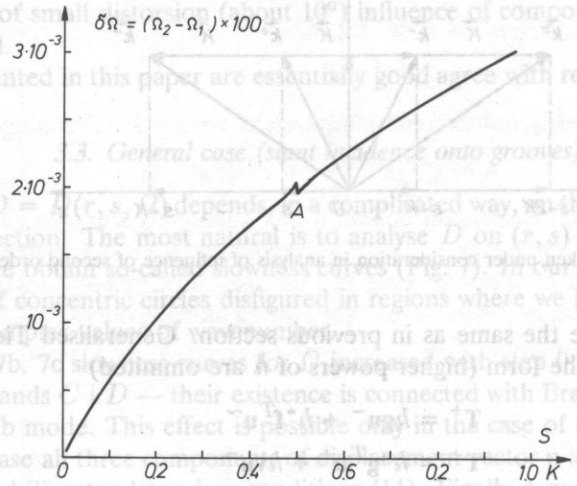

FIG. 9. Frequency correction caused by second order components.

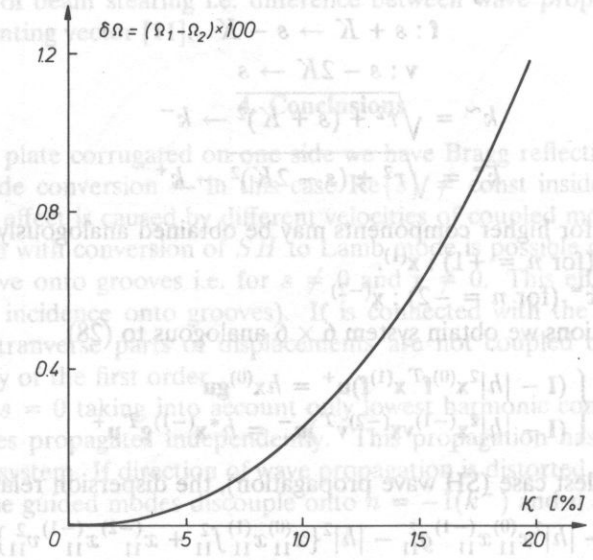

FIG. 10. $\Omega(\kappa)$ calculated with accounting of second order components.

The theory in the previous section predicts a linear dependence $\Omega_1(h)$ (38) (for small h). Calculations of components of second order show square type of this dependence — this is so called energy storage effect [12]. In Fig. 10 there is the difference $\delta\Omega = \Omega_2(h) - \Omega_1(h)$, where $\Omega_2(h)$ is calculated from (A8) formula.

Appendix B

Let us consider elastic plate corrugated on both sides (Fig. 11):
period of corrugation on both sides is the same (Λ), corrugation is small,
grooves on both sides are parallel to x axis,
amplitude of corrugation on bottom surface is $\bar{h}$,
stresses and displacements on bottom surface may be written in the form: $\bar{\mathbf{T}} = [\bar{T}_6, \bar{T}_2, \bar{T}_4]$, $\bar{\mathbf{u}} = [\bar{u}_1, \bar{u}_2, \bar{u}_3]$.

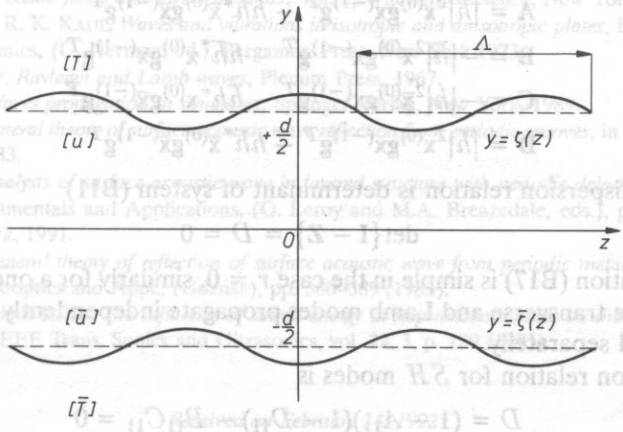

FIG. 11. Elastic plate corrugated on both sides (cross-section).

Generalized Tiersten boundary condition in the case of double corrugation have the form

$$\mathbf{T}^+ = h\mathbf{g}\mathbf{u}^- \quad \mathbf{T}^- = h^*\mathbf{g}^T\mathbf{u}^+ \quad y = +\frac{d}{2} \tag{B1}$$

$$\bar{\mathbf{T}}^+ = \bar{h}\mathbf{g}\bar{\mathbf{u}}^- \quad \bar{\mathbf{T}}^- = \bar{h}^*\mathbf{g}^T\bar{\mathbf{u}}^+ \quad y = -\frac{d}{2} \tag{B2}$$

and impedance relations

$$\mathbf{u} = \mathbf{x}\mathbf{T} + \bar{\mathbf{x}}\bar{\mathbf{T}} \tag{B3}$$

$$\bar{\mathbf{u}} = -\bar{\mathbf{x}}\mathbf{T} - \mathbf{x}\bar{\mathbf{T}} \tag{B4}$$

$$\tag{B5}$$

Non-zero elements of matrix $\bar{\mathbf{x}}$ may be determined analogously to [10]

$$\bar{x}_{11} = \frac{1}{\mu \cdot \Delta_T} \tag{B6}$$

$$\bar{x}_{22} = \frac{1}{2\mu \cdot \Delta_L}\alpha(k^2 + \beta^2)\left(\sin\alpha\frac{d}{2}\sin\beta\frac{d}{2}\Delta_l + \cos\alpha\frac{d}{2}\cos\beta\frac{d}{2}\Delta_2\right) \tag{B7}$$

$$\bar{x}_{33} = \frac{1}{2\mu \cdot \Delta_L}\beta(k^2 + \beta^2)\left(\sin\alpha\frac{d}{2}\sin\beta\frac{d}{2}\Delta_2 + \cos\alpha\frac{d}{2}\cos\beta\frac{d}{2}\Delta_l\right) \tag{B8}$$

$$\bar{x}_{23} = j\frac{k}{2\mu \cdot \Delta_L}\left((-2\alpha\beta\Delta_2 + (k^2 - \beta^2)\Delta_l)\sin\beta\frac{d}{2}\cos\alpha\frac{d}{2} + \right.$$
$$\left. + (2\alpha\beta\Delta_L - (k^2 - \beta^2)\Delta_2)\sin\alpha\frac{d}{2}\cos\alpha\beta\frac{d}{2}\right) \tag{B9}$$

$$\bar{x}_{32} = \bar{x}_{23} \tag{B10}$$

Our problem may be reduced to system of 6×6 equations

$$\{\mathbf{I} - \mathbf{Z}\}\mathbf{u} = \mathbf{0} \tag{B11}$$

where $\mathbf{u} = [u_i^+; \overline{u}_i^+]^T i = 1, 2, 3$.

While $\mathbf{Z}$ is matrix 6×6 build of 4 blocks.

$$[\mathbf{Z}] = \begin{bmatrix} \mathbf{A} & \mathbf{B} \\ \mathbf{C} & \mathbf{D} \end{bmatrix} \tag{B12}$$

$$\mathbf{A} = |h|^2 \mathbf{x}^{(0)} \mathbf{g} \mathbf{x}^{(-1)} \mathbf{g}^T - \overline{h} h^* \overline{\mathbf{x}}^{(0)} \mathbf{g} \overline{\mathbf{x}}^{(-1)} \mathbf{g}^T \tag{B13}$$

$$\mathbf{B} = -|\overline{h}|^2 \overline{\mathbf{x}}^{(0)} \mathbf{g} \mathbf{x}^{(-1)} \mathbf{g}^T - h \overline{h}^* \mathbf{x}^{(0)} \mathbf{g} \overline{\mathbf{x}}^{(-1)} \mathbf{g}^T \tag{B14}$$

$$\mathbf{C} = -|h|^2 \overline{\mathbf{x}}^{(0)} \mathbf{g} \mathbf{x}^{(-1)} \mathbf{g}^T - \overline{h} h^* \mathbf{x}^{(0)} \mathbf{g} \overline{\mathbf{x}}^{(-1)} \mathbf{g}^T \tag{B15}$$

$$\mathbf{D} = |\overline{h}|^2 \mathbf{x}^{(0)} \mathbf{g} \mathbf{x}^{(-1)} \mathbf{g}^T - h \overline{h}^* \overline{\mathbf{x}}^{(0)} \mathbf{g} \overline{\mathbf{x}}^{(-1)} \mathbf{g}^T \tag{B16}$$

Finally the dispersion relation is determinant of system (B11)

$$\det\{\mathbf{I} - \mathbf{Z}\} = D = 0 \tag{B17}$$

Solution of equation (B17) is simple in the case $r = 0$, similarly for a one-sided corrugated plate in that case transverse and Lamb modes propagate independently of each other and may be analysed separatelly.

The dispersion relation for SH modes is

$$D = (1 - A_{11})(1 - D_{11}) - B_{11}C_{11} = 0 \tag{B18}$$

Assuming that

$$\overline{h} = h_2 \exp\left\{-j\frac{\varphi}{2}\right\}; h = h_1 \exp\left\{j\frac{\varphi}{2}\right\} \tag{B19}$$

where $h_1 > 0$ i $h_2 > 0$ are the amplitudes of corrugation on upper and lower surface, respectively. Equation (B18) may be written in the form

$$D = 1 - \{(h_1^2 + h_2^2)x_{11}^{(0)} x_{11}^{(-1)} - 2h_1 h_2 \cos\varphi \cdot \bar{x}_{11}^{(0)} \bar{x}_{11}^{(-1)}\} g_{11}^2 + \\ + h_1^2 h_2^2 (\bar{x}_{11}^{(0)2} - x_{11}^{(0)2})(\bar{x}_{11}^{(-1)2}) g_{11}^4 = 0 \tag{B20}$$

We may approximate the frequency band width — analogously it was made in Sect. 3.1. So we obtain the equation

$$D = (\Omega^2 - s^2)(\Omega^2 - (s - K)^2) + \chi - \kappa^2(\Omega^2 - s(s - K))^2 = 0 \tag{B21}$$

where

$$\kappa = \frac{1}{d}\sqrt{h_1^2 + h_2^2 - 2h_1 h_2 \cos\varphi}, \tag{B22}$$

$$\chi = h_1^2 h_2^2 (\Omega^2 - s(s - K))^4, \tag{B23}$$

when $h_1 \neq 0$ and $h_2 \neq 0$ solution depends on angle φ.

There are two special cases:

1. $\varphi = 0$ then $\kappa = |h_1 - h_2|d$, when $h_2 = h_1$ equation (B21) describes propagation of uncoupled modes — there is no Bragg reflection.

2. $\varphi = \pi$ then $\kappa = |h_1 + h_2|/d$, when $h_1 = h_2$ small component χ may be ommited, so we have a case of equivalent plate corrugated on one side but with amplitude $2h$.

References

[1] E. DANICKI, *Perturbation theory of surface acoustic wave reflection from a periodic structure with arbitrary angle of incidence*, Arch. Mech., **36**, 5, pp. 639–650 (1984).

[2] A. A. MARADUDIN, A. P. MAYER, and W. ZIERAU, *Surface acoustic waves propagation along the groves of a periodic grating*, J. Appl. Phys., **69**, 4, pp. 1942–1947 (1990).

[3] Y. GULYAYEV and V. P. PLESKY, *Propagation of acoustic surface waves in periodic structures*, Sov. Phys. Usp., **32**, 1, pp. 51–74 (1989).

[4] E. DANICKI, *Rezonator z afp z konwersją modów*, Biuletyn WAT, **37**, 11, pp. 117–121 (1988).

[5] B. A. AULD, *Acoustic fields and waves in solids*, Vol. 2, Wiley Interscience, New York, 1973.

[6] Y. H. PAO and R. K. KAUL, *Waves and vibrations in isotropic and anisotropic plates*, In: R.D. Mindlin and Applied Mechanics, (G. Herman, ed.), Pergamon Press, New York 1973.

[7] I. A. VIKTOROV, *Rayleigh and Lamb waves*, Plenum Press, 1967.

[8] J. E. DOYLE, *Waves propagation in structures*, Springer Verlag, New York, 1989.

[9] E. DANICKI, *General theory of surface acoustic wave reflection from periodic grooves*, in Proc. of ICA (Paris), pp. 97–100, 1983.

[10] E. DANICKI, *Analysis of surface acoustic wave in layered structure with periodic delamination*, In: Physical Acoustic Fundamentals and Applications, (O. Leroy and M.A. Breazedale, eds.), pp. 281–285, Plenum Press, New York, 1991.

[11] E. DANICKI, *General theory of reflection of surface acoustic wave from periodic metal strips*, in Proc. Sec. Spr. on Acoustooptics and Appl., (Gdańsk), pp. 380–389 (1983).

[12] J. MELNGAILIS and R. LI, *The influence of stored energy at step discontinuities on the behaviour of surface wave gratings*, IEEE Trans. Sonics and Ultrasonics, vol. **22**, 3, p. 189 (1975).

Received on February 14, 1992

ARCHIVES OF ACOUSTICS
18, 1, 131–156 (1993)

EXPERIMENTAL INVESTIGATION OF DISCRETE SOUND PRODUCTION IN DEEP CAVITY EXPOSED TO AIRFLOW

M. MEISSNER

Institute of Fundamental Technological Research
Polish Academy of Sciences
(00-049 Warszawa, ul. Świętokrzyska 21)

The results are presented of the experimental investigation of the discrete sound generation in the process of airflow over the deep cavity. During the increase of the airflow velocity, three discrete components, referred to as A, B and C, are excited successively, which, as indicated by a analysis of results, are the f_{13}, f_{12} and f_{11} modes, respectively. In the process of sound generation two stages have been distinguished: stage 1, characterized by strong dependence of the frequencies of the discrete components A, B and C on the velocity of the airflow and stage 2, where the frequency, of the discrete component C, as the function of the velocity, varies approximately ten times less as compared with the stage 1. In stage 1 the "leading edge — trailing edge interaction" is of fundamental significance in the production of the discrete components, whereas the stage 2 is dominated by the feedback involving the effect of cavity-resonance modes on the disturbances of the shear layer.

1. Introduction

Frequently the airflow over a cavity is accompanied by generation of discrete sound, i.e. the acoustic signal consisting of discrete frequency components. This feature, exploited in musical instruments [1–3], is undesirable in wind tunnels with slotted walls [4, 5], in the industrial flow installations [6] and during the motion of various objects (aircraft, for example) in a static medium [7, 8] (detailed discussion of the sound generation phenomenon during flow over cavities can be found in review articles [9, 10]). So far, main research effort was placed on understanding the mechanism of the discrete sound generation and the role of the cavity in this process (shallow cavity [11–14], deep cavity [15–22], the cavity in the form of a Helmholtz resonator [23–27]) as well as the flow structure (laminar or turbulent flow [21, 28]). In case of the airflow over a deep cavity the experimental studies [19, 20] revealed the occurrence of the three different kinds of discrete components: pipetones, sheartones and turbulence-generated tones; the latter constitute a "passive response of cavity" to the turbulences in the airflow. The mechanism of pipetones generation, analogous to the process in organ pipes, is based on the mutual interactions between shear layer disturbances and cavity-resonance modes. In the process of the sheartone generation, the basic is the "leading edge — trailing edge interaction", i.e. the effect of the acoustic perturbations occurring at the leading edge, on the shear

layer disturbances at the trailing edge. Similar mechanism produces discrete sound when the air stream flows over shallow cavities [7, 11, 13] and also in generating edge-tones [29–31], where jumps in frequency of tones and hysteresis are observed.

This study presents the experimental results of generation of the discrete sound by the airflow over the deep cavity with rectangular opening. In the experimental setup, planar jet was used to excite oscillations in the cavity, in contrast to the methods used by other authors. The aim of this study is to identify the mechanism of discrete component generation.

2. Experimental arrangement and apparatus

The experimental setup is shown in Fig. 1a. The main components of the system are:

a) inlet nozzle *1* of circular cross-section,

b) settling chamber *2*,

c) preliminary nozzle *3*, of 3 × 30 mm cross-section and 60 mm length,

d) nozzle head *4*, with outlet nozzle and cavity opening: dimensions are l = 8 mm, s = 28 mm and thickness d_0 = 2 mm (Fig. 1b).

e) cavity *5* with s = 28 mm, w = 40 mm and depth d: 12 cm, 14 cm, 16 cm and 18 cm, respectively.

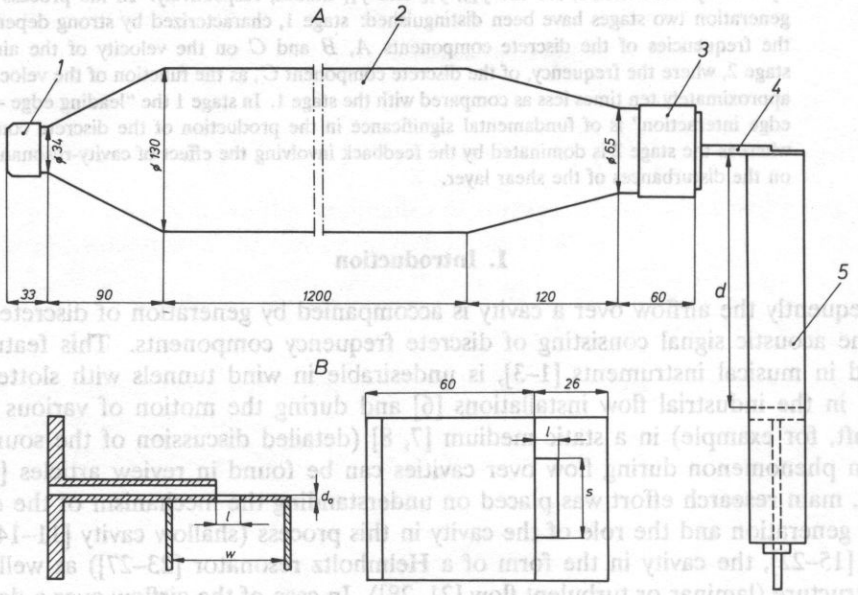

FIG. 1. Experimental setup: a) general layout, b) outlet attachment.
1 — inlet nozzle, *2* — settling chamber, *3* — preliminary nozzle, *4* — nozzle head, *5* — cavity.

The measuring system was supplied with the compressed air at the max. pressure 0.5 MPa. The air was fed through the control valve to the settling chamber *2*, and subsequently exited via the nozzle *3* and head *4*. The flow rate, in m^3/s, was measured with model PG 08–704 rotameter made by Prüfgerate-Werk Medingen. Acoustic measurements were

made with Brüel and Kjaer instrumental setup consisting of the microphone 1" type 4145, preamplifier 2203 and narrowband spectrum analyser 2033. All the measurements were conducted in an anechoic room. The microphone was mounted at the distance 1.5 m from the cavity opening: the line joining the centre of the microphone and the centre of the orifice made 90° angle with the air stream axis and crossed the plane of the orifice at 30°. The experiments contained the following:

a) measurement of the frequency f and the acoustic pressure level P of the discrete components at the low stream velocities,

b) recording of the selected sound spectra.

With the spectrum analyser 2033 the frequency analysis of the signal can be made within the defined frequency range. The accuracy of the frequency measurement is the same at a given frequency range. For the cavity depths equal 12 cm, 14 cm, 16 cm and 18 cm, the frequency range was up to 1000 Hz, with the accuracy of the frequency readout 2.5 Hz, for the first two and up to 500 Hz for the remaining two, accurate to 1.25 Hz. The acoustic pressure level P has been measured with the accuracy 0.1 dB in the whole frequency range. Choosing one of the modes of 2033 spectrum analyser, with 16–samples linear averaging, it was possible to eliminate the errors due to fluctuations of the main flow.

The selected sound spectra have been recorded with the data analysis system providing for the screen-copy of 2033 analyser. The system consists of an IBM XT computer as a control unit, IEC 625 interface, the spectrum analyser 2033 and Star SG–10 printer.

3. Sound spectra

In Figs. 2, 3 the sound spectra are shown, obtained at one of the four cavity depths (d = 12 cm) at the different values of the average stream velocities U (U = flow rate per outlet nozzle area). As follows from Figs. 2a, b, c the first discrete component (A — component) in the sound spectrum arises at the flow velocity U of order of a few m/s. This component is almost monochromatic and at relatively high acoustic pressure level ($P \leq 49$ dB) can easily be distinguished against broadband noise. Strong dependence of A–component frequency is observed on the airflow velocity. At U = 4.75 m/s (P–maximum of A–component) the frequency is 512.5 Hz (Fig. 2a), whereas at the velocities U: 5.16 m/s and 5.57 m/s the frequencies are 535 Hz (Fig. 2b) and 560 Hz (Fig. 2c), respectively. At the velocity U = 6.05 m/s (Fig. 2d) the first qualitative change takes place in the observed phenomenon: the discrete component A disappears and the second discrete component, referred to as component B, arises in the sound spectrum. It follows from Figs. 2c, 2d, that the component B maintains the tonal character but its frequency at U = 6.05 m/s (f = 492.5 Hz) is much lower than that of component A at U = 5.57 m/s. Further increase of U effects a fast increase of B–component frequency. In the case of the maximum of P for this component, the frequency amounts to 505 Hz (Fig. 2e) which, as one can see comparing Fig. 2a, approaches the frequency of component A at its value of the maximum P. At the velocity U = 6.48 m/s (Fig. 2f) another qualitative change is observed in the phenomenon: the discrete component B vanishes and the third discrete component (component C) in the sound spectrum occurs. It follows from Figs. 2e, 2f that, in the velocity range 6.28–6.48 m/s, consecutive, sudden drops in the frequency of the generated sound, take place.

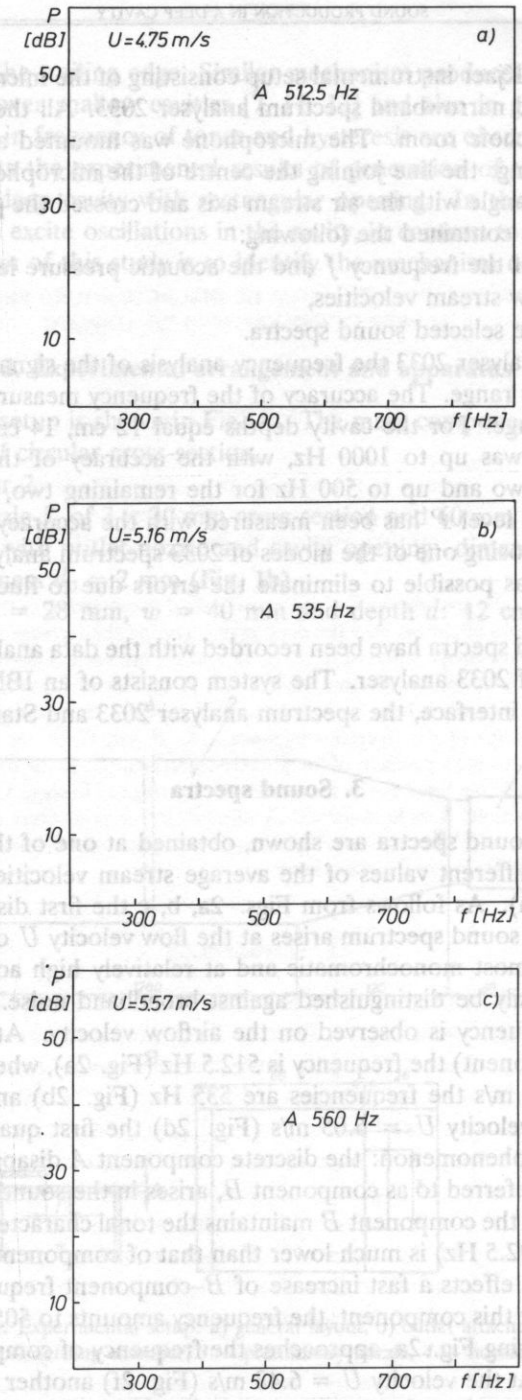

FIG. 2. Sound spectra at the flow velocities U: a) 4.75 m/s, b) 5.16 m/s, c) 5.57 m/s,

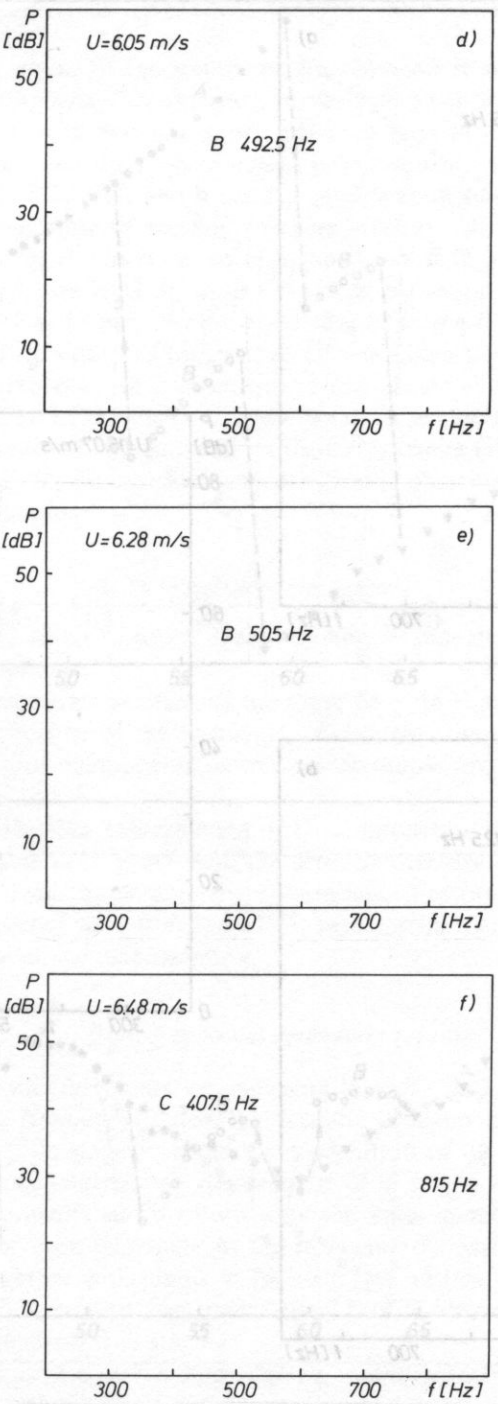

FIG. 2. Sound spectra at the flow velocities U: d) 6.05 m/s, e) 6.28 m/s, f) 6.48 m/s. Cavity depth $d = 12$ cm.

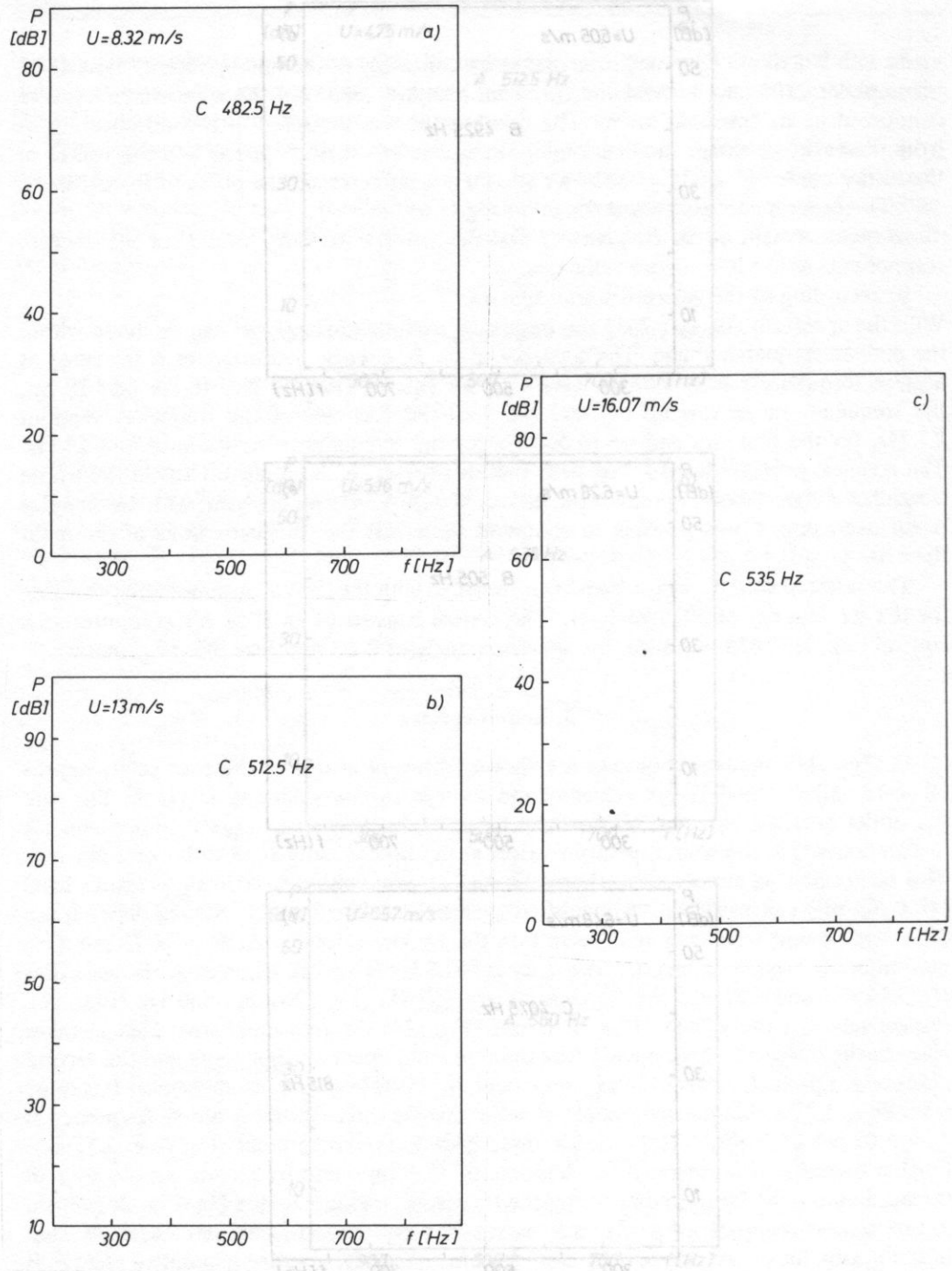

FIG. 3. Sound spectra at the flow velocities U: a) 8.32 m/s, b) 13 m/s, c) 16.07 m/s. Cavity depth d = 12 cm.

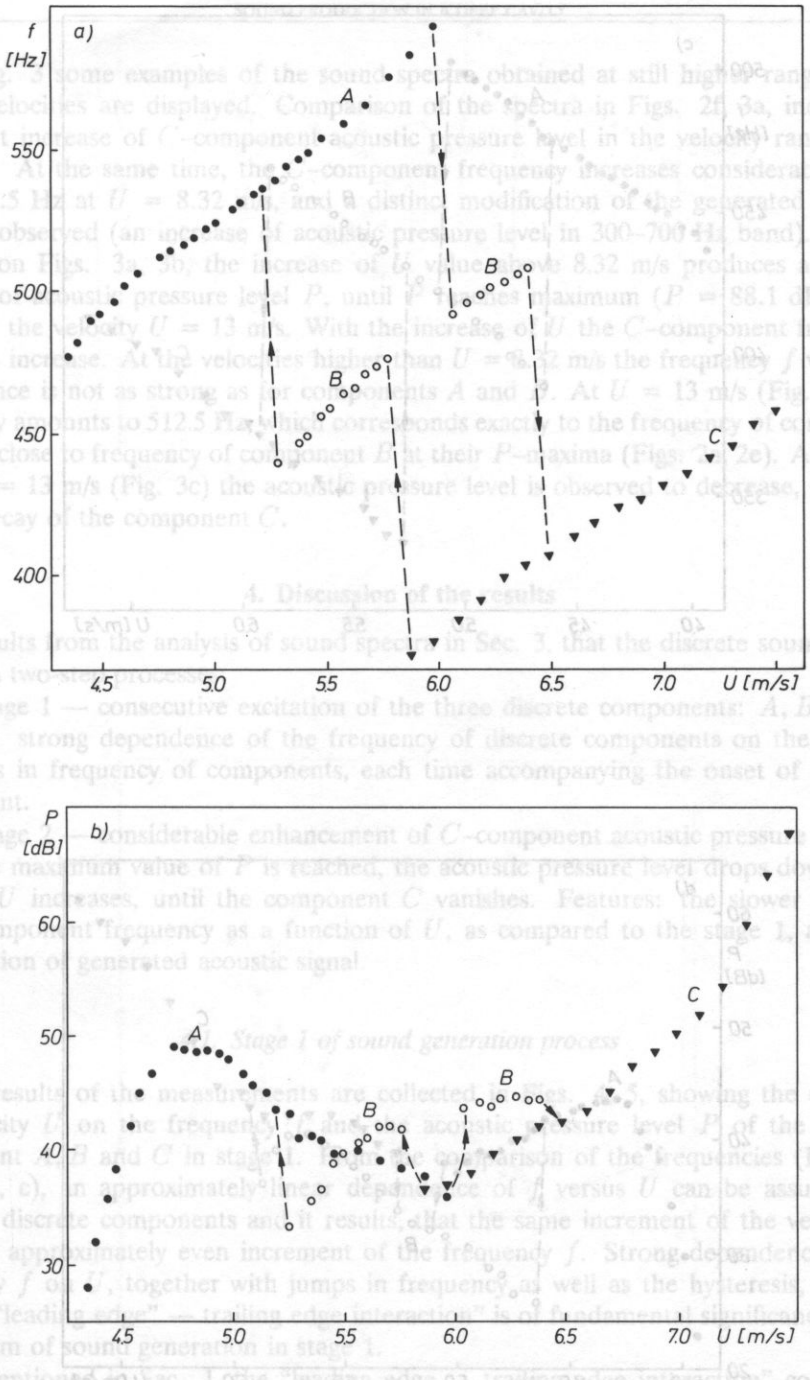

FIG. 4a,b. Frequency f and the acoustic pressure level P of the discrete components A, B and C in stage 1 of the sound generation process d = 12 cm.

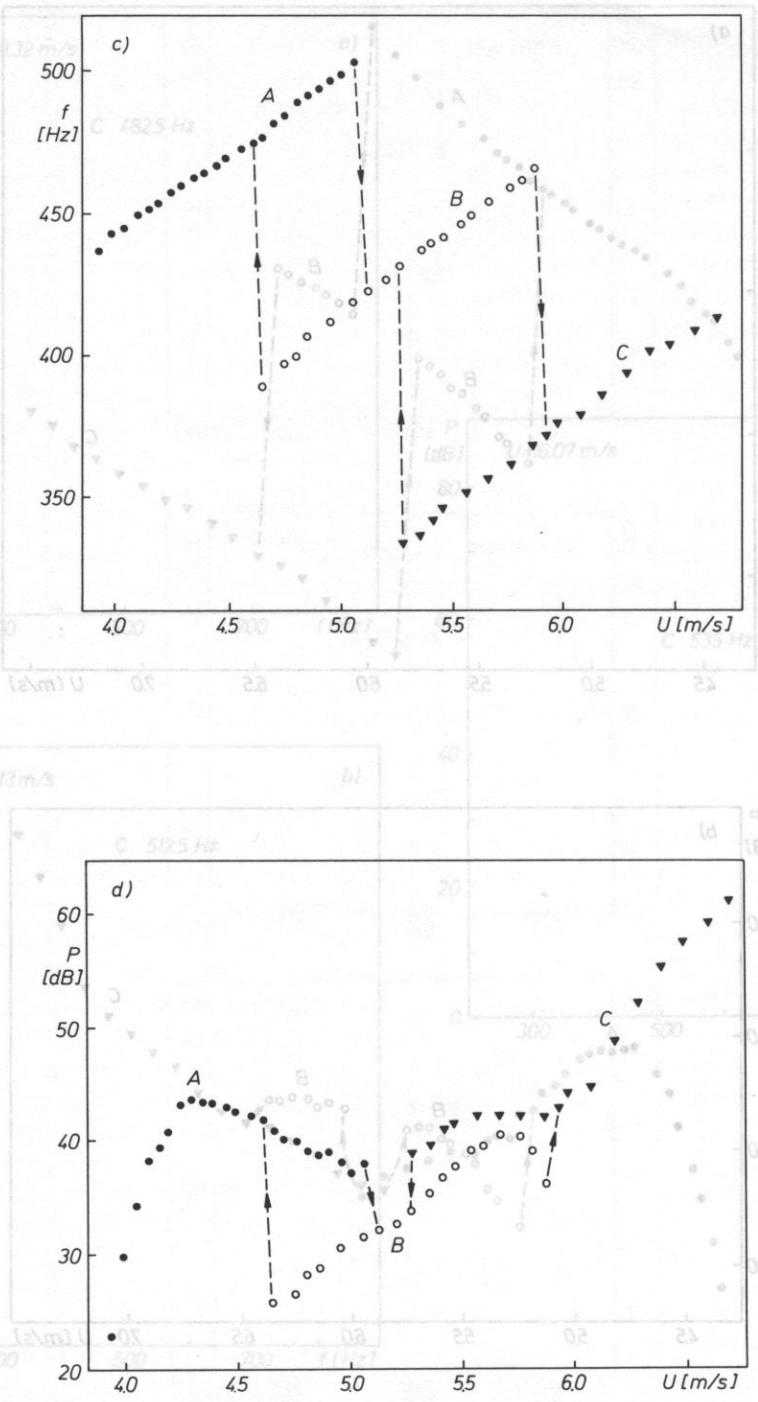

FIG. 4c,d. Frequency f and the acoustic pressure level P of the discrete components A, B and C in stage 1 of the sound generation process $d = 14$ cm.

In Fig. 3 some examples of the sound spectra obtained at still higher range of the airflow velocities are displayed. Comparison of the spectra in Figs. 2f, 3a, indicates a significant increase of C–component acoustic pressure level in the velocity range 6.48–8.32 m/s. At the same time, the C–component frequency increases considerably up to $f = 482.5$ Hz at $U = 8.32$ m/s, and a distinct modification of the generated acoustic signal is observed (an increase of acoustic pressure level in 300–700 Hz band). As can be seen on Figs. 3a, 3b, the increase of U value above 8.32 m/s produces a gradual increase of acoustic pressure level P, until P reaches maximum ($P = 88.1$ dB) which occurs at the velocity $U = 13$ m/s. With the increase of U the C–component frequency does also increase. At the velocities higher than $U = 8.32$ m/s the frequency f versus U dependence is not as strong as for components A and B. At $U = 13$ m/s (Fig. 3b) the frequency amounts to 512.5 Hz, which corresponds exactly to the frequency of component A and is close to frequency of component B at their P–maxima (Figs. 2a, 2e). Above the value $U = 13$ m/s (Fig. 3c) the acoustic pressure level is observed to decrease, followed by the decay of the component C.

4. Discussion of the results

It results from the analysis of sound spectra in Sec. 3, that the discrete sound generation is a two-step processes:

a) Stage 1 — consecutive excitation of the three discrete components: A, B and C. Features: strong dependence of the frequency of discrete components on the velocity U, jumps in frequency of components, each time accompanying the onset of the next component.

b) Stage 2 — considerable enhancement of C–component acoustic pressure level P. After the maximum value of P is reached, the acoustic pressure level drops down gradually as U increases, until the component C vanishes. Features: the slower increase of C–component frequency as a function of U, as compared to the stage 1, apparent modification of generated acoustic signal.

4.1. Stage 1 of sound generation process

The results of the measurements are collected in Figs. 4, 5, showing the effect of the velocity U on the frequency f and the acoustic pressure level P of the discrete component A, B and C in stage 1. From the comparison of the frequencies (Figs. 4a, c and 5a, c), an approximately linear dependence of f versus U can be assumed for all three discrete components and it results, that the same increment of the velocity U produces approximately even increment of the frequency f. Strong dependence of the frequency f on U, together with jumps in frequency as well as the hysteresis, indicate that the "leading edge" — trailing edge interaction" is of fundamental significance in the mechanism of sound generation in stage 1.

As mentioned in Sec. 1, the "leading edge — trailing edge interaction" constitutes one of two available mechanisms of the discrete sound generation by airflow over deep cavity. The main mechanism is based on the mutual interaction between shear layer disturbances and cavity-resonance modes (first-order flow-acoustic feedback). If in the process of sound generation, only this kind of feedback occurred, the frequency f of the

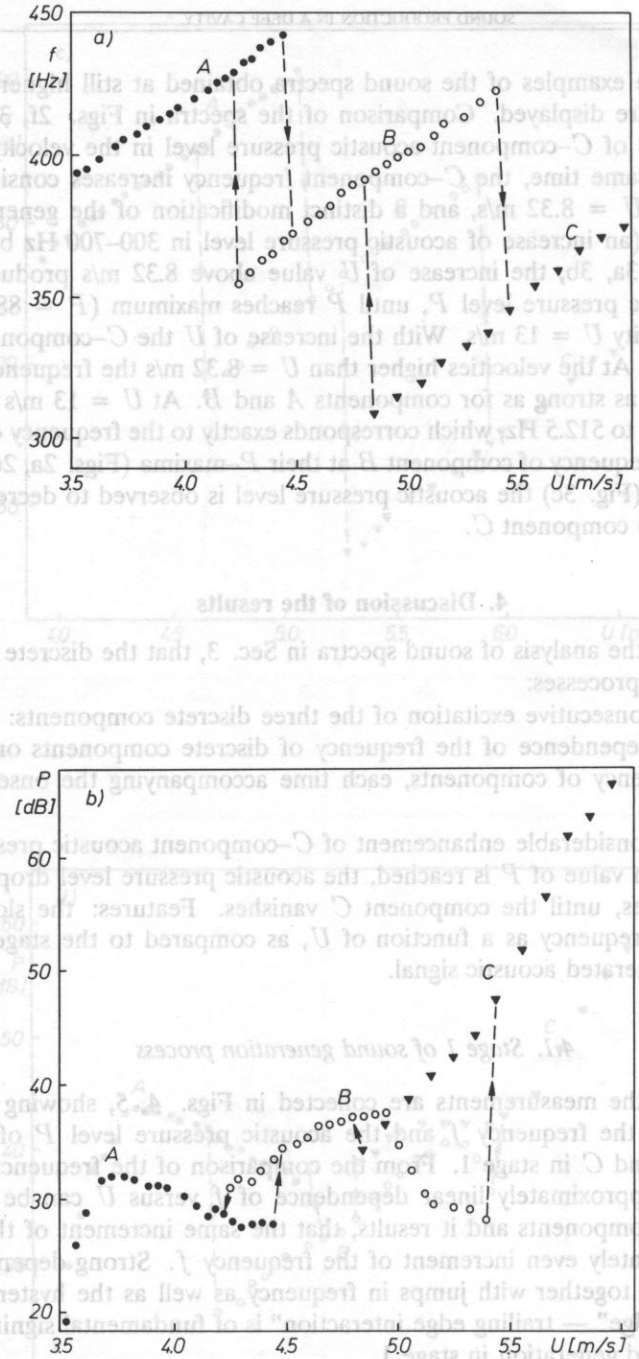

FIG. 5a,b. Frequency f and the acoustic pressure level P of the discrete components A, B and C in stage 1 of the sound generation process $d = 16$ cm.

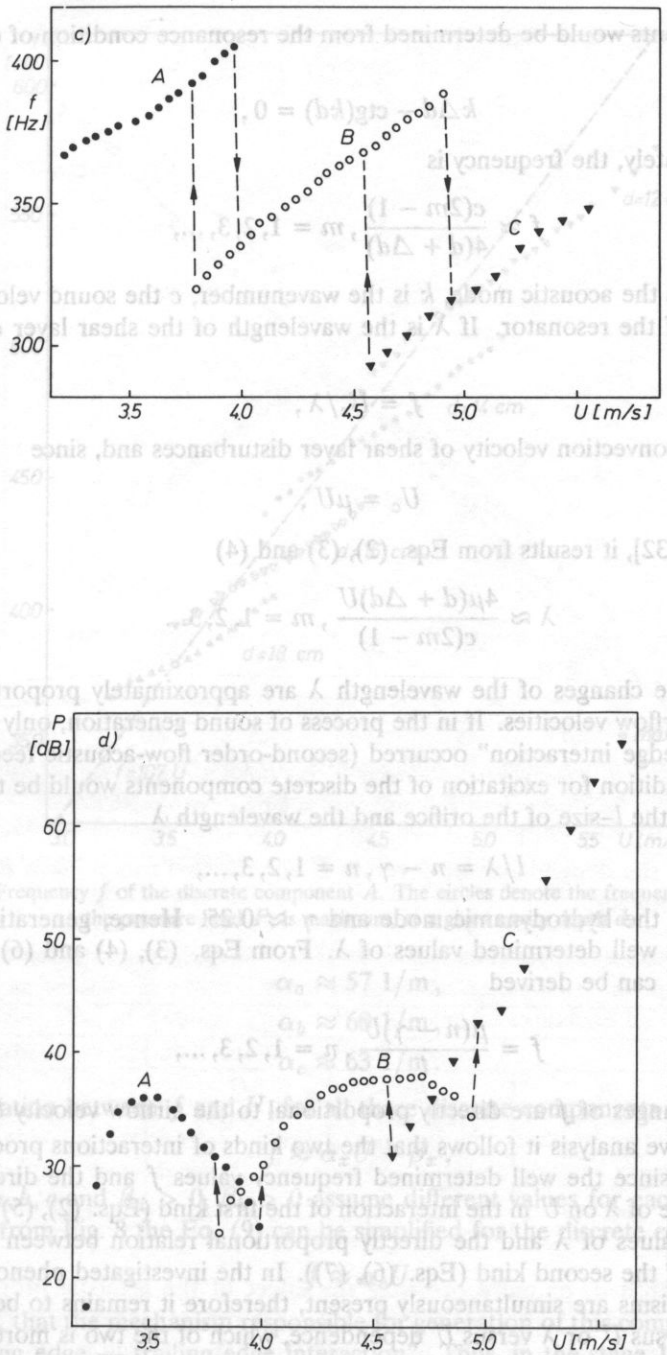

FIG. 5c,d. Frequency f and the acoustic pressure level P of the discrete components A, B and C in stage 1 of the sound generation process $d = 18$ cm.

discrete components would be determined from the resonance condition of quarter-wave resonator

$$k\Delta d - \operatorname{ctg}(kd) = 0\,, \tag{1}$$

hence, approximately, the frequency is

$$f \approx \frac{c(2m-1)}{4(d+\Delta d)}\,, m = 1,2,3,..., \tag{2}$$

where m denotes the acoustic mode, k is the wavenumber, c the sound velocity, Δd the end correction of the resonator. If λ is the wavelength of the shear layer disturbances, then

$$f = U_c/\lambda\,, \tag{3}$$

where U_c is the convection velocity of shear layer disturbances and, since

$$U_c = \mu U\,, \tag{4}$$

where $\mu \approx 0.62$ [32], it results from Eqs. (2), (3) and (4)

$$\lambda \approx \frac{4\mu(d+\Delta d)U}{c(2m-1)}\,, m = 1,2,3... \tag{5}$$

It means, that the changes of the wavelength λ are approximately proportional to the changes of the airflow velocities. If in the process of sound generation, only the "leading edge — trailing edge interaction" occurred (second-order flow-acoustic feedback), then the necessary condition for excitation of the discrete components would be the following relation between the l–size of the orifice and the wavelength λ

$$l/\lambda = n - \gamma\,, n = 1,2,3,..., \tag{6}$$

where n denotes the hydrodynamic mode and $\gamma \approx 0.25$. Hence, generation of sound can only occur at well determined values of λ. From Eqs. (3), (4) and (6) the relation between f and U can be derived

$$f = \frac{\mu(n-\gamma)U}{l}\,, n = 1,2,3,..., \tag{7}$$

therefore, the changes of f are directly proportional to the airflow velocity U.

From the above analysis it follows that the two kinds of interactions produce entirely opposite effects, since the well determined frequency values f and the directly proportional dependence of λ on U in the interaction of the first kind (Eqs. (2), (5)) correspond to the discrete values of λ and the directly proportional relation between f and U in the interaction of the second kind (Eqs. (6), (7)). In the investigated phenomenon both feedback mechanisms are simultaneously present, therefore it remains to be decided on the basis of f versus U or λ versus U dependence, which of the two is more important.

From the analysis of the data collected separately for the discrete component A, B and C (Figs. 6–8), conclusion can be reached that at each cavity depth d, the frequency f versus U dependence is similar. These dependencies can be characterized with $\Delta f/\Delta U$ ratios denoted α_a, α_b and α_c for the components A, B and C, respectively, amounting to

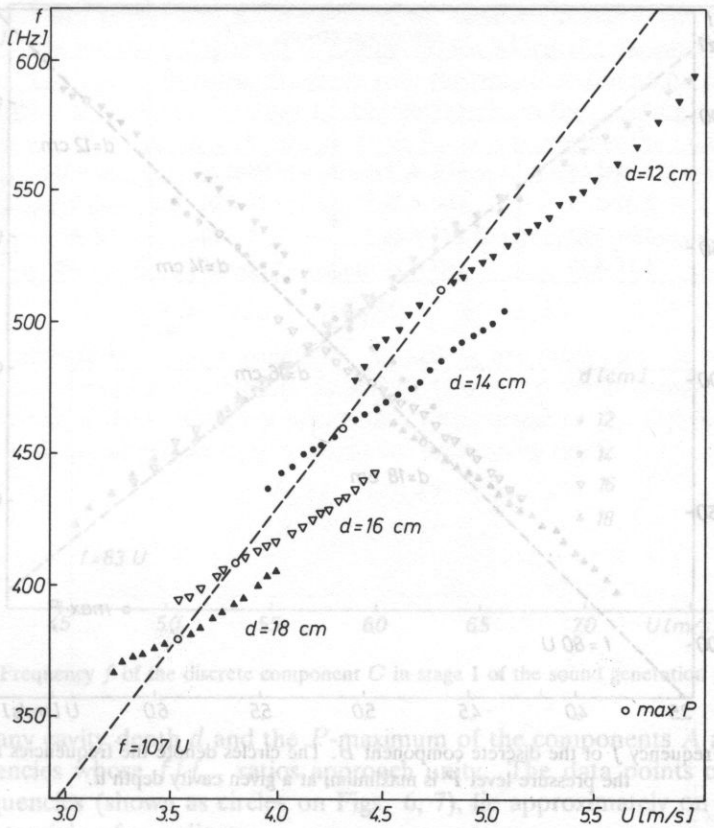

FIG. 6. Frequency f of the discrete component A. The circles denote the frequencies at which the pressure level P, is maximum, at a given cavity depth d.

$$\alpha_a \approx 57\ 1/\mathrm{m}, \quad \alpha_b \approx 60\ 1/\mathrm{m}, \quad \alpha_c \approx 63\ 1/\mathrm{m}. \tag{8}$$

Thus, the relation between f and U, for all three discrete components is

$$f \approx \alpha_x U + \beta_x, \tag{9}$$

where $x = a, b, c$ and $\beta_a > 0$, $\beta_b > 0$ assume different values for each cavity depth d. As it results from Fig. 8 the Eq. (9) can be simplified for the discrete component C

$$f \approx \alpha_c U \tag{10}$$

which means, that the mechanism responsible for generation of this component originates in the "leading edge — trailing edge interaction". Thus, in the stage 1, this component exhibits the character of the edgetone of the shear layer. Fast increase of f as a function of U, evident in the remaining two situations (Figs. 6, 7) shows that this kind of interaction is also of fundamental importance in producing the discrete components A and B. On the other hand, the fact that the values β_a and β_b in Eq. (9), are different from

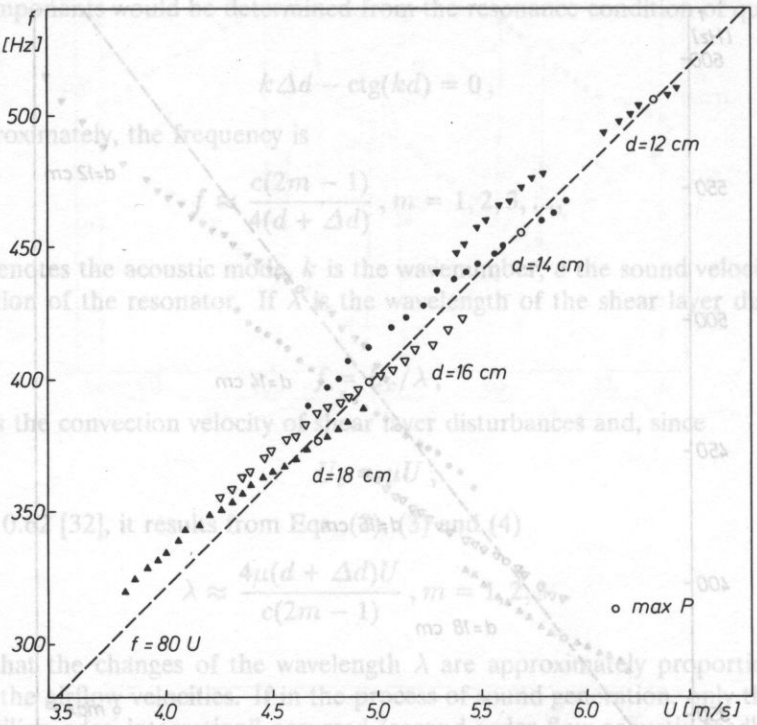

FIG. 7. Frequency f of the discrete component B. The circles denote the frequencies at which the pressure level P is maximum, at a given cavity depth d.

zero, means that the dependence of f versus U for the two components is modified by the first-order feedback.

Table 1. Frequencies ratios f/f_{res} of the discrete components A, B and C during stage 1 of the sound generation process

d [cm]	f/f_{res}				
	range			maximum P	
	A	B	C	A	B
12	0.93–1.16	0.86–1.00	0.73–0.90	1.000	0.985
14	0.96–1.10	0.85–1.02	0.73–0.91	1.005	0.995
16	0.98–1.10	0.88–1.05	0.77–0.93	1.012	0.991
18	0.97–1.07	0.85–1.03	0.76–0.92	1.003	0.997

The cavity depth d, or more precisely the effect of the acoustic properties of the resonator on the sound generation process, results in different frequency ranges at each value of d, as it can be seen in Figs. 6–8. Table 1 lists the limiting values of f/f_{res} ratio and the values of f/f_{res} corresponding to the maxima of acoustic pressure level P of the components A and B. The frequency f_{res} is that one at which the acoustic pressure level P of the component C, reaches the maximum value at a given cavity depth (Table 3). From these results it is evident that the range of f/f_{res} variations of each discrete component

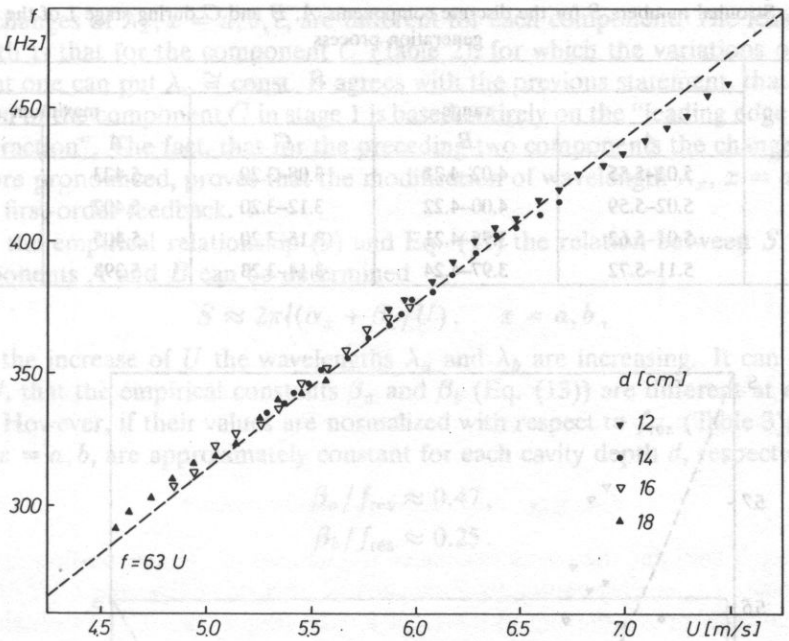

FIG. 8. Frequency f of the discrete component C in stage 1 of the sound generation process.

is similar at any cavity depth d and the P-maximum of the components A and B occurs at the frequencies whose f/f_{res} ratios approach unity. The data points corresponding to these frequencies (shown as circles on Figs. 6, 7), lie approximately on straight lines intersecting at origin of coordinates.

The effect of the acoustic properties of the resonator on the process of sound generation consists in the different, for each value of d, range of velocities U, in which a given discrete components occurs (Figs. 6–8). There is a correlation between the d and U variations, since the velocity at which a given component appears or vanishes, is observed to rise, with the decrease of d value. This correlation can be explained by the data collected in Table 2, where S is Strouhal number defined below

$$S = 2\pi f l/U\,. \tag{11}$$

One notices, that the range of S values, associated with each component, is practically independent of the cavity depth d. This rule has a simple physical meaning. Since, from Eqs. (3), (4) and (11)

$$\lambda = 2\pi\mu l/S\,, \tag{12}$$

therefore:

a) different wavelengths λ_a, λ_b and λ_c correspond to the three discrete components A, B and C,

b) $\lambda_a < \lambda_b < \lambda_c$,

c) quantity $\lambda_x, x = a, b, c$ assumes values within a precisely defined range.

Moreover, as it results from data in Table 2, $\lambda_a \cong$ const and $\lambda_b \cong$ const in the case of maximum P. Various sets of S values corresponding to each discrete component imply

Table 2. Strouhal numbers S for the discrete components A, B and C during stage 1 of the sound generation process

d [cm]	S				
	range			maximum P	
	A	B	C	A	B
12	5.01–5.55	4.02–4.21	3.08–3.20	5.423	4.042
14	5.02–5.59	4.00–4.22	3.12–3.20	5.402	4.034
16	5.01–5.62	3.95–4.21	3.15–3.20	5.405	4.049
18	5.11–5.72	3.97–4.24	3.14–3.23	5.393	4.025

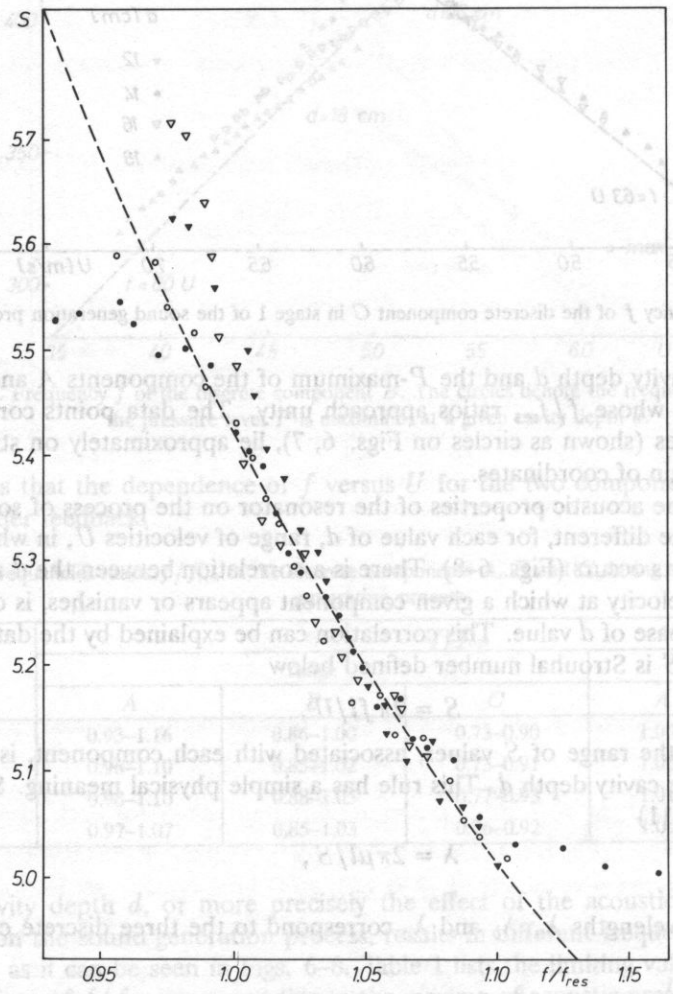

FIG. 9. The dependence of Strouhal number S on the f/f_{res} frequency ratio for the discrete component A: (●) d = 12 cm, (○) d = 14 cm, (▼) d = 16 cm, (▽) d = 18 cm, (- - -) S-values calculated from Eq. (16).

that the changes of $\lambda_x, x = a, b, c$, are different for each component. The least modified wavelength is that for the component C (Table 2), for which the variations of S are so small, that one can put $\lambda_c \cong$ const. It agrees with the previous statement, that the sound generation of the component C in stage 1 is based entirely on the "leading edge — trailing edge interaction". The fact, that for the preceding two components the changes of S are much more pronounced, proves that the modification of wavelength λ_x, $x = a, b$, results from the first-order feedback.

From the empirical relationship (9) and Eq. (11) the relation between S and U for the components A and B can be determined

$$S \approx 2\pi l(\alpha_x + \beta_x/U), \quad x = a, b, \tag{13}$$

i.e. with the increase of U the wavelengths λ_a and λ_b are increasing. It can be seen in Figs. 6, 7, that the empirical constants β_a and β_b (Eq. (13)) are different at each cavity depth d. However, if their values are normalized with respect to f_{res} (Table 3), the ratios $\beta_x/f_{\text{res}}, x = a, b$, are approximately constant for each cavity depth d, respectively

$$\begin{aligned} \beta_a/f_{\text{res}} &\approx 0.47, \\ \beta_b/f_{\text{res}} &\approx 0.25. \end{aligned} \tag{14}$$

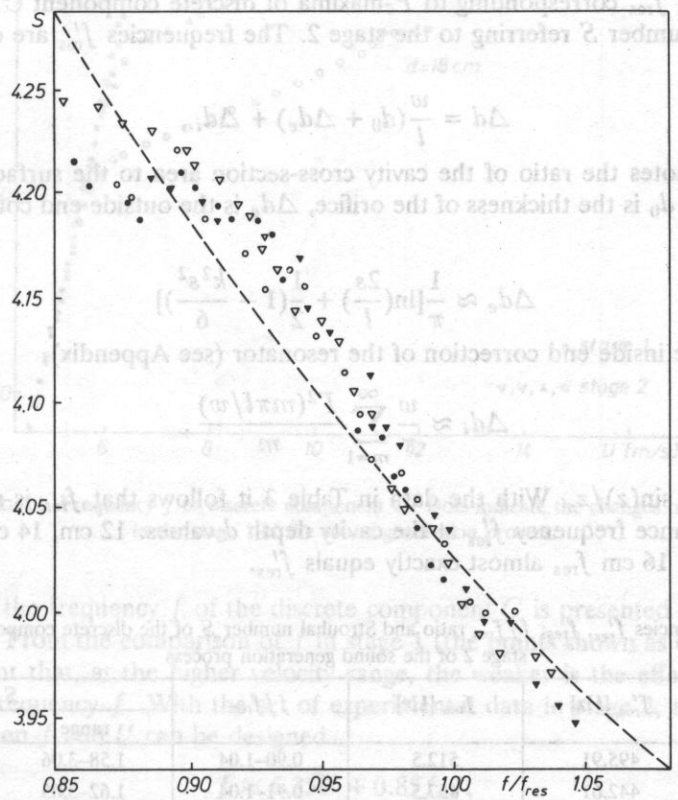

FIG. 10. The dependence of Strouhal number S on the frequency ratio f/f_{res} for the discrete component B: (•) d = 12 cm, (○) d = 14 cm, (▼) d = 16 cm, (▽) d = 18 cm, (- - -) S-values calculated from Eq. (17).

Equation (13) can be given in the alternative form

$$S \approx \frac{2\pi l \alpha_x}{1 - \beta_x / f}, \quad x = a, b, \tag{15}$$

hence, using Eqs. (8) and (14) one arrives at the expression for the component A

$$S \approx \frac{2.87}{f/f_{\text{res}} - 0.47}(f/f_{\text{res}}) \tag{16}$$

and

$$S \approx \frac{3.02}{f/f_{\text{res}} - 0.25}(f/f_{\text{res}}) \tag{17}$$

for the component B. It is evident from Figs. 9, 10 that S values calculated by the above two, equations agree with the experimental data.

4.2. Stage 2 of sound generation process

The Table 3 contains the cavity resonance frequencies f'_{res} under no-flow conditions, the frequencies f_{res} corresponding to P-maxima of discrete component C, f/f_{res} ratios and Strouhal number S referring to the stage 2. The frequencies f'_{res} are obtained from Eq. (1) with

$$\Delta d = \frac{w}{l}(d_0 + \Delta d_e) + \Delta d_i, \tag{18}$$

where w/l denotes the ratio of the cavity cross-section area to the surface area of the cavity opening, d_0 is the thickness of the orifice, Δd_e is the outside end correction of the resonator [22]

$$\Delta d_e \approx \frac{1}{\pi}[\ln(\frac{2s}{l}) + \frac{1}{2}(1 - \frac{k^2 s^2}{6})] \tag{19}$$

and Δd_i — the inside end correction of the resonator (see Appendix)

$$\Delta d_i \approx \frac{w}{\pi} \sum_{m=1}^{\infty} \frac{\Gamma^2(m\pi l/w)}{m}, \tag{20}$$

where $\Gamma(z) = \sin(z)/z$. With the data in Table 3 it follows that f_{res} is slightly higher than the resonance frequency f'_{res} at the cavity depth d values: 12 cm, 14 cm and 18 cm, whereas at $d = 16$ cm f_{res} almost exactly equals f'_{res}.

Table 3. Frequencies f'_{res}, f_{res}; f/f_{res} ratio and Strouhal number S of the discrete component C during stage 2 of the sound generation process

d [cm]	f'_{res} [Hz]	f_{res} [Hz]	f/f_{res}	S	
				range	max P
12	495.91	512.5	0.90–1.04	1.58–3.06	1.980
14	442.61	457.5	0.91–1.04	1.62–3.05	2.021
16	400.03	402.5	0.94–1.07	1.66–3.12	2.214
18	365.15	377.5	0.93–1.04	1.64–3.11	1.989

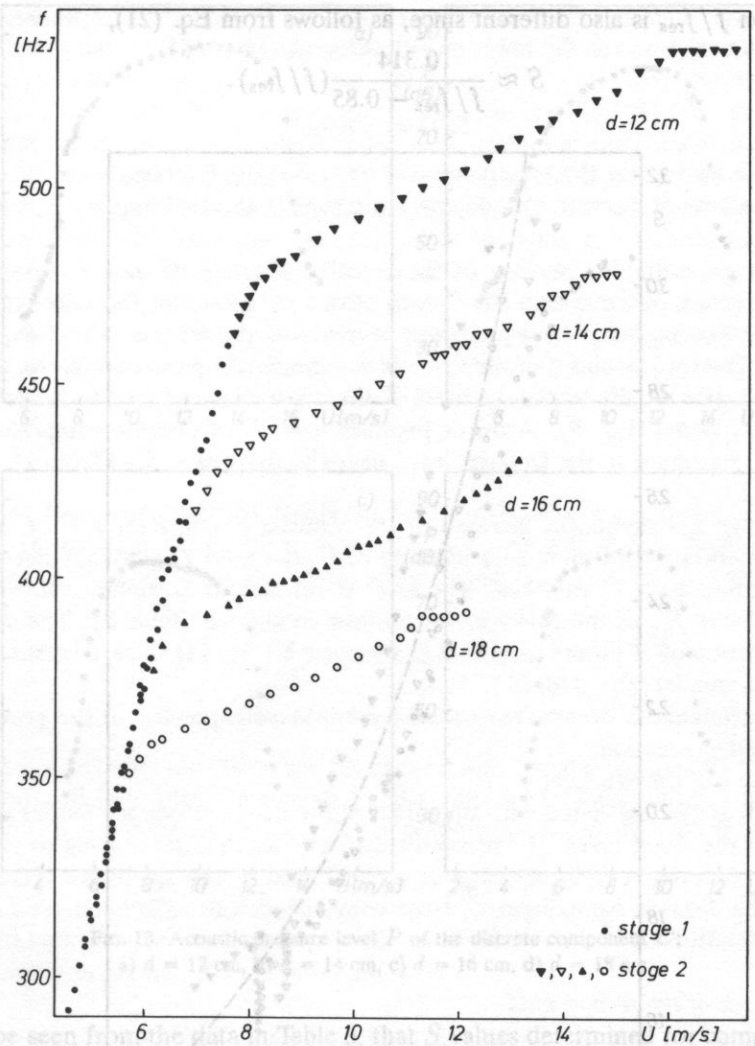

FIG. 11. Frequency f of discrete component C. Dots indicate the changes of f in the stage 1 of the sound generation process.

In Fig. 11 the frequency f of the discrete component C is presented as the function of velocity U. From the comparison of f in stage 1 (the points shown as dots) and stage 2 it is apparent that, at the higher velocity range, the weaker is the effect of the value of U on the frequency f. With the set of experimental data in stage 2, an approximate relation between f and U can be designed

$$f \approx 6.25U + 0.85 f_{\text{res}}, \tag{21}$$

Thus, the increase of f versus U is nearly ten times smaller than that in stage 1. Consequently, the range of f/f_{res} ratios is much smaller (Table 3). The dependence of Strouhal

number S on f/f_{res} is also different since, as follows from Eq. (21),

$$S \approx \frac{0.314}{f/f_{res} - 0.85}(f/f_{res}) . \tag{22}$$

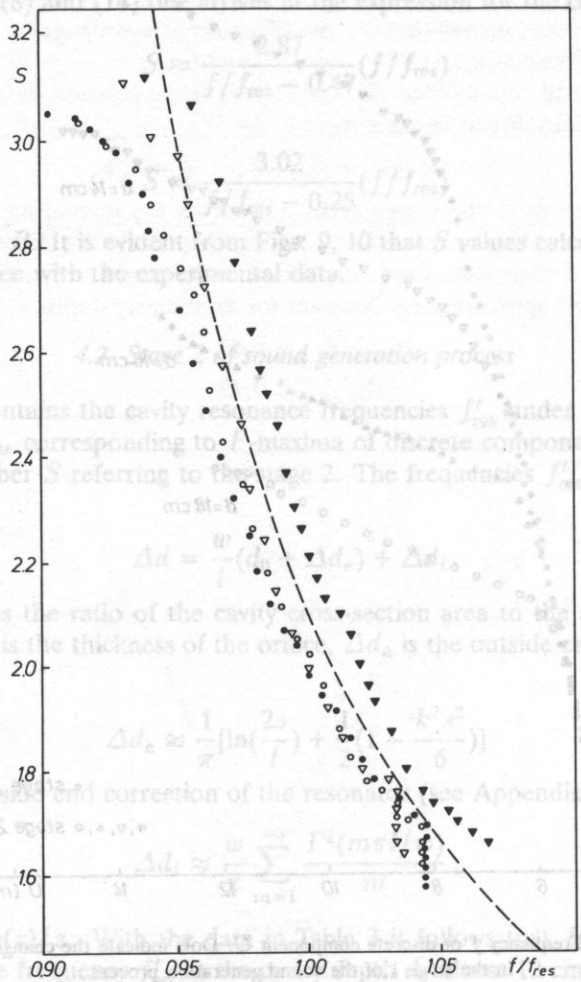

FIG. 12. The dependence of Strouhal number S on the frequency ratio f/f_{res} for the discrete component C in the stage 2 of the sound generation process: (•) d = 12 cm, (○) d = 14 cm, (▼) d = 16 cm, (▽) d = 18 cm, (- - -) S-values calculated from Eq. (22).

It results from the data in Table 3, that S range is very similar at all four values of the cavity depth d, thus the changes of λ_c are roughly independent of d. The fact that this range is much larger than that observed for the discrete components in stage 1 (Table 2), indicates that there is significant increase of λ_c value occurring at the higher stream velocities. According to our earlier conclusions, it proves a dominant role of the first-order feedback in stage 2.

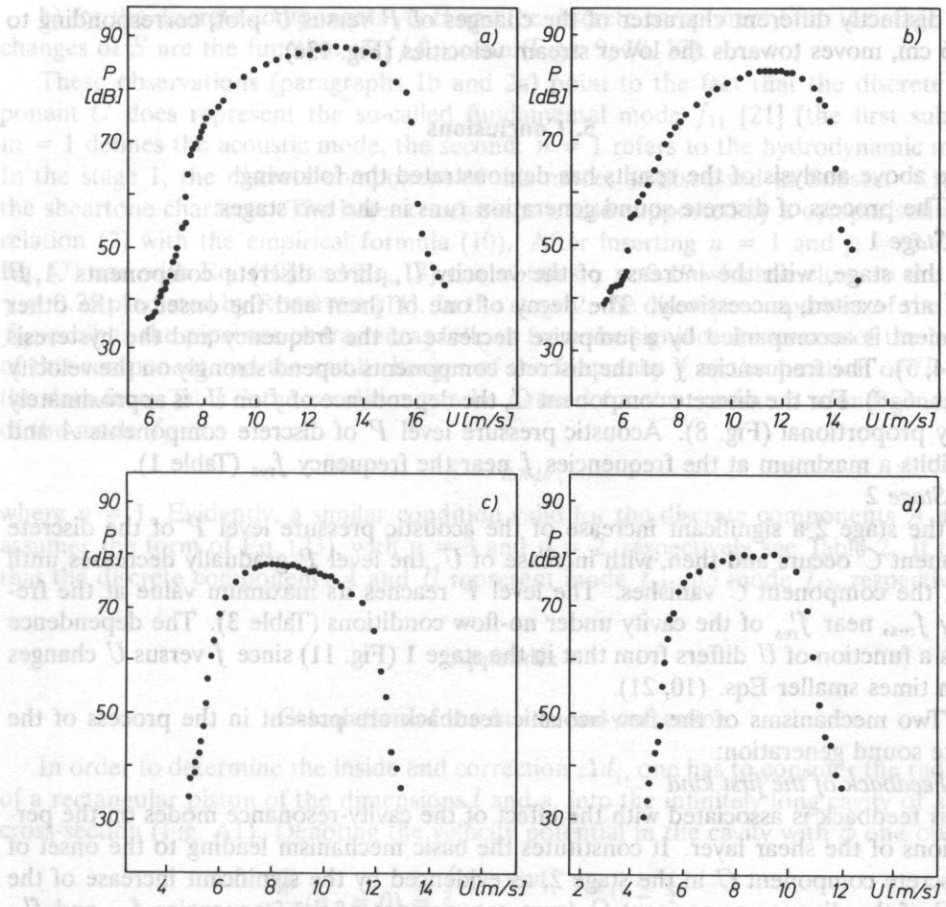

FIG. 13. Acoustic pressure level P of the discrete component C:
a) $d = 12$ cm, b) $d = 14$ cm, c) $d = 16$ cm, d) $d = 18$ cm.

It can be seen from the data in Table 3, that S values determined for component C at the maximum of P are observed to converge only at the cavity depth d equal 12 cm, 14 cm and 18 cm. Evidently larger value of S for the maximum of P ($S = 2.214$) and somewhat different range of f/f_{res} ratio observed for the cavity depth $d = 16$ cm, indicate that the measurement of the frequency f_{res} based on variation of P for the component C, may be in error. The extent to which this error affects the results of the measurement, can be seen in Fig. 12, where Strouhal number S has been plotted as a function of f/f_{res} ratio in stage 2. Large differences can be seen between the S values determined at the same f/f_{res} ratio, for the cavity depth $d = 16$ cm and for the remaining three values of d.

The error in the measurement of the frequency f_{res} is not due to a lack of precision of the method. For the cavity depth $d = 16$ cm the frequency and the acoustic pressure level can be measured accurately to 1.25 Hz and 0.1 dB, respectively (Sec. 2). On the other hand, the errors resulting from a main flow fluctuations, are eliminated by the averaging of spectra. The cause of the inaccuracy in the determination of f_{res} for $d = 16$ cm lies

in the distinctly different character of the changes of P versus U plot, corresponding to $d = 16$ cm, moves towards the lower stream velocities (Fig. 13c).

5. Conclusions

The above analysis of the results has demonstrated the following:

1) The process of discrete sound generation runs in the two stages:

a) *Stage* 1

In this stage, with the increase of the velocity U, three discrete components A, B and C are excited, successively. The decay of one of them and the onset of the other component is accompanied by a jumpwise decrease of the frequency and the hysteresis (Figs. 4, 5). The frequencies f of the discrete components depend strongly on the velocity U (Figs. 6–8). For the discrete component C, the dependence of f on U, is approximately directly proportional (Fig. 8). Acoustic pressure level P of discrete components A and B exhibits a maximum at the frequencies f near the frequency f_{res} (Table 1).

b) *Stage* 2

In the stage 2 a significant increase of the acoustic pressure level P of the discrete component C occurs and then, with increase of U, the level P gradually decreases until finally, the component C vanishes. The level P reaches its maximum value at the frequency f_{res}, near f'_{res} of the cavity under no-flow conditions (Table 3). The dependence of f as a function of U differs from that in the stage 1 (Fig. 11) since f versus U changes are ten times smaller Eqs. (10, 21).

2) Two mechanisms of the flow-acoustic feedback are present in the process of the discrete sound generation:

a) *Feedback of the first kind*

This feedback is associated with the effect of the cavity-resonance modes on the perturbations of the shear layer. It constitutes the basic mechanism leading to the onset of the discrete component C in the stage 2, as evidenced by the significant increase of the level P of the discrete component C, large convergence of the frequencies f_{res} and f'_{res} and the small influence of the velocity U on the frequency f of the generated sound (Figs. 11, 13).

b) *Feedback of the second kind*

This feedback is associated with the "leading edge — trailing edge interaction", i.e. the effect of the acoustic perturbations, occurring at the leading edge of the cavity orifice, on the shear layer disturbances at the trailing edge. This kind of coupling is decisive in the generation of the discrete components A and B as well as the discrete component C in the stage 1. It has been evidenced by the strong dependence of the frequency f on the velocity U, the jumpwise changes of f occurring at the excitation of successive discrete components and by hysteresis (Figs. 4, 5).

3) Three different wavelengths: $\lambda_a < \lambda_b < \lambda_c$ refer to the discrete components A, B and C, correspondingly. The range of λ_x values, with $x = a, b, c$ is strinctly defined, as evidenced from the similar ranges of Strouhal number S, obtained for each component at the various depths d of cavity (Tables 2, 3).

4) The modification of the wavelength $\lambda_x, x = a, b, c$, is the result of the feedback of the first kind. This conclusion is supported by the following observations:

a) the largest range of S values occurs in the stage 2 (Table 3),

b) for the discrete components A, B and the discrete component C in the stage 2, the changes of S are the function of f/f_{res} ratio (Figs. 9, 10, 12).

These observations (paragraphs 1b and 2a) point to the fact that the discrete component C does represent the so-called fundamental mode f_{11} [21] (the first subscript $m = 1$ defines the acoustic mode, the second: $n = 1$ refers to the hydrodynamic mode). In the stage 1, the discrete component of this mode, as discussed in Subsec. 4.1, is of the sheartone character. The latter conclusions is also supported by a comparison of the relation (7) with the empirical formula (10). After inserting $n = 1$ and $\mu = 0.62$ into Eq. (7) and with Eq. (10) and Eq. (8) one obtains $\gamma = 0.19$ which is close to the value $\gamma = 0.25$ predicted by ROSSITER [11]. In the stage 2, the discrete component of the mode f_{11}, exhibits the pipetone character, as follows from the significant increase of the level P of this component and the small changes of the frequency f as the function of U. With the data from Table 3 the condition can be defined for the maximum sound generation of the mode f_{11}

$$S = n\pi\mu\,, \tag{23}$$

where $n = 1$. Evidently, a similar condition valid for the discrete components A and B assumes the form of Eq. (23), with $n = 3$ and $n = 2$, respectively see Table 2. It means that the discrete components A and B represent mode f_{13} and mode f_{12}, respectively.

Appendix

Calculation of the inside end correction

In order to determine the inside end correction Δd_i, one has to consider the radiation of a rectangular piston of the dimensions l and s, into the infinitely long cavity of s by w cross-section (Fig. A1). Denoting the velocity potential in the cavity with ϕ one obtain

$$\frac{\partial\phi}{\partial x_2}(x_2 = 0) = \begin{cases} Ve^{-j\omega t}, & |x_1| \leq \frac{l}{2}, \\ 0, & \frac{l}{2} < |x_1| \leq \frac{w}{2}. \end{cases} \tag{A1}$$

From the condition A1 and Fig. A1 it results, that

$$\phi = Ve^{-j\omega t} \int_{-\frac{s}{2}}^{\frac{s}{2}} \int_{-\frac{l}{2}}^{\frac{l}{2}} G(\overline{x}, \overline{y}) dy_1 dy_3\,, \tag{A2}$$

where $\overline{x} = (x_1, x_2, x_3)$, $\overline{y} = (y_1, 0, y_3)$ and Green's function G is the solution of the following equation

$$\nabla^2 G + k^2 G = -\delta(x_1 - y_1)\delta(x_2)\delta(x_3 - y_3)\,, \tag{A3}$$

and fulfills the boundary conditions

$$\frac{\partial G}{\partial x_1}\left(x_1 = -\frac{w}{2}\right) = \frac{\partial G}{\partial x_1}\left(x_1 = \frac{w}{2}\right) = 0\,, \tag{A4}$$

$$\frac{\partial G}{\partial x_3}\left(x_3 = -\frac{s}{2}\right) = \frac{\partial G}{\partial x_3}\left(x_3 = \frac{s}{2}\right) = 0\,. \tag{A5}$$

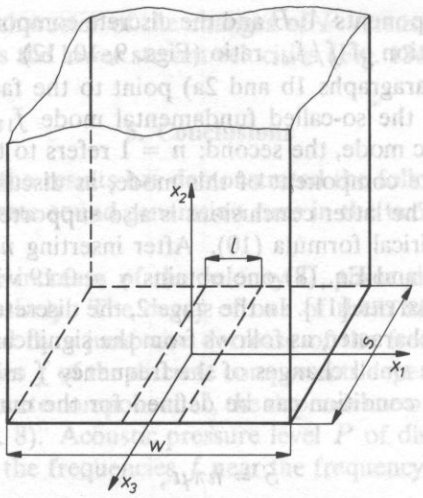

FIG. A1. Rectangular piston dimension l and s situated in the infinitely long channel wall and cross-section s by w.

Finally, the solution to Eq. (A3), under the boundary conditions (A1), (A4) and (A5), is the function G

$$G(\overline{x},\overline{y}) = \frac{j}{sw}\sum_{m=0}^{\infty}\sum_{n=0}^{\infty}\frac{\epsilon_m\epsilon_n\psi_{mn}(x_1,x_3)\psi_{mn}(y_1,y_3)}{k_{mn}}e^{jk_{mn}x_2}, \tag{A6}$$

where ϵ_m and ϵ_n is Neumann factor

$$\psi_{mn}(z_1,z_3) = \cos(2m\pi z_1/w)\cos(2n\pi z_3/s),$$
$$k_{mn} = [k^2 - (2m\pi/w)^2 - (2n\pi/s)^2]^{1/2}.$$

The reactive force of the medium due to vibrations of the piston in the cavity opening can be determined from the formula

$$F = |F|e^{-j\omega t} = -\int_{-\frac{s}{2}}^{\frac{s}{2}}\int_{-\frac{l}{2}}^{\frac{l}{2}} p(x_2 = 0)dx_1dx_3, \tag{A7}$$

where $p(x_2 = 0)$ is the pressure acting upon the piston

$$p(x_2 = 0) = j\omega\varrho\phi(x_2 = 0), \tag{A8}$$

hence, after substituting (A8) in (A7), using (A2) and (A6) and integrating, one obtains

$$|F| = l^2s^2V\left[\frac{\varrho c}{sw} + \frac{2\varrho\omega}{sw}\sum_{m=1}^{\infty}\frac{\Gamma^2(m\pi l/w)}{k_m}\right], \tag{A9}$$

where $\Gamma(z) = \dfrac{\sin(z)}{z}$ and $k_m = [k^2 - (2m\pi/w)]^{1/2}$. In the case of the frequency ω much lower than the higher modes frequencies of the cavity

$$k_m \approx 2jm\pi/w, \tag{A10}$$

therefore, from (A9)

$$\frac{|F|}{l^2 s^2 V} \approx \frac{\varrho c}{sw} - \frac{j\varrho\omega}{sw}\left[\frac{w}{\pi}\sum_{m=1}^{\infty}\frac{\Gamma^2(m\pi l/w)}{m}\right]. \tag{A11}$$

The first term of the right hand side of the Eq. (A1) is the wave impedance of the cavity (plane wave impedance), whereas the second term represents the impedance of the acoustic inertance M of the co-vibrating medium

$$M = \frac{\varrho}{sw}\Delta d_i\,, \tag{A12}$$

thus

$$\Delta d_i \approx \frac{w}{\pi}\sum_{m=1}^{\infty}\frac{\Gamma^2(m\pi l/w)}{m}\,. \tag{A13}$$

References

[1] L. Cremer, H. Ising, *Die selbsterregten Schwingungen von Orgelpfeifen*, Acustica, **19**, 143–153 (1967/68).

[2] J. W. Coltman, *Sounding mechanism of sound production in organ pipes*, J. Acoust. Soc. Am. **44**, 983–992 (1968).

[3] N. H. Fletcher, *Sound production by organ flue pipes*, J. Acoust. Soc. Am. **60**, 4, 926–936 (1976).

[4] J. L. King, P. Boyle, J. B. Ogle, *Instability in slotted wall tunnels*, J. Fluid Mech. **4**, 283–305 (1958).

[5] G. F. McCanless, J. R. Boone, *Noise reduction in transonic wind tunnels*, J. Acoust. Soc. Am. **56**, 5, 1501–1510 (1974).

[6] J. C. Bruggeman, *Flow induced pulsations in pipe systems*, Ph.D. thesis, Eindhoven, 1987.

[7] C. K. Tam, P. J. Block, *On the tones and pressure oscillations induced by flow over rectangular cavities*, J. Fluid Mech. **89**, 373–399 (1978).

[8] W. L. Hankey, J. S. Shang, *Analyses of pressure oscillations in an open cavity*, AIAA J. **18**, 8, 892–898 (1980).

[9] D. Rockwell, E. Naudascher, *Review — self-sustaining oscillations of flow past cavities*, J. Fluids Engineering, Trans. ASME **100**, 152–165 (1978).

[10] D. Rockwell, *Oscillations of impinging shear layers*, AIAA J. **21**, 5, 645–664 (1983).

[11] J. E. Rossiter, *Wind tunnel experiments on the flow over rectangular cavities at subsonic and transonic speeds*, RAE Report No. 64037 (1964).

[12] H. H. Heller, D. G. Holmes, E. E. Covert, *Flow-induced pressure oscillations in shallow cavities*, J. Sound Vib. **18**, 4, 545–553 (1971).

[13] A. J. Bilanin, E. E. Covert, *Estimation of possible excitation frequencies for shallow rectangular cavities*, AIAA J. **11**, 3, 347–351 (1973).

[14] V. Sarohia, *Experimental investigation of oscillations in flow over shallow cavities*, AIAA J. **15**, 7, 984–991 (1977).

[15] L. F. East, *Aerodynamically induced resonance in rectangular cavities*, J. Sound Vib. **3**, 3, 277–287 (1966).

[16] E. E. Covert, *An approximate calculation of the onset velocity of cavity oscillations*, AIAA J. **8**, 12, 2189–2194 (1970).

[17] S. A. Elder, *Self-excited depth-mode resonance for wall-mounted cavity in turbulent flow*, J. Acoust. Soc. Am. **64**, 3, 877–890 (1978).

[18] S. A. Elder, *Forced oscillations of separated shear layer with application to cavity flow-tone effects*, J. Acoust. Soc. Am. **67**, 3, 774–781 (1980).

[19] M. L. Pollack, *Flow-induced tones in side-branch pipe resonators*, J. Acoust. Soc. Am. **67**, 4, 1153–1156 (1980).

[20] M. S. Howe, *The influence of mean shear on unsteady aperture flow, with application to acoustical diffraction and self-sustained oscillations*, J. Fluid Mech. **109**, 125–146 (1981).

[21] S. A. ELDER, T. M. FARABEE, F. C. DEMETZ, *Mechanisms of flow-excited tones at low Mach number*, J. Acoust. Soc. Am. **72**, 2, 532–549 (1982).
[22] M. MEISSNER, *Self-sustained deep cavity oscillations induced by grazing flow*, Acustica, **62**, 3, 220–228 (1987).
[23] R. L. PANTON, J. M. MILLER, *Excitation of a Helmholtz resonator by turbulent boundary layer*, J. Acoust. Soc. Am. **58**, 4, 800–806 (1975).
[24] J. S. ANDERSON, *The effect of an air flow on a single side branch Helmholtz resonator in a circular duct*, J. Sound Vib. **52**, 3, 423–431 (1977).
[25] P. A. NELSON, N. A. HALLIWELL, P. E. DOAK, *Fluid dynamics of a flow excited resonance, Part* I: *Experiment*, J. Sound Vib. **78**, 1, 15–38 (1981).
[26] P. A. NELSON, N. A. HALLIWELL, P. E. DOAK, *Fluid dynamics of a flow excited resonance, Part* II: *Flow acoustic interaction*, J. Sound Vib. **91**, 3, 375–402 (1983).
[27] M. MÖSER, *Aktive Kontrolle einfacher, selbsterregter Resonatoren*, Acustica, **69**, 4, 175–184 (1989).
[28] F. C. DEMETZ, T. M. FARABEE, *Laminar and turbulent shear flow induced resonances*, AIAA paper 77–1293 (1977).
[29] A. POWELL, *On the edgetone*, J. Acoust. Soc. Am. **33**, 4, 395–409 (1961).
[30] D. K. HOLGER, T. A. WILSON, G. S. BEAVERS, *Fluid dynamics of the edgetone*, J. Acoust. Soc. Am. **62**, 5, 1116–1128 (1977).
[31] S. OHRING, *Calculation of self-excited impinging jet flow*, J. Fluid Mech. **163**, 69–98 (1986).
[32] M. E. GOLDSTEIN, *Aeroacoustics*, Mc Graw-Hill, New York 1976, p. 91.

Received on August 30, 1990; English version April 15, 1992

ARCHIVES OF ACOUSTICS
18, 1, 157–161 (1993)

BRIEF NOTES

AN INFLUENCE OF VAPOURS OF SOME ORGANIC COMPOUNDS AND WATER ON ACOUSTIC PROPERTIES OF SELECTED POLYMER LAYERS

W. JAKUBIK and M. URBAŃCZYK

Institute of Physics, Silesian Technical University
(44-100 Gliwice)

The present paper deals with an investigation of the interaction of thin polymer layers with on ambient atmosphere in view to using them to design gas sensors.

The changes in physical properties of a polymer layer were recorded as a change in a differential frequency of dual acoustic delay line with a surface wave. The preliminary results demonstrate a selective sensitivity of polymer layers to gases in the ambient atmosphere.

1. Introduction

The development of polymer technology has permitted scientists to obtain compounds which change their properties as a result of interaction with ambient atmosphere. This fact creates possibilities for using polymer compounds as selective sensors of various gases. The change of physical properties of specially prepared thin polymer layers affect the conditions for propagation of a surface acoustic wave (SAW) in a layered structure: piezoelectric waveguide — polymer layer. Particularly, as a result of a change of mass and the electrical conductivity of the polymer layer, the velocity of propagation of a SAW undergoes a change [1]. This phenomenon has been used for the investigation on the influence an ambient gas medium on acoustic properties of selected polymer layers.

The changes of physical properties of the investigated polymer layer under the influence of some organic compounds and water vapour have been observed as a change in the differential frequency of dual acoustic delay lines: the delay line with an active polymer layer and the reference delay line. The experimental setup secured autocompensation of the temperature influence on the acoustic properties of the waveguide medium, which enabled acquisition of a high time stability [2].

For setting the initial conditions, the reference path has a metallic surface between transmitting and receiving transducers which ensured the electric short-circuit of the surface regardless of the condensation level of the interacting molecules on it.

The oscillator frequency of the frequency generating with the acoustic delay line in the positive feedback loop of a signal amplifier is specified by phase dependence [5]:

$$\Phi_A + 2\Phi_{\mathrm{tr}} + 2\pi f t = 2\pi n \tag{1}$$

where n is an integer, and gives the number of frequency modes of the oscillator, Φ_A and Φ_{tr} are the phase shift introduced by the amplifier and transducer, respectively.

It results from the expression (1), that the oscillator frequency is:

$$f = \frac{2\pi\nu - \Phi_e}{2\pi l} v \tag{2}$$

where v is the velocity of propagation of acoustic wave on the piezoelectric waveguide surface, and

$$\Phi_e = \Phi_A + 2\Phi_{tr} \tag{3}$$

A differential frequency of two acoustic paths (the measuring and reference delay lines) is specified by the following formula:

$$\Delta f = f - f_0 = \frac{2\pi n - \Phi_e}{2\pi l}(v - v_0) \tag{4}$$

From the expression (4) results an increase in the propagation velocity of acoustic wave in the measuring path under a constant velocity v_0 in the reference delay line, and leads to a positive increase of the differential frequency Δf. This situation occurs during a change of electric conditions on the surface of the piezoelectric waveguide as a result of condensation of polar molecules of the investigated substance.

This effect will be referred to as the electrostatic effect (EE). The size of the electrostatic effect depends on the electromechanic coupling coefficient of the waveguide material.

Apart from the EE there is also a mass effect connected with the mass loading of the acoustic waveguide surface with the condensating molecules. The increase in the mass loading of the acoustic waveguide causes a decrease of the propagation velocity in the acoustic wave. The expression (4) shows a negative increase in differential frequency Δf in this case.

During the interaction of vapours of the investigated organic compounds and water on polymer layers, the magnitude of the differential frequency depends on the resultant effect of the electrostatic and mass interaction.

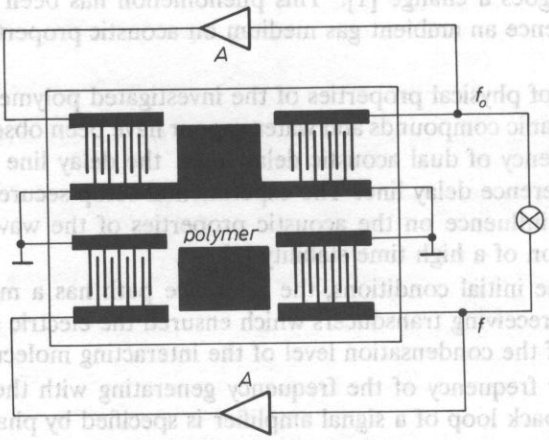

FIG. 1. Experimental system diagram.

2. Experimental setup

The experimental system is shown in the Fig. 1. The main parts of this setup were two acoustic waveguides fabricated on the piezoelectric substrate $LiNbO_3$. The transducers of the surface wave, made by the photolitography method, have 15 electrode pairs each, and were placed at 20 mm apart. The oscillation frequency was about 20 MHz. The acoustic path formed two generating systems. The generating frequency of the measuring delay line, in which an active polymer layer was placed, was influenced by the adsorption of organic compound molecules in a thin polymer layer. The frequencies obtained from each oscillator were mixed in a double balance mixer to provide the low-frequency differences signal. This signal was the measure of the interaction between vapours of organic compounds or water vapours with the polymer layer.

3. Experimental results

The experiments were carried out on the polymer layers: PVAC — poly(vinylacetate), PBA — poly n — butylakrylate, P(VAC-CO-BA), PVAC-PBA shell, PBA-PVAC shell.

The preparation of the layers to the experiments consisted in a uniform spreading of a polymer liquid drop on the area of about 5 × 3 mm. When the polymer was dry, the experimental system together with the reagent (whose vapours were to interact with the polymer) were placed on an open dish and put into a closed chamber. The pressure in the chamber was decreased to about 1 Tr. During evaporation the differential frequency of acoustic paths was measured.

The influence of acetone and methanol vapours is shown in Fig. 2, 3 and 4. Fig. 5 shows the influence of the humidity of the medium on acoustic properties of PVAC polymer. The frequency f_0 corresponds with the differential frequency for the stipulated instant $t = 0$.

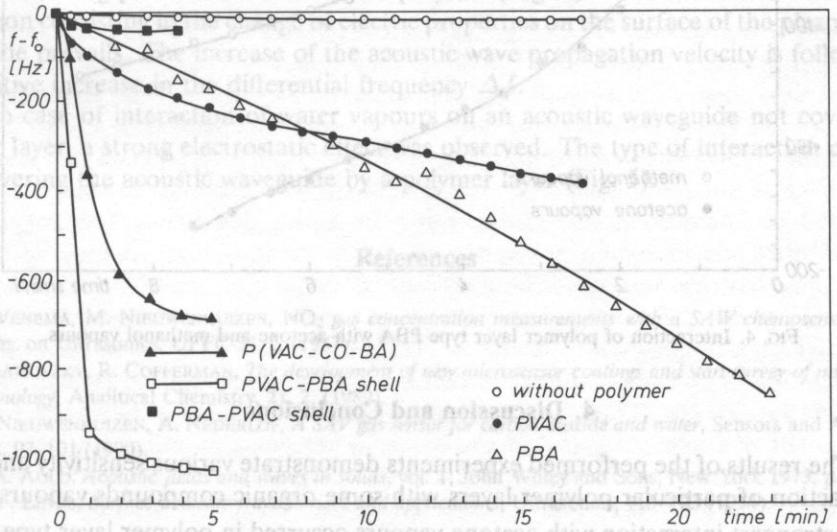

FIG. 2. Interaction of acetone vapours and the polymer layers.

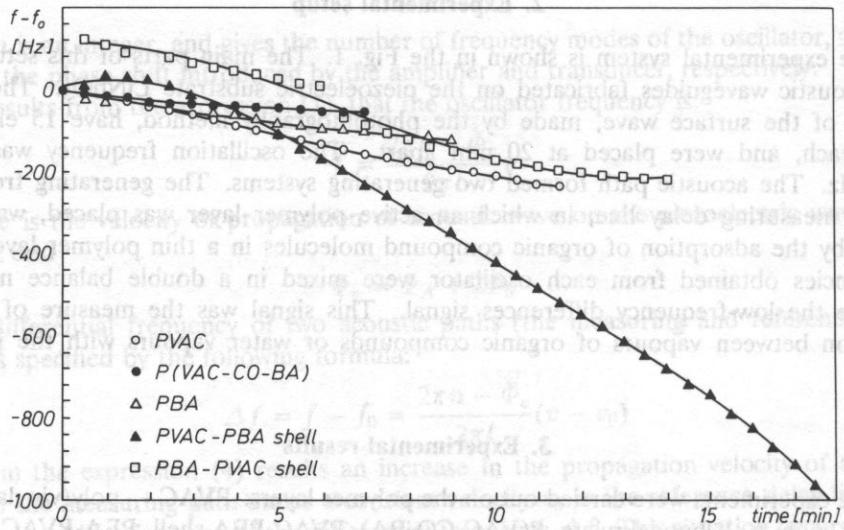

FIG. 3. Interaction of methanol vapours and the polymer layers.

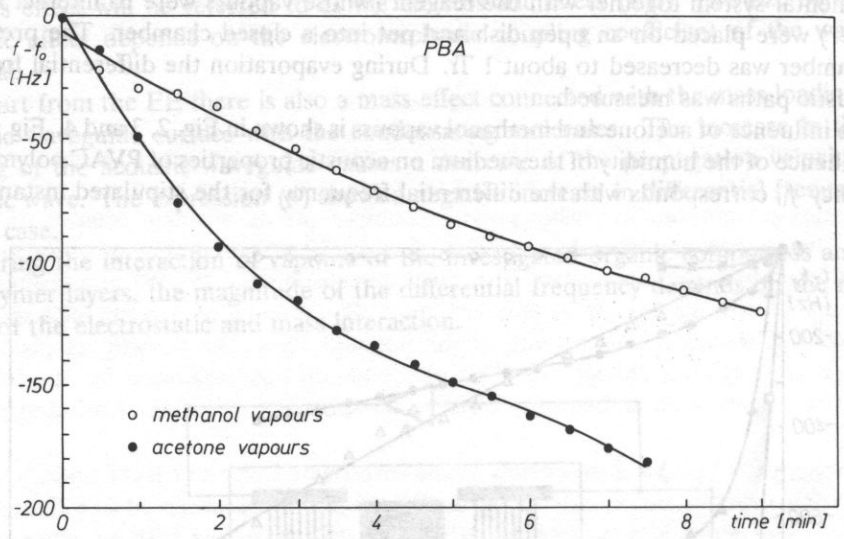

FIG. 4. Interaction of polymer layer type PBA with acetone and methanol vapours.

4. Discussion and Conclusions

A. The results of the performed experiments demonstrate various sensitivity and speed of interaction of particular polymer layers with some organic compounds vapours.

The strongest interaction with acetone vapours occurred in polymer layer type PVAC-PBA shell. The polymer type PBA is sensitive to acetone vapours, while its interaction with methanol vapours is weak.

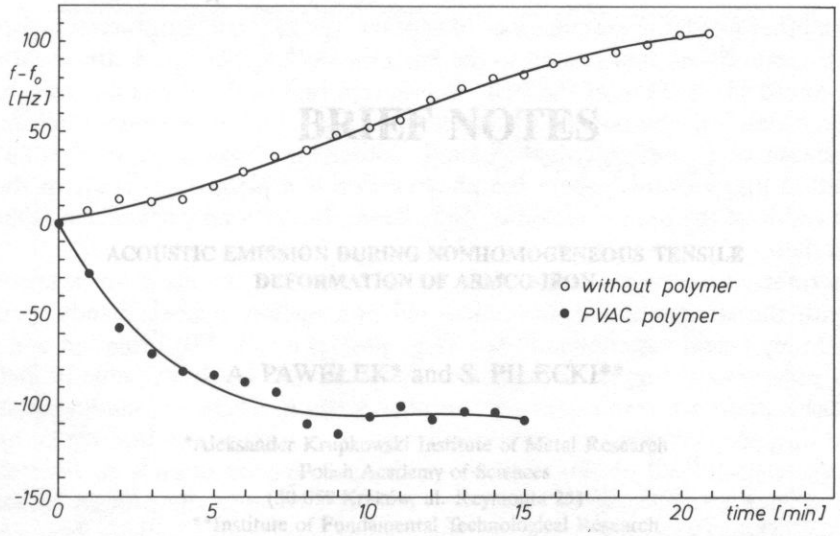

FIG. 5. Influence of water vapour on polymer layer type PVAC.

B. The negative values of differential frequency point to a mass character of the polymer layer interaction with vapours of the chemical compound used in the experiment. The interaction causes a decrease in the acoustic wave propagation velocity, and results in a decrease in the oscillation frequency in the measuring path.

C. The positive magnitude of the differential frequency has been observed as well. In one instance, it appeared during the interaction of the polymer layer type PVAC-PBA shell with methanol vapours (Fig. 3), and during condensation of water vapour molecules on the measuring path not covered by the polymer (Fig. 5). In this case the electrostatic interaction consisting in the change of electric properties on the surface of the piezoelectric waveguide prevails. The increase of the acoustic wave propagation velocity is followed by the positive increase in the differential frequency Δf.

D. In case of interaction of water vapours on an acoustic waveguide not covered by polymer layer, a strong electrostatic effect was observed. The type of interaction changed after covering the acoustic waveguide by a polymer layer (Fig. 5).

References

[1] A. VENEMA, M. NIEUWENHUIZEN, NO_2 *gas concentration measurements with a SAW chemosensor*, IEEE Trans. on Ultrasonics, UFFC-34, 2, (1987).

[2] J. KATRITZKY, R. COFFERMAN, *The development of new microsensor coatings and start survey of microsensor technology*, Analitical Chemistry, **21**, 2, (1989).

[3] M. NIEUWENHUIZEN, A. NEDERLOF, *A SAV gas sensor for carbon dioxide and water*, Sensors and Actuators, B, 2, 97–101 (1990).

[4] B. A. AULD, *Acoustic fields and waves in solids*, vol. 1; John Willey and Sons, New York 1973, p. 285.

[5] M. F. LEWIS, *Surface acoustic wave devices and applications*, Ultrasonics, 115–123 (1974).

Received on February 6, 1992

ARCHIVES OF ACOUSTICS
18, 1, 163–170 (1993)

BRIEF NOTES

ACOUSTIC EMISSION DURING NONHOMOGENEOUS TENSILE DEFORMATION OF ARMCO-IRON

A. PAWEŁEK* and S. PILECKI**

*Aleksander Krupkowski Institute of Metal Research
Polish Academy of Sciences
(30-059 Kraków, ul. Reymonta 25)
**Institute of Fundamental Technological Research
Polish Academy of Sciences
(00-049 Warszawa, ul. Świętokrzyska 21)

Measurements of acoustic emission count rates and RMS value in the ARMCO-iron have been carried out in tensile loading. Specimens of the ARMCO-iron have been used in two stands: annealed or pre-rolled and cut in parallel or perpendicular direction. Experimental results have been discussed in the light of possibility of dislocation proliferation and annihilation as well as their accelerated and decelerated movement.

1. Introduction

There is not any great number of works dealing with the correlation between nonhomogeneous deformation — mainly such types as Lüders bands, Portevin-LeChatelier bands and shear bands — and its influence on the behaviour of acoustic emission (AE) activity. The first most important observation of AE during Lüders deformation was made by FISHER and LALLY [1]. They observed that during tensile deformation of 0.1% carbon steel, a peak of AE activity occurred near the upper yield point and afterwards, i.e., in the region of Lüders bands propagation this activity rapidly decreased and remained at a nearly constant level after which it again decreased monotonically with increasing strain hardening. The authors suggested that such AE behaviour resulted from the fast collective movement of a great number of dislocations however, they did not discuss any particular mechanism of direct reasons of AE. A similar observation of a strong increase of the AE activity during the nucleation of a Lüders band in the region of the upper yield point in Fe-Si alloys was carried out by TANDOM and TANGRI [2], who related this fact to the observed dislocation pile-ups, the presence of which they explained by the operation of the dislocation sources in the grain boundaries. Another behaviour of AE activity in the region of the Lüders plateau, discussed in details in Sect. 3 of this paper, was recently reported in [3] where the AE sources are related, also in a general way, to dislocation movement, to the overcoming of obstacles by dislocations as well as to the slip bands nucleation and propagation.

On the other hand, the examinations of another type of nonhomogeneous deformation by the AE method, i.e., that related to the Portevin-LeChatelier effect, are so far slightly more advanced [4–8]. One of the first studies, reported in the literature available, was that by PASCUAL [4], who noticed that each local peak of the flow strain is accompanied by an increase of the AE activity. A similar observation was made by CACERES and BERTORELLO [6]. In both papers the phenomenon is explained generally in the same way, as a result of the multiplication of dislocations, but also no particular mechanism is discussed there.

Furthermore, to our knowledge there are no reports in the literature available concerned with the studies of the nucleation and propagation of shear bands by the AE method. Many recent experimental data (e.g., [9–11]) on the SB formation and propagation in polycrystals, suggest strongly that the collective, highly dynamic properties of moving dislocations are responsible for this phenomenon. There are simultaneously synchronized in space and time, and successively organized from micro- through meso- up to macroscopic well-defined objects. Moreover, this propagation often occurs across many grains by a "non-crystallographic" way, i.e., without change in the primary direction of propagation. Hence we suppose that the specific behaviour of AE activity should be then observed. Therefore the main aim of this paper is to report on the AE behaviour during tensile deformation of pre-rolled polycrystalline ARMCO iron where shear bands nucleation and propagation are visible even with the naked eye, and to explain a particular type of AE behaviour during tensile deformation of annealed polycrystalline ARMCO iron in the region of the Lüders plateau.

2. Experiments and results

A. AE in annealed ARMCO iron

The cylindrical samples for measuring AE parameters were cut from ARMCO iron containing 2% C, rolled rods of a 20–30 mm diameter. The final specimens of 65 mm in length and 12 mm in diameter were annealed at 950° C for 1 hour in the vacuum and then furnace cooled to room temperature. The tensile tests were carried out at strain rate $\dot{\varepsilon} = 2.8 \times 10^{-4}\ s^{-1}$ using the testing machine of the ZWICK-10T type. AE characteristics were meassured by applying the Structural Integrity Monitoring System SIMS device, developed by the TRODYNE Company (USA), which contains an analog and digital system for the conversion of electric signals. The following AE parameters were measured: AE count rate in unit time base equal to 0.3 s and the RMS (root mean square), i.e., the effective value of an electric signal. These magnitudes were recorded by total amplification equal to 98 dB (including that from the preamplifier) and at the discriminator threshold equal to 0.25 V. The applied piezoelectric transducer of resonant frequency 200 kHz was made from PP type ceramics produced in Poland or Germany (see also [3]).

Figure 1 shows both mechanical and AE characteristics during the tensile deformation of annealed ARMCO iron. A specific type of AE behaviour is seen in the Lüders plateau region. The AE count rate has (Fig. 1a), as usual, the peak at the yield point; however, in the Lüders region it is not nearly constant at a considerably low level — as it was observed in most cases so far (see, e.g. [1, 12]) — but varies nearly periodically reaching at maxima values even higher than at the yield point. This is clearly visible in Fig. 1b where the

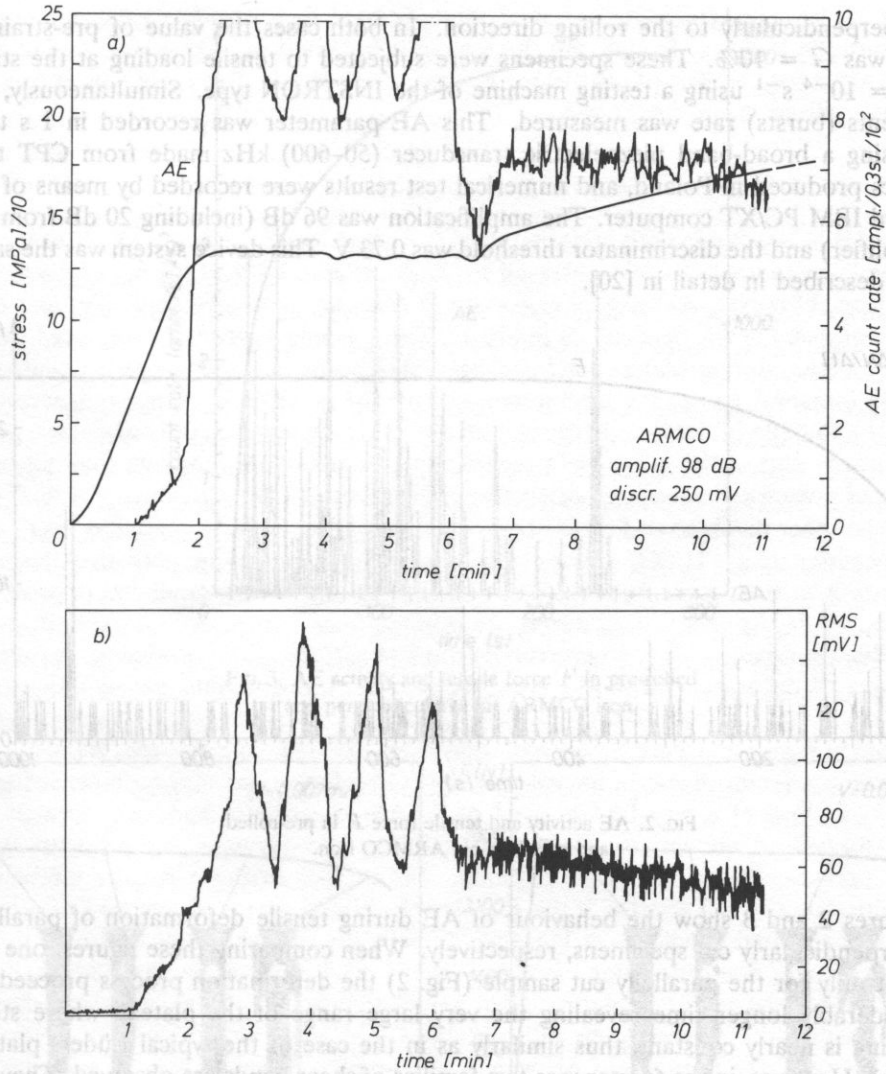

FIG. 1. AE activity in annealed ARMCO iron: a — stress curve and AE count rate, b — effective voltage of AE signal RMS [3].

time dependence of the RMS is shown. In the region of increasing strain hardening the AE count rate (Fig. 1a) and also RMS (Fig. 1b) are considerably less than within the Lüders plateau, reaching a nearly constant level with a tendency to decrease — according to earlier observations reported, e.g., in [1, 2, 12].

B. AE in pre-rolled ARMCO iron

Planar samples of size 80 mm × 12 mm × 1 mm were made from the rolled sheet of 2% C ARMCO iron. Two kinds of specimens were made: one cut parallelly and the

other perpendicularly to the rolling direction. In both cases the value of pre-strain in rolling was $G = 10\%$. These specimens were subjected to tensile loading at the strain rate $\dot{\varepsilon} = 10^{-4}\ s^{-1}$ using a testing machine of the INSTRON type. Simultaneously, the AE events (bursts) rate was measured. This AE parameter was recorded in 1 s time base using a broad-band piezoelectric transducer (50–600) kHz made from CPT type ceramics produced in Poland, and numerical test results were recorded by means of the standard IBM PC/XT computer. The amplification was 96 dB (including 20 dB from the preamplifier) and the discriminator threshold was 0.73 V. This device system was the same as that described in detail in [20].

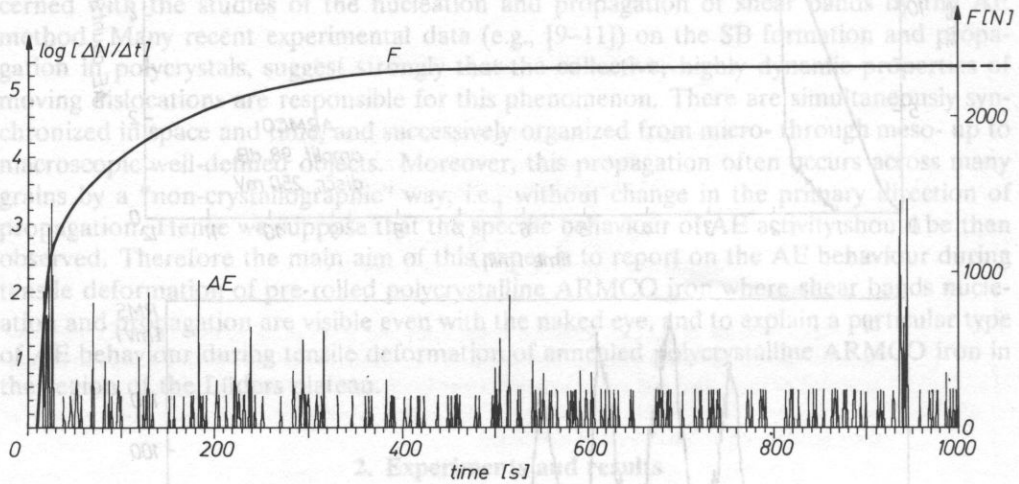

FIG. 2. AE activity and tensile force F in pre-rolled and parallelly cut ARMCO iron.

Figures 2 and 3 show the behaviour of AE during tensile deformation of parallelly and perpendicularly cut specimens, respectively. When comparing these figures, one can see that only for the parallelly cut sample (Fig. 2) the deformation process proceeds in a considerably longer time revealing the very large range of the plateau where strain hardening is nearly constant, thus similarly as in the case of the typical Lüders plateau (Fig. 1a). However, in the former case two families of shear bands are observed. They are similar to Lüders ones, but they cross each other, and, in the courses of the deformation process, they are successively converted into micro- and finally — at the beginning of the necking — into macroshear bands visible even with the naked eye. This is illustrated, for example, in Fig. 4 in the scale 1:2 [The load curve at the beginning of deformation is different here from the one in Fig. 2, due to different values of pre-strains, but such a picture of shear bending is very typical in both cases (see, e.g. KORBEL)].

Now, we make a general comparison between the AE behaviour within the typical Lüders plateau in the annealed sample (Fig. 1a) and the AE behaviour in the parallelly cut sample (Fig. 2). One can see, apart from the region of the yield point where AE activity is very high in both cases, that in the latter case the AE varies incidentally reaching very high and sharp local maxima, whereas in the typical Lüders case these maxima are very smooth and they proceed rather in a more regular way. A more precise comparison is,

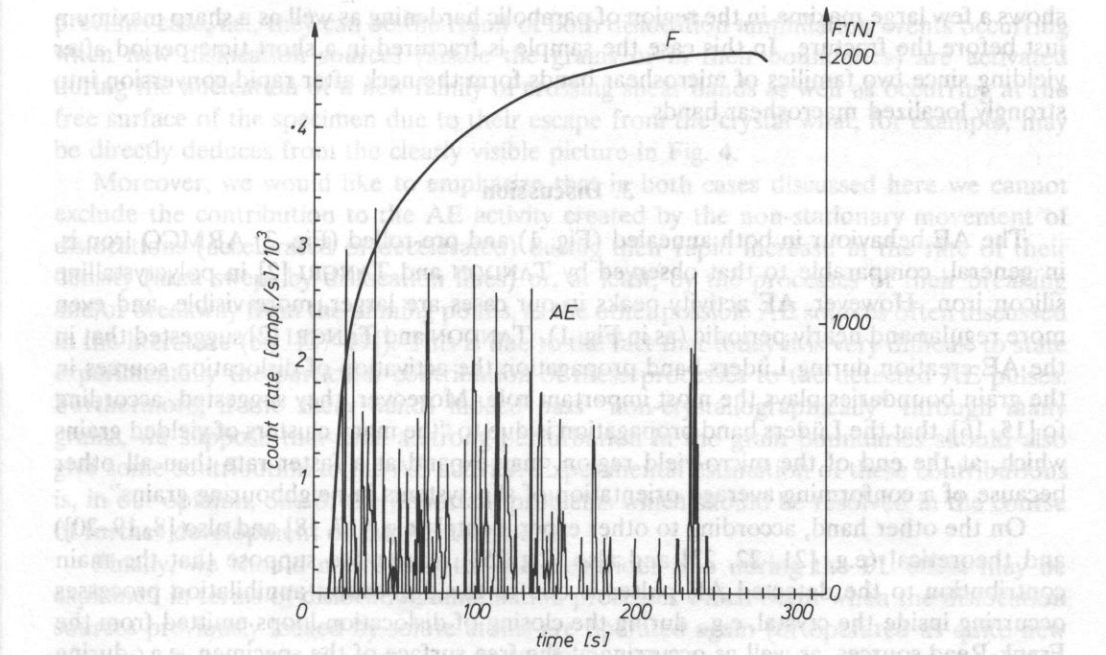

FIG. 3. AE activity and tensile force F in pre-rolled and perpendicularly cut ARMCO iron.

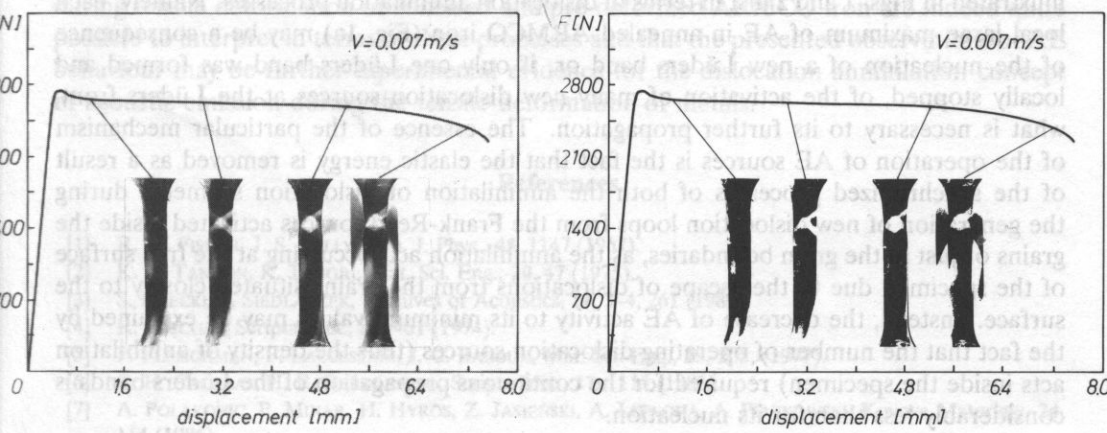

FIG. 4. Formation and propagation of two families of crossing shear bands as a typical mechanical characteristic of pre-rolled and parallelly cut ARMCO iron (after [9]).

however, not possible since the results illustrated in Figs. 1 and 2 were obtained using different techniques.

On the other hand, in the case of the perpendicularly cut specimen (Fig. 3), one can see that the plasticity is considerably smaller and the deformation process without of very large region of constant strain hardening. AE activity is also high at the yield point and

shows a few large maxima in the region of parabolic hardening as well as a sharp maximum just before the fracture. In this case the sample is fractured in a short time period after yielding since two families of microshear bands form the neck after rapid conversion into strongly localized macroshear bands.

3. Discussion

The AE behaviour in both annealed (Fig. 1) and pre-rolled (Fig. 2) ARMCO iron is, in general, comparable to that observed by TANDON and TANGRI [2] in polycrystalline silicon iron. However, AE activity peaks in our cases are larger, more visible, and even more regular and nearly periodic (as in Fig. 1). TANDON and TANGRI [2] suggested that in the AE creation during Lüders band propagation the activation of dislocation sources in the grain boundaries plays the most important role. Moreover, they suggested, according to [15, 16], that the Lüders band propagation is due to "the many clusters of yielded grains which, at the end of the micro-yield region, may expand at a faster rate than all other because of a conforming average orientation of slip systems in neighbouring grains".

On the other hand, according to other experimental (e.g. [17, 18] and also [8, 19–20]) and theoretical (e.g. [21, 22, 23] and also [24, 25]) results, we suppose that the main contribution to the detected AE pulses is due to the dislocation annihilation processes occurring inside the crystal, e.g., during the closing of dislocation loops emitted from the Frank-Read sources, as well as occurring at the free surface of the specimen, e.g., during the escape of dislocations from the crystal interior (i.e., the annihilation of dislocations with their virtual images). We would like to show that it is possible to explain results illustrated in Figs. 1 and 2 just in terms of dislocation annihilation processes. Namely, each local large maximum of AE in annealed ARMCO iron (Fig. 1a) may be a consequence of the nucleation of a new Lüders band or, if only one Lüders band was formed and locally stopped, of the activation of many new dislocation sources at the Lüders front, what is necessary to its further propagation. The essence of the particular mechanism of the operation of AE sources is the fact that the elastic energy is removed as a result of the synchronized processes of both the annihilation of dislocation segments during the generation of new dislocation loops from the Frank-Read sources activated inside the grains or just in the grain boundaries, as the annihilation acts occurring at the free surface of the specimen due to the escape of dislocations from the grains situated closely to the surface. Instead, the decrease of AE activity to its minimum values may be explained by the fact that the number of operating dislocation sources (thus the density of annihilation acts inside the specimen) required for the continuous propagation of the Lüders bands is considerably less than for its nucleation.

In a similar way the AE behaviour in a pre-rolled ARMCO-iron specimen cut parallelly to the rolling direction (Fig. 2) may be interpreted. First of all, it is necessary to emphasize the fact that the deformation mechanism responsible for the existence of the large plateau region without the work-hardening is strongly related to the nucleation and propagation of two families of shear bands (quite similar to the Lüders ones) crossing each other and operating simultaneously up to the moment of the beginning of necking where they strongly localize and the form the macroshear bands of "cross" shape, (Fig. 4) clearly visible. Hence we suppose that the more or less regular sharp peaks of AE activity appearing in the course of the deformation process may be also explained similarly as the

previous case, i.e., they can be the result of both dislocation annihilation events occurring when new dislocation sources (inside the grains or in their boundaries) are activated during the nucleation of a new family of crossing shear bands as well as occurring at the free surface of the specimen due to their escape from the crystal what, for example, may be directly deduces from the clearly visible picture in Fig. 4.

Moreover, we would like to emphasize that in both cases discussed here we cannot exclude the contribution to the AE activity created by the non-stationary movement of dislocations (accelerated or decelerated) during their rapid increase in the rate of their density (area swept by dislocation lines) or, at least, by the processes of their breaking and/or breakway from the pinning points, as the other possible AE sources often discussed in the literature (e.g. [27–29]). This is due to the fact that today it is very difficult to state experimentally the particular contribution of these processes to the detected AE pulses. Furthermore, if the shear bands indeed pass "non-crystallographically" through many grains, we suppose that such a strong perturbation in the grain boundaries should also give some contribution to the AE activity. Experimental estimation of these contributions is, in our opinion, one of the important problems which should be resolved in the course of further development of the AE technique.

Finally, we should notice that the AE behaviour also during the PL effect may be explained in terms of dislocation annihilation processes which occur when the dislocation sources previously locked by solute atoms are operated again (or operated as quite new sources), what was mentioned earlier in [8, 20, 30]. Hence we are strongly convinced that the main contribution to the detected AE pulses is due to the dislocation annihilation processes. And we believe that the observations presented here of the peaks of AE activity during tensile deformation of annealed and pre-deformed ARMCO iron are indeed quite possible to interpret in terms of these processes and that the presented observations of AE behaviour may be further experimental evidence for the dislocation annihilation concept of acoustic emission during the tensile deformation of metals.

References

[1] R. M. Fisher, J. S. Lally, Can. J. Phys., **45**, 1147 (1967).
[2] K. N. Tandon, K. Tangri, Mat. Sci. Eng., **20**, 47 (1975).
[3] S. Pilecki, J. Siedlaczek, Archives of Acoustics, **14**, 3–4, 261 (1989).
[4] R. Pascual, Scripta Met., **8**, 1461 (1974).
[5] P. Fleischman, F. Lalcestani, J. C. Baboux, Mat. Sci. Eng., **29**, 205, (1977).
[6] C. H. Caceras, H. R. Bertorello, Scripta Met., **17**, 1115 (1983).
[7] A. Polakovic, P. Minar, H. Hyros, Z. Jasieński, A. Litwora, A. Piątkowski, Kovove Materialy, **24**, 114 (1986).
[8] A. Pawełek, H. Dybiec, W. Bochniak, W. Stryjewski, Archives of Metallurgy, **34**, 239 (1989).
[9] A. Korbel, M. Martin, Acta Met., **36**, 2575 (1988).
[10] A. Korbel, Archives of Metallurgy, **35**, 175 (1990).
[11] A. Korbel, Scripta Met., **24**, 1229 (1990).
[12] A. Pawełek, A. Korbel, Phil. Mag. B61, 829 (1990).
[13] H. N. G. Wadley, C. B. Scruby, J. H. Speake, Int. Met. Rev., **249**, 41 (1980).
[14] W. Stryjewski, G. Zapalski, A. Pawełek, Archives of Metallurgy, **33**, 485 (1988).
[15] A. Hultgren, Scand. J. Met., **1**, 17 (1972).
[16] R. W. Moon, Mat. Sci. Eng., **8**, 235 (1971).
[17] V. S. Boiko, R. I. Garber, L. F. Krivenko, ZhETF, **71**, 708 (1976).

[18] V. S. BOIKO, R. I. GARBER, V. F. KIVSHIK, L. F. KRIVENKO, Fiz. Tverd. Tela **16**, 1233 (1974).
[19] A. PAWEŁEK, W. STRYJEWSKI, W. BOCHNIAK, H. DYBIEC, Phys. Stat. Sol. (a) **90**, 531 (1985).
[20] A. PAWEŁEK, W. STRYJEWSKI, H. DYBIEC, W. BOCHNIAK, Archives of Acoustics, **15**, 211 (1990).
[21] S. PILECKI, Archiwum Akustyki, **21**, 109 (1986).
[22] V. D. NATSIK, A. N. BURKHANOV, Fiz. Tverd. Tela, **14**, 1289 (1972).
[24] A. PAWEŁEK, J. Appl. Phys., **63**, 5320 (1989).
[25] A. PAWEŁEK, Archives of Metallurgy, **35**, 71 (1990).
[26] A. PAWEŁEK, Archives of Metallurgy (in press).
[27] R. T. SEDGWICK, J. Appl. Phys., **39**, 1728 (1967).
[28] D. R. JAMES, S. E. CARPENTER, J. App. Phys., **42**, 4685 (1971).
[29] E. P. HIGGENS, S. H. CARPENTER, Acta Met., **26**, 133 (1978).
[30] A. PAWEŁEK, Z. Metall. **80**, 614 (1989).
[31] W. BOCHNIAK, A. PAWEŁEK, Archives of Metallurgy, **32**, 481 (1987).

Received on March 27, 1991

ARCHIVES OF ACOUSTICS
18, 1, (1993)

C H R O N I C L E

5-TH INTERNATIONAL SPRING SCHOOL ON ACOUSTO-OPTICS AND APPLICATIONS. GDAŃSK-JURATA, 25–29 MAY, 1992.

The international spring meetings on Acousto-optics and Applications are organized every three years since 1980.*)

The 5-th School was organizes by the University of Gdańsk, Institute of Experimental Physics in co-operation with the Quantum and Molecular Acoustics section of the Polish Acoustical Society, the Committee of Acoustics of the Polish Academy of Sciences and sponsored by the Ministry of Education and by SPIE the International Society of Optical Engineering in association with the Polish Chapter of SPIE.

The Scientific Committee included: Prof. L. ADLER, Ohio State University, USA; Prof. A. ALIPPI, Instituto di Acustica, Rome Italy; Prof. P. BANERJEE, University of Alabama, USA; Dr E. BLOMME, Technisch Institut, BELGIUM; Prof. M. A. BREAZEALE, Univ. of Mississippi, USA; Dr R. C. CHIVERS, University of Surrey, U.K.; Prof. I. GABRIELLI, Univ. Trieste, Italy; Prof. H. W. JONES, Halifax, Canada; Prof. Z. KLESZCZEWSKI, Silesian Techn. Univ., Poland; Prof. A. KORPEL, Dept. ECE., Univ. of Iowa, USA; Prof. S. V. KULAKOV, Inst. Aviat. Instr., Petersburg, Russia; Prof. O. LEROY, Kath. Univ., Leuven-Kortrijk, Belgium; Prof. M. ŁABOWSKI, Univ. A. Mickiewicza, Poland; Prof. I. MALECKI, Polish Acad. Sci., Poland; Prof. W. MAYER, Georgetown University, USA; Prof. R. MERTENS, Roy. Belg. Acad. Sci., Belgium; Prof. A. OPILSKI, Silesian Techn. Univ., Poland; Prof. V. PARYGIN, Moscow State University, Russia; Prof. T. C. POON, Polyt. Inst. State Univ., Virginia, USA; Prof. V. PROKLOV, Acad. Sci., Moscow, Russia; Prof. J. RANACHOWSKI, Inst. Fund. Techn. Res. Polish Acad. of Sciences, Poland; Dr R. REIBOLD, PTB, Braunschweig, Germany; Prof. J. SAPRIEL, Centr. Nat. d'Etudes Tel., Paris, France; Prof. M. SZUSTAKOWSKI, Military Techn. Acad., Poland; Prof. Chen Tsai, Univ. California, Irvine, USA; Prof. A. ZAREMBOWITCH, Dep. Rech. Phys., Paris, France.

---

*)The previous took place:

1-st School, Gdańsk-Wieżyca, 1980, May 26–30 proceedings issued by the University of Gdańsk; a report published in Arch. Acoust. 6, 85 (1981) and in Ultrasonics, **19**, 44 (1981).

2-nd School, Gdańsk-Wieżyca, 1983, May 24–29 proceedings issued by the University of Gdańsk; a report published in Arch. Acoust. 9, 381 (1984) and Ultrasonics **22**, 15 (1984).

3-rd School, Gdańsk-Wieżyca, 1986, May 26–31 proceedings issued by the University of Gdańsk; a report published in Ultrasonics, **25**, 182 (1987).

4-th School, Gdańsk-Sobieszewo, 1989, May 23–27 proceedings published by World Scientific, Singapore-New Jersey-London-Hong Kong, 1990.

The organizing Committee consisted of Prof. A. ŚLIWIŃSKI, president, Prof. P. KWIEK, vice president, Dr M. KOSMOL, secretary and members: Prof. Cz. LEWA, Dr M. BORYSEWICZ, Dr B. LINDE, Dr A. MARKIEWICZ and Dr A. SIKORSKA.

The meeting took place at Jurata situated on the Hel Peninsula 70 km from Gdańsk and gathered 46 specialists from different countries: Belgium (3), Bielorussia (1), Canada (2), France (1), Germany (4), Italy (1), Lithuania (1), Poland (22), Russia (4), Switzerland (1), USA (4). 34 papers were presented among which there were 16 invited lectures, 11 other oral contributions and 7 posters.

Besides physical and technological topics typical for acousto-optics, comprising light ultrasound interaction in solids (including surface waves) and liquids, the programme covered some problems of photoacoustics concerning generation of sound by light and acoustic microscopy. Many practical problems related to acousto-optical signal processing and construction of acousto-optical devices (modulators, filters, convolvers and analyzers) were subjects of interest.

The programme of the School included:

General papers

1. Fresnel phenomena in the nearfield of light diffracted by ultrasound.
   E. Blomme, R. Briers, O. Leroy
2. Imaging properties of SAM.
   S. Boseck
3. Towards transducer interferometry in water.
   R. C. Chivers, R. D. Bacon, J. N. Som
4. Light interaction with thermal waves.
   D. Čiplys, R. Rimeila, J. Paskauskas
5. Acousto-optic Image Correlators.
   P. Das, C. DeCusatis
6. Analysis of the light vector in the diffraction by few waves of two antiparallel ultrasonic beams.
   I. Gabrielli
7. Some Comments on Reconstruction Problems in Acoustic Tomography.
   H. Jones
8. On ultrasound light diffraction.
   R. Reibold, P. Kwiek
9. Description of Several Analytical Methods Used in the Past Fifty Years of Acousto-Optic Research in Belgium.
   O. Leroy
10. Acousto-optical Confirmation of the Localized Wave Phenomena.
    D. Kent Lewis
10. Collinear Light Diffraction on a Gaussian Acoustic Beam.
    V. N. Parygin
11. Guided wave Multichannel Acoustooptic Devices Based on Collinear Wave Propagation.
    V. V. Proklov, E. M. Korablev

12. Acousto-optics of Semiconductor Crystals and Superlattices.
J. Sapriel, P. Renosi
13. Acousto-optical examination of material properties.
A. Śliwiński
14. Performance of Acoustooptic Devices in the Presence of Noise.
Chen-Wen Tarn, Partha P. Banerjee, Jaw-Jueh Liu, P. Pliszka
15. Close to Collinear Acousto-Optical Interaction in TeO_2 Single Crystal.
V. B. Voloshinow

Oral contribution papers

1. Additional Phase Shift Effects in Acoustooptic Interaction and its Applications.
V. I. Balakshy
2. Photoacoustic imaging of semiconductor structures.
J. Bodzenta, B. Pustelna, Z. Kleszczewski
3. Diffraction of Inhomogeneous waves from Simple Rough Surface.
R. Briers, O. Leroy
4. Acousto-optic Devices for Digital Optical Holographic Gratings.
C. DeCusatis, P. Das, D.M. Lityński
5. Coherent and incoherent processes of acoustooptic interaction on the rough surface.
I. B. Esipov, N. N. Andreyev
6. The Scanning Ultrasound Microscope (ELSAM) and it's Application On the Inspection of Biological Tissues.
H. J. Hein
7. Thickness measurements on multilayered structures by SAW dispersion.
J. Krause
8. Digital generation of high quality periodic signals for the use with acousto-optic modulators.
M. Roland-Mieszkowski, P. Kwiek, A. Śliwiński
9. Time-frequency analysis of pulse photoacoustic signals.
J. Motylewski, K. Marasek
10. Photoacoustic cell for liquids and solids investigations.
J. Ranachowski, J. Motylewski, J. Rzeszotarska, W. Opydo
11. High resolution pin scanning microscopy.
J. Zieniuk

Poster form papers

1. Acoustooptic interactions in nematic liquid crystal.
M. Borysewicz, M. Kosmol
2. Photodeflection Spectroscopy of the Flowing Gyrotropic Media.
G. S. Mityurich, P. V. Astakhov
3. Photoacoustic transformation in gyrotropic media at interaction of two light beams.
G. S. Mityurich, V. P. Zelyony, A. N. Serdyukov
4. Physics and Technology of Ultrasound in Moscow.
N. Shibanova

5. Photoacoustic spectra of ethanolic solutions of malachite green adsorbed on a silica gel surface.
   A. Sikorska, S. Zachara
6. Elastic mean Free Path of Acoustic Waves in Randomly Inhomogeneous Media.
   E. Soczkiewicz
7. Application of Infrared Absorption and Fourier Transformed Infrared Photoacoustic Spectra for Investigating Molecular Vibrations in Europium Chelates.
   S. Zachara, A. Sikorska

The sessions involved numerous debates, in addition the Round Table discussion was arranged on three topics: acousto-optical imaging, acoustic and optical microscopy and reverse problem in acousto-optics. A wide information and opinion exchange among specialists took place during a long fruitful discussions.

The proceedings of the School are published by the International Society of Optical Engineering (SPIE) (Acousto-Optics and Applications, A. Śliwiński, P. Kwiek, B. Linde, A. Markiewicz [Eds.] Proc. SPIE 1844, 1–361, 1992). Some selected papers in extended versions will be published in a special issue of the journal ULTRASONICS.

The next 6-th International Spring School on Acousto-optics and Applications will be organized in May 1995.

Antoni S. Śliwiński